Measurement of Z-boson production and luminosity monitoring using 5.02 TeV and 13 TeV ATLAS Run-2 pp collision data

Thesis submitted in accordance with the requirements of the University of Liverpool for the degree of Doctor in Philosophy by

Harry John Lyons

March 2022

Department of Physics
Oliver Lodge Laboratory
University of Liverpool

Abstract

Measurement of Z-boson production and luminosity monitoring using 5.02 TeV and 13 TeV ATLAS Run-2 pp collision data

Two analyses involving Drell-Yan production using ATLAS Run-2 pp collision data are presented. First, the monitoring of luminosity at 60 second granularity using the Z-counting method is presented. This involves the selection of $Z \to ee$ and $Z \to \mu\mu$ events combined with data-driven efficiency calculations and pileup dependent corrections from Monte Carlo. Comparisons of luminosity estimates are performed using the full Run-2 dataset from 2015-2018, where internal consistency is shown between $Z \to ee$ and $Z \to \mu\mu$ methods and year-dependent trends of size 1% are shown between Z-counting and the baseline ATLAS luminosity measurement. An additional study is performed to quantify statistical bias in the Z-counting methodology, which is observed to be negligible for most Run-2 conditions but can be as large as 2% when the instantaneous luminosity is low. Second, the measurement of a triple-differential Drell-Yan cross-section in $m_{\ell\ell}$, $|y_{\ell\ell}|$ and $\cos(\theta^*_{CS})$ is presented. These measurements use the special low-μ runs from 2017 and 2018, constituting 256.8 pb^{-1} at $\sqrt{s} = 5.02\,\text{TeV}$ and 335.2 pb^{-1} at $\sqrt{s} = 13\,\text{TeV}$. This includes the derivation of muon trigger efficiency scale factors, the estimation of multijet background contribution and the implementation of an unfolding procedure. The unfolded differential cross-sections are shown to be statistically limited in most analysis bins, and the inclusive fiducial cross-sections are shown to be limited by the luminosity uncertainty in the central-mass region.

Declaration

I hereby confirm this work is my own, except where other works are referenced. This work has not previously been submitted to any institute, including this one. This thesis does not exceed the relevant word count.

Harry John Lyons

Acknowledgements

Firstly, I would like to express sincere gratitude to my supervisor Jan Kretzschmar for his patience and guidance throughout the PhD. I also extend this thanks to Simone Amoroso for overseeing my work while studying at DESY. I want to thank you both for the countless hours of discussion and the invaluable help with all my questions, from physics to software. The content of this thesis would not be possible without either of you.

I am grateful to have worked alongside my colleagues in the low-μ analysis group and the Z-counting team. I thank all I worked alongside for all of the provided help, and I wish to highlight how proud I am of our hard work and progress on these exciting analyses. I am also grateful to all those in the DESY single-boson meetings for providing invaluable discussion beyond the scope of my studies. I also thank the Liverpool ATLAS group, the Liverpool HEP department and the DESY ATLAS group for providing me with the opportunity to do this PhD, for the continued support of my research, and the organisation of the trips and conferences I was able to attend.

I extend my thanks to all my friends, both inside and outside the world of physics. Your support helped me through all of the challenges of this PhD, especially those not directly related to the study of physics. Finally, I thank my family for their loving support through the writing of this thesis, the eight years of my undergraduate and PhD academic study, and most importantly, for supporting my interest in science since childhood.

Contents

1 Introduction

The ultimate goal of particle physics is to study and understand the building blocks and mechanics of the universe around us. Throughout the last century, our understanding has evolved and expanded numerous times and has led to what is now called the Standard Model (SM) of particle physics. The SM is a framework for describing the physical properties of all known particles and the interactions between them through the electromagnetic, weak and strong forces. The SM has predicted many results before their eventual measurement and has withstood huge amounts of experimental scrutiny. However, it is not a complete theory, and there are many open questions. These include, but are not limited to: a lack of explanation for the dark matter observed in astrophysical and cosmological measurements, a lack of explanation for the gravitational force at the quantum scale, and no explanation for the asymmetry observed between matter and antimatter in the universe. These shortcomings have motivated many theories on physics beyond the SM (BSM), which future experiments can provide valuable insight.

Since it began operation in 2008, the Large Hadron Collider (LHC) has produced an immense amount of proton-proton (pp) collisions delivered to the various attached detectors. This thesis discusses data collected by the ATLAS detector, which has facilitated hundreds of experimental measurements ranging from measurements of known processes to searches for rare SM processes and searches for BSM physics. Many analyses are approaching the realm where statistical uncertainties are comparable to or are dominated by systematic uncertainties.

The first analysis discussed in this thesis is a new measure of luminosity by counting Z-boson event rates. The Z-counting method provides two independent measures of luminosity in the $Z \to ee$ and $Z \to \mu\mu$ channels with a self-calibrating procedure shown to be robust under high-luminosity conditions. In this thesis, it is studied as a relative measure of luminosity using the full $\sqrt{s} = 13\,\text{TeV}$ Run-2 dataset. Luminosity uncertainty is often a large uncertainty on cross-section measurements and knowledge of the luminosity is necessary for scaling background contributions in searches. This new method can contribute to improving the precision of luminosity measurement at ATLAS.

The second analysis discussed in this thesis is a triple differential cross-section measurement of the Drell-Yan process at $\sqrt{s} = 5.02\,\text{TeV}$ and $\sqrt{s} = 13\,\text{TeV}$ using using special sets of data using a substantially lower pileup than standard running conditions (denoted as low-μ runs). The unique benefits of these datasets over previous Drell-Yan measurements are that they allow the selection of leptons with considerably lower $p_T(\ell)$ due to lowering of single-lepton trigger thresholds to $p_T(\ell) > 15\,\text{GeV}$ compared to $p_T(\ell) > 20\,\text{GeV}$ and $p_T(\ell) > 25\,\text{GeV}$ used elsewhere. In addition, these datasets are prescribed the most precise estimates of luminosity performed

by ATLAS. The measurement is binned in three dimensions: The di-lepton invariant mass $m_{\ell\ell}$, the absolute di-lepton rapidity $|y_{\ell\ell}|$ and the quantity $\cos(\theta^*_{CS})$ where θ^*_{CS} is the decay polar angle in the Collins-Soper angle. The bins selected to improve sensitivity to Parton Distribution Functions and electroweak parameters. These results can be used in future fits to improve theoretical modelling and constrain modelling uncertainties in other analyses.

Thesis Outline

Part I: Theoretical Overview This begins with Chapter 2, which discusses the Standard Model. Chapter 3 then discusses the theory behind physics processes at hadron colliders before giving an overview of the Drell-Yan process. In addition, there is also a discussion on simulating physics processes using Monte Carlo event generators.

Part II: Experimental Overview This begins with Chapter 4, which discusses the Large Hadron Collider, the ATLAS experiment, luminosity measurement and pileup. Chapter 5 discusses the reconstruction of physics objects used within the analyses. Chapter 6 discusses the calibration and correction procedures used for the low-μ datasets.

Part III: Analysis This begins with Chapter 7, which presents the monitoring of ATLAS luminosity by counting $Z \to \ell\ell$ events using Run-2 data. Chapter 8 presents work towards a triple-differential cross-section measurement of the Drell-Yan process using $\sqrt{s} = 5.02\,\text{TeV}$ and $\sqrt{s} = 13\,\text{TeV}$ data taken under low-μ conditions.

A summary of the results is provided in Chapter 9.

Personal Contributions

In Chapter 6 the derivation of the low-μ muon trigger scale factors was performed by myself. The remaining calibrations and corrections were derived by colleagues in the low-μ analysis group, electron performance group and muon performance groups. In Chapter 7 my personal contribution was the derivation of Monte Carlo correction factors, the derivation of the uncertainty formulae and the study of statistical bias in the methodology. I also contributed to the stability studies of the Z-counting results using the Run-2 dataset, which was performed collaboratively within the Z-counting analysis group. The implementation of the $Z \to \mu^+\mu^-$ channel into the analysis framework existed prior to the starting of my PhD and the implementation of $Z \to e^+e^-$ was mostly performed by a colleague. In Chapter 8 the analysis was constructed using software and calibration files provided by colleagues in the low-μ analysis group. The statistical combination of electron and muon results was performed by a colleague. The remaining work was performed by myself. All plots and tables in this thesis were created by myself, unless specifically referenced to another source.

Part I

Theoretical Overview

2 Standard Model

The Standard Model (SM) is the theory underlying modern particle physics, providing a unified description of all known elementary particles and a description of their interactions via the electromagnetic, weak and strong nuclear forces. The SM was developed during the 1900s in an interplay between theoretical and experimental advancements. This chapter discusses the particles within the SM and gives an overview of the mathematical framework that describes these particles and their interactions.

2.1 Constituent Particles

Particles in the SM are separated into two categories: fermions and bosons. Fermions are particles of spin $\frac{1}{2}$ that obey Fermi-Dirac statistics, and bosons are particles of integer spin that obey Bose-Einstein statistics.

The 12 fermions in the SM are separated into six quarks and six leptons divided into three generations of increasing mass. Each lepton generation consists of one massive particle with electric charge (electron e, muon μ, tau τ) and a corresponding neutrino (electron neutrino ν_e, muon neutrino ν_μ, tau neutrino ν_τ). Originally neutrinos were envisaged as being exactly massless, it is now known from measurements of neutrino oscillation experiments [1] that neutrinos have finite differences between their masses, and hence cannot be said to be massless. Direct constraints on the neutrino mass [2] result in an upper limit of $m_\nu < 0.8\,\text{eV}$, which is largely irrelevant for collider physics. Each generation of quark consists of an "up-type" (up u, charm c, top t) and "down-type" (down d, strange s, bottom b) massive particle of electric charge $+\frac{2}{3}$ and $-\frac{1}{3}$ respectively, expressed in units of proton electric charge. Quarks also carry a "colour" charge, prescribed by the colours *red*, *green* or *blue*. Each fermion has a corresponding anti-fermion counterpart of identical mass and opposite charge, and where applicable, colour-charge. Composite particles formed from combinations of strongly interacting quarks that result in colour-charge neutral states are called hadrons. Mesons are formed as pairs of quarks, baryons as groups of three, and recently discovered tetraquarks and pentaquarks containing four and five constituent quarks, respectively. Notable baryons are protons (uud) and neutrons (udd) which, in combination with electrons, produce nuclei and atoms that constitute the universe's visible matter.

The three interactions described by the SM are mediated via gauge bosons (spin-1 bosons). Electromagnetic interactions occur between charged particles and are propagated by a massless neutral photon γ of infinite range. Weak interactions are mediated by three heavy particles:

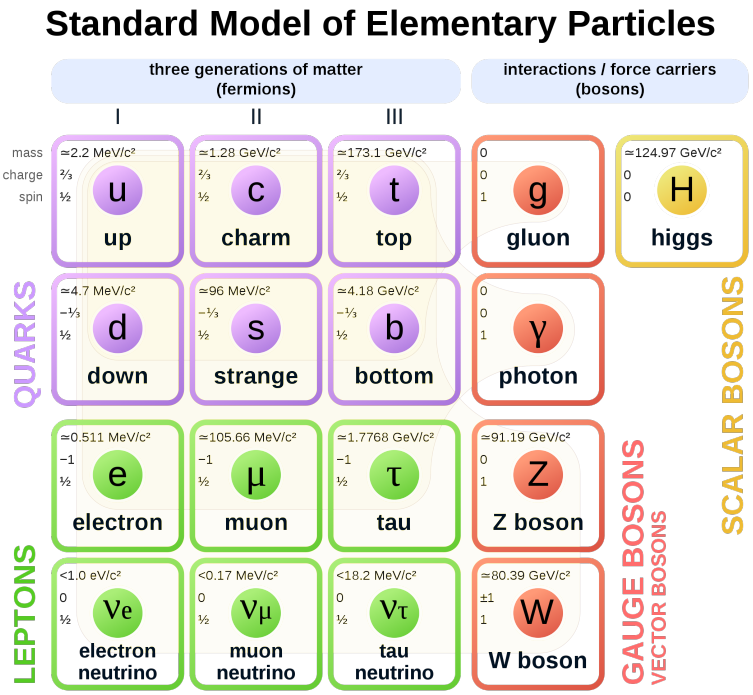

Figure 2.1: The fundamental particles of the SM of particle physics: fermions, gauge bosons and the Higgs boson. The properties shown take data from the Particle Data Group [3]. Graphic obtained from [4].

the charged W^+ and W^--bosons and the neutral Z-boson. At low energies, the relatively large mass of the weak bosons causes a short-range force or a weakly interacting force from which its name originates. In the SM, the electromagnetic and weak force are unified into a single electroweak interaction. Interactions propagated by the W^+-boson and W^--boson are referred to as "charged current" interactions. Mixing the electromagnetic and weak force results in a "neutral current" interaction that involves a mixture of Z and γ, collectively denoted Z/γ^* where γ^* specifically referrs to a virtual photon. The strong force is substantially stronger than the others and is carried by eight unique massless gluons with no electroweak charge but with different colour-charges of colour and anti-colour pairs. The strong force has a strength that increases for low energies or large distances, giving rise to the confinement of quarks and gluons into hadronic states.

Finally, the SM contains a scalar spin-0 boson called the Higgs boson, which provides the origin of mass for the W- and Z-bosons through spontaneous symmetry breaking (the Higgs mechanism) as well as the mechanism for fermions to acquire mass.

2.2 Quantum Fields and Symmetries

The SM is a Quantum Field Theory (QFT), which is a framework that combines quantum mechanics with special relativity. QFT follows classical mechanics principles and summarises the dynamics of a system by defining a lagrangian density $\mathcal{L}$ (usually referred to as just a

lagrangian). The lagrangian is a generalised function of fields ϕ and their space-time derivatives $\partial_\mu\phi$ where the dynamics of a field are evaluated from the Euler-Lagrange equation

$$\partial_\mu\left(\frac{\partial\mathcal{L}}{\partial(\partial_\mu\phi)}\right) - \frac{\partial\mathcal{L}}{\partial\phi} = 0. \tag{2.1}$$

Interactions between fields in the SM arise by imposing that the constructed lagrangian is invariant with respect to local gauge choice, which introduces fields for the force-carrying gauge boson particles. The full SM is constructed to be symmetric with respect to three group transformations:

$$\mathrm{SU}(3)_C \otimes \mathrm{SU}(2)_L \otimes \mathrm{U}(1)_Y, \tag{2.2}$$

where $\mathrm{SU}(3)_C$ describes the QCD interactions of quarks and gluons and their corresponding colour-charges, and $\mathrm{SU}(2)_L \otimes \mathrm{U}(1)_Y$ describes electroweak interactions and the corresponding hypercharge Y and weak isospin for left-handed chirality states. The terms $\mathrm{U}(n)$ and $\mathrm{SU}(n)$ are defined by,

- Unitary Group $\mathrm{U}(n)$: group consisting of n^2 generators (unitary $n \times n$ matrices where $U^\dagger \cdot U = U \cdot U^\dagger = I$).
- Special Unitary Group $\mathrm{SU}(n)$: group consisting of a subset of $\mathrm{U}(n)$ for which the determinant $\det(U(n)) = 1$ consists of $n^2 - 1$ generators.

The transformation of a group $\psi(x) \to \psi'(x)$ is given by

$$\psi'(x) = U(x)\psi(x) = e^{it_a\alpha^a(x)}\psi(x), \tag{2.3}$$

where t_a denotes a given generator a for the group. The groups in the SM specifically have the generators,

- U(1): A single generator a 1×1 matrix, or rather 1 itself.
- SU(2): Three generators $\frac{1}{2}\sigma_a$, which are expressed by the Pauli spin matrices σ_a.
- SU(3): Eight generators, represented by the Gell-Mann matrices λ_a.

2.2.1 Quantum Electrodynamics

Quantum Electrodynamics (QED) describes the interaction between the vector field A_μ, which we commonly associate with the photon, and the charged fermion spinor fields ψ of charge q and mass m. To obtain $\mathcal{L}_{\mathrm{QED}}$ it is customary to begin with the Dirac lagrangian for a free fermion,

$$\mathcal{L}_{\mathrm{Dirac}} = i\bar{\psi}\gamma^\mu\partial_\mu\psi - m\bar{\psi}\psi, \tag{2.4}$$

where γ^μ are the Dirac matrices. The Dirac lagrangian is invariant under a global U(1) transformation such as $\psi \to e^{i\alpha}\psi$ but not under a local U(1) transformation such as $\psi \to e^{i\alpha(x)}\psi$ where

$\alpha(x)$ explicitly has time and space coordinates. This is rectified by introducing the covariant derivative D_μ defined by,

$$D_\mu \equiv \partial_\mu + iqA_\mu, \tag{2.5}$$

in which the gauge field A_μ and parameter q is introduced. This gauge field transforms under a local gauge transformation of $A_\mu \rightarrow A_\mu - \frac{1}{q}\partial_\mu\alpha(x)$. Introduction of the gauge field A_μ necessitates introduction of terms to describe a free gauge field, notably the kinetic energy term $-\frac{1}{4}F_{\mu\nu}F^{\mu\nu}$ where,

$$F_{\mu\nu} = \partial_\mu A_\nu - \partial_\nu A_\mu \tag{2.6}$$

leaving the total QED lagrangian as,

$$\mathcal{L}_{\text{QED}} = i\bar{\psi}\gamma^\mu\partial_\mu\psi - q\bar{\psi}\gamma^\mu\psi A_\mu - m\bar{\psi}\psi - \frac{1}{4}F_{\mu\nu}F^{\mu\nu}. \tag{2.7}$$

The term $q\bar{\psi}\gamma^\mu\psi A_\mu$ has introduced the interaction between fermions and the gauge field A_μ, with a coupling proportional to the fermion charge q. Explicitly a term $\frac{1}{2}m_A^2 A_\mu A^\mu$ would be expected in association with A_μ but is not included as this would spoil the $U(1)$ local gauge invariance. In electromagnetism, this coincides with the observation that photons are massless particles.

Though QED only describes the electromagnetic force, it forms the basis for the derivation of lagrangians for the strong and electroweak interactions by selecting an appropriate covariant derivative for some local gauge transformation with the introduction of a gauge field and some kinetic term.

2.2.2 Quantum Chromodynamics

Quantum Chromodynamics (QCD) [5–7] describes the interactions between quarks and the eight gluons associated with the $\text{SU}(3)_C$ symmetry. The QCD Lagrangian is derived similarly to the QED Lagrangian by ensuring local gauge invariance with respect to $\text{SU}(3)_C$ transformations by the introduction of a covariant derivative,

$$(D_\mu)_{\alpha\beta} = \delta_{\alpha\beta}\partial^\mu - g_s T^a_{\alpha\beta} G^a_\mu, \tag{2.8}$$

where $\alpha, \beta = 1, 2, 3$ run over the three colour charges (*red*, *green*, *blue*), $a = 1, 2, ..., 8$ runs over the eight generators T^a of the $\text{SU}(3)_C$ symmetry, and the gauge field G^a_μ has been introduced, recognised as the gluon field. A kinetic energy term $-\frac{1}{4}G^a_{\mu\nu}G^{a,\mu\nu}$ is also introduced with the definition,

$$G^a_{\mu\nu} = \partial_\mu G^a_\nu - \partial_\nu G^a_\mu - g_s f^{abc} G^b_\mu G^c_\nu \tag{2.9}$$

where f^{abc} are the structure constants of the $\text{SU}(3)_C$ group, which in contrast to QED introduces triple and quartic self-interactions of the gluon field. The full QCD lagrangian $\mathcal{L}_{\text{QCD}}$ is then given by,

$$\mathcal{L}_{\text{QCD}} = \bar{\psi}_\alpha i\gamma^\mu\partial_\mu\psi_\alpha - m\bar{\psi}_\alpha\psi_\alpha - g_s\bar{\psi}_\alpha\gamma^\mu T^a_{\alpha\beta}G^a_\mu\psi_\beta - \frac{1}{4}G^a_{\mu\nu}G^{\mu\nu}_a \tag{2.10}$$

where there is an implied sum over fermi-spinors ψ and over α over for all quark flavours and quark colours. The coupling constant is often redefined as $\alpha_s = g_s^2/4\pi$.

An important feature of QFT is the running coupling constant, i.e. the coupling evolves with the energy scale of the interaction. For QCD this is given by,

$$\alpha_s(Q^2) = \frac{12\pi}{(11n_c - 2n_f)\ln(Q^2/\Lambda^2_{\text{QCD}})} \tag{2.11}$$

where Q is a given energy scale, $n_c = 3$ and $n_f = 6$ are the number of colours and number of quark flavours respectively and $\Lambda_{\text{QCD}} \approx 200\,\text{MeV}$ which is the QCD scale which generally separates two regimes of this function,

- Confinement: $\alpha_s(Q^2) \to \infty$ as $Q^2 \to 0$ which means the interaction between two quarks grows as they are separated. At some point it becomes energetically favourable to form a new quark-(anti-quark) pair between the original quarks. It is because of this that individual quarks cannot be isolated at low-energy, and are only observed in colour-neutral composite hadrons.
- Asymptotic Freedom: $\alpha_s(Q^2) \to 0$ as $Q^2 \to \infty$ which means that at high energies or very short distances the strong force shrinks and quarks become close to free states. In this region the perturbative expansion of QCD is applicable as an approach in calculations.

2.2.3 Electroweak Interactions

Weak interactions and electromagnetic interactions appear different at low-energy; however, in the SM, they are described under a unified electroweak theory derived by Yang, Mills, Glashow, Weinberg and Salam [8–11]. Electroweak theory is described by ensuring local gauge invariance of two symmetries $\text{SU}(2)_L \otimes \text{U}(1)_Y$, where the three $T^{1,2,3}$ isospin operators are the generators of the $\text{SU}(2)_L$ symmetry and Y is the hypercharge operator which acts as the generator of the $\text{U}(1)_Y$ symmetry. Hypercharge is defined as $Y = 2(Q - T^3)$ and is a function of the conserved electric charge Q and the third isospin component T^3. As in QED and QCD, the following covariant derivative is introduced,

$$D_\mu = \partial^\mu - igW_\mu^a T^a + ig' B_\mu Y \tag{2.12}$$

where $a = 1, 2, 3$ runs over the generators of the $\text{SU}(2)_L$ symmetry and three corresponding gauge fields have been introduced $W_\mu^{1,2,3}$ with a coupling strength of g. The B_μ gauge field associated with the $\text{U}(1)_Y$ symmetry is also introduced with a coupling strength of g'. The electroweak lagrangian then introduces kinetic energy terms of $-\frac{1}{4}B_{\mu\nu}B^{\mu\nu}$ and $-\frac{1}{4}W^a_{\mu\nu}W^{a,\mu\nu}$ for each generator $a = 1, 2, 3$. The field tensors are defined as,

$$W^a_{\mu,\nu} = \partial^\mu W^a_\nu - \partial^\nu W^a_\mu + g\varepsilon^{abc} W^b_\mu W^c_\nu \tag{2.13}$$

and

$$B_{\mu,\nu} = \partial^{\mu} B^{a}_{\nu} - \partial^{\nu} B^{a}_{\mu} \tag{2.14}$$

where ε^{abc} is the Levi-Civita tensor, which as in QCD, introduces triple and quartic self-interactions of the $W^{1,2,3}_{\mu}$ fields.

The full electroweak lagrangian $\mathcal{L}_{\mathrm{EW}}$ is given by,

$$\mathcal{L}_{\mathrm{EW}} = \bar{\psi}_{\alpha} i\gamma^{\mu} D_{\mu} \psi_{\alpha} - \frac{1}{4} B_{\mu\nu} B^{\mu\nu} - \frac{1}{4} W^{a}_{\mu\nu} W^{a,\mu\nu} \tag{2.15}$$

where there is an implied sum over fermi spinors ψ, over α, and over all quarks and leptons and D_{μ} specifically refers to the electroweak covariant derivative. Fermion fields can be separated into right-handed and left-handed helicity doublets via:

$$\psi_{R,L} = \frac{1}{2}(1 \pm \gamma^{5})\psi; \psi = \psi_{R} + \psi_{L}, \tag{2.16}$$

where positive (negative) denotes the right-handed (left-handed) components respectively. The Dirac matrices are used to define $\gamma_5 = i\gamma_0\gamma_1\gamma_2\gamma_3$. The terms in the covariant derivative D_{μ} act on the left-handed and right-handed components differently:

$$D_{\mu}\psi_{L} = \left(\partial^{\mu} - igW^{a}_{\mu} T^{a} + ig' B_{\mu} Y\right)\psi_{L}, \tag{2.17}$$

$$D_{\mu}\psi_{R} = \left(\partial^{\mu} + ig' B_{\mu} Y\right)\psi_{R}, \tag{2.18}$$

where the gauge fields $W^{1,2,3}_{\mu}$ act only on the left-handed component and B_{μ} acts on both left-handed and right-handed components equally.

The gauge fields $W^{1,2,3}_{\mu}$ and B_{μ} do not coincide with the gauge bosons observed in experiment, $W^{\pm}$-bosons as ($W^{\pm}_{\mu}$ fields), Z-bosons (as Z^{0}_{μ} fields), and photons (as A_{μ} fields). These are instead produced via the linear combinations of fields,

$$W^{\pm}_{\mu} = \frac{1}{\sqrt{2}}(W^{1}_{\mu} \mp iW^{2}_{\mu}) \tag{2.19}$$

and

$$\begin{pmatrix} A_{\mu} \\ Z^{0}_{\mu} \end{pmatrix} = \begin{pmatrix} \cos(\theta_W) & \sin(\theta_W) \\ -\sin(\theta_W) & \cos(\theta_W) \end{pmatrix} \cdot \begin{pmatrix} B_{\mu} \\ W^{3}_{\mu} \end{pmatrix} \tag{2.20}$$

where the Weinberg or weak mixing angle θ_W has been introduced to control the mixing of the B_{μ} and W^{3}_{μ} fields. The Weinberg angle can be expressed in terms of the coupling constants g and g',

$$\cos(\theta_W) = \frac{g}{\sqrt{g^2 + g'^2}} \quad \text{and} \quad \sin(\theta_W) = \frac{g'}{\sqrt{g^2 + g'^2}} \tag{2.21}$$

A major issue with the electroweak theory described so far is that there are no mass terms for the fermion and gauge fields. This is a requirement to ensure the $\mathrm{SU}(2)_L \otimes \mathrm{U}(1)_Y$ local gauge invariance is satisfied, but it does not reflect nature as all SM particles with the exception of photons and gluons have finite mass. With this knowledge it is clear that an additional mechanism is required to facilitate the requirement.

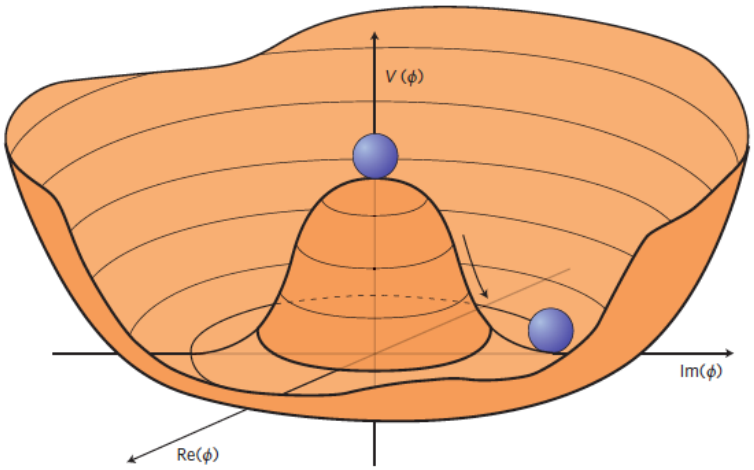

Figure 2.2: The Higgs potential $V(\Phi)$ in the $Re(\Phi)$ and $Im(\Phi)$ plane. When $\mu^2 > 0$ the global minimum of the field occurs at non-zero values due to the "mexican hat" shape of the potential, with an infinite number of possible minima. [12]

2.2.4 EW Symmetry Breaking

In the SM, the introduction of mass terms is accomplished through the concept of spontaneous symmetry breaking [13, 14], often referred to as the Higgs mechanism. This introduces a doublet ϕ of complex scalar fields,

$$\Phi = \begin{pmatrix} \phi^+ \\ \phi^0 \end{pmatrix}, \tag{2.22}$$

defined with four degrees of freedom, correpsonding to the scalar fields $\phi_1, \phi_2, \phi_3, \phi_4$ that are related by,

$$\phi^+ = \frac{\phi_1 + i\phi_2}{\sqrt{2}}, \phi^0 = \frac{\phi_3 + i\phi_4}{\sqrt{2}} \tag{2.23}$$

This scalar doublet is used to define the Higgs sector lagrangian,

$$\mathcal{L}_{\text{Higgs}} = (D_\mu \Phi)^\dagger (D^\mu \Phi) - V(\Phi), \tag{2.24}$$

where the covariant derivative D_μ maintains the electroweak definition used in Equation 2.12. The term $V(\phi)$ is the Higgs potential defined by,

$$V(\Phi) = \mu^2(\Phi^\dagger \Phi) + \lambda(\Phi^\dagger \Phi)^2, \tag{2.25}$$

which introduces two free parameters μ the mass parameter and λ the self-coupling parameter. This definition provides invariance of the Higgs lagrangian under $SU(2)_L \otimes U(1)_Y$ transformations. The form of the Higgs potential is illustrated in Figure 2.2.

Depending on the sign of μ^2, the minimum of the potential is found to be either a unique minimum at $|\Phi_{\text{min}}| = 0$:

$$\mu^2 \leq 0 : \frac{dV}{d\Phi} = 0 \rightarrow |\Phi_{\text{min}}| = 0 \tag{2.26}$$

or

$$\mu^2 > 0 : \frac{\mathrm{d}V}{\mathrm{d}\Phi} = 0 \rightarrow |\Phi_{\mathrm{min}}| = \sqrt{\frac{\mu^2}{2\lambda}} = \frac{v}{\sqrt{2}}, \tag{2.27}$$

where the term v is referred to as the vacuum expectation value (VEV). This can be related to the scalar fields by,

$$\frac{1}{2}(\phi_1^2 + \phi_2^2 + \phi_3^2 + \phi_4^2) = \frac{v^2}{2}, \tag{2.28}$$

where there are an infinite number of possible minima satisfying this condition. Spontaneous symmetry breaking occurs when a specific minimum is selected. It is common to choose the VEVs of three of the four fields be zero, while the remaining field, conventionally ϕ_3, is non-zero. The ground-state of Φ is hence given by,

$$\Phi_0 = \begin{pmatrix} 0 \\ \frac{v}{\sqrt{2}} \end{pmatrix}. \tag{2.29}$$

Applying the unitary gauge [15] and expanding around the minimum this can be rewritten as

$$\Phi' = \begin{pmatrix} 0 \\ \frac{v+H}{\sqrt{2}} \end{pmatrix}, \tag{2.30}$$

where a neutral scalar field H has been introduced corresponding to the Higgs boson. Substituting Φ' into the Higgs lagrangian produces mass terms for the electroweak gauge bosons and the Higgs boson itself, with relations defined by:

$$v^2\lambda H^2 \rightarrow m_H \rightarrow \sqrt{2v^2\lambda}, \tag{2.31}$$

$$\left(\frac{1}{2}vg\right)^2 W_\mu^+ W^{-,\mu} \rightarrow m_W = \frac{1}{2}vg, \tag{2.32}$$

$$\frac{1}{8}(W_\mu^3, B_\mu)\begin{pmatrix} g^2 & -gg' \\ -gg' & g'^2 \end{pmatrix}\begin{pmatrix} W^{3,\mu} \\ B^\mu \end{pmatrix} \rightarrow \begin{pmatrix} m_Z = \frac{1}{2}v\sqrt{g^2+g'^2} \\ m_A = 0 \end{pmatrix}. \tag{2.33}$$

The Higgs field also couples to all SM fermion fields providing a mechanism for the origin of fermion mass through Yukawa couplings. For a given fermion field ψ, the Yukawa lagrangian term is,

$$\mathcal{L}_{\mathrm{Yukawa,f}} = -\frac{v\lambda_f}{\sqrt{2}}\bar{\psi}\psi - \frac{\lambda_f}{\sqrt{2}}H\bar{\psi}\psi, \tag{2.34}$$

where λ_f is the fermion Yukawa coupling and the mass term can be extracted from

$$m_f = \frac{\lambda_f v}{\sqrt{2}}. \tag{2.35}$$

Notably, the coupling strength of the Higgs boson to the fermion is proportional to m_f.

3 Theory of the Drell-Yan Process and Event Generation

The theory described in Chapter 2 does not yet explain how one would observe a physics process in a particle collider experiment. In this chapter, there will be a discussion of hadron-hadron colliders and the use of the factorisation theorem and parton distribution functions to describe physics processes. There will then be an overview of the Drell-Yan process, which relates to the analyses discussed in this thesis.

3.1 Factorisation Theorem

Collisions of hadrons (e.g. protons) involve the interaction of composite particles of strongly-interacting quarks and gluons. The theory discussed in Section 2.2.2 provides the ingredients for performing perturbative QCD calculations of cross-sections for interactions between quarks and gluons as an expansion in α_s for large momentum transfers (large Q^2). For example the cross-section for the interaction of two quarks a and b to produce the final state V is given by:

$$\sigma_{a+b\to V} = \underbrace{\sigma_0}_{\text{LO}} + \underbrace{\sigma_1\alpha_s(\mu_R^2)}_{\text{NLO}} + \underbrace{\sigma_2\alpha_s^2(\mu_R^2)}_{\text{NNLO}} + ... \tag{3.1}$$

where LO is leading order, NLO is next-to-leading order and NNLO is next-to-next-to-leading order. The term μ_R is the renormalisation factor, an arbitrary scale introduced as a consequence of QCD renormalisation required to control divergences in the calculation. This is often referred to as the partonic cross-section as it is only applicable for free quarks and gluons (collectively referred to as partons).

In order to obtain a cross-section for the scattering of two hadrons h_1 and h_2, there also needs to be consideration of the non-perturbative effects from low momentum transfers (low Q^2). This notably includes the structure of hadrons and the distribution of partons, which is accounted for by absorbing the divergences of non-perturbative processes into Parton Distribution Functions (PDFs) $f_i(x, Q^2)$ considered at some arbitrary sufficiently large energy scale $Q^2 = \mu_F^2$. This is known as the Factorisation theorem, which states that the total cross-section for collision of h_1 and h_2 that scatter into some final state V can be obtained by,

$$\sigma_{h_1(p_1)+h_2(p_2)\to V} = \sum_{a,b}\int_0^1\int_0^1 \mathrm{d}x_a\mathrm{d}x_b f_a(x_a,\mu_F^2)f_b(x_b,\mu_F^2)\times\sigma_{a+b\to V}(x_a,x_b,\mu_F^2) \tag{3.2}$$

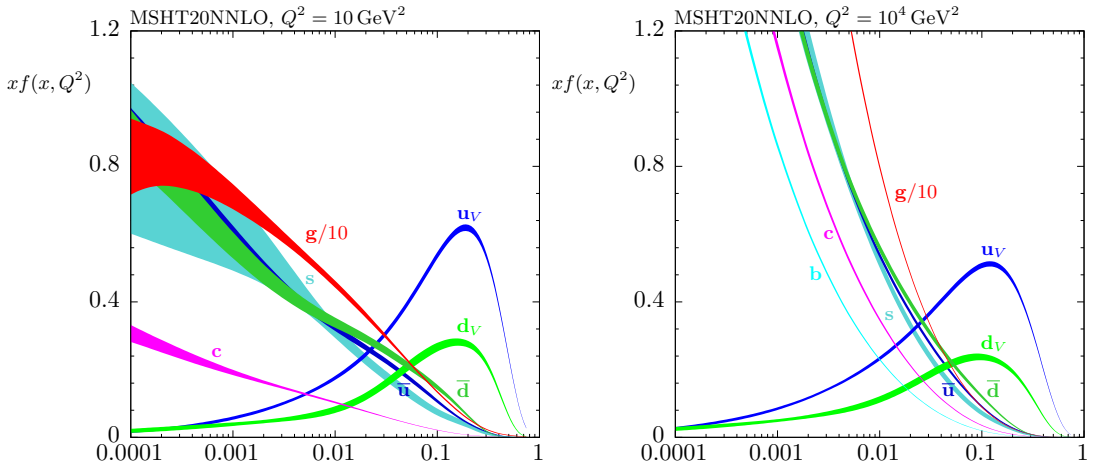

Figure 3.1: The parton momenta fraction x (on the x-axis) for MSHT20 NNLO PDFs at $Q^2 = 10\,\text{GeV}^2$ and $Q^2 = 10 \times 10^4\,\text{GeV}^2$ with the associated 68% uncertainty bands [16].

where the total hard-scattering process cross-section $\sigma_{h_1(p_1)+h_2(p_2)\to V}$ has been obtained by weighting the contributing partonic cross-section $\sigma_{a+b\to V}(x_a, x_b, \mu_F^2)$ by the PDF values $f_a(x_a, \mu_F^2)$ and $f_b(x_b, \mu_F^2)$. Introducing the factorisation scale μ_F separates the perturbative and non-perturbative regimes. The sum over a, b runs over all possible parton-pairs that can contribute to the process.

3.2 Parton Distribution Functions

Parton Distribution Functions (PDFs) $f_i(x, Q^2)$ for all partons $i = u, d, ..., g$ represent the probability density to find a parton carrying a certain fraction x of the protons total momentum at a given energy scale Q^2. PDFs are determined from fits to data usually using data from deep-inelastic lepton-nucleon scattering experiments, but recently also utilising LHC measurements such as measurements of the Drell-Yan process (Section 3.3). To perform a PDF fit, it is first necessary to parameterise the PDFs using a functional form with the flexibility to describe the data at some low Q^2. These PDFs are then evolved to higher energy scales using the DGLAP evolution equations [17–19]. From these, at the relevant scale, cross-sections can be computed using the factorisation theorem. The parameters of the PDF parameterisation can then be fitted by comparing predictions to experimental data. Examples of PDFs for the proton are shown in Figure 3.1 at two energy scales $Q = 2\,\text{GeV}$ and $Q = 100\,\text{GeV}$. Here are shown the *valence* up- and down- quarks whose number distributions integrate to 2 and 1 respectively to correspond to the simple proton composition *uud*. Also shown are quarks originating from gluons splitting into quark-antiquark pairs (collectively referred to as *sea* quarks) which exist for up-quarks and down-quarks (labelled $\bar{u}$ and $\bar{d}$) but also the heavy flavours s, c and b. Finally, the distributions for gluons themselves are shown. Valence quarks make the largest contribution to proton structure at high-x. The evolution of Q^2 to $Q^2 = 10^4\text{GeV}^2$ shows strong enhancement of the gluon and heavy-flavour quarks for low-x. Various parameterisations obtained with varying datasets have been produced. PDFs encountered in this thesis originate from the CTEQ [20] and NNPDF [21] groups.

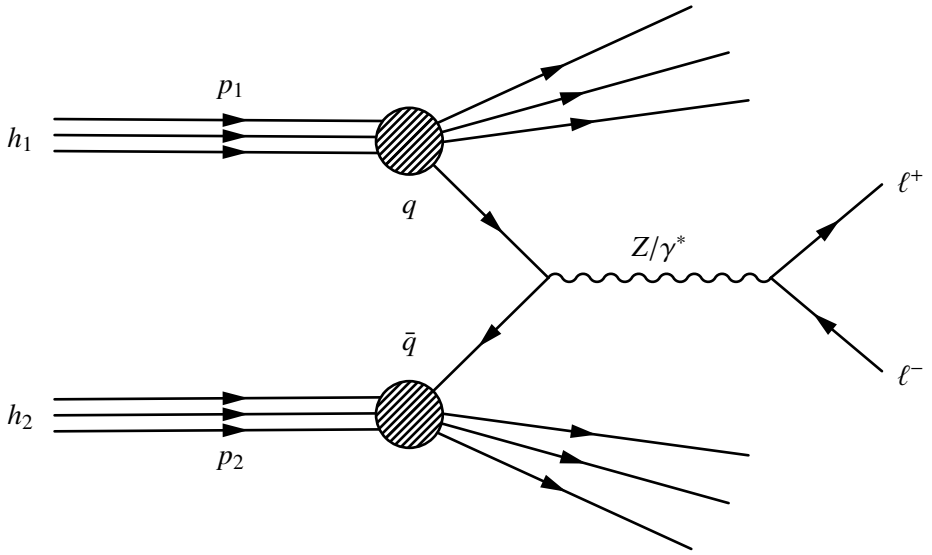

Figure 3.2: Feynman diagram of the Drell–Yan process showing two incoming hadrons h_1 and h_2 of momentum p_1 and p_2 where a Z-boson or γ^* has been produced by two incoming quarks of momentum $x_a p_1$ and $x_b p_2$.

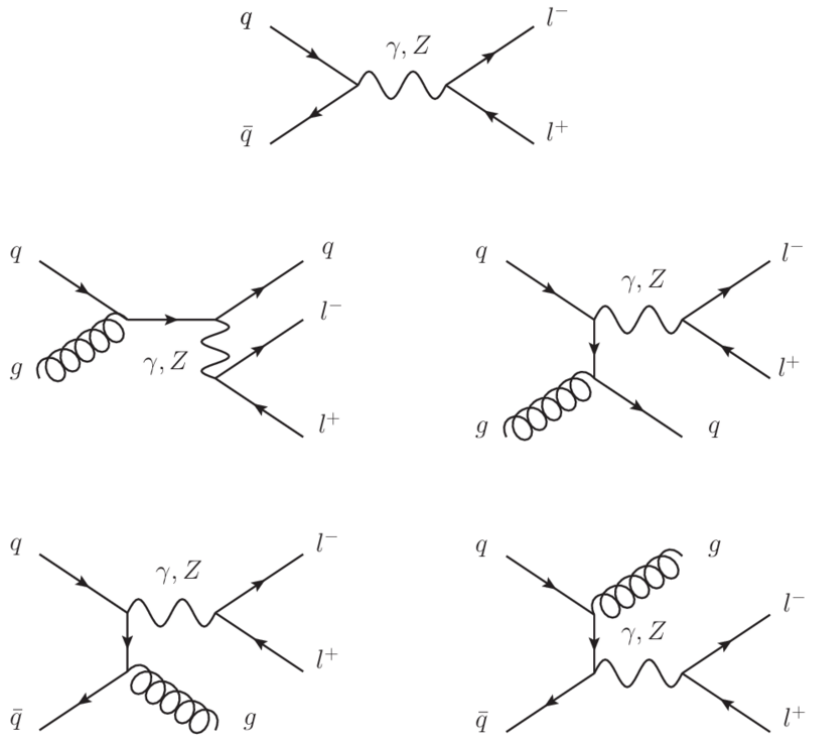

Figure 3.3: Example feynman diagrams for Z/γ^* production at parton level. The LO diagram is shown at the top with various NLO diagrams shown below. Figure taken from Ref. [22].

3.3 The Drell-Yan Process

The Drell-Yan process [23] is one of the simplest possible processes at a hadron-hadron collider. This thesis considers neutral-current (NC) production in which a quark-antiquark pair is annihilated through an s-channel exchange, mediated by virtual photons γ^* and Z-bosons. The produced bosons instantaneously decay into a pair of same flavour, oppositely charged leptons.

Here we will consider the $Z/\gamma^* \to e^+e^-$ and $Z/\gamma^* \to \mu^+\mu^-$ final states, collectively referred to as $Z/\gamma^* \to \ell^+\ell^-$ or di-lepton production. The process is given by:

$$q + \bar{q} \to (Z/\gamma^* \to \ell^+ + \ell^-) + X, \tag{3.3}$$

where the q and $\bar{q}$ originate from the incoming hadrons h_1 and h_2. X is the final state containing any QCD radiation and the fragments of the colliding hadronic particles. The di-lepton system provides a clean signature that allows measurement of the fundamental physics without reconstructing X. The Feynman diagram of the process is shown in Figure 3.2. In this thesis, the process is interchangably denoted in shorthand as $Z/\gamma^* \to \ell\ell$ where the lepton charges are neglected but still implied, and $Z \to \ell\ell$ where the γ^* contribution is implied, usually being used where there is significantly more contribution from Z-boson production than γ^* production.

Understanding the Drell-Yan process was crucial for the Z-boson discovery by the UA1 [24] and UA2 [25] experiments. Over the last few decades, it has become a useful test-bed for developing and improving cross-section calculations using the factorisation theorem of increasing perturbative orders of α_s. The process is one of the few examples in hadron-hadron physics where the factorisation theorem has been shown to hold [26, 27]. The precision of Drell-Yan cross-section predictions has improved beyond LO α_s over the decades by including higher-order diagrams in the perturbative calculation. The first notable improvements came in 1978-1979 [28–31] with upgrades to NLO precision (some example NLO Feynman Diagrams are shown in Figure 3.3) and harmonisation of PDF evolution to be consistent between DIS and hadron-hadron collisions. The NLO corrections were large, necessitating the improvement beyond NLO. NNLO corrections were computed in the early 1990s with differential cross-sections available in the 2010s [32–38]. Recently there have been ongoing studies of the inclusive cross-section at N^{3}LO [39–41]. A testament to the strength of QCD physics and the factorisation theorem is that the precision of these calculations is now at the level of 1% or lower, which is below the typical uncertainty expected from PDF modelling.

Measurements of the Drell-Yan process can provide great insight into physics modelling. Drell-Yan production is sensitive to electroweak parameters such as $\sin^2(\theta_W)$, through measurements of the forward-backward asymmetry. These measurements can provide valuable constraints in global fits of electroweak observables [42, 43]. Z-boson production at the LHC has a significant contribution from strange quark initial states, which has been shown to provide improved modelling of the strange quark PDFs [44].

3.3.1 Drell-Yan Measurements at the LHC

There is a rich history of Drell-Yan cross-section measurements at the LHC. Previous ATLAS measurements of Drell-Yan cross-sections differential in mass and rapidity have been performed at $\sqrt{s}$ =7 TeV [44] and 5.02 TeV [47], and a triple-differential measurement at 8 TeV [48]. Inclusive cross-sections have also been measured at 2.76 TeV [49] and 13 TeV [50]. Figure

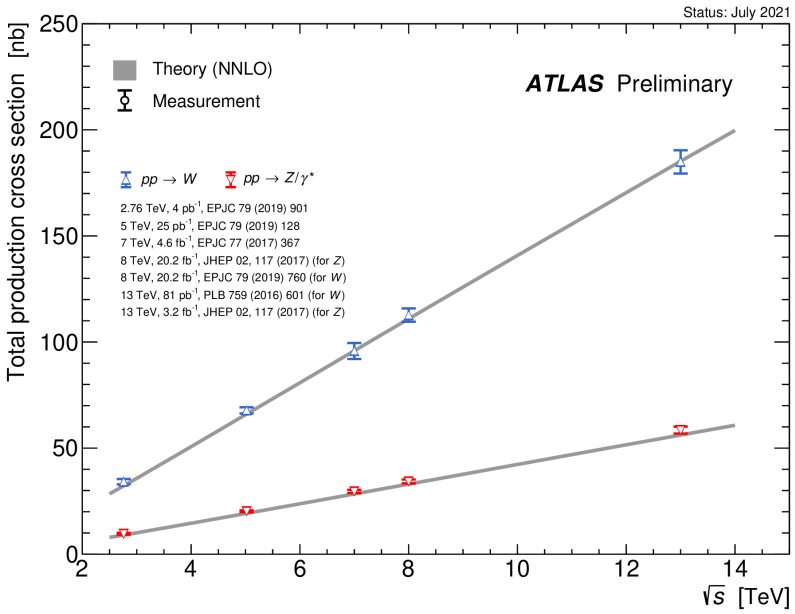

Figure 3.4: Shows the $\sqrt{s}$ dependence of electroweak boson inclusive cross-sections taken from various ATLAS measurements [45] compared to NNLO predictions from the DYNNLO program [46].

3.4 shows the $\sqrt{s}$ dependence of inclusive Z-boson production using these various ATLAS measurements.

Double differential Drell-Yan cross-sections have been measured by CMS at $\sqrt{s}$ =7 TeV [51] and 8 TeV [52], while at 13 TeV only single-differential cross-sections differential in mass [53] and rapidity [54] have been measured. Drell-Yan cross-sections at forward dilepton rapidity have also been measured at $\sqrt{s}$ =7 TeV [55, 56] 8 TeV [57, 58] and 13 TeV [59, 60] by the LHCb Collaboration.

3.3.2 Drell-Yan Kinematics

Measurements of the Drell-Yan process rely on the reconstruction of the two final state leptons and reconstructing the di-lepton system by combining the two lepton four-vectors $p^{\mu}_{\ell,1}$ and $p^{\mu}_{\ell,2}$ into the di-lepton four-vector $p^{\mu}_{\ell\ell}$. It is useful to understand the quantities measured for the individual reconstructed leptons relate to quantities in the di-lepton system.

The centre-of-mass energy $\sqrt{s}$ for a proton-proton collision is evaluated using each proton (p_1,p_2) four-momenta $p^{\mu}_{p,1}$, $p^{\mu}_{p,2}$:

$$\sqrt{s} = \sqrt{(p^{\mu}_{p,1} + p^{\mu}_{p,2})^2}. \tag{3.4}$$

The quark and anti-quark carry fractions of the total proton momenta, x_1, x_2 respectively, such that the transferred momentum, Q^2 is,

$$Q^2 = (x_1 p^{\mu}_{p,1} + x_2 p^{\mu}_{p,2})^2 = x_1 x_2 s = \hat{s}. \tag{3.5}$$

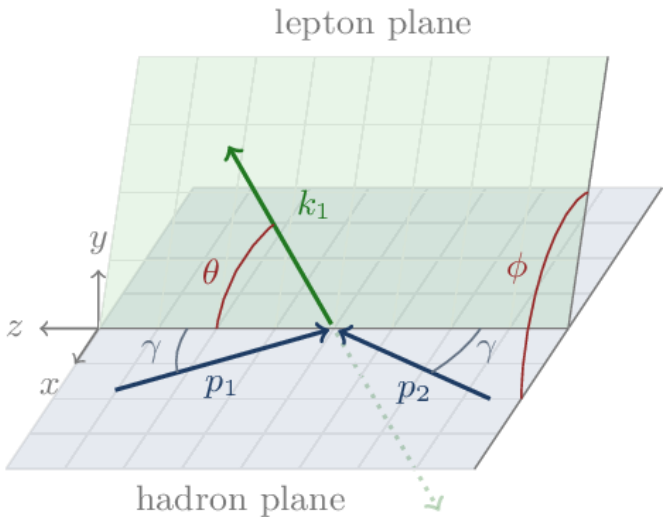

Figure 3.5: Definition of Collins-Soper frame and the corresponding lepton decay angles θ and ϕ. p_1 and p_2 are the directions of the incoming partonic momenta in the lepton rest frame, k_1 is the negative lepton momentum and k_2 is the positive lepton [61].

A useful quantity for a particle is the rapidity y defined by,

$$y = \frac{1}{2}\ln\left(\frac{E + p_z}{E - p_z}\right), \tag{3.6}$$

where the convention that p_z is the component along the beam axis is used. The x-axis and y-axis components define the transverse plane and can be combined into the transverse momentum $p_T = \sqrt{p_x^2 + p_y^2}$. The range of allowed rapidity for a Z can be related to the centre-of-mass energy and Z-boson mass such that,

$$|y_Z^{\max}| = \ln\left(\frac{\sqrt{s}}{M_Z}\right) \tag{3.7}$$

which for $M_Z \approx 0.0912\,\text{TeV}$ [3] is $|y_Z^{\max}| \approx 4.96$ at $\sqrt{s} = 13\,\text{TeV}$ and $|y_Z^{\max}| \approx 4.01$ at $\sqrt{s} = 5.02\,\text{TeV}$. The rapidity of a Z-boson is related to the momentum fraction carried by the initial partons, which at leading order can be written simply as,

$$x_{a,b} = \frac{M_Z e^{\pm y_Z}}{\sqrt{s}} \tag{3.8}$$

The di-lepton four vector can then be used to define the di-lepton invariant mass:

$$m_{\ell\ell} = \sqrt{(p_{\ell,1}^{\mu} + p_{\ell,2}^{\mu})^2} \tag{3.9}$$

and the di-lepton rapidity:

$$y_{\ell\ell} = \frac{1}{2}\ln\left(\frac{E_{\ell\ell} + p_{\ell\ell,z}}{E_{\ell\ell} - p_{\ell\ell,z}}\right) \tag{3.10}$$

At leading order, the transverse momentum of the di-lepton system is expected to be zero to match that of the incoming protons, however with higher orders introducing QCD initial state

radiation, this is no longer true. The di-lepton rest frame can be easily reconstructed, but to measure an angle there needs to be a consistent axis definition, which the lab frame axis no longer satisfies. It is also useful to define angles with respect to the incoming quark and anti-quark, however, due to the symmetry of proton-proton colliders it is not clear which direction the quark and anti-quark have come from. To facilitate these issues, the angular measurements are defined in the Collins-Soper frame [62], where the angular variable is defined by,

$$\cos(\theta^*_{CS}) = \frac{p_z^{\ell\ell}}{|p_z^{\ell\ell}|} \frac{2(p_1^+ p_2^- - p_1^- p_2^+)}{m_{\ell\ell}\sqrt{m_{\ell\ell}^2 + (p_T^{\ell\ell})^2}}. \tag{3.11}$$

Here the shorthand

$$p_i^{\pm} = \frac{1}{\sqrt{2}(E_i \pm p_{z,i})} \tag{3.12}$$

is used and $i = 1, 2$ referrs to the negative lepton and positive anti-lepton respectively.

The angles in this frame are defined with respect to the lepton momentum vectors and a longitudinal axis bisecting the momentum vectors of the incoming partons. This frame is useful as the first term correlates with the direction of $p_z^{\ell\ell}$, which corresponds to the direction of the quark carrying more momentum. This is more frequently from the u and d quarks for LHC collisions as valence quarks dominate at high-x. The Collins-Soper frame is shown in Figure 3.5.

3.3.3 Triple Differential Cross-Section

To increase the information content of an experimental measurement of the Drell-Yan cross-section, it is common to perform measurements differentially. At LO, the triple-differential cross-section in $m_{\ell\ell}$, $y_{\ell\ell}$ and $\cos(\theta^*_{CS})$ is given by [48],

$$\frac{\mathrm{d}^3\sigma}{\mathrm{d}m_{\ell\ell}\mathrm{d}y_{\ell\ell}\mathrm{d}\cos(\theta^*_{CS})} = \frac{\pi\alpha^2}{3 \cdot s \cdot m_{\ell\ell}} \sum_q P_q\left(m_{\ell\ell}, \cos(\theta^*_{CS})\right)\left[f_q(x_1, Q^2) f_{\bar{q}}(x_1, Q^2) + (q \leftrightarrow \bar{q})\right] \tag{3.13}$$

where α is the QED fine structure constant and s is the centre-of-mass energy. The term $(q \leftrightarrow \bar{q})$ is included due to the symmetry of pp collisions which account for cases in which the parent protons of the q and $\bar{q}$ are interchanged . The dependence on rapidity $y_{\ell\ell}$ arises from the dependence of x_1 and x_2 on $m_{\ell\ell}$, $y_{\ell\ell}$ and $\sqrt{s}$. The term $P_q(m_{\ell\ell}, \cos(\theta^*_{CS}))$ can be decomposed into contributions from pure γ^* exchange, pure Z-boson exchange and an interference term:

$$\begin{aligned} P_q\left(m_{\ell\ell}, \cos(\theta^*_{CS})\right) &= P_{\gamma^*}(1 + \cos^2(\theta^*_{CS})) \\ &+ P_{Z/\gamma^*}\left[v_\ell v_q(1 + \cos^2(\theta^*_{CS})) + 2a_\ell a_q \cos(\theta^*_{CS})\right] \\ &+ P_Z\left[(a_\ell^2 + v_\ell^2)(a_q^2 + v_q^2)(1 + \cos^2(\theta^*_{CS})) + 8a_\ell v_\ell a_q v_q \cos(\theta^*_{CS})\right] \end{aligned} \tag{3.14}$$

where m_Z and Γ_Z are the Z-boson mass and width, e_ℓ and e_q are the lepton and quark electric charges and the terms v_q, a_q and v_ℓ, a_ℓ are the vector and axial couplings for the quark and

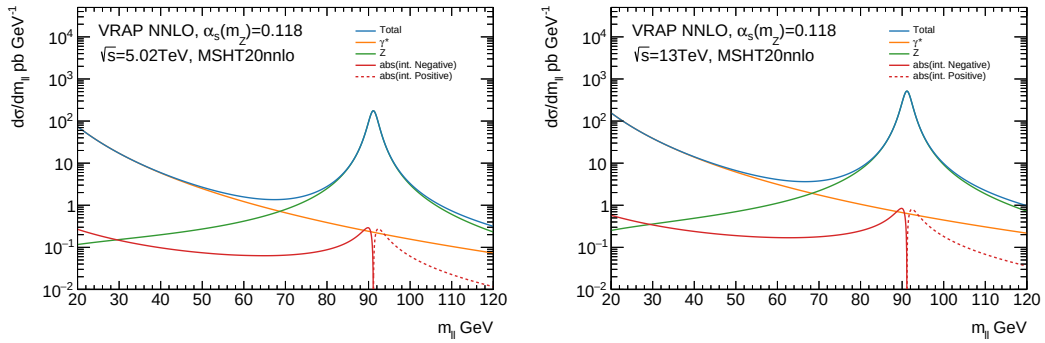

Figure 3.6: Predictions of the 5.02 TeV and 13 TeV 1D Drell-Yan cross-sections measured differentially in di-lepton invariant mass $m_{\ell\ell}$. The plots show the contributions of γ^* and Z-boson production as well as the $Z\gamma^*$ interference term (*int.*) simulated using VRAP [63] evaluated at NNLO using MSHT20nnlo and $\alpha_s(M_Z) = 0.118$. The absolute value of the interference contribution has been taken to allow plotting.

lepton respectively. The terms P_{γ^*}, P_{Z/γ^*} and P_Z are written in terms of their corresponding couplings and propagators:

$$\begin{aligned} P_{\gamma^*} &= e_\ell^2 e_q^2 \\ P_{Z/\gamma^*} &= e_\ell e_q \frac{2m_{\ell\ell}^2(m_{\ell\ell}^2 - m_Z^2)}{\sin^2(\theta_W)\cos^2(\theta_W)[(m_{\ell\ell}^2 - m_Z^2)^2 + \Gamma_Z^2 m_Z^2]} \\ P_Z &= \frac{m_{\ell\ell}^4}{\sin^4(\theta_W)\cos^4(\theta_W)[(m_{\ell\ell}^2 - m_Z^2)^2 + \Gamma_Z^2 m_Z^2]} \end{aligned} \tag{3.15}$$

For a given fermion f the vector and axial couplings are defined by:

$$a_f = T^3 \tag{3.16}$$

$$v_f = T^3 - 2\sin^2(\theta_W)e_f, \tag{3.17}$$

where T^3 is the fermion weak isospin and e_f is the fermion electric charge.

The $m_{\ell\ell}$ dependence of Drell-Yan production is characterised by a $1/m_{\ell\ell}^2$ fall-off originating from the pure virtual photon contribution, a Breit-Wigner resonance peak depending on $m_{\ell\ell}$ with centre and width of m_Z and Γ_Z respectively and a Z/γ^* interference term that changes sign from negative to positive as $m_{\ell\ell}$ passes the m_Z threshold. The relative contribution of each term is shown as a function of $m_{\ell\ell}$ in Figure 3.6. Sensitivity to the PDFs arise primarily from the dependence on $y_{\ell\ell}$ (and therefore x_1,x_2). In addition, the contribution from up-quark and down-quark initial states differs depending on $m_{\ell\ell}$ with strong $u\bar{u}$ and sizeable $c\bar{c}$ contributions where γ^*-exchange is the dominant process and notably stronger $d\bar{d}$ and $s\bar{s}$ contributions where Z-exchange is the dominant process.

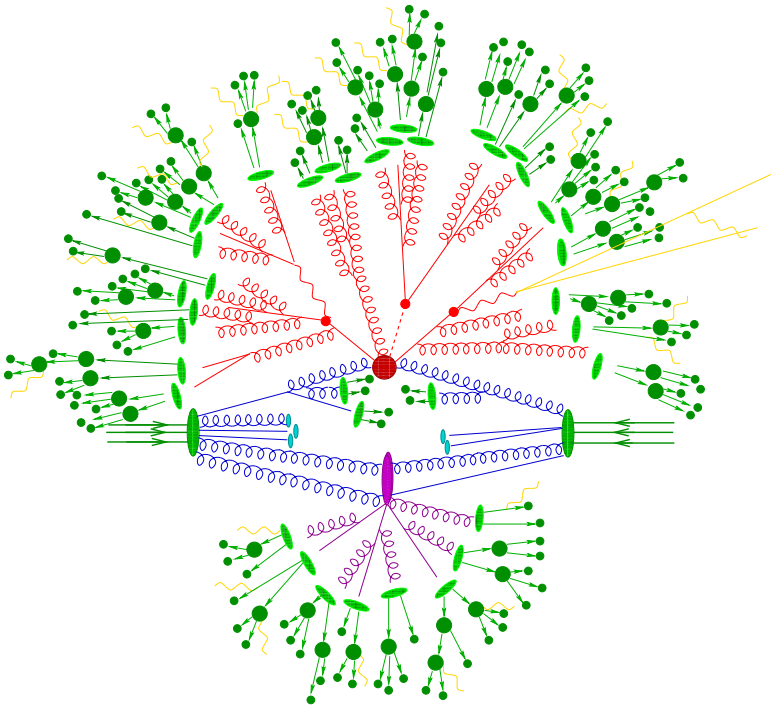

Figure 3.7: Diagram representing an example $t\bar{t}H$ event resulting from a LHC pp collision. This diagram represents the hard interaction (large red blob) followed by particle decays of the top quarks and Higgs (small red blobs). Initial State and Final State QCD radiation are highlighted with (blue) and (red) gluons, respectively. A secondary interaction also occurs, as highlighted by the (purple blob). Final state partons go on to hadronise (light green blobs) before hadronic decay (dark green blobs). FSR photon radiation also occurs throughout (yellow photons). The figure is taken from Ref. [64].

3.4 Monte Carlo Event Generation and Simulation

3.4.1 Monte Carlo Event Generation

Monte Carlo (MC) event generators are used to produce simulated datasets at a particle level with modelling for all aspects of a given particle collision [65]. After the simulation of particles, their interaction with the detector and the pileup environment of the collision is simulated. Generation of a single pp collision event at the LHC is performed in a series of steps, usually calculated sequentially though this does not necessarily match the chronology of an event in nature. Figure 3.7 shows the various components of simulating a pp physics event. An overview of each of these steps is now provided.

Hard-Scatter Process The partonic cross-section of the process governs the hard process being studied as calculatable from perturbative QCD. At LO, the partonic cross-section for $2 \to n$ processes is given by:

$$\mathrm{d}\sigma_{\mathrm{LO}} = \frac{1}{2\hat{s}}\mathrm{d}\Phi_n |\mathcal{M}_{\mathrm{LO}}(\Phi_n; \mu_F, \mu_R)|^2 \tag{3.18}$$

where $\mathrm{d}\Phi_n$ is the n-particle phase space and $\mathcal{M}_{\mathrm{LO}}$ is the squared matrix element of the process, summing over all possible Feynman diagrams to the order of the calculation. In simulations this

involves random sampling of the parton momenta fractions from the PDF probability distributions, hence providing the partonic centre-of-mass energy $\hat{s}$. The matrix element calculations are often complex, and the Monte Carlo method provides a simulated sample of particles in the phase space Φ_n.

Parton Shower Modelling of Parton splittings (e.g. $g \to q\bar{q}$, $q \to qg$ and $g \to gg$) can be performed within the matrix element calculation if well-separated high-p_T jets are required. However, this is not practical for describing the many subsequent splittings at softer and softer momentum scales in the collinear limit (opening angle between the partons goes to zero or π) expected in a pp event, which would include many more QCD vertices than it is feasible to calculate. This behaviour is hence modelled by assuming each parton in the event at a given time is treated as splitting independently of the partons that produced it. The Parton Shower (PS) formalism is then implemented as a probabilistic model that constructs a long chain of successive $1 \to 2$ splittings of decreasing momentum down to a scale in which perturbation theory breaks down $\approx 0.5\,\text{GeV}$. This is a clear sequence for FSR processes; however, for ISR, there is the condition that the hard-scatter momenta should be satisfied. The development of ISR is provided by backward evolution, starting at the scale of the hard process and evolving to the initial partons [66, 67].

Similar showering algorithms are used to model the radiation of photons (bremsstrahlung radiation) that arise from QED corrections to the kinematics of charged particles.

Hadronisation Due to QCD confinement, partons cannot be observed freely and are found only within colour-neutral hadronic states. The process of a soft parton forming a hadronic final state is referred to as hadronisation. Hadronisation is non-perturbative and instead simulations rely on QCD-inspired phenomenological models such as the string model [68] and cluster model [69]. The initially produced hadrons may decay into further hadrons resulting in hadronic jets that can be resolved in the detector.

Underlying Event and Multiple Parton Interactions In pp collisions, the underlying event (UE) is defined as any hadronic activity additional to what is attributed to the hard-scatter and the associated ISR and FSR. This activity originates from interactions between partons that did not cause the hard-scatter to occur. This also includes the beam-beam remnants that describe the protons' breakup after the hard scatter has occurred, usually concentrated along the beam direction. The UE is simulated with a phenomenological model that has been tuned to dedicated measurements constructed to provide UE sensitivity (see the A14 tune [70]).

Decays of Unstable Particles The decau of unstable particles produced in these collisions with short lifetimes must be modelled. These decays can include heavy final state particles such as top quarks and tau leptons and lighter particles resulting from hadronisation such as pions

and kaons. The branching ratios are obtained from the PDG [3]; however, specialised packages are often employed to provide improved kinematics [71].

ATLAS Detector Simulation Modelling of how the generated truth-level events interact with the detector is accomplished using dedicated software [72] which models the full geometry, and the material composition of the detector. The GEANT4 [73, 74] toolkit is used to simulate the passage and interactions of particles through the detector sub-systems and the corresponding energy deposits left in the detector components. A "digitisation" step is then performed where the energy depositions are translated into electrical signals, providing detector "hits" that can be processed by the same reconstruction software used on data.

Pileup Simulation At high luminosity, multiple pp collisions occur in a single bunch crossing (in-time pileup, up to about 60 in Run-2), and further collisions in neighbouring bunch crossings also overlap (out-of-time pileup). These are simulated using the Pythia8 A3 tune [75] to describe the full spectrum of inelastic pp interactions (including diffractive interactions). These events are processed with the same detector simulation, and the pileup "hits" are combined [72] with the hard-scatter "hits" before the digitisation step. Some assumption is made on the distribution of pileup, which may require reweighting to the profile observed in the data. This is usually the case when the correct distribution is not known when preparing the sample.

3.4.2 Common MC Event Generators

The ATLAS simulation infrastructure produces MC samples using various event generators and software tools. Where needed, it is also possible to interface different tools together. Loosely speaking, there are multi-purpose generators capable of simulating the full analysis chain and matrix element (ME) generators specifically designed for simulation of the hard scatter which require an interface to a multi-purpose generator to simulate the remaining steps. The generators discussed in this thesis are:

- Powheg [76–79] is a NLO ME generator. It is based on the Powheg method for merging NLO calculations with parton showers. It requires an interface to multi-purpose generators for simulation of the remaining components.
- Pythia [80] is a multi-purpose generator. It performs ME calculations at LO and has libraries for simulating all steps of the event generation.
- Herwig [81, 82] is a multi-purpose generator. It performs ME calculations at LO and NLO and has libraries for simulating all steps of event generation.
- Sherpa [83, 84] is a multi-purpose generator. It performs ME calculations at LO and NLO and has libraries for simulating all steps of event generation.
- Photos++ [85, 86] is a precision tool for generation of QED radiative corrections in the decays of W- and Z-bosons.

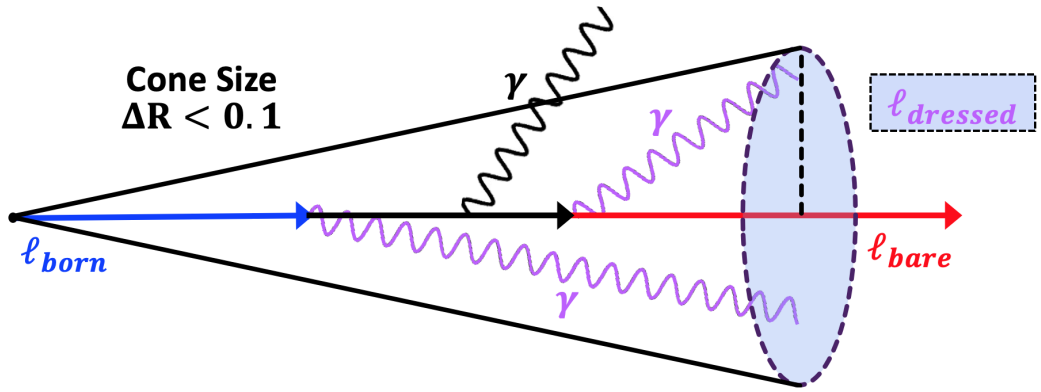

Figure 3.8: Diagram illustrating the various definitions of lepton ($\ell = e, \mu$) kinematics. A "Born" lepton (blue) undergoes FSR photon radiation resulting in a "bare" lepton (red) after all photon radiation has occured. A "dressed" lepton is then defined by combining the "bare" lepton kinematics with all photons inside a cone of size $\Delta R < 0.1$ (purple).

- EvtGen [87] is a precision tool for simulating heavy-flavour hadron decays.

3.4.3 AZNLO Tune

At ATLAS, the baseline MC sample used for simulation of $Z/\gamma^* \rightarrow \ell^+\ell^-$ production is Powheg+Pythia8 AZNLO. This is used by both analyses described in this Thesis, so a detailed summary of its production is given here.

The Powheg[v1] MC generator simulates the hard-scatter of the $Z/\gamma^* \rightarrow \ell^+\ell^-$ process at NLO precision. This is then interfaced to Pythia [8.186] for the modelling of the parton shower, hadronisation, and underlying event, with parameters set according to the AZNLO tune [88]. The AZNLO tune was performed using $\sqrt{s} = 7$ TeV ATLAS data and adjusts internal parameters in Pythia to best describe the Z-boson transverse momentum $p_T(Z)$ distribution. The CT10nlo PDF set [89] was used for the hard-scattering processes, whereas the CTEQ6L1 PDF set [90] was used for the parton shower. The effect of QED final-state radiation was simulated using Photos++3.52, and the EvtGen1.2.0 program was used to decay bottom and charm hadrons.

Nominal ATLAS signal samples are generated with invariant mass cut of $m_{\ell\ell} > 60$ GeV using a Born leptons (see Section 3.4.4). An additional set of signal samples extending from 10 GeV $< m_{\ell\ell} < 60$ GeV was also generated to facilitate the measurement of the Drell-Yan cross-section at low-mass.

3.4.4 Truth-Level Definition

For consistency with various other experiments and prior analyses, it is important to measure particle properties in an unambigous way. This involves the definition of "truth"-level [91] kinematics, where "truth" denotes that these are the properties of the particle itself, separated

from any changes caused by the detector. It is important that these definitions can be consistently reproduced by independent experiments to allow for an exact comparison of measurements. It is also important that they are well defined theoretically, such that they are maximally independent of any technical details of the MC generators. These considerations are used by the RIVET toolkit [92] which facilitates the preservation of experimental data and provides a framework for producing predictions from various MC generators with the exact definitions of the experimental measurement.

Particle-level objects should be defined as close as possible to the definitions used for experimental reconstruction. This Thesis deals with electrons and muons, which can be defined with kinematics η and $p_T(\ell)$ close to that of the experimental selections. The largest complication for electrons and muons arises from photon emission due to QED final state radiation (FSR). This is a large correction, but its effect is fully calculable. With this in mind, there are three classifications of truth-level lepton defined with various considerations of FSR:

- **Born Leptons:** Born leptons are defined prior to any FSR or, more technically, at the lowest-order diagram in α_{QED}. This is often the level at which the kinematics are calculated in event generators when calculating the hard-scatter matrix element. Born leptons are fully comparable objects, so Born electrons and Born muons can be directly combined.
- **Bare Leptons:** Bare leptons are defined after all FSR has occurred, which has a strong dependency on the technical details and implementation of QED within the MC generator.
- **Dressed Leptons:** Dressed Leptons are defined by clustering and combining all photons within a cone following the direction of the "bare" lepton, which provides a partial recovery of QED radiation. Typically ATLAS uses a cone of size $\Delta R < 0.1$ (see Section 4.2.1)

$$p^{\ell}_{T,\text{dressed}} = p^{\ell}_{T,\text{bare}} + \sum_{\Delta R(\gamma,\ell)<0.1} p^{\gamma}_{T} \tag{3.19}$$

The comparison of "born", "bare" and "dressed" lepton kinematics is shown in Figure 3.8.

Part II

Experimental Overview

4 The LHC and ATLAS Detector

4.1 The Large Hadron Collider and CERN Accelerator Complex

The Large Hadron Collider (LHC) [93] is the world's largest and highest-energy particle accelerator. It was designed to provide two beams of protons pp or two beams of heavy-ions (Pb-Pb, p-Pb, Xe-Xe) that can be collided together at high energy to facilitate a large number of studies of experimental particle physics. The LHC is a circular collider of circumference 27 km and is located in a tunnel 45 to 175 m underground at the European Organisation for Nuclear Research (CERN) in Geneva, Switzerland.

The LHC is the final stage in a large chain of accelerators called the CERN accelerator complex. The complex is subject to changes over time and serves particle beams for additional experiments beyond the LHC. This section will specifically describe the proton acceleration chain used for LHC Run-2 operations (2015 to 2018). The acceleration process begins with a bottle of compressed hydrogen gas guided through a pulsating electric field that strips away electrons from the protons and pulls the protons in packets towards the next stage. The protons are then injected into the linear accelerator LINAC2, which accelerates the protons with radio-frequency (RF) cavities to the energy of 50 MeV. The beams are then passed through three separate circular synchrotrons of increasing maximum bean energy, starting with the Proton Synchrotron Booster (PSB) accelerating to an energy of 1.4 GeV, followed by the Proton Synchrotron (PS) accelerating to an energy of 25 GeV, and finally, the Super Proton Synchrotron (SPS) accelerating to an energy of 450 GeV. Finally, the protons are injected into the LHC, separating into two parallel beam pipes that circulate one beam in a clockwise direction and the other in an anti-clockwise direction. The remaining acceleration of the beams up to (E_b = 6.5 TeV for $\sqrt{s}$ = 13 TeV collisions or E_b = 2.51 TeV for $\sqrt{s}$ = 5.02 TeV collisions) is provided by 16 RF cavities housed along the circumference which are also used to bunch the protons into up to 2556 distinct bunches of about 10^{11} protons with a spacing of about 7 m or 25 ns. Typically beams are separated into bunch trains, groups of 48-72 bunches, with gaps between them. Most of the LHC circumference constitutes 1232 superconducting dipole magnets of field strength 8.3 T required to bend the proton beam and keep them within the beam pipe. When the beams reach their final energy, they are crossed at several interaction points (IPs), four of which house the large experiments ATLAS, CMS, LHCb and ALICE. The full complex for Run-2, as well as the location of the four experiments, are shown in Figure 4.1.

The LHC succesfully began it's first operational run "Run-1" in 2009 with high-energy pp collisions at $\sqrt{s}$ = 7 TeV and at $\sqrt{s}$ = 8 TeV in 2012. In 2013 and 2014 the LHC then

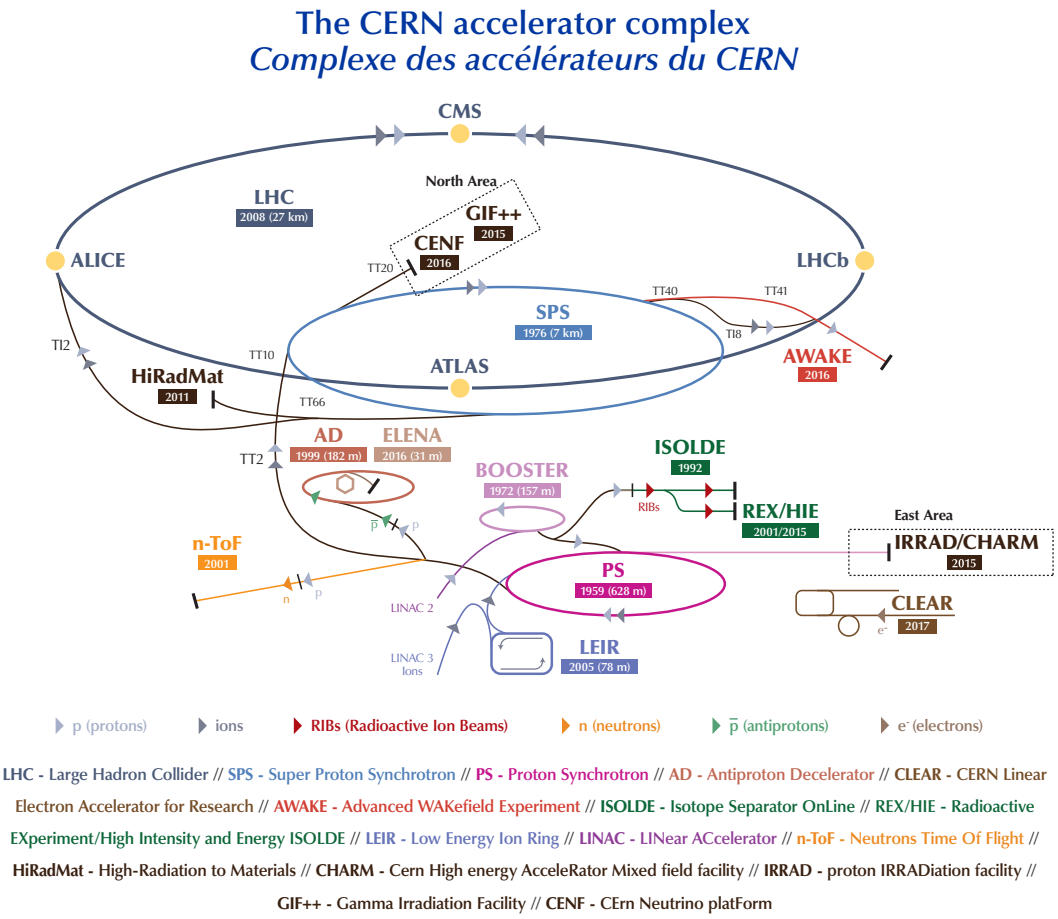

Figure 4.1: The CERN accelerator complex during the LHC Run-2 (2015-2018) data period and the location of each of the four large experiments [94].

underwent a maintenance period, long shutdown 1 (LS1). LHC operations restarted with "Run-2" in which the major dataset collected was pp collision data at $\sqrt{s} = 13\,\text{TeV}$, collected during 2015-2018. From 2019-2021 the LHC then underwent a second maintenance period, long shutdown 2 (LS2) with "Run-3" scheduled to start in 2022 with pp collisions of $\sqrt{s} = 13.6\,\text{TeV}$. In addition to the major data-taking periods, the LHC also executed shorter runs with unique conditions including the dedicated low-pileup runs discussed in Section 4.5.1. There were also pPb and PbPb heavy-ion collisions which will not be discussed in this thesis, though it should be noted a short pp dataset was taken in 2015 at $\sqrt{s} = 5.02\,\text{TeV}$ to correspond to the heavy-ion per-nucleon energy of $\sqrt{s_{\text{NN}}} = 5.02\,\text{TeV}$.

4.2 The ATLAS Detector

ATLAS (A Toroidal LHC ApparatuS) [95] is a general-purpose detector designed to cover a broad range of physics analyses, spanning from searches for new physics such as supersymmetry or exotic particles, precision measurements of Standard Model processes including electroweak bosons, top quarks and Higgs-boson properties, as well as studies of heavy-ion collisions and

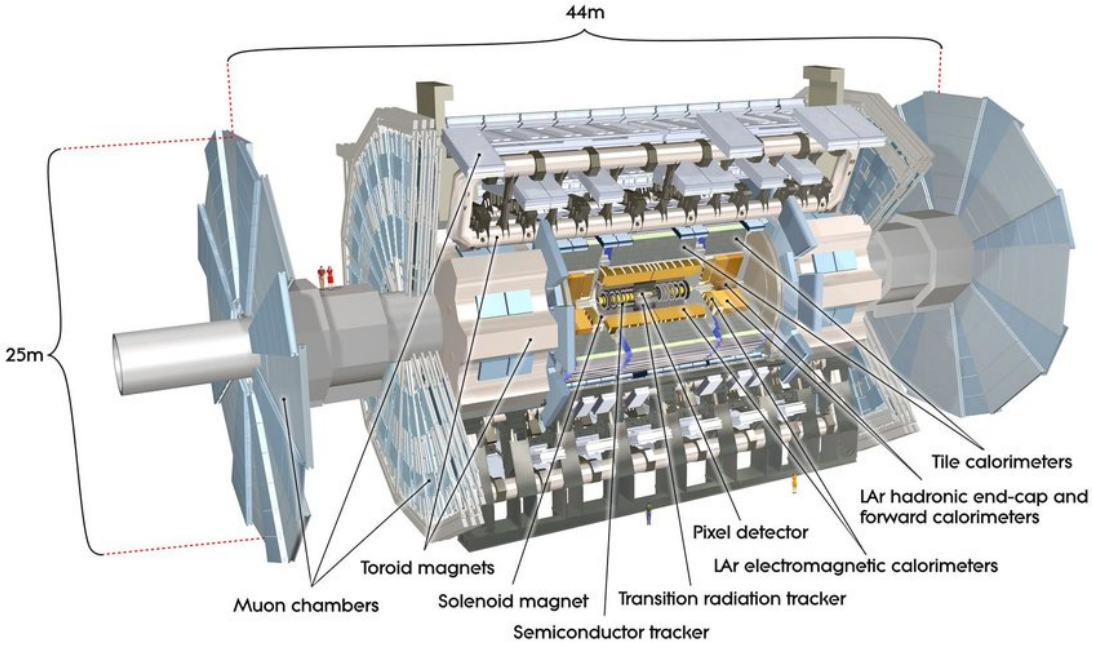

Figure 4.2: Diagram showing the ATLAS detector, highlighting the locations of the individual sub-systems it is contructed from [96].

heavy flavour physics. Is it constructed with a cylindrical shape to be symmetric around the LHC beam line, providing an almost hermetic 4π coverage. It is the largest of the LHC experiments with dimensions of about 44 m metres in length along the beampipe and about a 25 m diameter. A diagram of the ATLAS detector is shown in Figure 4.2 where it is shown that it is constructed from multiple sub-systems. In addition, ATLAS is complemented by a collection of forward detectors located further down the beamline.

4.2.1 Coordinate System and Particle Kinematics

ATLAS uses a "right-handed" coordinate system with the origin $(x, y, z) = (0, 0, 0)$ at the nominal interaction point. The x-axis points from the IP to the centre of the LHC ring, and the y-axis points upwards. The z-axis points in the direction of the beam pipe, where the positive z-direction is labelled as the A-side, and the negative z-direction is the C-side. The azimuthal angle ϕ is defined as the angle around the z-axis in the transverse (x,y) plane. The polar angle θ is defined as the angle with respect to the z-axis. A reconstructed particle will have a corresponding 4-vector $p^{\mu} = (E, p_x, p_y, p_z)$ defined with its energy and projected momentum in the x, y, z directions. It is more common to define the kinematics of a particle with the quantities more easily measured in the detector, for example, the measurement of momentum in the transverse (x, y) plane p_T. A commonly used kinematic quantity for an object is an approximate measure of it's longitudinal boost the pseudorapidity η, which is defined by the limit of rapidity y as the particles mass approaches zero,

$$\eta = -\ln \tan\left(\frac{\theta}{2}\right). \tag{4.1}$$

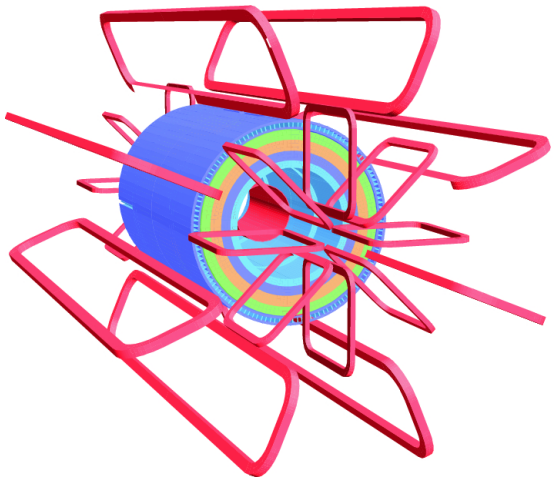

Figure 4.3: Geometric layout of the ATLAS magnet systems, showing the Barrel Toroid and End-cap Toroids in red, with the Central Solenoid in the centre encased by calorimeter layers. [95].

Differences in pseudorapidity are invariant under longitudinal boosts and is usually an easier quantity to consider than angle θ due to being more evenly distributed. A Lorentz invariant angular distance between two vectors is commonly defined in ϕ and η with $\Delta R = \sqrt{(\Delta\eta)^2 + (\Delta\phi)^2}$.

4.2.2 Magnet Systems

ATLAS has a system of superconducting magnets to curve the trajectory of charged particles as they traverse the detector. The motion of a charged particle in a magnetic field is described by the Lorentz force,

$$\vec{F} = q\vec{v} \times \vec{B}, \tag{4.2}$$

where a force $\vec{F}$ is inflicted on a particle of charge q and velocity $\vec{v}$ when subjected to a magnetic field $\vec{B}$. The force $\vec{F}$ is perpendicular to $\vec{v}$ and $\vec{B}$, which results in a curved path traversed by the particle. By applying a known magnetic field, $\vec{B}$, the quantities q and $\vec{v}$ (which relates to momentum through $\vec{p} = \gamma m\vec{v}$ where γ is the Lorentz factor) can be calculated simply by measuring the trajectory of a particle.

The Central Solenoid (CS) is a superconducting solenoid system that provides a 2 T magnetic field, located between the Inner Detector and the Electromagnetic Calorimeter. The Barrel Toroid (BT) and End-cap Toroid (ECT) are superconducting toroidal magnet systems providing a magnetic field of 0.5 to 1 T to the MS. The system of magnets is shown in Figure 4.3.

4.2.3 Inner Detector

The Inner Detector (ID) shown in Figure 4.4 is the innermost sub-detector positioned closest to the IP.

It was designed to measure the tracks of charged particles through ionisation signals (referred to as hits) left in active sensors while minimising the energy lost due to this interaction. Identified

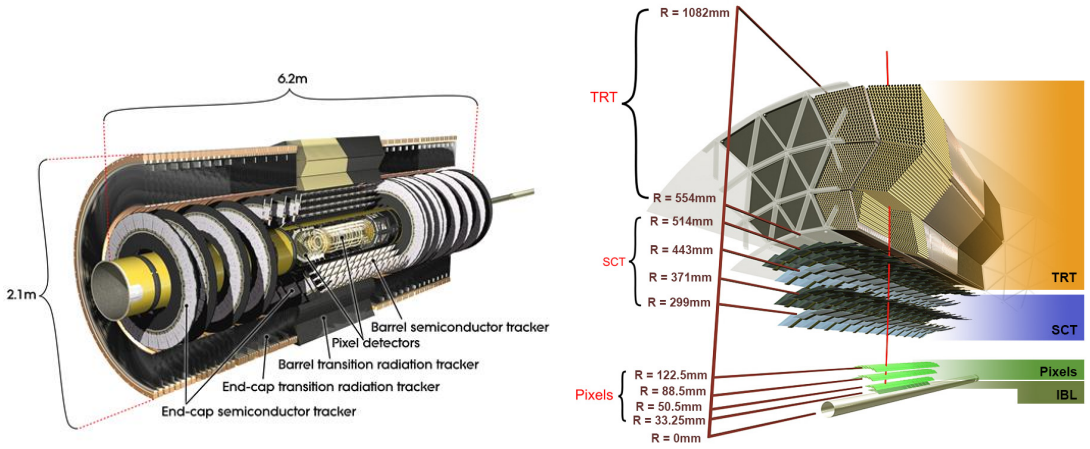

Figure 4.4: Schematic view of the ID showing the relative positions of the major components shown as the transverse cross-section and longitudinally. [95, 98].

tracks can be used to measure primary and secondary vertex positions as well the momenta of charged particle tracks for momenta above about 0.5 GeV with an acceptance extending up to $|\eta| < 2.5$ [97]. The total length of the ID is 7 m and extends to a radius of 115 cm. As it is close to the beam line, the ID is subject to a high radiation environment with a high track density, necessitating a fine detector granularity to discern individual tracks. The ID consists of three major components: the Silicon Pixel Detector, the Semiconductor Tracker (SCT), and the Transition Radiation Tracker (TRT).

Pixel Detector The Pixel detector uses highly granular high-resolution silicon pixels due to being the closest component to the beam line. Originally this consisted of three pixel detector barrel layers at a radius of 50.5 mm, 88.5 mm and 122.5 mm from the z-axis. However, in 2014 a fourth layer known as the Insertable B-Layer (IBL) was installed to improve tracking performance (specifically for b-tagging) at the higher luminosity expected from Run-2 [99]. The IBL sits at a radius of 33.3 mm. In addition there are three discs in the end-cap regions at $|z|$ of 495 mm, 580 mm and 650 mm. The pixel detector is composed of "modules", which are identical rectangular devices containing 46,080 pixels. These are arranged into the three concentric layers, resulting in a total of about 92 million readout channels. In the Pixel detector, position is measured with precision of 8μm ($R-\phi$) and 40μm (z) in the IBL, 10μm ($R-\phi$) and 115μm (z) in the barrel, 10μm ($R-\phi$) and 155μm (R) in the endcaps.

Semiconductor Tracker The SCT uses similar techniques to the Pixel detector, though experiencing decreased track density in comparison. It uses cheaper hardware with coarser granularity to allow coverage of a larger surface area, specifically silicon microstrip detectors covering the radial distance between 299 mm and 560 mm and consists of 4088 modules arranged in four cylindrical layers in the barrel region and two end caps with nine discs each extending from 853.8 mm and 2720.2 mm. Modules consist of two layers of silicon microstrips and are shaped to tailor their radial location. In the SCT, position is measured with a precision of 17 μm ($R-\phi$) and 580 μm (z) in the barrel, and 17 μm ($R-\phi$) and 580 μm (R) in the endcaps.

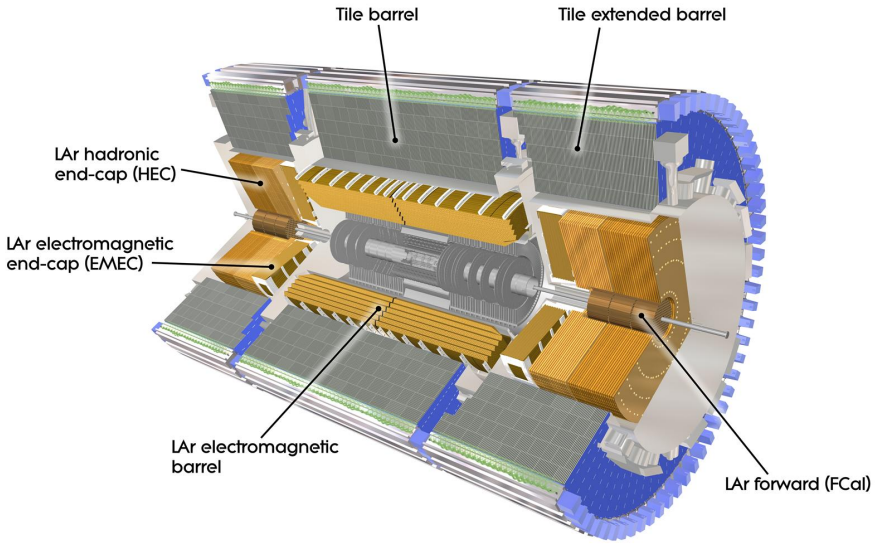

Figure 4.5: Schematic view of the full ATLAS calorimeter system showing the electromagnetic, hadronic and forward systems. [95].

Transition Radiation Tracker The Transition Radiation Tracker is the outer-most component of the ID covering a radial distance of 563 mm to 1066 mm and it extends to $|\eta| < 2$. It utilises straw drift-tube detectors (polyimide straws) of diameter 4 mm separated with polypropylene fibres. The drift tubes were designed to contain a mixture of Xe (70%), CO_2 (27%) and O_2 (3%), though in Run-2 were partially operated with an Ar based mixture due to gas leaks. A gold-plated tungsten wire runs through the centre of each tube which is held at ground potential, while the walls of the tubes are kept at −1.5 kV. When a charged particles traverse the TRT, it ionises the gas inside the tubes where drift electrons are collected on the wire, amplified and read out. The TRT measures position in $R - \phi$ and $z - \phi$ with a resolution of 130 mm for both. It can produce up to 36 additional measurements for each track, and because of the larger covered radius, it offers improved curvature measurement. The polymer fibres between the straws are in place to create transition radiation, which highly relativistic charged particles may emit as they traverse the material boundary. This induced radiation deposits additional energy into the gas, providing additional hits. Deposits with transition radiation are identified as high-threshold hits instead of low-threshold hits where less transition radiation exits. The TRT provides useful information for particle identification as the amount of transition radiation depends on the Lorentz factor $\gamma = E/m$, which is higher for electrons than for pions of the same momentum (or energy).

4.2.4 Calorimeter System

The calorimeter systems in ATLAS (shown in Figure 4.5) are designed to completely absorb and measure the energy of all SM particles except muons and neutrinos. They are all sampling calorimeters designed from alternating layers of absorbing high-density material, to promote particle showers of incident particles, and layers of "active" material, designed to measure the

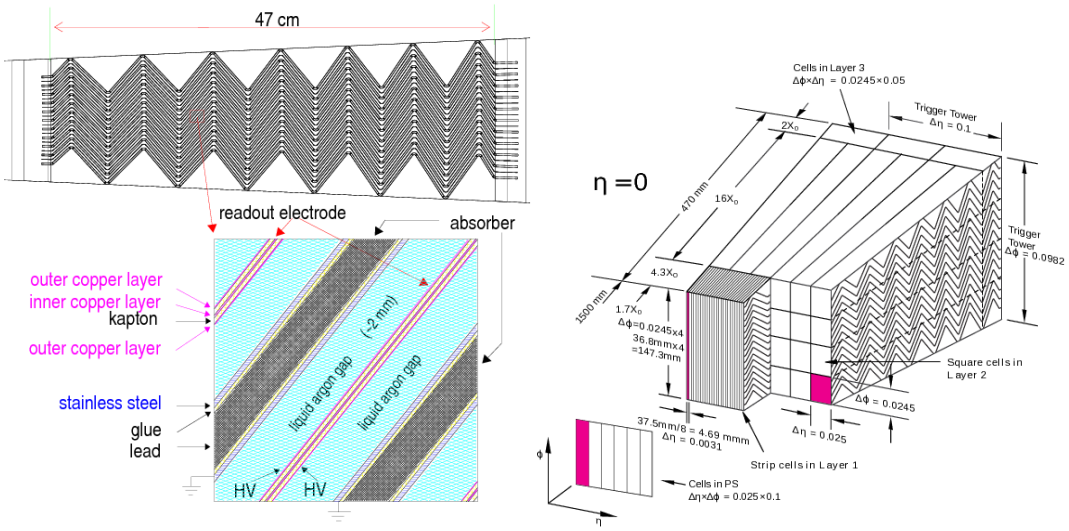

Figure 4.6: Schematic view of the barrel module of the liquid argon electromagnetic calorimeter (left) and the accordion-shaped geometry [95].

deposited energy from particle showers. The systems are distinguished by both the material of the active layers and the particles they are optimised to measure. The electromagnetic calorimeters are optimised to measure electrons and photons and use liquid argon technology. The hadronic calorimeters use a combination of LAr calorimeters and plastic scintillating tile calorimeters (TileCal) to measure hadronic particles such as protons, neutrons and pions. The geometry of the calorimeters is optimised to contain showers, minimising the leakage of particles into the next detector system.

The electromagnetic calorimeter systems are designed to induce electromagnetic showers for incident electrons (or positrons) and photons via a chain of pair-production (photons converting into e^+e^- pairs) and Bremsstrahlung radiation (e^+ and e^- radiating photons). These interactions are often parameterised by the radiation length X_0, the mean distance an electron traverses before losing $1/e$ of its initial energy, and $7/9$ of the mean free path of a photon before e^+e^- pair production occurs.

The hadronic calorimeters are designed to induce hadronic showers driven by particle-nucleus interactions that produce charged particles, ionisation of detector material. About $1/3$ of the produced hadrons in these nuclear reactions are π^0 particles which decay via $\pi^0 \rightarrow \gamma\gamma$, introducing an electromagnetic shower component. The hadronic calorimeter is characterised by the interaction length λ, the mean distance a hadron traverses a material before undergoing a nuclear interaction.

Electromagnetic Calorimeters The electromagnetic calorimeters at ATLAS are built with an accordion-shaped geometry (shown in Figure 4.6) to provide complete azimuthal symmetry. They are structured with steel and lead absorbing material, and LAr cooled to 90 K as an active material, with both interleaved by copper-Kapton readout electrodes. As shower particles ionise the LAr material, the produced electrons are collected at the electrodes operating with potential

$\approx 2\,\text{kV}$. The ECAL is divided into the barrel and end-cap regions that, in total, provide a radiation length coverage of at least $22X_0$.

The barrel calorimeter (EMB) constitutes of two half-barrels covering $|\eta| < 1.475$ of length 3.2 m extending between radii of 1.4 m and 2 m. The end-cap calorimeters (EMEC) are wheels attached to the sides of the EMB with thickness 63 cm extending between radii of 0.33 m and 2.1 m. The EMEC consist of two co-axial wheels with the outer wheel section (OW) covering $1.375 < |\eta| < 2.5$ and an inner wheel section (IW) covering $2.5 < |\eta| < 3.2$. It is split into three or four layers: a thin presampler layer for correcting energy losses in material upstream of the EM calorimeter located (only for $|\eta| < 1.8$), a first layer which is finely segmented and provides precise measurement of η, a second layer which has a large interaction length X_0 with cells of granularity $\Delta\eta \times \Delta\phi = 0.025 \times 0.025$ where most energy is deposited, and a final sampling layer to characterise the development of the shower. The half-barrels are separated by a small 4 mm gap, and a transition region between the LAr barrel and end-cap regions is located at roughly $1.37 < |\eta| < 1.52$ which is dedicated to detector services, and is not fully instrumented.

Hadronic Calorimeters The hadronic calorimeters are separated into two components. The TileCal covers the barrel region outside the EMB and the Hadronic Endcap (HEC) comprises of two independent wheels outside of the EMEC.

The TileCal extends between radii of 2.2 m and 4.25 m with the central barrel covering $|\eta| < 1.0$ with length 5.8 m and two extended barrels covering $0.8 < |\eta| < 1.7$ each of length 2.6 m. The detector is segmented into three layers radially, and is constructed of small modules sized $\Delta\eta \times \Delta\phi = 0.1 \times 0.1$ in the first two layers and $\Delta\eta \times \Delta\phi = 0.2 \times 0.1$ in the outer layer, with most energy expected to be captured within the first two layers. The modules are constructed of steel as absorbing material, plastic scintillating tiles as active material. Readout is via photomultiplier tubes (PMTs) located at the outer radii. As charged particles interact with the scintillating tiles, photons of UV wavelengths are produced and collected by fibres that are subsequently read out by photomultiplier tubes (PMTs) at the module's exterior. The layers of the calorimeters have interaction lengths of $\lambda = 1.5, 4.1, 1.8$ in the barrel and $\lambda = 1.5, 2.6, 3.3$ in the extended barrels.

The two HEC detectors consist of two wheels (HEC1, HEC2) per end-cap (four wheels for the full detector) and cover the range $1.5 < |\eta| < 3.2$ with an inner radius of 37.2 cm or 47.5 cm to an outer radius of 2.03 m. The HEC wheels are built from 64 identical wedge-shaped modules constructed with copper as the absorbing material and LAr as the active material. The two wheels provide granularity of $\Delta\eta \times \Delta\phi = 0.1 \times 0.1$ for $1.5 < |\eta| < 2.5$ and $\Delta\eta \times \Delta\phi = 0.2 \times 0.2$ for $2.5 < |\eta| < 3.2$. The HEC calorimeters provide interaction lengths $\lambda \approx 10$.

Forward Calorimeter The Forward Calorimeter (FCal) is a collection of three components (FCal1, FCal2, FCal3) based on LAr technology that is designed to withstand high particle fluxes with a coverage of $3.1 < |\eta| < 4.9$. FCal1 uses copper as the absorbing material and is

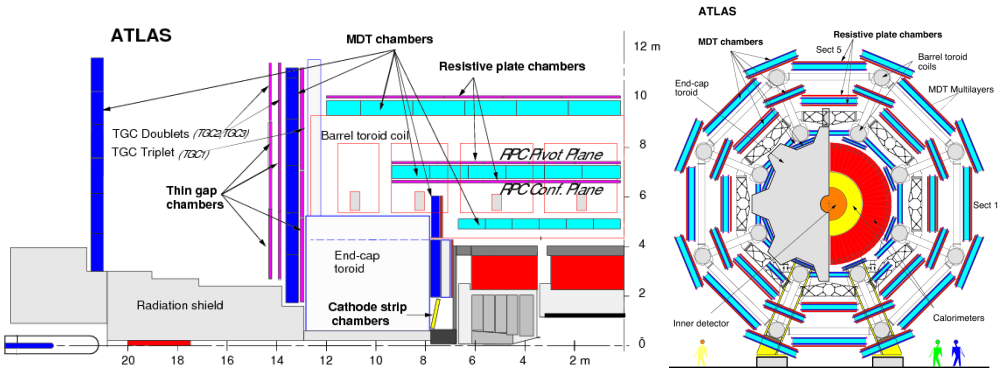

Figure 4.7: The longitudinal (left) and transverse (right) view of the Muon Spectrometer and the components that constitute it [100].

optimised for electromagnetic measurements. FCal2 and FCal3 use tungsten and are optimised for hadronic measurements.

4.2.5 Muon Spectrometer

The Muon Spectrometer (MS) is the outermost and largest sub-detector of ATLAS and is designed to precisely measure the trajectory and momentum of muons after they exit the calorimeters. These measurements are accomplished by measuring the muon curvature caused by the barrel toroid in the region ($|\eta| < 1.4$), the end-cap toroid in the range $1.6 < |\eta| < 2.7$ and a combination of both magnet systems in the intermediate region. These allow measurement of muon momentum in the range $3\,\text{GeV} < p_T(\mu) < 3\,\text{TeV}$. The MS system (shown in Figure 4.7) consists of four sub-systems; Monitored Drift Tube (MDT) chambers, Cathode Strip Chambers (CSCs), Resistive Plate Chambers (RPCs) and Thin Gap Chambers (TGCs), which are broadly separated as precision chambers (MDT and CSC) or trigger chambers (RPC and TGC). The barrel MS is positioned between and on the BT system, forming three concentric cylindrical shells of radii 5 m, 7.5 m and 10 m. The end-cap is constructed from four large wheels, perpendicular to the z-axis, located at a $|z|$ from the IP of 7.4 m, 10.8 m, 14 m, 21.5 m. The chambers follow the structure of the BT magnets and, as a result, have a 16-fold azimuthal symmetry in the transverse plane.

The MDTs are 29.9 mm diameter aluminium drift tubes filled with a pressurised Ar/CO_2 (93% / 7%) mixture with a central tungsten-rhenium wire of diameter 50 µm as the anode, held at a potential of 3 kV. They are organised in three layers covering $|\eta| < 2.7$, except for the innermost end-cap layer, where this is limited to $|\eta| < 2.0$. On average, a muon is expected to hit 20 individual MDT tubes. The region $2.0 < |\eta| < 2.7$ has a count rate too high for MDTs to measure, so this is compensated by using CSCs. There are a total of 16 CSCs on each side of the ATLAS detector, which are multiwire proportional chambers filled with an AR/CO_2 (80% / 20%) mixture with cathode strips running perpendicular to the anode wires, operating with a potential of 1.9 kV. The CSCs offer an improvement in maximum hit rate frequency over the MDTs by a factor of about 7.

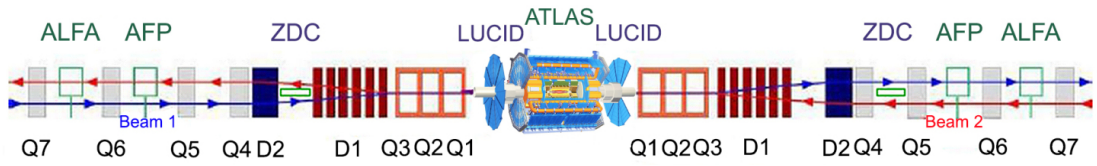

Figure 4.8: Diagram of the four ATLAS forward detectors housed on each side of the main detector [101].

The RPC and TGC detectors facilitate the muon trigger system by providing fast signals. The region $|\eta| < 1.05$ consists of three cylindrical layers of RPC chambers. The end-cap region ($1.0 < |\eta| < 2.4$) is covered by three layers of TGCs. The RPCs are electrode-plate detectors consisting of two parallel plates separated by a 2 mm gap filled $C_2H_2F_4$/Iso-C_4H_{10}/SF_6, where ionised electrons are collected at the anode and the signal is read out with capacitive couplings using electrodes mounted on the outer faces of the plates. The TGC are similar in operation to the CSCs, but with smaller spacing between the wire and the cathode than the spacing between multiple wires providing an increased granularity. A gas mixture of CO_2/C_5H_{12} is used to produce strong signals with high signal to noise even in high rate conditions.

4.2.6 Forward Detectors

In addition to the central ATLAS detector, four smaller detectors are located at high pseudorapidity much further down the beam pipe on both sides of the IP.

ALFA & AFP ALFA (Absolute Luminosity For ATLAS) is the furthest detector from the IP installed at a distance of about ±240 m and designed to measure the elastic scattering of protons at small angles originally for luminosity measurement. It can also detect protons that stay intact after diffractive pp interactions. ALFA is constructed from four Roman Pot stations placed close to the beamline with tracking detectors to measure protons in the transverse plane. The AFP (ATLAS Forward Proton) is the newest forward detector and is installed at distances from the IP of about ±205 m and ±217 m. It was designed to measure similar interactions to ALFA, in which one or two protons emerge intact from the pp collisions. Each station is constructed with silicon-based trackers and Cherenkov based time of flight detectors.

ZDCs (The Zero Degree Calorimeters) ZCDs are compact calorimeter systems (both electromagnetic and hadronic) located at about ±140 m from the IP at the position the separate LHC beam-pipes are merged into a single beam-pipe. They nominally operate during the heavy-ion runs with occasional usage in pp collisions. They are constructed to measure forward neutrons and photons with $|\eta| > 8.3$ by exploiting the fact that the LHC bending magnets do not affect neutral particles.

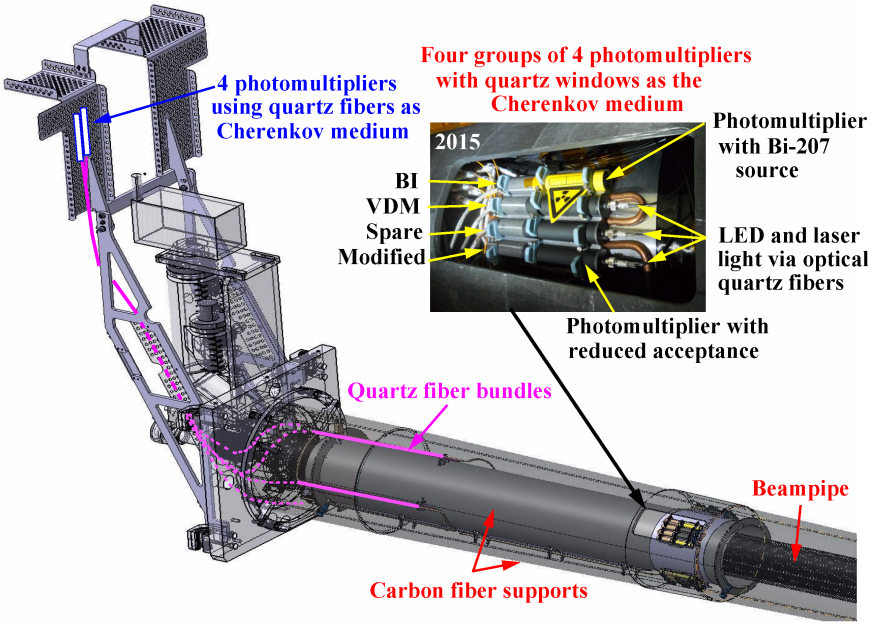

Figure 4.9: Diagram showing one of the two LUCID detector systems (A-side or C-side) showing the individual PMT components [102].

LUCID (Luminosity measurements Using Cherenkov Integrating Detector) is the only ATLAS detector system dedicated solely to luminosity measurement. The original detector, LUCID-1 from Run-1, was upgraded to LUCID-2 (which will henceforth be referred to as just LUCID) in 2015 to allow measurements at high luminosity as expected in Run-2. LUCID (shown in Figure 4.9) is installed ±17 m from the IP and provides a coverage of $5.6 < |\eta| < 5.9$. Each detector consists of 16 10 mm diameter photomultipliers (PMTs) that are arranged around the beam-pipe in four groups which operate on the principle that particles produced at the IP will traverse the quartz window of the PMT and release Cherenkov photons which are measured by the PMT systems. In addition, four bundles of quartz fibres attached to PMTs are situated 1.5 m from the detector, housed within further shielding. For each group of four PMTs, one is modified to contain a radioactive ^{207}Bi allowing studies of the gain and stability of the PMT systems. This hardware provided the online and offline estimates for Run-2 luminosity, which is described in Section 4.4.

4.3 Trigger and Data Acquisition

Recording a physics event requires the readout of many detector systems and the storage of the order of 1MB of raw data. With a nominal bunch-crossing rate of 40 MHz for Run-2, it is not possible to record all events due to both storage and bandwidth constraints. In addition, most pp interactions result in soft QCD events or events with low p_T final states, with a notably larger production rate compared to some of the rarer hard-scattering processes ATLAS would like to study. Naturally, it is not useful to store all of these low p_T events, and ideally, a system should be constructed to maximise the chances of recording the rarer high p_T processes. ATLAS accomplishes this with an online trigger system [103] that makes choices on detector readouts

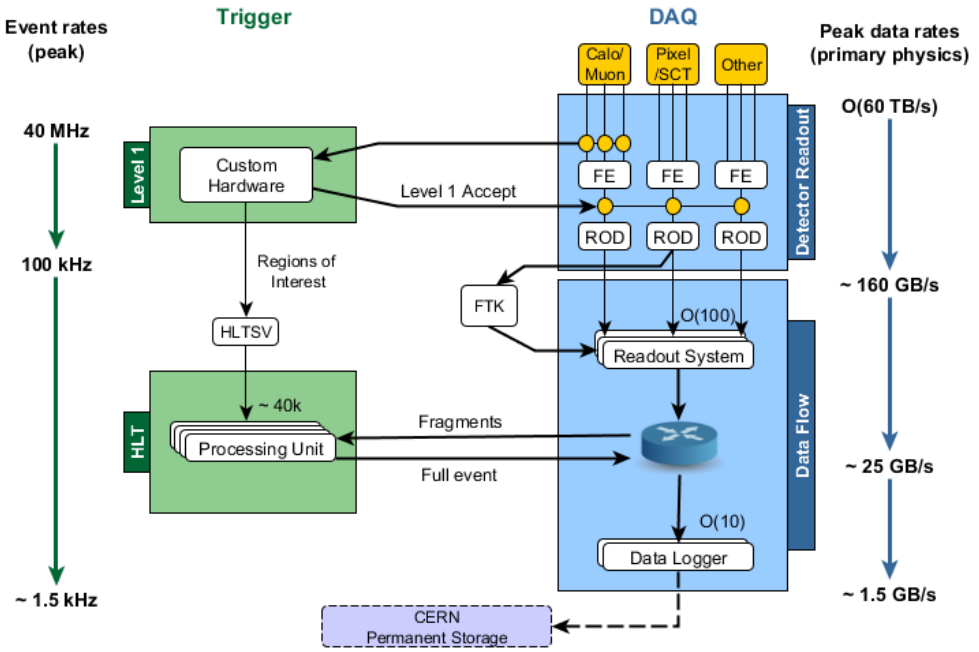

Figure 4.10: The ATLAS trigger and data acquisition system (TDAQ) [104] showing the flow of data from detector readout, through the L1 trigger, to the HLT and finally permanent storage on disk.

during the runtime to identify events that likely contain high-quality objects useful for physics analysis whilst maintaining a practical trigger rate abiding by bandwidth constraints. The full ATLAS trigger system is shown in Figure 4.10. The trigger system consists of a hardware-based first level trigger (Level-1 or L1) that uses custom electronics to analyse coarse readout data from the calorimeter (Level-1 Calo) and MS (Level-1 Muon) to determine Regions-of-Interest (RoIs) in the detector consisting of regions in $\eta - \phi$ space containing potential "physics objects". The MS information (from the RPC and TGC) is used to identify possible muons, whereas the calorimeter information is used with reduced granularity to help identify possible electrons, photons, τ-leptons, jets and events with large missing transverse energy E_T^{miss}. The L1 trigger makes decisions at less than about 2.5 µs and significantly lowers the event recording rate down to at most 100 kHz [105].

After an L1 trigger decision, the full detector readout is performed and temporarily buffered before being passed to the next trigger system, the software-based High-Level Trigger (HLT), which combines both the RoI seeds from L1 with detector information in full granularity as measured either within the RoI or for the full event itself depending on the physics object. The HLT uses sophisticated algorithms using detector measurements and partially reconstructed objects (to the extent required by the algorithm) to quickly make an improved selection beyond the L1. It decides which events are saved to disk. The HLT brings a further reduction of the recording rate down to around 1.2 kHz within a processing time of about 200 ms. The accepted events are then sent to CERN's permanent storage facilities and are processed to allow offline analysis.

Trigger Name	Lepton	Data Period	p_T or E_T Threshold [GeV]
HLT_e24_lhmedium_L1EM20VH	Electron	2015	24
HLT_e60_lhmedium	Electron	2015	60
HLT_e120_lhloose	Electron	2015	120
HLT_e26_lhtight_nod0_ivarloose	Electron	2016-2018	26
HLT_e60_lhmedium_nod0	Electron	2016-2018	60
HLT_e140_lhloose_nod0	Electron	2016-2018	140
HLT_e15_lhloose_nod0_L1EM12	Electron	low-μ	15
HLT_mu20_iloose_L1MU15	Muon	2015	20
HLT_mu50	Muon	2015	50
HLT_mu26_ivarmedium	Muon	2016-2018	26
HLT_mu50	Muon	2016-2018	60
HLT_mu14	Muon	low-μ	14

Table 4.1: Single lepton triggers for electrons and muons used for the Run-2 data taking trigger menus.

4.3.1 HLT Electron Trigger

The electron HLT trigger [106] is seeded by L1 RoIs defined from calorimeter information. For all electron triggers with threshold $p_T > 15\,\text{GeV}$, a "fast" reconstruction is performed using a neural-network-based "Ringer" algorithm which exploits the properties of EM shower development, analysing in a cone shape around the initial particle direction. If the criteria for the "fast" algorithms are satisfied, a set of "precision" algorithms that have similarities to offline reconstruction and identification (discussed in Section 5.2) are performed. The selection of electrons uses a likelihood discriminant with four working points: "lhvloose", "lhloose", "lhmedium" and "lhtight". The differences from offline analysis are that the discriminating variables used have different resolution, and the correction for bremsstrahlung radiation is not made. Some electron triggers exclude from the likelihood the transverse impact parameter, d_0, and its significance $|d_0/\sigma(d_0)$ (see Section 5.1) to mitigate the absence of the bremsstrahlung correction. These triggers have the suffix "nod0".

4.3.2 HLT Muon Trigger

The muon HLT trigger [107] is seeded by L1 RoIs defined from the calorimeter and muon trigger chambers. Next, a "fast" reconstruction is performed using the muon stand-alone algorithm and MDT hits within the L1 candidate RoI for all muon triggers. This algorithm utilises computationally fast parameterisation functions to obtain the muon p_T and then extrapolates the fitted track back to the IP, combining it with tracks in the ID, forming combined muon candidates (see 5.3). Finally, if the criteria for the "fast" algorithms are satisfied, a set of "precision" algorithms is applied, utilising all MS detectors in the track fitting and combining these with ID track information.

4.3.3 HLT Trigger Menu

The analyses described in this thesis make use of HLT single-lepton triggers for both electrons and muons, typically running with multiple distinct triggers optimised for different thresholds of lepton p_T that are summarised in Table 4.1. In addition to the previously described suffixes, the requirement of isolation is available for the electron and muon triggers, with a similar definition to the offline isolation (see Sections 5.2 and 5.3). These triggers are suffixed denoted with "iloose" or "ivarloose", depending on the definition of the isolation used.

4.4 Luminosity

The rate of events per unit time for a given physics process is given by

$$\frac{dN_{\text{process}}}{dt} = \mathcal{L}\sigma_{\text{process}}. \tag{4.3}$$

Here, σ_{process} is the process cross-section and $\mathcal{L}$ is the instantaneous luminosity. Over a given data taking period this gives the number of produced events N_{process} by

$$N_{\text{process}} = \mathcal{L}_{\text{int}}\sigma_{\text{process}}, \tag{4.4}$$

where the integrated luminosity $\mathcal{L}_{\text{int}} = \int \mathcal{L}dt$ is the time integral of the instantaneous luminosity. The precision of the integrated luminosity estimate translates directly into the precision of a cross-section measurement and is also important in the normalisation of background processes in searches.

The SI units of luminosity are $\text{m}^{-2}\,\text{s}^{-1}$ but at the LHC it is often given in $\text{cm}^{-2}\,\text{s}^{-1}$. The units for integrated luminosity remove the time dimension. Integrated luminosity is then given in inverse barns b^{-1} where $1\,\text{b} = 10^{28}\text{m}^2$. At the LHC it is common to discuss integrated luminosities measured in pb^{-1} and fb^{-1}.

4.4.1 Connection to Collider Parameters

The instantaneous luminosity delivered to ATLAS by two colliding bunches $\mathcal{L}_b$ is related to the beam parameters by,

$$\mathcal{L}_b = \frac{f_r n_1 n_2}{2\pi\Sigma_x\Sigma_y} \tag{4.5}$$

where f_r is the LHC revolution frequency of $\approx$ 11.2 kHz and n_1 and n_2 are the number of protons in the colliding bunches. The parameters Σ_x and Σ_y characterize the beam profiles in the horizontal and vertical dimensions. They are generalised to not assume beam profiles depend on a Gaussian distribution which remains a valid formalism when beams collide at non-zero

crossing angles. The luminosity for a given bunch crossing $\mathcal{L}_b$ can also be expressed as

$$\mathcal{L}_b = \frac{f_r \mu_b}{\sigma_{\text{inel.}}}, \tag{4.6}$$

where μ_b is the mean number of inelastic proton collisions per bunch crossing for a given bunch pair and the inelastic proton cross-section is $\sigma_{\text{inel.}}$. The total instantaneous luminosity $\mathcal{L}$ is calculated as the sum over all n_b bunches

$$\mathcal{L} = \sum_{b=1}^{n_b} \mathcal{L}_b = \frac{n_b f_r \mu}{\sigma_{\text{inel.}}} \tag{4.7}$$

where $\mu = \langle \mu_b \rangle$ is the mean number of interactions per bunch crossing, averaged over all n_b bunch pairs, and is referred to as the pileup parameter. Equation 4.6 cannot yet be used directly for measurement as $\sigma_{\text{inel.}}$ is not known well [108] and μ cannot be directly measured. It is therefore useful to define the quantity μ_{vis} as the mean rate of some observable quantity in the detector measured per bunch crossing, related to the inelastic cross-section by,

$$\mu = \frac{\sigma_{\text{inel}}}{\sigma_{\text{vis}}} \mu_{\text{vis}}, \tag{4.8}$$

allowing the definition

$$\mathcal{L} = \frac{n_b f_r \mu_{\text{vis}}}{\sigma_{\text{vis}}}. \tag{4.9}$$

Here σ_{vis} is the visible cross-section for the observable and is generally unknown, requiring calibration to obtain its value.

4.4.2 ATLAS Baseline Luminosity Measurement

Before discussing the details of luminosity measurement at ATLAS, it is useful to define a few commonly used terms.

- **LHC Fill** : A period of LHC operation is usually of the order of multiple hours to a day, which includes from the injection of beams, the ramp-up in beam energy, the period of data taking, and finally, the dump of the beam when intensity has reduced to a level where starting a new fill will maximise the integrated luminosity delivered.
- **ATLAS Run** : An LHC Fill in which ATLAS is collecting data.
- **Luminosity Block (LB)** : A unit of data-taking within an LHC Fill over which detector conditions are thought to be constant, which is typically of 60s duration.
- **Good Run List (GRL)** : The GRL lists for all luminosity blocks whether the quality of the data is good enough for use in physics analysis [110]. Failures are usually caused by the LHC beams not yet being stable, or ATLAS magnets or sub-detectors being switched off.

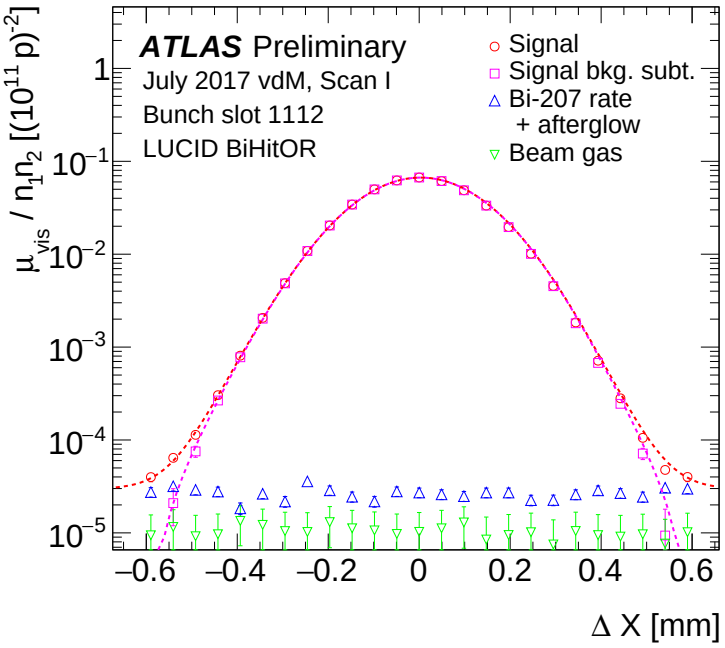

Figure 4.11: Shows an example scan of visible interaction rate μ_{vis} per bunch population product $n_1 \cdot n_2$ as a function of horizontal beam separation Δx. This plot specifically shows the response of the LUCID BiHitOR algorithm [109]. It should be noted the parameters n_1 and n_2 are not necessary to extract information about the beam width.

- **Luminometer** : A detector or algorithm that measures luminosity, which can be dedicated hardware but can also arise from a combination of detector quantities. The results of independent luminometers are frequently compared to ensure the reliability of the luminosity estimate.
- **Luminosity Levelling** : Control of the two beams to provide a constant instantaneous luminosity over a long period, combating the natural decay of the beam luminosity.

Luminosity Measurement with LUCID

The primary luminometer used for the ATLAS baseline luminosity estimate uses the LUCID detector, which was purpose-built for luminosity measurement. The visible cross-section is obtained by combining raw signals from the photomultipliers using multiple algorithms, changing the nominal algorithm throughout Run-2 [109]. One of the simplest algorithms is the HitOR algorithm which calculates the average probability of any one PMT to record a hit P_{HIT} via,

$$P_{\text{HIT}} = \frac{N_{\text{HIT}}}{N_{\text{BC}} N_{\text{PMT}}} = 1 - e^{-\mu_{\text{vis}}}, \tag{4.10}$$

where N_{HIT} is the total number of PMT hits summed over all PMTs in a given time period, N_{BC} is the number of colliding bunches in the same time period, and N_{PMT} is total the number of PMTs. The relation to μ_{vis} arises from Poisson statistics where the mean μ_{vis} hits yields $e^{-\mu_{\text{vis}}}$ as the probability to obtain zero hits, and hence $1 - e^{-\mu_{\text{vis}}}$ is the probability to obtain at least one.

The equation is inverted to give

$$\mu_{\text{vis}} = -\ln(1 - P_{\text{HIT}}) \tag{4.11}$$

where it should be noted the calculation is only solvable if P_{HIT} is not equal to unity. In 2015 the ATLAS baseline luminosity wad derived from the BiEventORA algorithm requiring a hit in any of the bismuth-calibrated LUCID PMTs on the A-side detector as the C-side PMTs displayed significant timing drifts. In 2016 and 2017 the BiHitOR algorithm was used counting the average number of hits on both the A and C sides. In 2018 a significant number of PMTs stopped working during the data-taking year so an algorithm (C12) was used to count the average number of hits of a single PMT (labelled C12).

Absolute Calibration of LUCID

The calibration of σ_{vis} for LUCID [109] is obtained using van der Meer scans [111], which are taken in special LHC fills during each data-taking year. These fills are tailored to minimise beam interactions by having a larger fraction of empty bunches, less protons per bunch and LHC optics settings with zero crossing angle. The transverse size of the beam is broadened to about 90 μm and special care is taken to shape the beams into Gaussian-like profiles in both the x and y axes. The VdM scan proceeds by slowly displacing the beams through each other such that the convolution of the two beams rises (as the overlapping region between the beams increases) and falls (when they begin to seaprate again). As the overlap increases, the measured rate of a given luminometer $R(x)$ is expected to rise, as shown in Figure 4.11. The scan of Δx can then be used to obtain Σ_x by

$$\Sigma_x = \frac{1}{\sqrt{2\pi}} \frac{\int \mathcal{R}(\Delta x) \mathrm{d}\Delta x}{\mathcal{R}(0)}; \tag{4.12}$$

where $\mathcal{R}$ is used to signify that the measurement is not a calibrated luminosity. Due to the cancellation between numerator and denominator any measurement proportional to luminosity can be used. The same calculation is performed for Σ_y as a function of Δy. The factor σ_{vis} is then calculated via a combination of Equation 4.5 and Equation 4.8,

$$\sigma_{\text{vis}} = \mu_{\text{vis}}^{\text{max}} \frac{2\pi\Sigma_x\Sigma_y}{n_1 n_2}, \tag{4.13}$$

where $\mu_{\text{vis}}^{\text{max}}$ is the visible interaction rate per bunch crossing specifically at the peak of the scan curve. Measurement of bunch populations n_1 and n_2 is done using LHC DC current transformers (DCCT) and fast beam-current transformers (FBCT) as well as complimentary information from the LHCb experiment [109].

Calibration Transfer

The absolute calibration of LUCID was performed under the special VdM scan conditions, which is at least three orders of magnitude lower luminosity than typical data-taking would

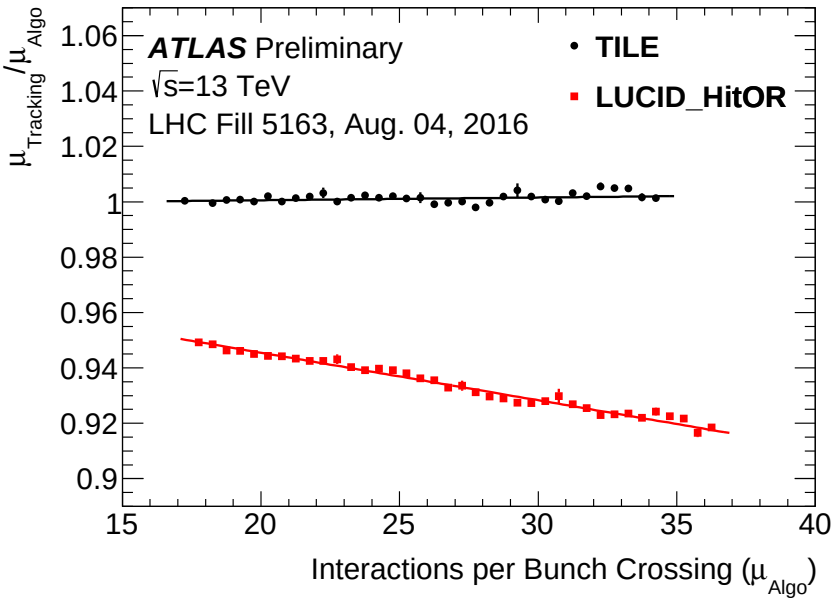

Figure 4.12: Shows the ratio of instantaneous luminosities measured by track-counting and LUCID BiHitOR (red) and a TILE algorithm (black). The TILE integrated luminosity has been normalised to that of track-counting for this plot [109].

experience. Luminometers typically react differently to conditions of an increase in pileup, and it becomes unclear whether the calibrated luminometer is accurate under these conditions. By comparing luminosity from LUCID to luminosity from other luminometers, corrections to the LUCID μ_{vis} are derived to cover both the differences. Other luminometers at ATLAS are:

- Track-counting: Determines μ_{vis} by measuring multiplicity of charged particle tracks in the inner detector.
- TILE: Determines μ_{vis} from photomultiplier currents in the scintillating-tile hadronic calorimeter.
- EMEC and FCal: Determines μ_{vis} from liquid-argon gap currents in the EMEC and FCal calorimeter systems.

To derive a correction for LUCID, a second luminometer is required. Additionally, it is important to check that the selected luminometer also displays stability with a third luminometer. Figure 4.12 shows the track-counting luminosity compared to both the LUCID HitOR algorithm and the TILE luminometer. Compared to LUCID, a sizeable $O(10\%)$ trend is observed, whereas compared to TILE, good stability is observed. Finally, the slope of Figure 4.12 is used to derive a correction for LUCIDs non-linearity.

Long Term Stability Studies

VdM scans require a dedicated effort and take away time from nominal high-luminosity running so they are typically performed only once or twice a year. It is, therefore, necessary to study whether LUCID has any drift over the year by comparing luminosity estimates from various

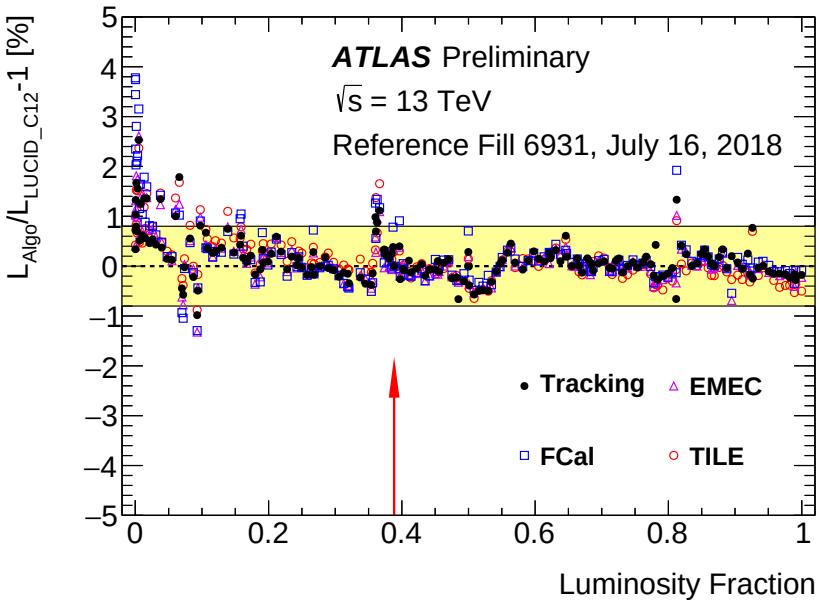

Figure 4.13: Fractional differences of fill-integrated luminosities between LUCID C12 single-PMT algorithm and other luminometers Track-counting, EMEC, FCal, TILE. Luminosity has been normalised to the anchor run indicated by the red arrow. A ±0.8% uncertainty was applied, indicated by the yellow band [109].

Data Period	No. of LHC Fills	Typical $\langle\mu\rangle$	$\mathcal{L}_{\text{int}}$ (fb^{-1})	Total Unc. (%)
13 TeV high-μ Run-2	582	33.7	139.0	1.7
13 TeV high-μ 2015,2016	64, 144	13.4, 25.1	36.2	2.1
13 TeV high-μ 2017	183	37.8	44.3	2.4
13 TeV high-μ 2018	191	36.1	58.5	2.0
13 TeV low-μ 2017,2018	6, 5	2 or 1 (levelled)	0.3351	1.5
5.02 TeV low-μ 2017	15	0.5-4	0.2568	1.6

Table 4.2: A table summarising results [109, 112] for the ATLAS luminosity estimate for high-μ and low-μ data taking periods. The grouping of 13 TeV high-μ in 2015 and 2016 and 13 TeV low-μ 2017 and 2018 have been shown as the corresponding uncertainty has been calculated for both periods combined. The levelling of low-μ runs at $\sqrt{s} = 13$ TeV is denoted as the delivered μ was held constant for each LHC fill at either $\mu = 1, 2$. The number of LHC fills that contain at least one LB passing the GRL is also given.

algorithms as a function of time at the granularity of each LHC fill. An example of this stability study is shown in Figure 4.13 where drifts are observed comparing multiple luminometers to LUCID with as large as 1% trends observed over the year. These trends are used to quantify time-dependent corrections to the baseline luminosity and provide an uncertainty prescribed using a band that encloses the observed trends. The Z-counting luminosity method described in Section 7 offers a novel way of performing this study without reference to VdM scans.

Run-2 Luminosity

The ATLAS luminosity analyses for the Run-2 data is documented in Ref. [109], as well as the special low-μ data taking periods in Ref. [112]. These analyses need to consider many

systematic uncertainty sources, notably the vdM calibration, the calibration transfer, and the long-term stability. A summary of the luminosity related parameters, the corresponding integrated luminosity, and the prescribed uncertainty is provided in Table 4.2. It is remarkable that the uncertainty on these estimates tends to be around or below 2%, which is only possible due to extensive studies of the VdM scan data and studies of the stability of multiple luminometers. The dominant uncertainty sources for the full high-μ dataset arise from the calibration transfer (1.3%) and the long-term stability (0.6%). To improve the luminosity measurement further, the introduction of the Z-counting luminosity method described in Section 7 can provide novel insight into these sources.

4.5 The case for low-pileup datasets

The LHC physics program requires large integrated luminosities to facilitate studies of rare physics processes. The LHC was designed to deliver a high instantaneous luminosity of about $10^{34}\text{cm}^2\text{s}^{-1}$ which was exceeded by a factor of about two in Run-2. The trend of increasing luminosity is also set to continue with the High Luminosity LHC (HL-LHC) [113] upgrade planned for completion in 2026, which is designed to provide luminosity up to about $7.5 \times 10^{34}\text{cm}^2\text{s}^{-1}$.

The drawback of the increasing instantaneous luminosity is the increase in pileup $\langle\mu\rangle$, which is given by:

$$\langle\mu\rangle = \frac{\mathcal{L}\sigma_{\text{inel.}}}{n_b} \tag{4.14}$$

where $\mathcal{L}$ is the operating instantaneous luminosity, $\sigma_{\text{inel.}}$ is the inelastic pp cross-section of about 80mb, $n_b = 2800$ the total number of bunch pairs. For the Run-2 peak luminosity of $2 \times 10^{34}\text{cm}^2\text{s}^{-1}$ this yields a mean number of interactions per bunch crossing of $\mu \approx 60$. For the the HL-LHC the peak luminosity of $7.5 \times 10^{34}\text{cm}^2\text{s}^{-1}$ yields a mean number of interactions per bunch crossing of $\mu \approx 200$.

When selecting a hard-scatter physics event for analysis, the final states of these additional interactions will also leave signals within the detector. Interactions originating from the same bunch crossing as the hard-scatter event, arescalled "in-time pileup". Some parts of the detector, notably the LAr calorimeter systems, are also sensitive to deposits from previous bunches, known as "out-of-time pileup", due to their processing integrating signals over ≥ 5 crossings. An example $Z \to \mu\mu$ candidate collected in 2017 is shown in Figure 4.14 where data was collected at $\langle\mu\rangle \approx 53$. The impact of pileup is clear from the large number of additional vertices reconstructed in addition to that of the identified Z-boson candidate. Energy deposits arising from pileup interactions interfere with particle reconstruction and selection, which leads to worsened efficiencies and resolutions on measured quantities. In W-boson physics the resolution of the hadronic recoil u_T (the vector sum of momenta in the transverse plane of all final state particles not associated to the lepton) has a strong dependence on $\langle\mu\rangle$ as shown in Figure 4.15. This parameter is the only experimental measure of W-boson transverse momentum $p_T(W)$ in the $W \to \ell\nu$ channel, the modelling of which is crucial for precision studies of the SM

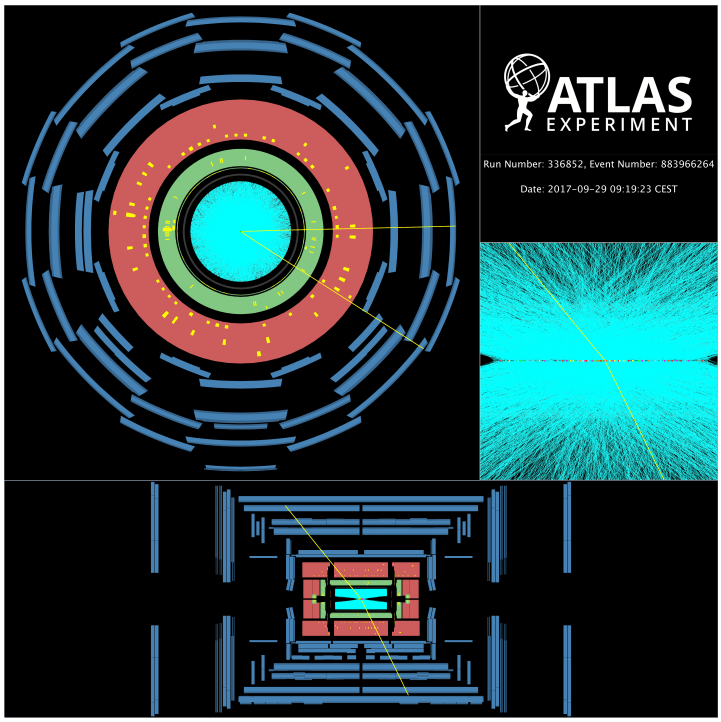

Figure 4.14: An example $Z \to \mu\mu$ candidate recorded on the 29th of September 2017 taken when $\langle\mu\rangle \approx 53$ taken from the ATLAS public event displays [116]. Calorimeter cells with $E_T > 500\,\text{MeV}$ are shown. The upper left display presents a transverse view of the event (x-y plane) where the yellow lines show the two muons' paths. The upper right display shows the 66 reconstructed vertices. The bottom display presents the event in longitudinal view (z-r plane). Tracks with $p_T > 100\,\text{MeV}$ are displayed.

through the W-boson mass [114]. The inability to precisely measure u_T under high-μ conditions motivated the collection of a special subset of data taken under low-μ conditions [115].

4.5.1 Low-pileup Data

During November of 2017 ATLAS collected 256.8pb^{-1} of data at $\sqrt{s} = 5.02\,\text{TeV}$ and 144.9pb^{-1} of data at $\sqrt{s} = 13\,\text{TeV}$. An additional set of data was collected in July 2018 recording a further 190.2pb^{-1} of data at $\sqrt{s} = 13\,\text{TeV}$. During collection the beams were steered such that a constant $\langle\mu\rangle \approx 2$ was maintained. The $\langle\mu\rangle$ profile for this data is shown in Figure 4.16.

Inside the calorimeters, the presence of pileup events produces electronic noise that requires some mitigation. In high-μ running, this is performed by use of a noise threshold parameter σ_{noise} requiring that a certain significance is passed before a cell is used in the clustering. The low-μ datasets were reconstructed with this threshold lowered to increase the sensitivity of the calorimetry measurement to smaller signals [115].

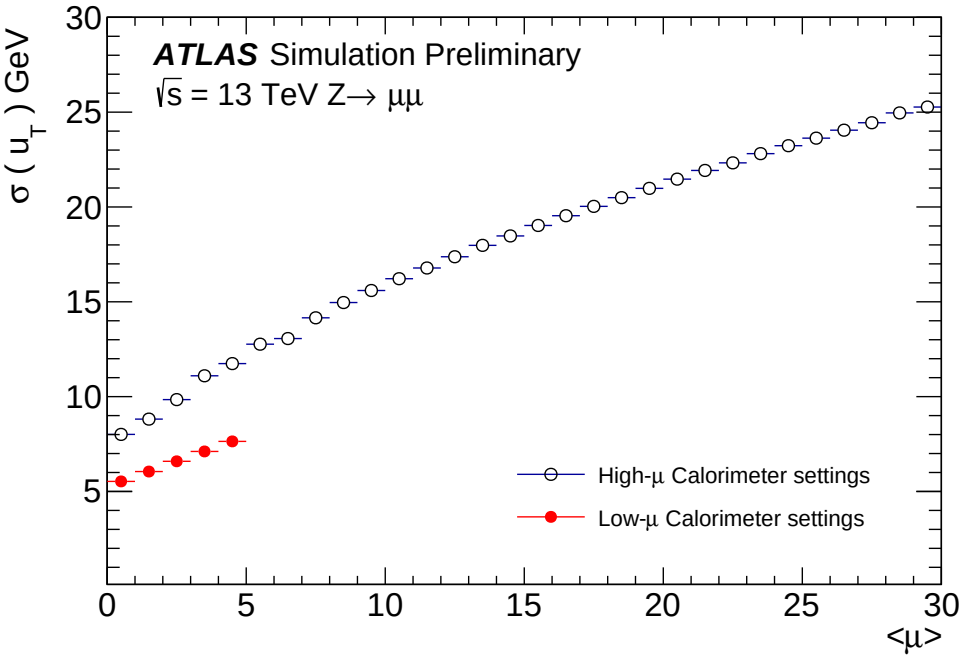

Figure 4.15: The resolution of the hadronic recoil u_T as calculated using simulated $Z \rightarrow \mu\mu$ events [115], showing a strong dependence on $\langle\mu\rangle$. Also shown is the impact of lowering the calorimeter noise threshold parameter σ_{noise} used in clustering, as was performed for the low-μ datasets.

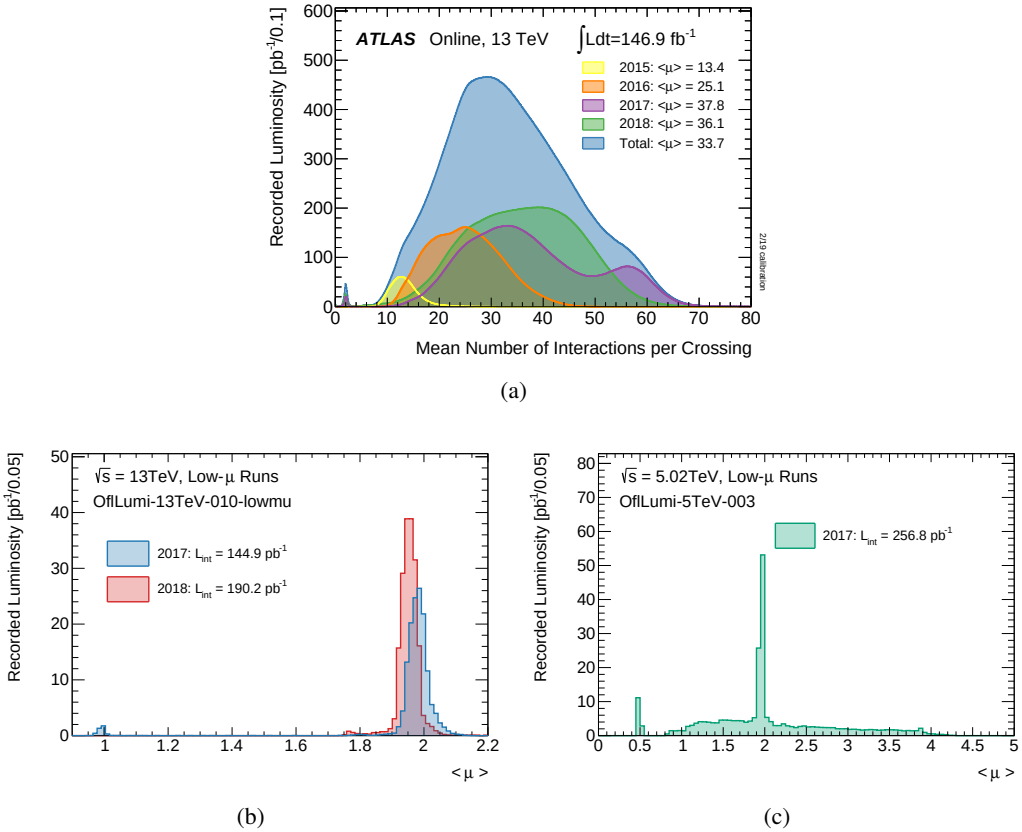

(a)

(b)

(c)

Figure 4.16: Profiles showing the mean number of interactions per crossing ($\langle\mu\rangle$) for data collected in (a) $\sqrt{s} = 13\,\text{TeV}$ Run-2 (both high-μ and low-μ are shown) [117], (b) $\sqrt{s} = 13\,\text{TeV}$ low-μ runs and (c) $\sqrt{s} = 5.02\,\text{TeV}$ low-μ runs. The profile in (a) is constructed from all ATLAS recorded luminosity. The profiles in (b) and (c) are constructed with the additional requirement of being "good-for-physics" luminosity obtained from the most up to date luminosity tags.

5 Reconstructing Physics Objects

Signals produced by the detector subsystems as measured in data or resulting from the digitisation step of simulation must be processed to identify and reconstruct physics objects used in analyses. The work described in this thesis requires definitions of candidates for charged-particle tracks, electrons and muons. A reconstructed particle should provide a four-vector describing the candidates momentum and should also provide a summary of quality criteria that can control the purity of selecting genuine physics objects from background processes that "fake" the same signature as the candidate.

5.1 Charged Particle tracks and Primary Vertices

Charged-particle tracks are reconstructed by combining "hits" from the ID subsystems. The trajectory of a charged-particle track in the presence of a solenoid magnetic field can be described with a helix. Track reconstruction in ATLAS employs the 5-dimensional helix parameters evaluated at the point of a tracks closest approach to the z-axis:

$$(d_0, z_0, \phi, \theta, q/p) \tag{5.1}$$

where d_0 is defined as the shortest distance between a track and the z-axis, z_0 is the z-coordinate of the point at which d_0 is calculated, ϕ and θ are the azimuthal and polar angles derived at the point where d_0 and z_0 are defined, and q/p is the ratio of the particles charge to the magnitude of its momentum. These perigee scheme track parameters are shown in Figure 5.1.

5.1.1 Track Reconstruction

The main algorithm used for ID track reconstruction [119, 120] is the *inside-out* pattern recognition sequence consisting of the following steps:

- **Formation of Space-Points:** First steps are the creation of clusters (neighbouring hits) in the Pixel and SCT and drift-circles (describing the radii from the anode in which the particle traversed a given straw) in the TRT. These are then transformed into 3D space points.
- **Seeding:** Seeds are created based on three unique space points from either Pixel only, SCT only, or a mixture of the two.

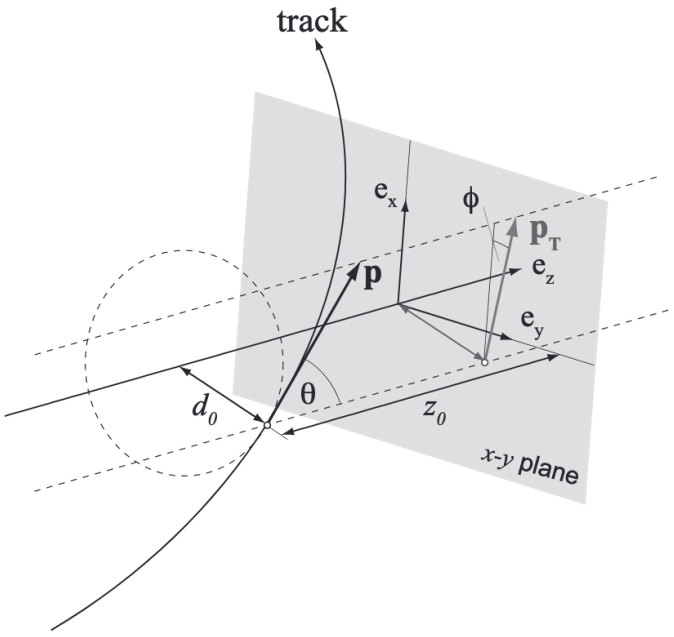

Figure 5.1: Shows the 5D track coordinates in the perigee scheme. [118]

- **Track Candidates:** The seeds are used to estimate a trajectory and are required to be compatible with a fourth additional space point. A combinatorial Kalman filter [121] is then used to complete track candidates within the silicon detectors.
- **Ambiguity Solving:** Track candidates are assigned a track score based on multiple quantities such as the absence of clusters in detector layers, quality of the curvature fit and shared clusters with other candidates. Tracks are rejected if they fail to meet basic quality criteria. The remaining tracks with no shared clusters with other candidates are accepted. Tracks with shared clusters are fed through a neural network designed to separate multiple tracks associated withthe same cluster [122].
- **TRT Extension:** Track candidates are extended to the TRT where there are matching hits. This extended track is then refit to yield an improved track resolution.

5.1.2 Vertex Reconstruction

To identify the proton-proton interaction point it is important to find common intersection points (vertices) between sets of reconstructed tracks, ensuring they have originated from the same interaction. This is accomplished using an iterative vertex reconstruction algorithm [123, 124] consisting of the following steps:

- **Seeding:** A single seed is calculated taking the transverse position as the centre of the beam spot, and the position of the seed is taken as the mode of the z_0 value for all tracks taken with respect to the centre of the beamspot.

- **Iterative Fitting:** Tracks and the seed are used to estimate the best fitting vertex position. An iterative procedureis used in which least compatible tracks are down-weighted and the vertex position is recomputed. Eventually the weights of incompatible tracks have small weights and have very little effect on the fit. The iteration is continued until the fit stabilises.
- **Additional Vertices:** Tracks that are deemed incompatible with the vertex are removed from it and allowed to be used in the determination of additional vertices. The process is then repeated with the remaining tracks in the event.

A "primary vertex" is a vertex where the corresponding tracks are consistent with originating from a pp interaction. A "secondary vertex" is defined as a vertex that is spatially displaced from the primary vertices, indicating they originate from the decay of long-lived particles.

To define a physics event for analysis it is first necessary to select a "hard-scatter vertex" where the corresponding tracks are expected to originate from a hard-scatter process. This is obtained by constructing primary vertex candidates where all vertices contain at least two charged particle tracks of $p_T > 500\,\text{MeV}$, and selecting the vertex with the highest sum of squared transverse momentum over all its associated tracks $\sum_{\text{tracks}} p_T^2$. All other primary vertex candidates are treated as originating from pileup and disregarded in any further processing.

5.1.3 Impact Parameters

The impact parameters of a track with respect to its primary vertex are defined by

- **Transverse Impact Parameter: d_0 Significance:** the ratio of d_0 to the fitted uncertainty on d_0, $d_0/\sigma(d_0)$ the ratio
- **Longitudinal Impact Parameter: $z_0 \sin(\theta)$:** The projection of a tracks point of closest approach projected onto the z-axis.

5.2 Electrons

5.2.1 Electron Reconstruction

Electrons are characterised by clustered energy deposits in the electromagnetic calorimeter matched to a charged-particle ID track, as shown in Figure 5.2. These electrons can only be reconstructed in the range $|\eta| < 2.47$ due to the coverage of the ID. There are also definitions for "forward electrons" that can be reconstructed in the range $|\eta| > 2.5$ using information from the FCal. However, as these are not used in this thesis, they will not be discussed further. Typically electrons used for analysis are only reconstructed outside the barrel and end-cap transition region $1.37 < |\eta| < 1.52$, commonly referred to as the "crack region". This is due to the presence of passive material and services resulting in a worsened quality reconstruction.

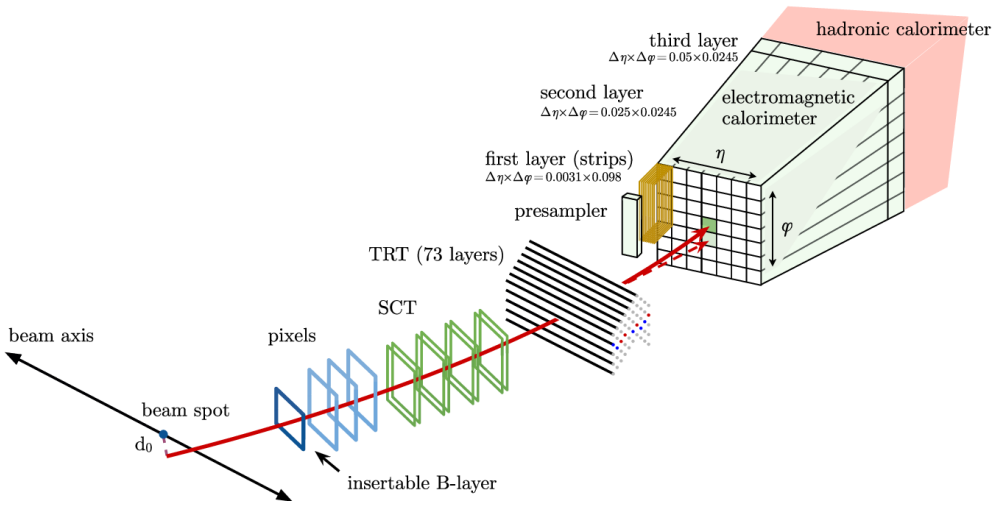

Figure 5.2: A view of an electron's path (shown in red) passing through layers of the ATLAS detector (Pixel, SCT, TRT and EM calorimeter). The dashed line shows Bremsstrahlung radiation occurring within the ID before the calorimeter [125].

A major challenge for matching clusters to ID tracks in ATLAS arises from a large amount of material within the ID volume causing traversing electrons to radiate energy via bremsstrahlung radiation. This radiation can then pair-produce electron-positron pairs, leaving additional collimated tracks within the ID consistent with the calorimeter cluster. Therefore, electron reconstruction algorithms are designed with energy losses and multiple collimated ID tracks considered.

Electron reconstruction in ATLAS [125, 126] starts by first reconstructing clusters from information in the electromagnetic calorimeter. In offline processing, this was accomplished with a topocluster reconstruction algorithm [126]. However, the more simple sliding-window algorithm [127] was used for online reconstruction, notably by the electron HLT trigger [106]. Both of these algorithms are discussed in more detail below. Selected clusters are then used as seeds for the matching of ID tracks. Reconstructed tracks are refitted using a Gaussian Sum Filter [128] (GSF), which corrects for energy losses expected from bremsstrahlung radiation, and are then matched to the localised clusters using the cluster barycenter as the point of reference for matching in (η, ϕ) space. Multiple track matches are resolved with an ambiguity algorithm using multiple track parameters and the distance between the track and cluster barycenter, which better excludes converted photons from faking electron candidates.

Clustering: Topocluster Reconstruction

Topocluster reconstruction begins with constructing proto-clusters in both the electromagnetic and hadronic calorimeter systems based on the noise-threshold $\varsigma_{\text{cell}}^{EM}$,

$$\varsigma_{\text{cell}}^{EM} = \frac{E\text{cell}^{EM}}{\sigma\text{noise, cell}^{EM}}, \tag{5.2}$$

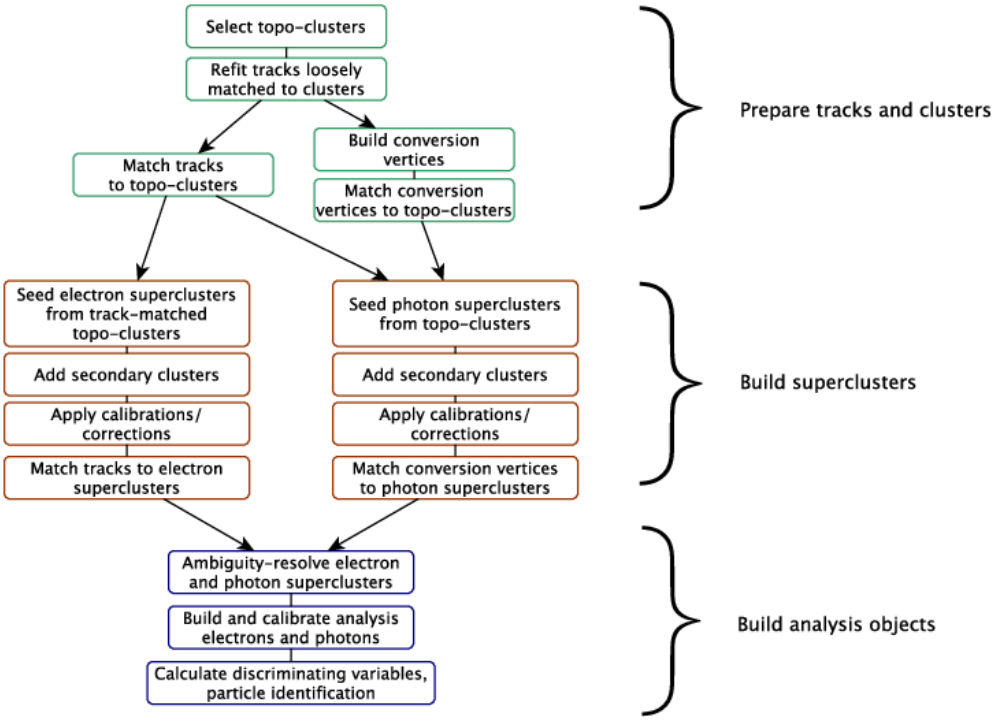

Figure 5.3: Algorithm used for electron and photon reconstruction via topocluster reconstruction [126].

where $E\text{cell}^{EM}$ is the signal scale accounting for the energy deposited in the calorimeter via EM showers and $\sigma\text{noise, cell}^{EM}$ is the expected noise in the cell accounting for electronic noise and pile-up induced noise tuned according to the data-taking conditions. A Proto-cluster is formed around a cell with $\varsigma^{EM}_{\text{cell}} \geq 4$, in which are added neighbouring cells that satisfy $\varsigma^{EM}_{\text{cell}} \geq 2$. Each cell satisfying $\varsigma^{EM}_{\text{cell}} \geq 2$ becomes a seed in the next iteration collecting each of its own neighbours in the proto-cluster. If two proto-clusters share a cell with $\varsigma^{EM}_{\text{cell}} \geq 2$, then the proto-clusters are merged. Finally, after all cells have been collected an additional set of neighbouring cells is added to the cluster with $\varsigma^{EM}_{\text{cell}} \geq 0$. This full chain is commonly known as 4-2-0 topocluster reconstruction. If two cells with $E^{EM}_{\text{cell}} > 500\,\text{MeV}$ maxima are found within the proto-cluster, they are split into separate clusters. The construction of an electron supercluster (a connection of topoclusters) involves a complex algorithm (shown in Figure 5.3) performed in two steps. First, the found topoclusters are tested as seeds for the supercluster, and secondly, nearby topoclusters are identified as satellite clusters that have emerged from Bremsstrahlung radiation. Topoclusters are sorted by decreasing E_T, and seeds are considered only when $E_T > 1\,\text{GeV}$ and they match a track containing at least four hits in the silicon tracking detectors. Finally, clusters cannot be used as seeds if they are added as a satellite in another seed cluster. Satellites are added for all topoclusters within the window $\Delta\eta \times \Delta\phi = 0.075 \times 0.125$ around the seed clusters barycenter, as well as for any topocluster within $\Delta\eta \times \Delta\phi = 0.125 \times 0.3$ that shares a best-matched track with the seed cluster. Multivariate calibration is applied on the selected supercluster, which is used to define the final electron object used for analysis. This multivariate algorithm is trained on simulated single electrons to provide the best energy resolution.

Clustering: Sliding Window

The electromagnetic calorimeter is divided into a grid of 200×256 towers in $(\eta \times \phi)$ space of granularity 0.025×0.025. Energy deposits within the tower across all layers are approximately calibrated before being summed to provide a towers total deposited energy. A sliding window of 3×5 towers in $\eta \times \phi$ is then scanned over the entire $\eta \times \phi$ grid, and any configuration yielding a summed E_T exceeding 2.5 GeV is seeded as a cluster candidate. If two seed candidates are in close proximity, defined as an overlap within area $\eta \times \phi = 5 \times 9$, a decision is made by comparing the cluster E_T values as follows. If two clusters are separated by at least 10% in E_T, the higher E_T cluster is retained. If two clusters are within 10% in E_T, the cluster with the highest E_T central tower (in the 3×5 space) is kept. The remaining tower in both cases is removed.

5.2.2 Electron Identification

Electron Identification working points are defined to improve selection of prompt (labelled as signal) electrons from non-prompt (labelled background) sources such as electrons from photon conversions and decays of heavy-flavour hadrons. This is accomplished using a likelihood-based (LH) method that constructs a discriminant based on numerous inputs from the ID measurements, the calorimeter measurements, and a combination of both. Given a set of measurements as a vector $\vec{x}$, the likelihood of a given electron originating from signal L_S or background L_B is defined by

$$L_{S(B)}(\vec{x}) = \prod_{i=1}^{n} P_{S(B),i}(x_i), \tag{5.3}$$

where $P_{S,i}$ and $P_{B,i}$ are the probability densities for signal or background respectively, for the input variable x_i. For each electron candidate, a discriminant d_L is formed:

$$d_L = \frac{L_S}{L_S + L_B}. \tag{5.4}$$

A modified discriminant d'_L is defined by taking the inverse sigmoid transform to provide a more convenient discriminant for defining working points.

$$d'_L = -\tau^{-1} \ln\left(d_L^{-1} - 1\right), \tag{5.5}$$

where $\tau = 15$ is fixed. As the probability of an electron being signal increases, the discriminant also increases. The common working points Loose, Medium and Tight (also labelled LooseLH, MediumLH, TightLH) are defined in increasing thresholds of the modified discriminant. Run-2 identification efficiencies are presented as a function of E_T and η in Figure 5.4 where notable increases in identification efficiency are observed going from TightLH to MediumLH to LooseLH, respectively. The LooseLH criteria offer the highest efficiency at the expense of increased non-prompt electron contamination.

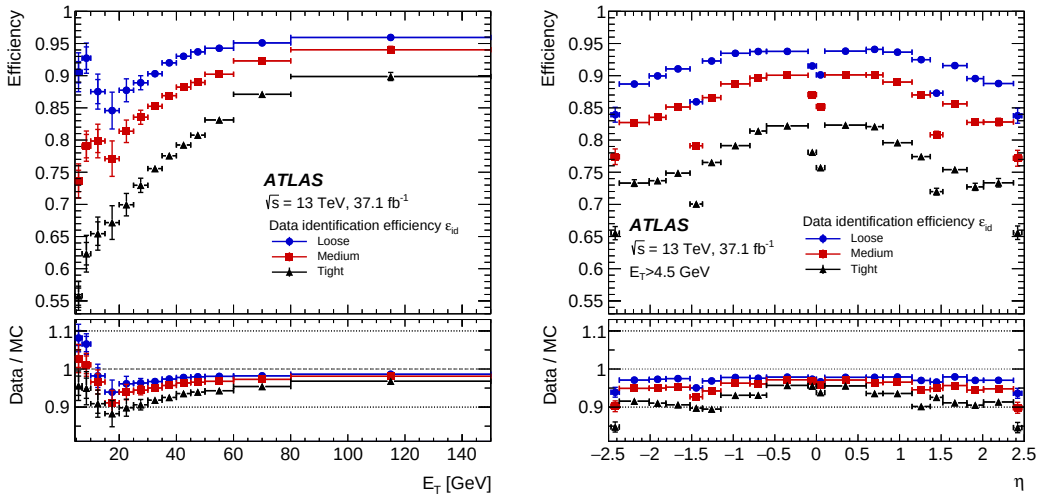

Figure 5.4: Measured likelihood based electron-identification efficiencies for the working points: Loose (LooseLH) in blue, Medium (MediumLH) in red and Tight (TightLH) in black. The dependency of each efficiency is shown in both E_T (left) and η (right) [125].

5.2.3 Electron Isolation

Electron isolation is applied to identified electrons to further improve purity. Isolation is measured by p_T^{coneXX} where a cone of size $\Delta R = XX/100$ is defined and summing the p_T of all trackes contained within the cone not associated with the electron. Similarly E_T^{coneXX} is defined by summing E_T for calorimeter clusters within the cone not associated with the electron. Although it is not strictly necessary for the analyses presented in this thesis, isolation variables are typically defined such that the cone shrinks for increasing lepton p_T. This definition is used for improved identification of electrons in more complex final states where additional hadronic activity may be present. This varying cone is defined as $p_T^{\text{varconeXX}}$ where Δr varies as,

$$\Delta R = \min\left(\frac{10\,\text{GeV}}{p_T\text{GeV}}, \Delta R_{\text{max}}\right). \tag{5.6}$$

Typically $\Delta R_{\text{max}} = 0.2, 0.4$ depending on analysis, and this can be used as a selection variable, or a specific working point. A working point used in this thesis is "LooseTrackOnly". It is defined by varying the selection requirement on $p_T^{\text{varcone20}}$ as a function of η and p_T such that the signal efficiency is constant at 99% for all η and p_T.

5.3 Muons

5.3.1 Muon Reconstruction

Muons are characterised by measured tracks in both the ID and MS and a minimum-ionising signature in the calorimeters. This signature is unique to muons as they are the only non-neutrino particle that can escape the calorimeter systems without being absorbed. Tracking is performed independently in both the ID and MS, and the two reconstructed tracks are combined

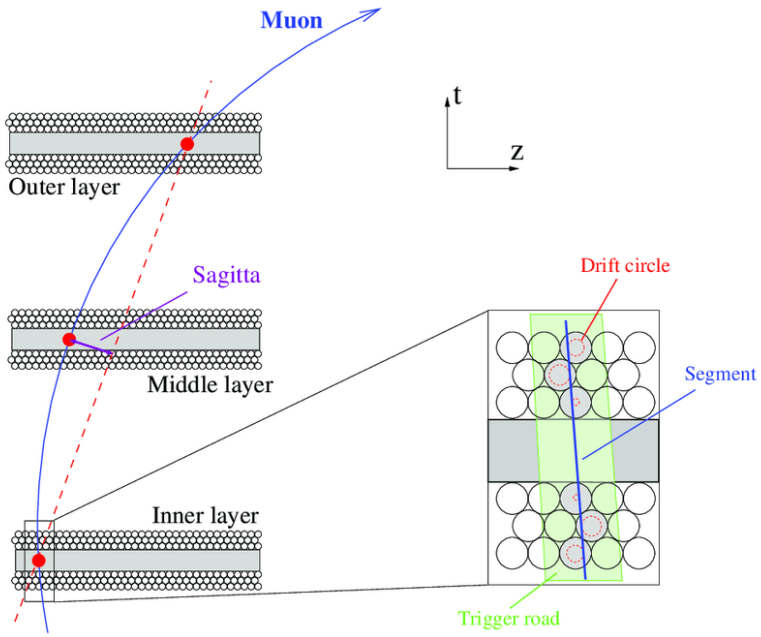

Figure 5.5: Illustration of a muon traversing layers in the muon spectrometer and how the sagitta is defined relative to the muon track curvature [130].

to construct the muon physics object. The ID tracks are constructed as described in Section 5.1 and provide coverage over the range $|\eta| < 2.5$. The MS tracks provide coverage of $|\eta| < 2.7$ and are constructed with a different selection.

Track Reconstruction in the MS

Track candidates are constructed using a segment-seeded algorithm [129] that fits hits from segments in different layers of the MDT. The algorithm starts by seeding with segments generated in the middle layer of the detector where more trigger hits are available before extending to use the inner and outer layers as seeds. Track candidates in the barrel region require at least two segments matched by position and angle and various quality requirements on hit multiplicity and quality of fit. Track candidates in the barrel-endcap transition region can be constructed from a single high-quality segment. After all track candidates are obtained, an overlap removal algorithm identifies the best assignment of segments to a single track or whether multiple tracks can share segment information. Finally, all hits associated with a track candidate are fitted globally, and only tracks with good χ^2 values are accepted.

The curved trajectory of a muon track due to the presence of the magnetic field B is used to obtain the muon track momentum p. This curvature can be summarised via the track sagitta s, obtained from circular geometry treating the track as an arc as shown in Figure 5.5.

Combined Reconstruction

Muon reconstruction is performed by various algorithms depending on the available information from the ID, MS and calorimeters. Four types of muons are commonly used in physics analysis which are optimised for different detector regions.

- **Combined Muons (CB):** Track reconstruction is performed independently in the ID and MS before a combined track is formed via the global refit using hits from both the ID and MS. Most muons are reconstructed using an *outside-in* pattern recognition, where MS tracks are extrapolated and matched to ID tracks. The energy losses within the calorimeter systems are compensated during the fitting of a combined muon.
- **Segment-Tagged Muons (ST):** A track from the ID is extrapolated to the MS, and tracks matched with at least one track segment in the MDT or CSC chambers are classified as muons. ST muons are used for muons where only one layer of the MS chambers was crossed, either due to falling outside of the MS acceptance or due to their low $p_T(\mu)$.
- **Calorimeter-Tagged Muons (CT):** A track from the ID is extrapolated to the calorimeter system, and tracks matched with an energy deposit consistent with a minimum-ionising particle are classified as muons. This generally offers poor purity but recovers acceptance in the region $|\eta| < 0.1$ where the MS is only partially instrumented, and is optimised for the range $15\,\text{GeV} < p_T(\mu) < 100\,\text{GeV}$
- **Extrapolated Muons (ME):** A track from the MS is extrapolated with a loose requirement on the compatibility of it originating from the IP. The kinematics of the MS track are corrected for energy loss in the calorimeters and defined by assuming it originates from the IP. ME muons are optimised for the region $2.5 < |\eta| < 2.7$ where the acceptance is increased beyond what the ID can measure. In general, a ME muon must hit at least two layers of the MS in the barrel region or three layers in the end-caps.

Muon Type Overlap

Detector hits can be used to define multiple types of muon, which have to be resolved before producing the final analysis-level muon objects. For example, when two muon candidates share the same ID track, a preference is given to CB muons first, ST muons second, and finally CT muons. The overlap with the ME muons is resolved by analysing the track hit content and selecting the tracks with more hits and those with a better quality fit.

5.3.2 Muon Identification

Muon Identification working points (WPs) are defined to improve the selection of prompt (labelled as signal) muons from non-prompt (labelled background) sources such as muons from heavy-flavour hadrons. Muon identification WPs provided in ATLAS are *Medium*, *Loose*, *Tight*

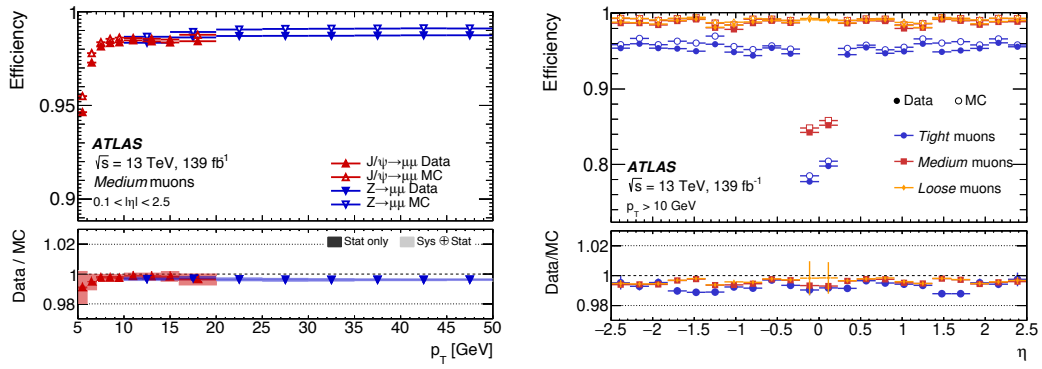

Figure 5.6: Left: Muon reconstruction and identification efficiency for the Medium working point shown versus p_T. Right: Muon reconstruction and identification efficiency for the working points: Loose (yellow), Medium (red) and Tight (blue) shown versus η. [125].

and *High-*p_T, which are optimised to the needs of different physics analyses. The analyses in this thesis use *Medium* muons, so this WP will be discussed in detail. Medium muons are the default selection at ATLAS and are constructed to minimise systematic uncertainties associated with the reconstruction and calibration. CB muons are selected with a requirement of ≥ 3 hits in at least two layers of the MDT, except for tracks with $|\eta| < 0.1$ where tracks with at least one MDT layer but no more than one MDT hole are allowed. ME tracks are also selected with a requirement of at least three MDT/CSC layers, but are only used in the $2.5 < |\eta| < 2.7$ region. To suppress contamination from hadrons, medium muons require a loose selection on the compatibility of the ID and MS by comparing the q/p significance via

$$|(q/p)_{\text{ID}} - (q/p)_{\text{MS}}| / \sqrt{\sigma^2_{(q/p),\text{ID}} + \sigma^2_{(q/p),\text{MS}}} < 7 \tag{5.7}$$

Run-2 muon identification and reconstruction efficiencies are presented as a function of p_T and η in Figure 5.6 where the Medium efficiency displays a flat dependency on η for all region except $|\eta| < 0.1$.

5.3.3 Muon Isolation

Muon isolation is applied to identified muons to further improve purity, similarly electron isolation. The same quantities p_T^{coneXX}, E_T^{coneXX} and $p_T^{\text{varconeXX}}$ can be derived with the same definitions, but with respect to a muon object. Similarly, $p_T^{\text{varconeXX}}$ is defined by

$$\Delta R = \min\left(\frac{10\,\text{GeV}}{p_T\text{GeV}}, \Delta R_{\text{max}}\right), \tag{5.8}$$

where, typically $\Delta R_{\text{max}} = 0.2$ or 0.4 depending on the analysis. This can be used as a selection variable, or a specific working point can be used. A working point used in this thesis is "LooseTrackOnly". It is defined by varying the selection requirement on $p_T^{\text{varcone30}}$ as a function of η and p_T such that the signal efficiency is constant at 99% for all η and p_T.

6 Lepton Calibration

The reconstruction and selection of leptons is performed the same algorithms in data and simulation. However, the performance of these algorithms on data is generally not expected to be perfectly modelled in simulation, which is a requirement for physics analysis. These discrepancies can occur for various reasons, for example, the mismodelling of pileup and its impact on lepton reconstruction or the degradation of detector components that is not accounted for in the detector simulation. Improving the modelling of reconstruction and selection of leptons in simulation is achieved by introducing various calibration techniques and correction factors. These include calibration of the electron and muon energy and momentum scales and corrections for lepton identification and isolation selection efficiencies. These calibrations and corrections are derived using data-driven techniques, usually using di-lepton events from the $Z \to \ell\ell$ resonance. A summary of corrections used for low-μ analyses is now provided.

6.1 Electron Scale and Resolution Correction

The energy of electron objects is first calibrated using a dedicated high-μ procedure [132, 133], outlined in Figure 6.1, which is applied to both data and MC. A summary of each step is:

1. **Training of MC-based Calibration:** MC simulated events are used to train a multivariate model that corrects raw cluster energy to the "true" electron energy.

2. **Longitudinal Layer Intercalibration:** Corrections are applied to the data to account for residual differences between data and simulation. The response in data is equalised with respect to simulation and is calibrated in different layers due to the longitudinal segmentation of the EM calorimeter. The first correction is the derivation of the intercalibration factor between the first and second layer of the EM calorimeter by comparing the energy deposition in each layer using $Z \to \mu^+\mu^-$ events. The second correction accounts for the energy scale of just the presampler layer and is determined from the ratio of presampler energies in data and simulation using unconverted photons from radiative Z-boson decays and inclusive photon production.

3. **MC-based Calibration:** Application of the step 1 calibration to both data and MC.

4. **Uniformity Corrections:** Correction for known non-uniformity in the detector response vs ϕ in certain (η, ϕ) regions. One example is the impact of gravity on the gaps between barrel modules.

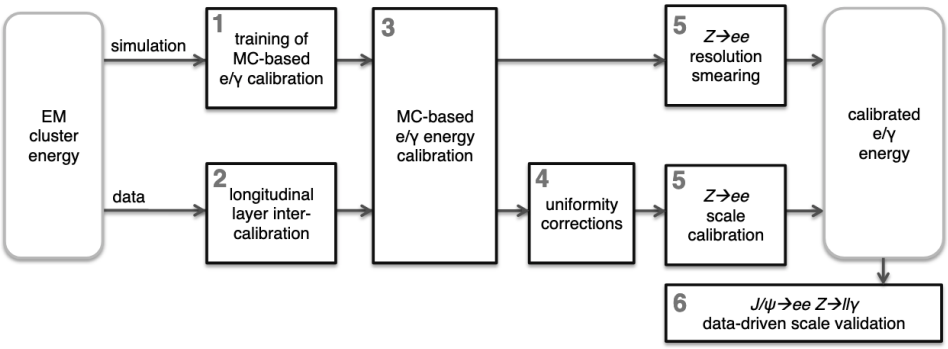

Figure 6.1: Schematic overview showing the calibration procedure for electron and photon energy response in ATLAS [131].

5. **Resolution and Scale Calibration:** The data is corrected with the energy scale factor α_i, parameterised in bins of pseudorapidity i according to,

$$E_i^{\text{data,corr}} = E_i^{\text{data,uncorr}}/(1+\alpha_i) \approx E_i^{\text{MC}} \tag{6.1}$$

where $E_i^{\text{data,corr}}$ and $E_i^{\text{data,unccorr}}$ are the corrected and uncorrected energy response and the scale parameter α_i for a given pseudorapidity bin is evaluated by equating to the energy response in MC E_i^{MC}. The resolution on the energy measurement E is expressed as the quadratic sum of three uncorrelated terms different in dependency on E,

$$\frac{\sigma(E)}{E} = \frac{a}{\sqrt{E}} \otimes \frac{b}{E} \otimes c. \tag{6.2}$$

Here, b is the electronics and pileup noise term, a is the stochastic term that relates to the development of the electromagnetic shower and c is a constant term that represents the non-uniformities, mechanical imperfections a in the detector. The c term is usually about 1% in the barrel and 1-2% in the calorimeter end-caps. These terms are obtained by minimising the χ^2 between the shape of the $Z \to ee$ mass distribution in MC and data.

6. **Data-Driven Scale Validation:** The accuracy of the calibration is validated using an independent cross-check using the $J/\psi \to ee$ resonance.

An additional constant correction is derived specifically for the low-μ datasets to compensate for any differences observed in the high-μ evaluation of c. The relative resolution is increased via the addition of a new constant term c_i' in quadrature as given by,

$$\left(\frac{\sigma(E)}{E}\right)_i^{data} = \left(\frac{\sigma(E)}{E}\right)_i^{MC} \otimes c_i', \tag{6.3}$$

where c_i' is derived for a given pseudorapidity bin. The optimal value of c_i' is obtained by minimising the χ^2 between the shape of the $Z \to ee$ in data and in MC.

The corrections α_i and c_i' are derived separately for both $\sqrt{s} = 5.02\,\text{TeV}$ and $\sqrt{s} = 13\,\text{TeV}$ as shown in Figure 6.2. The results for α are consistent for both $\sqrt{s} = 5.02\,\text{TeV}$ and $\sqrt{s} = 13\,\text{TeV}$. The results for c_i' are consistently lower at $\sqrt{s} = 5.02\,\text{TeV}$ than at $\sqrt{s} = 13\,\text{TeV}$, which could be

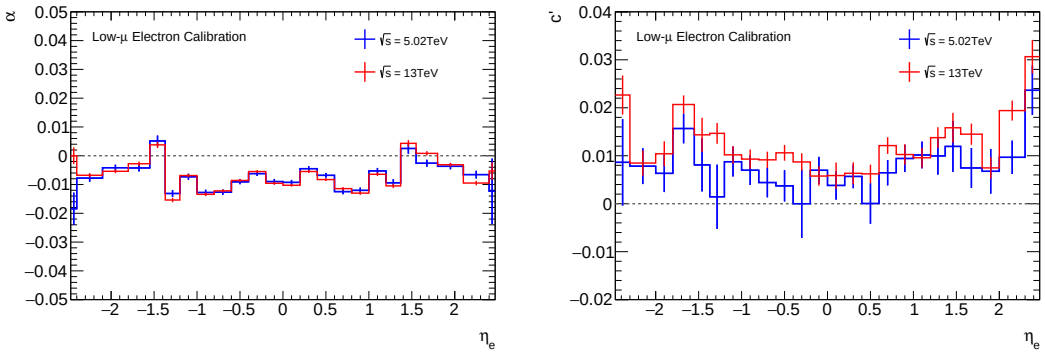

Figure 6.2: The Energy scale correction α (left) and resolution correction c' (right) defined in bins of electron pseudorapidity η. A separate derivation of the corrections is performed for both $\sqrt{s} = 5.02\,\text{TeV}$ and $\sqrt{s} = 13\,\text{TeV}$. Data uncertainties are all statistical components. Results taken from Ref. [134].

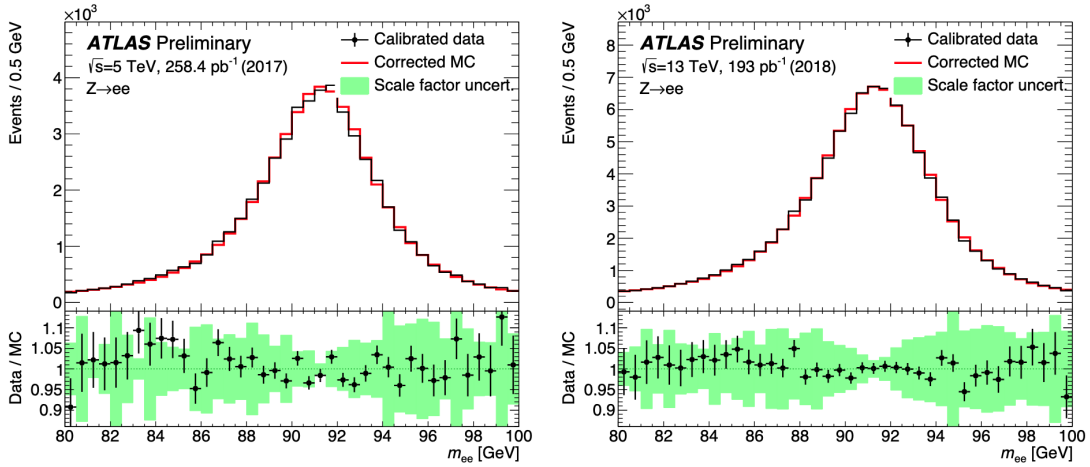

Figure 6.3: The di-electron invariant mass distribution showing good consistency of the calibrated data and calibrated MC. Shown is the 2017 $\sqrt{s} = 5.02\,\text{TeV}$ data (left) and the 2018 $\sqrt{s} = 13\,\text{TeV}$ data (right). A band showing uncertainties on the calibration is also shown in the ratio panel.. Results taken from Ref. [134].

related to the differing underlying event activity. Using these corrections, good consistency between the calibrated data and MC is observed, as shown in Figure 6.3 which shown for 2017 $\sqrt{s} = 5.02\,\text{TeV}$ data and 2018 $\sqrt{s} = 13\,\text{TeV}$ data.

The low-μ specific calibrations, α_i and c'_i, are defined in pseudorapidity bins, with a statistical uncertainty on the parameter evaluation resulting from the limited size of the data sample. Each independent bin uncertainty is propagated through the analysis independently and treated as a global correlated systematic uncertainty (across all analysis bins) on the result. Additional systematic effects in the high-μ calibration are propagated to the low-μ analysis as nuisance parameters as defined by the Egamma group [132, 133]. Each nuisance parameter is propagated separately through the analysis and treated as an independent uncertainty correlated across the measurement.

6.2 Muon Calibration

There are various alignment issues/distortions in the ID and MS, which necessitates a calibration procedure [135]. As with electrons, a calibration of momentum scale and resolution is employed. However, in contrast to electrons, an additional calibration is needed that has the opposite impact on μ^+ and μ^- respectively, known as the "sagitta bias" correction.

6.2.1 Muon Momentum Correction

Muon calibration is a correction for both muon momentum scale and resolution in the MC [136] . This is accomplished by separately correcting ID and MS tracks, and then propagated to correct the CB muon track. The corrected transverse momentum $p_T^{corr,Det}$ (where *Det* denotes either the ID or MS) is described by,

$$p_T^{corr,Det} = \frac{p_T^{MC,Det} + s^{Det}(\eta,\phi)}{1 + r^{Det}(\eta,\phi)}, \tag{6.4}$$

where $p_T^{MC,Det}$ is the uncorrected $p_T(\mu)$ as measured in MC simulation. The momentum scale term s^{Det} takes the form of a first-order polynomial as a function of $p_T^{MC,Det}$. The momentum resolution term Δr^{Det} takes the functional form $(p_T^{MC,Det})^m$ with $m = -1, 0, 1$, where each term is modified by a normally distributed random variables g_m with zero mean and unit width. The full form is written,

$$p_T^{corr,Det} = \frac{p_T^{MC,Det} + \sum_{n=0}^{1} s_n(\eta,\phi)(p_T^{MC,Det})^n}{1 + \sum_{m=0}^{2} \Delta r_m^{Det}(\eta,\phi)(p_T^{MC,Det})^{m-1} g_m}. \tag{6.5}$$

The coefficients s_n^{Det} and Δr_m^{Det} are defined in bins of (ϕ,η) over the full detector space. The factors used for low-μ analysis were defined using the high-μ data to improve statistical precision, with a validation study of the $J/\psi \to \mu\mu$ and $Z \to \mu\mu$ resonance distributions performed using the low-μ data. The full derivation of these parameters is outlined in Ref. [136].

6.2.2 Muon Sagitta Bias Correction

Small azimuthal rotations between the ID and MS subsystems and the various detector layers can lead to imperfect parameterisation of CB muon trajectories [137, 138]. This leads to a charge-dependent bias on the reconstructed momentum, referred to as the "sagitta bias", caused by over-estimation of curvature for one charge and under-estimation of curvature for the opposite charge. This effect is parameterised by

$$p_T^{meas} = \frac{p_T^{reco}}{1 + q \cdot \delta_{\text{sagitta},i} \cdot p_T^{reco}} \tag{6.6}$$

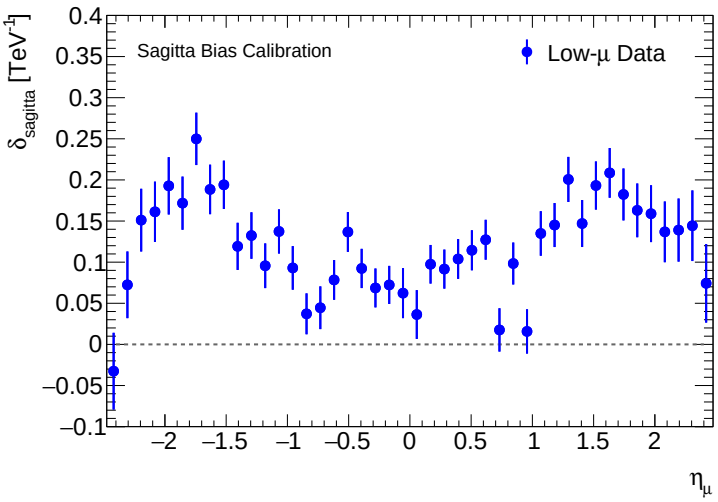

Figure 6.4: The sagitta bias correction $\delta s_{sagitta}$ used for the low-μ analyses. All uncertainties are statistical [135].

where p_T^{meas} is the measured momentum that contains a bias, p_T^{reco} is the unbiased reconstructed momentum, and the sagitta correction factor $\delta_{\text{sagitta},i}$ is defined in bins of pseudorapidity (denoted i). Multiple methods exist for calculating $\delta_{\text{sagitta},i}$:

- Use electrons from $Z \to ee$ and $W \to e\nu$ events to compare track momentum against energy deposits in the calorimeter. The bias is obtained by,

$$\delta_{\text{sagitta},i} = \frac{\langle E/p_{track}\rangle^{+} - \langle E/p_{track}\rangle^{-}}{2\langle p_T^{calo}\rangle}, \tag{6.7}$$

  where p_{track} is the momentum as measured in the ID, E is the energy measured in the EM calorimeter and p_T^{calo} is the projection of E into the transverse plane $p_T^{calo} = E\sin(\theta)$.

- The $p_T(\mu)$ method [139] determines the bias by using $Z \to \mu\mu$ events to observe the difference between $p_T(\mu^+)$ and $p_T(\mu^-)$ spectra. A small difference is expected from electroweak effects, but strong differences are explained by sagitta bias.

- The Z-mass method [139] determines the bias by using the invariant mass of $Z \to \mu\mu$ events. The difference between the reconstructed and observed mass-peak positions are used to obtain the bias.

A single correction is derived for both $\sqrt{s} = 5.02$ TeV and $\sqrt{s} = 13$ TeV and the distributions is shown in Figure 6.4. The details of this derivation are summarised in Ref. [140]. The correction is derived using the Z-mass method to best obtain the pseudorapidity dependence, with an additional global offset $\langle\delta_{sagitta}\rangle$ evaluated with the $p_T(\mu)$ method.

6.2.3 Muon Calibration Uncertainties

The low-μ sagitta bias correction $\delta_{sagitta}$ is defined in pseudorapidity bins. The uncertainty is dominated by the statistical contribution arising from the limited data sample. An additional

systematic uncertainty reflecting the global offset of the sagitta correction is also propagated. Each independent bin uncertainty is propagated through the analysis independently and treated as a correlated systematic uncertainty. The initial muon calibration defined with high-μ data consists of multiple nuisance parameters defined by the muon performance group that account for limitations in the calibration procedure [141]. These are variations on the ID and MS resolution and the overall scale correction. Each nuisance parameter is propagated separately through the analysis and treated as an independent uncertainty correlated across the measurement.

6.3 Low-μ Analysis Efficiency Corrections

Quality requirements on lepton selection will generally have an efficiency of less than 100%, leading to genuine leptons being missed in the event selection. For a fiducial cross-section measurement, it is important that these losses are corrected for and that the corrections are accurate. The efficiency modelling for a given selection criteria a, as provided by the MC detector simulation $\varepsilon_{(a)}^{MC}$, is not expected to be a perfect reflection of the true detector due to hardware degradation not modelled in the MC, imperfect modelling of object interactions with detector material, and imperfect modelling of background processes. Many of these efficiencies can be obtained using data-driven methods $\varepsilon_{(a)}^{data}$, mostly via the tag-and-probe method, which provide an experimental measure of the actual detector efficiencies. The efficiencies as measured in data are used to correct the MC simulation by the use of scale factors (SF) defined for selection a as the ratio of data efficiency to MC efficiency,

$$SF_{(a)} = \frac{\varepsilon_{(a)}^{data}}{\varepsilon_{(a)}^{MC}}. \tag{6.8}$$

The value of a scale factor is generally not expected to be uniform with respect to location in the detector or kinematic properties of the lepton object. It is, therefore, common to derive scale factors in bins of these quantities, referred to as scale factor maps. In the low-μ analyses, these maps are defined in η_ℓ and $p_T(\ell)$,

$$SF_{(a)}(\eta_\ell, p_T(\ell)) = \frac{\varepsilon_{(a)}^{data}(\eta_\ell, p_T(\ell))}{\varepsilon_{(a)}^{MC}(\eta_\ell, p_T(\ell))}, \tag{6.9}$$

or in η_ℓ and ϕ_ℓ

$$SF_{(a)}(\eta_\ell, \phi_\ell) = \frac{\varepsilon_{(a)}^{data}(\eta_\ell, \phi_\ell)}{\varepsilon_{(a)}^{MC}(\eta_\ell, \phi_\ell)} \tag{6.10}$$

6.3.1 Low-μ Analysis Scale Factors

Low-μ analyses use scale factor corrections for various electron and muon efficiencies. For electrons, the considered scale factor corrections are:

- **Electron Reconstruction Efficiency:** The efficiency for an electromagnetic cluster to be matched with a charged particle ID track with various quality requirements. Evaluated using high-μ data with an extrapolation systematic to account for low-μ differences. The same SF map is used for both $\sqrt{s} = 5.02\,\text{TeV}$ and $\sqrt{s} = 13\,\text{TeV}$.
- **Electron Identification Efficiency:** The efficiency of reconstructed electrons to pass a given working point (e.g. MediumLH) evaluated using low-μ data. Separate SF maps are derived for $\sqrt{s} = 5.02\,\text{TeV}$ and $\sqrt{s} = 13\,\text{TeV}$.
- **Electron Isolation Efficiency:** The efficiency of reconstructed and identified electrons to pass a given isolation requirement evaluated using low-μ data. Separate SF maps are derived for $\sqrt{s} = 5.02\,\text{TeV}$ and $\sqrt{s} = 13\,\text{TeV}$.
- **Electron Trigger Efficiency:** The efficiency of a reconstructed, identified and isolated electron to successfully fire the HLT_e15_lhloose_nod0_L1EM12 single electron trigger evaluated using low-μ data. Separate SF maps are derived for $\sqrt{s} = 5.02\,\text{TeV}$ and $\sqrt{s} = 13\,\text{TeV}$.

For muons, the considered scale factor corrections are:

- **Muon Reconstruction Efficiency:** The efficiency for a muon to be successfully reconstructed and identified with medium quality and have successfully matched ID and MS tracks evaluated using low-μ data. Separate SF maps are derived for $\sqrt{s} = 5.02\,\text{TeV}$ and $\sqrt{s} = 13\,\text{TeV}$.
- **Muon TTVA Efficiency:** The track-to-vertex association efficiency, the efficiency of a reconstructed and identification passing muon track to successfully match to the primary vertex evaluated using low-μ data. Separate SF maps are derived for $\sqrt{s} = 5.02\,\text{TeV}$ and $\sqrt{s} = 13\,\text{TeV}$.
- **Muon Isolation Efficiency:** The efficiency of reconstructed, identified, and primary vertex matched muon to pass a given isolation requirement evaluated using low-μ data. Separate SF maps are derived for $\sqrt{s} = 5.02\,\text{TeV}$ and $\sqrt{s} = 13\,\text{TeV}$.
- **Muon Trigger Efficiency:** The efficiency of a reconstructed, identified, primary vertex matched and isolated muon to successfully fire the HLT_mu14 single muon trigger evaluated using low-μ data. Separate SF maps are derived for $\sqrt{s} = 5.02\,\text{TeV}$ and $\sqrt{s} = 13\,\text{TeV}$.

The muon trigger efficiency will be discussed in detail in the following section. Plots of the remaining scale factors can be found in Appendix A.

6.3.2 Dilepton Event-Level Scale Factor Corrections

The total correction for a given $Z \to \ell\ell$ event, is given by the product of single-lepton efficiency terms:

- **Both Leptons Required:** If both leptons ($\ell 1$ and $\ell 2$) are required to pass a given efficiency to select the event this introduces an $\varepsilon^{\ell 1} \cdot \varepsilon^{\ell 2}$ term.
- **At Least One Lepton Required:** If at least one lepton ($\ell 1$ or $\ell 2$) or both leptons ($\ell 1$ and $\ell 2$) are required to pass a given efficiency, as is the case for the trigger efficiencies, this introduces a $(1 - (1 - \varepsilon^{\ell 1}) \cdot (1 - \varepsilon^{\ell 2}))$ term.

Electrons selected for $Z \to ee$ events are required to be successfully reconstructed (denoted *reco.*), pass a certain identification quality criteria (denoted *ID*), pass a certain isolation requirement (denoted *iso.*), and at least one of the two electrons must be matched to an electron triggering the event (denoted *trig.*). The total efficiency factor by combining individual components is given by,

$$\varepsilon_{event}^{Z\to ee} = \varepsilon_{reco.}^{\ell 1} \cdot \varepsilon_{reco.}^{\ell 2} \cdot \varepsilon_{ID}^{\ell 1} \cdot \varepsilon_{ID}^{\ell 2} \cdot \varepsilon_{iso.}^{\ell 1} \cdot \varepsilon_{iso.}^{\ell 2} \cdot \left(1 - (1 - \varepsilon_{trig.}^{\ell 1})(1 - \varepsilon_{trig.}^{\ell 2})\right) \tag{6.11}$$

The $Z \to ee$ event-level scale factor is derived as the necessary factor to transform the MC efficiency term in Equation 6.11 into a fully corrected efficiency (and hence if applied to MC events as a weight, fully corrects for all efficiencies). The full form is,

$$\begin{aligned} \mathrm{SF}_{event}^{Z\to ee} = \mathrm{SF}_{reco.}^{\ell 1} \cdot \mathrm{SF}_{reco.}^{\ell 2} \cdot \mathrm{SF}_{ID}^{\ell 1} \cdot \mathrm{SF}_{ID}^{\ell 2} \cdot \mathrm{SF}_{iso.}^{\ell 1} \cdot \mathrm{SF}_{iso.}^{\ell 2} \\ \cdot \left(\frac{\frac{\mathrm{SF}_{trig.}^{\ell 1}}{\varepsilon_{trig.,MC}^{\ell 2}} + \frac{\mathrm{SF}_{trig.}^{\ell 2}}{\varepsilon_{trig.,MC}^{\ell 1}} - \mathrm{SF}_{trig.}^{\ell 1} \cdot \mathrm{SF}_{trig.}^{\ell 2}}{\frac{1}{\varepsilon_{trig.,MC}^{\ell 2}} + \frac{1}{\varepsilon_{trig.,MC}^{\ell 1}} - 1} \right), \end{aligned} \tag{6.12}$$

Muons selected for $Z \to \mu\mu$ events are required to be successfully reconstructed and pass a certain identification quality criteria (denoted *reco.*), be successfully matched with the primary vertex (denoted $TTVA$), pass a certain isolation requirement (denoted *iso.*), and at least one of the two leptons must be matched to the muon triggering the event (denoted *trig.*). The total efficiency factor by combining individual components is given by,

$$\varepsilon_{event}^{Z\to \mu\mu} = \varepsilon_{reco.}^{\ell 1} \cdot \varepsilon_{reco.}^{\ell 2} \cdot \varepsilon_{TTVA}^{\ell 1} \cdot \varepsilon_{TTVA}^{\ell 2} \cdot \varepsilon_{iso.}^{\ell 1} \cdot \varepsilon_{iso.}^{\ell 2} \cdot \left(1 - (1 - \varepsilon_{trig.}^{\ell 1}) \cdot (1 - \varepsilon_{trig.}^{\ell 2})\right) \tag{6.13}$$

The $Z \to \mu\mu$ event-level scale factor is derived as the necessary factor to transform the MC efficiency term in Equation 6.13 into a fully corrected efficiency (and hence if applied to MC events as a weight, fully corrects for all efficiencies). The full form is,

$$\begin{aligned} \mathrm{SF}_{event}^{Z\to \mu\mu} = \mathrm{SF}_{reco.}^{\ell 1} \cdot \mathrm{SF}_{reco.}^{\ell 2} \cdot \mathrm{SF}_{TTVA}^{\ell 1} \cdot \mathrm{SF}_{TTVA}^{\ell 2} \cdot \mathrm{SF}_{iso.}^{\ell 1} \cdot \mathrm{SF}_{iso.}^{\ell 2} \\ \cdot \left(\frac{\frac{\mathrm{SF}_{trig.}^{\ell 1}}{\varepsilon_{trig.,MC}^{\ell 2}} + \frac{\mathrm{SF}_{trig.}^{\ell 2}}{\varepsilon_{trig.,MC}^{\ell 1}} - \mathrm{SF}_{trig.}^{\ell 1} \cdot \mathrm{SF}_{trig.}^{\ell 2}}{\frac{1}{\varepsilon_{trig.,MC}^{\ell 2}} + \frac{1}{\varepsilon_{trig.,MC}^{\ell 1}} - 1} \right). \end{aligned} \tag{6.14}$$

6.3.3 Single-Lepton Tag and Probe

Single-lepton tag-and-probe methods take advantage of the well-known resonance $Z \to \ell\ell$ (or $J/\psi \to \ell\ell$) and utilise the clear signature of two opposite-sign, same flavour leptons with a dilepton mass close to the resonance. The general overview of a tag-and-probe method is as follows,

1. **Tag Lepton Selection:** Select objects that have high confidence of being genuine leptons (electrons, muons). These are selected with tight quality criteria and must successfully match the corresponding lepton trigger.

2. **Probe Lepton Selection:** Also select kinematic objects with much looser selection. These can be lepton objects (electrons, muons) with looser criteria or lower-level objects such as detector tracks and calorimeter clusters.

3. **Tag-and-Probe Pair Selection:** The Tag-and-Probe pair are then required to be consistent with the Z-resonance, usually by requiring that the di-lepton invariant mass $m_{tag,probe}$ is in some window close to m_Z. As long as both leptons pass the tight criteria, a given event can be selected twice, where the role of tag and probe are inverted.

4. **Background Subtraction:** Background contributions from non-prompt leptons are subtracted from the selected probes. The selection of tag-probe pairs near the Z-boson mass gives a favourable signal to background ratio, but the loosening of criteria on the probe selection can still introduce a sizeable background contribution. Trigger efficiency tag-and-probe selections are typically pure, and in this case, the subtraction is ignored.

5. **Efficiency Calculation:** The efficiency is measured by counting the fraction of probes (corrected for backgrounds) that successfully pass an additional higher-level selection. This evaluates the efficiency of the selection, given the prior probe selection is ε(selection|selectedprobe).

6. **Efficiency Maps:** The efficiency calculation is then performed in kinematic bins using the probe kinematics, usually in η_ℓ, ϕ_ℓ, $p_T(\ell)$.

The procedure is then performed using both data and MC independently, where the evaluated efficiency maps are used to calculate scale factor maps as outlined in Section 6.3.

6.3.4 Muon Trigger Scale Factors

This section outlines the derivation of the single-muon trigger scale factor maps derived with the tag-and-probe method using low-μ data. These efficiency/SF maps were adapted to the specific data-taking conditions and triggers present in low-μ data and were derived specifically for use in low-μ analyses.

These maps were derived to improve on existing SF maps produced in 2018 by utilising improved MC statistics and improving the map binning scheme, specifically the goal was to:

- Extend map binning down to $p_T(\mu) > 15\,\text{GeV}$ which better utilises the lower threshold of $p_T(\mu) > 14\,\text{GeV}$ used by HLT_mu14. This is improvement is beneficial for low-mass studies of $Z \to \ell\ell$ events where selected events will largely contain $p_T(\mu) < 20\,\text{GeV}$.
- Obtain a binning scheme that highlights regions of $SF(\eta_\mu, p_T(\mu))$. This map should share boundaries with the calorimeter binning scheme used for the electron scale factors and allow for multiple finer bins between these boundaries. This is beneficial for future $W \to \ell\nu$ differential η_ℓ cross-section analyses where harmonising the correction binning between channels will simplify electron-muon channel combination.

The efficiency measured with this procedure is the efficiency of a reconstructed and isolated muon object to fire the HLT_mu14 trigger. A separate scale factor map (and efficiency map) is evaluated for both $\sqrt{s} = 5.02\,\text{GeV}$ and $\sqrt{s} = 13\,\text{GeV}$ using the corresponding data and MC events. The selections for the tag lepton and probe leptons are:

Tag Muon

- Medium Identification
- Isolation: $p_T^{\text{varcone20}}/p_T(\mu) < 0.1$
- Impact Parameter Selection: $|d_0/\sigma(d_0)| < 3.0$ and $|z_0 \sin(\theta)| < 0.5\,\text{mm}$
- Matched ($\Delta R < 0.1$) to muon firing trigger
- $|\eta_\mu| < 2.4$
- $p_T(\mu) > 15\,\text{GeV}$

Probe Muon

- Medium Identification
- Isolation: $p_T^{\text{varcone20}}/p_T(\mu) < 0.1$
- Impact Parameter Selection: $|d_0/\sigma(d_0)| < 3.0$ and $|z_0 \sin(\theta)| < 0.5\,\text{mm}$
- $|\eta_\mu| < 2.4$
- $p_T(\mu) > 15\,\text{GeV}$

Tag-Probe Pair

- Z-mass window: 81.2 GeV $< m_{tag,probe} <$ 101.2 GeV
- Tag-Probe pair have opposite charge

The quality criteria of the objects selected largely resemble those used in low-μ analyses, which is beneficial as it uses the same events also employed for the cross-section measurements. Efficiency is calculated by evaluating the fraction of probe muons that successfully match with a muon that fired the trigger ($\Delta R < 0.1$). No background estimation was performed as it was expected to be negligible after selecting two reconstructed and isolated muons. This was verified with the low-μ data by performing a same-sign selection and observing a negligible yield. The systematic variations performed on this estimate are used to evaluate residual background contamination. First the trigger scale factors are studied in 1D distributions of η_μ and $p_T(\mu)$ with fine binning, shown in Figure 6.6 and Figure 6.5, to highlight any regions far from unity that the final 2D binning should have sensitivity to. The general features observed are:

- $p_T(\mu)$ dependence appears relatively stable with a roughly 2% gradient across the full spectrum. There is a general offset of about 3%.
- η_μ dependence displays some significant data/MC offsets from unity by as much as 20% in the barrel region, with generally good agreement in the end-cap region. The regions with sizeable discrepancy are $-1.2 < \eta_\mu < -1.0$, $-0.8 < \eta_\mu < -0.6$, $-0.2 < \eta_\mu < 0.2$ and $0.6 < \eta_\mu < -0.9$.
- SF distributions at both $\sqrt{s} = 5.02$ TeV and $\sqrt{s} = 13$ TeV are comparable.

From these results, it is clear that extra care should be taken to produce an η_μ binning and the binning for $p_T(\mu)$ is less important. The small 2% trend observed in $p_T(\mu)$ could be explained by the dependency of η_μ and $p_T(\mu)$ in Z-boson final states, where higher $p_T(\mu)$ results tend to be more central around $\eta_\mu \approx 0$.

The electron calorimeter binning is,

- Pseudorapidity Bin Edges: -2.47, -2.37, -2.01, -1.81, -1.52, -1.37, -1.15, -0.8, -0.6, -0.1, 0.0, 0.1, 0.6, 0.8, 1.15, 1.37, 1.52, 1.81, 2.01, 2.37, 2.47

where the bin edges align with transitions between material and hardware systems in the calorimeter. The new binning scheme is defined with,

- Pseudorapidity Bin Edges: -2.4, -2.2, -2.01, -1.81, -1.65, -1.52, -1.37, -1.15, -1.05, -0.8, -0.7, -0.6, -0.45, -0.24, -0.05, 0.05, 0.24, 0.45, 0.6, 0.7, 0.8, 1.05, 1.15, 1.37, 1.52, 1.65, 1.81, 2.01, 2.2, 2.4
- $p_T(\mu)$ Bin Edges [GeV]: 15.0, 20.0, 25.0, 30.0, 35.0, 40.0, 45.0, 50.0, 80.0, 1000.0

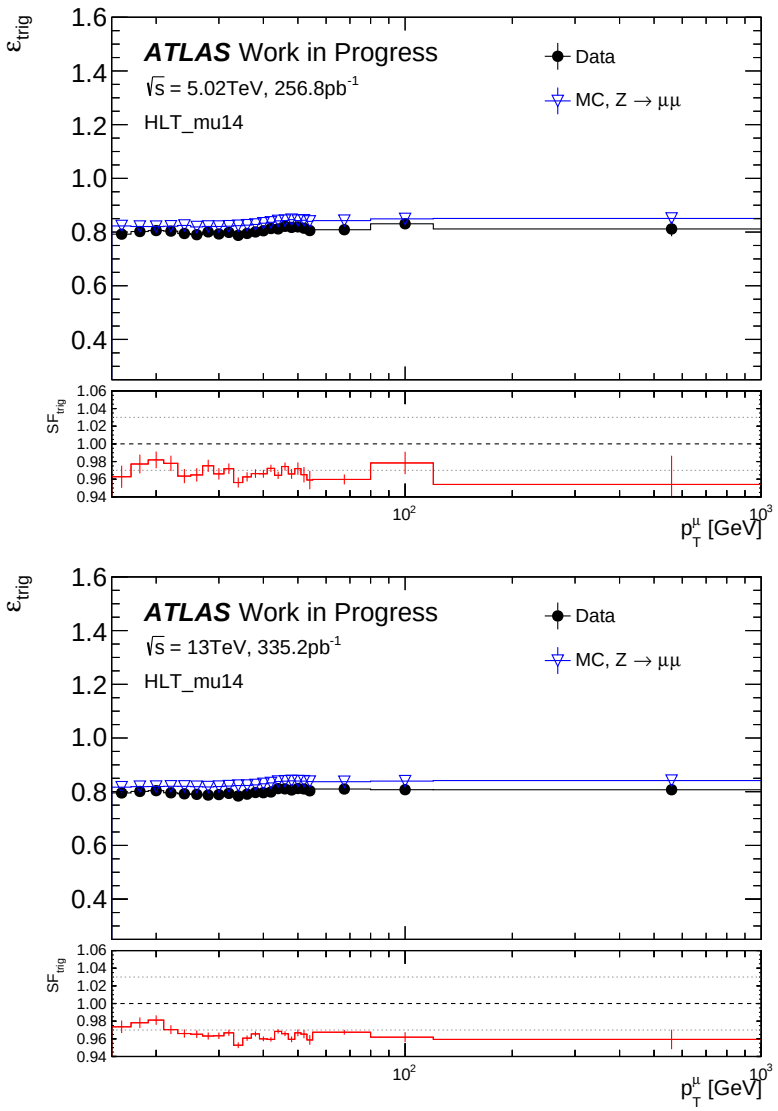

Figure 6.5: SF Map derivations for both $\sqrt{s} = 5.02\,\text{TeV}$ and $\sqrt{s} = 13\,\text{TeV}$ using a fine 1D $p_T(\mu)$ binning. Statistical uncertainties are shown on all points but are largely hidden by the markers.

where the new bin edges are chosen to share as many common bin edges with the electron calorimeter binning scheme as possible, but adding additional bin edges between them to best resolve η_μ dependent trends in scale factor value. Some compromises were made near the edges to better match the limit of the muon trigger system to $|\eta| < 2.4$ as well as inclusion of additional finer bins defined in the barrel region. The final SF maps are shown in Figure 6.6, where the η_μ dependence generally propagates across all $p_T(\mu)$ bins.

Muon Trigger Scale Factor Uncertainties

Each bin in the Muon Trigger scale factor map is given an uncorrelated statistical uncertainty, obtained by combining the statistical uncertainties on the data efficiency and the MC efficiency. Each bin uncertainty is propagated through the analysis as independent systematic variations globally correlated between analysis bins. In addition, several systematic uncertainties are

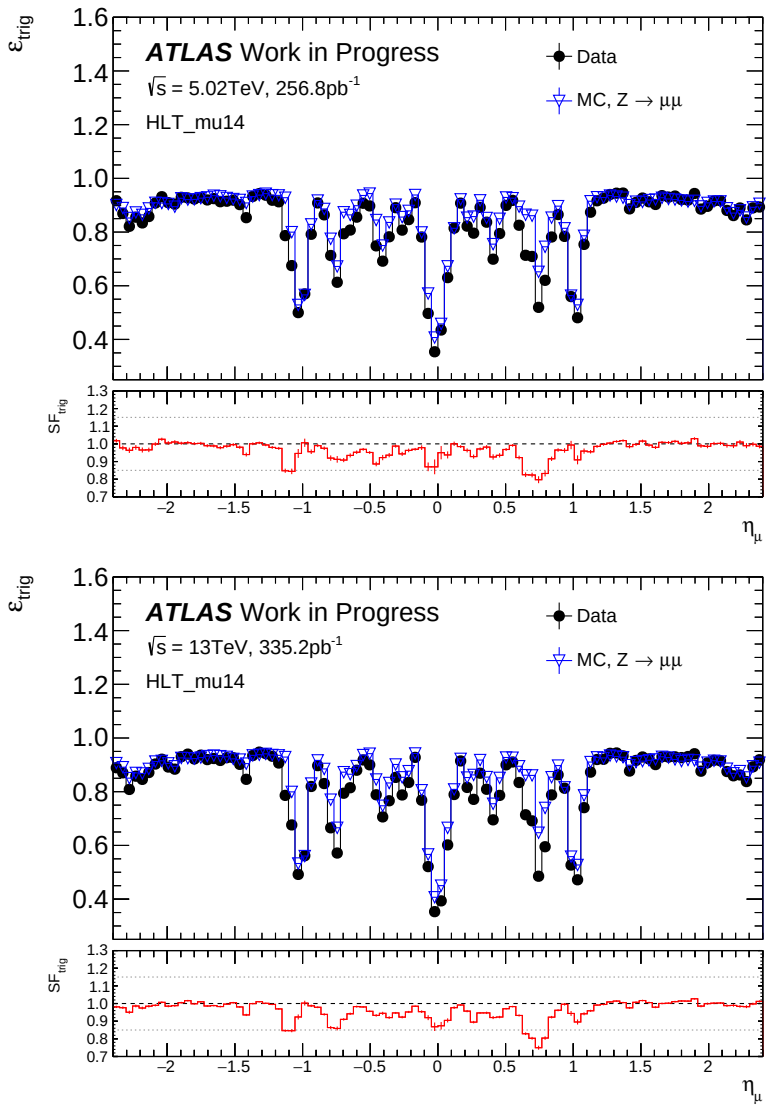

Figure 6.6: SF Map derivations for both $\sqrt{s} = 5.02\,\text{TeV}$ and $\sqrt{s} = 13\,\text{TeV}$ using a fine 1D η_μ binning. Statistical uncertainties are shown on all points but are largely hidden by the markers.

studied:

- **Tight $m_{\mu\mu}$:** A tighter window is used to evaluate the SF map. With this evaluation, the signal to background ratio should increase at the cost of reducing the sample size. The difference between the two maps is taken as an uncertainty.

- **Detector Symmetry:** This uncertainty removes strongly back-to-back events with a requirement that tag-probe pairs satisfy $\Delta\phi_{\mu\mu} < 3.0426$. This uncertainty is required due to the symmetries present in the ATLAS muon system (16-fold in the barrel, 12-fold in the endcaps). If the tag muon falls in a highly efficient detector region, the probe is also more likely to fall in a similar region. The difference between the two maps is taken as an uncertainty.

- **No Impact Parameters:** This uncertainty removes the impact parameter requirements on the tag and probe selections. This uncertainty can provide insight into the SF sensitivity

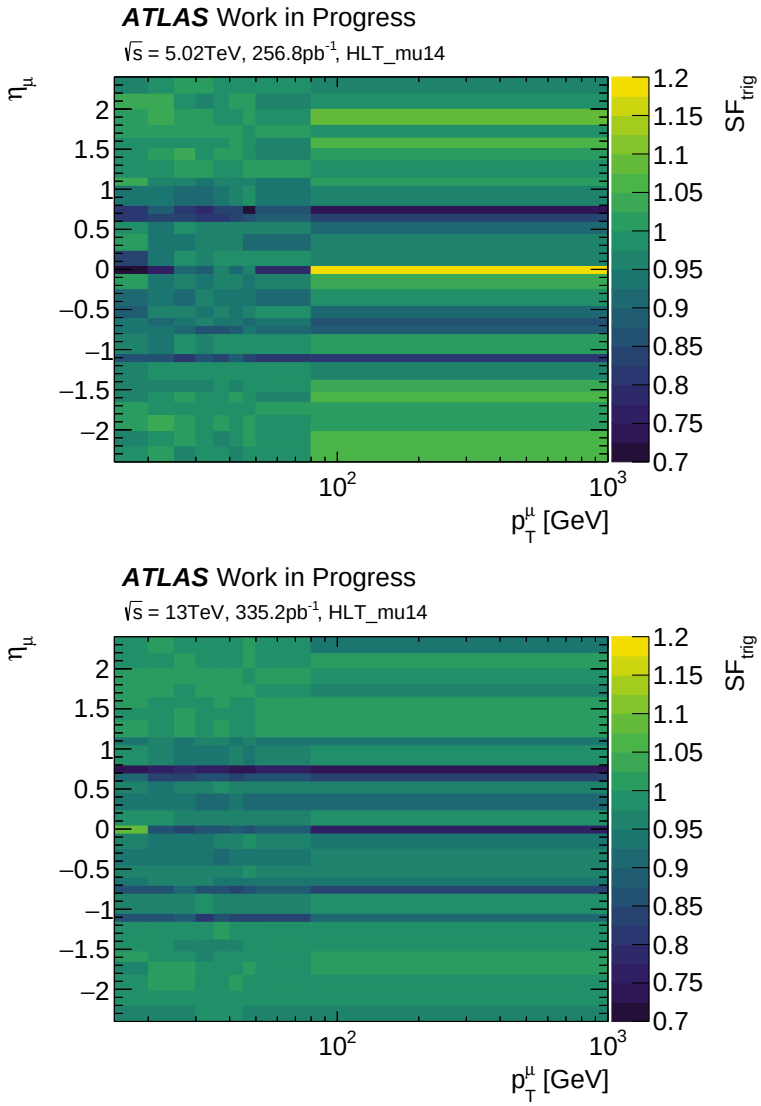

Figure 6.7: SF Maps for both $\sqrt{s} = 5.02\,\text{TeV}$ and $\sqrt{s} = 13\,\text{TeV}$ using the final 2D (η_μ, $p_T(\mu)$) binning scheme.

to pileup and QCD contamination. The difference between the two maps is taken as an uncertainty.

The fractional uncertainty from statistical sources is shown in Figure 6.8 with uncertainties ranging from 0.5-10%. The absolute systematic uncertainties are shown in Figure 6.9. The "No Impact Parameters" uncertainty is negligible, with most bins below 0.01%, the "Tight $m_{\mu\mu}$" uncertainty is largely in the range 0.01-0.1%, and the "Detector Symmetry" uncertainty is largely in the range 0.5-2.0%.

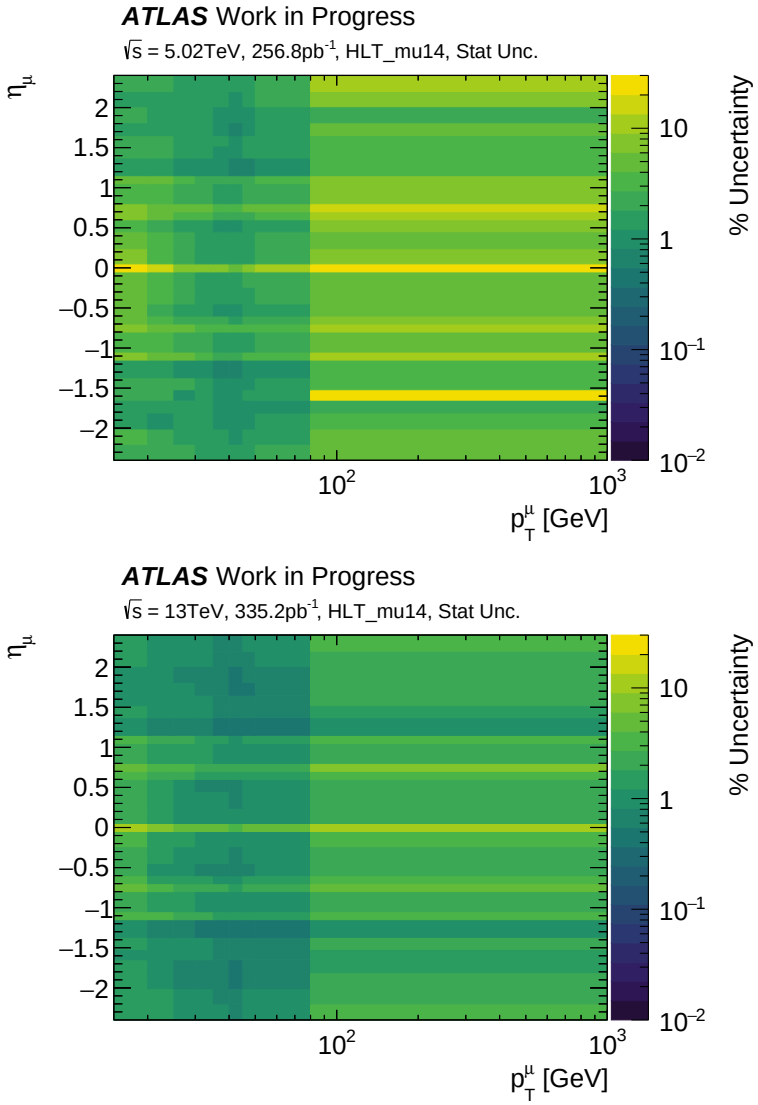

Figure 6.8: Statistical uncertainties on the muon trigger SF map derivations for both $\sqrt{s} = 5.02\,\text{TeV}$ and $\sqrt{s} = 13\,\text{TeV}$ using the final 2D (η_μ, $p_T(\mu)$) binning scheme.

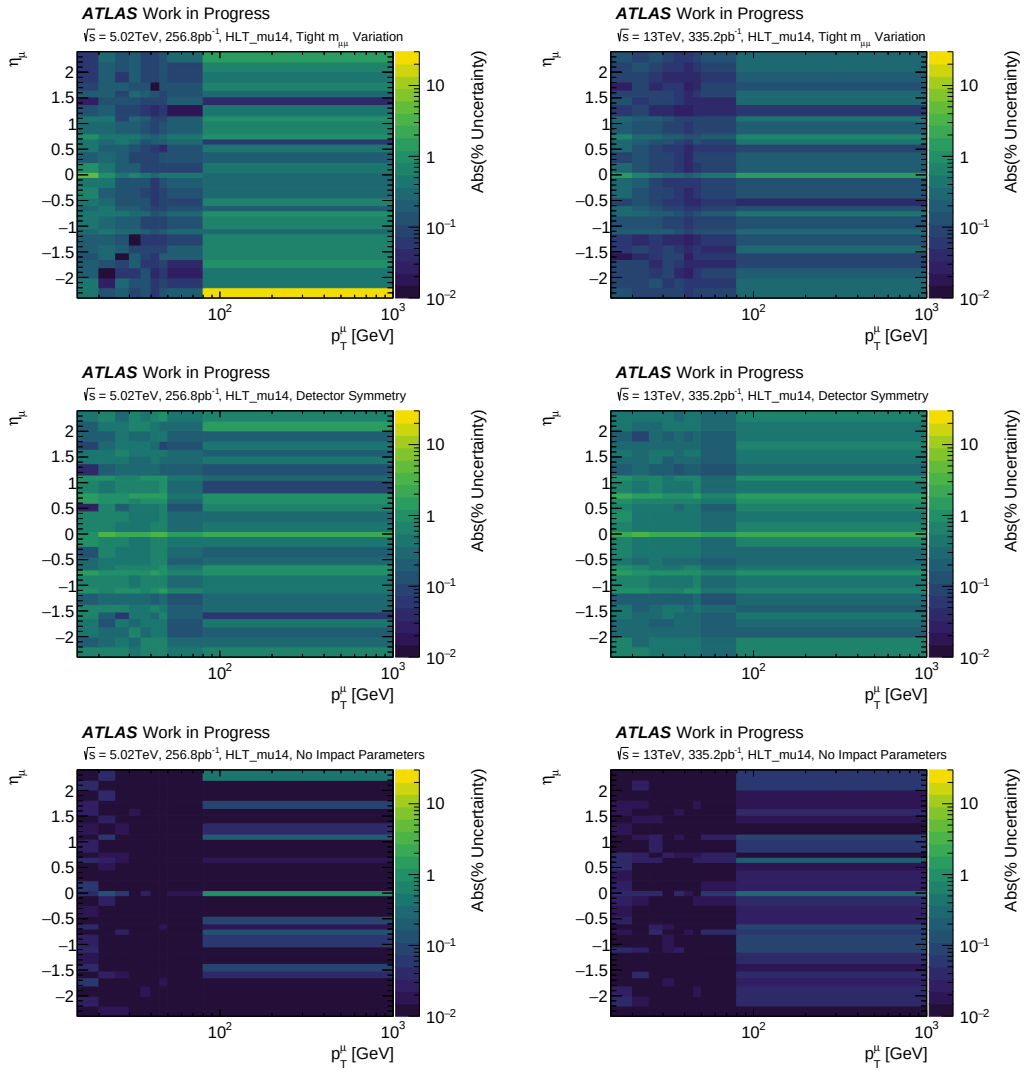

Figure 6.9: "Tight $m_{\mu\mu}$" systematic uncertainty (top), "Detector Symmetry" $\Delta\phi_{\mu\mu} < 3.0426$ systematic uncertainty (middle), "No Impact Parameters" systematic uncertainty (bottom), evaluated for the muon trigger SF map derivations at both $\sqrt{s} = 5.02\,\text{TeV}$ and $\sqrt{s} = 13\,\text{TeV}$ using the final 2D $(\eta_\mu, p_T(\mu))$ binning scheme. The variation is calculated with the correct sign, but to allow log-scale plotting the absolute value of the variation has been taken.

Part III

Analysis

7 Monitoring the ATLAS Luminosity by Counting $Z \to \ell\ell$ Events

7.1 Overview and Motivations

The luminosity measures described in Section 4.4.2 are reliant on inclusive particle production in pp scatters. The corresponding rates expected by the luminometers cannot be calculated from first principles and are instead obtained using the VdM calibration scans. In contrast, it is possible to avoid relying on VdM calibration by monitoring the production rate of a physics process with a calculable rate.

For a given process, the luminosity $\mathcal{L}_{\text{process}}$ is simply,

$$\mathcal{L}_{\text{process}} = \frac{N_{\text{process}}}{\sigma_{\text{process}}}, \tag{7.1}$$

where N_{process} is the number of recorded events for the given process corrected for efficiency and acceptance losses, and σ_{process} is the production cross-section for the given process. To obtain a precise luminosity estimate, the selected process must satisfy a few conditions:

- **Precise Cross-Section:** A precise estimate of σ_{process} should be available. This can be obtained from a theoretical calculation or from a dedicated experimental measurement designed to offer reduced experimental uncertainties compared to standard operation. The uncertainty on σ_{process} is likely to be the limiting uncertainty on this luminosity estimate.
- **Large Event Yield:** The statistical precision of the luminosity estimate depends on the number of recorded events N_{process}. This requires σ_{process} to be large enough that enough events can be recorded to perform the measurement. The yield should also be robust to all data-taking conditions with minimal changes in efficiency and acceptance.
- **Minimal Background Contribution:** The process should have minimal background to avoid sizeable systematic uncertainties originating from background modelling.

The selection of $Z \to e^+e^-$ and $Z \to \mu^+\mu^-$ (collectively $Z \to \ell^+\ell^-$) events provide the best compromise between the previously outlined requirements available at the LHC. These processes act as standard candles due to the well identified di-lepton signature with two high transverse momentum leptons of opposite charge with a di-lepton mass close to that of the Z-boson resonance. The production cross-section for di-lepton pair with mass $m_{\ell^+\ell^-} > 60\,\text{GeV}$ is a well understood physics process with a calculable large cross-section of about 2nb at $\sqrt{s} = 13\,\text{TeV}$.

Single-lepton data-driven efficiency estimates can be obtained via the tag-and-probe method utilising $Z \to \ell^+\ell^-$ events themselves which allows for an in situ self-calibrating methodology.

Before discussing the monitoring of $Z \to \ell^+\ell^-$ production, it is useful to mention some alternative processes and the benefits and drawbacks they have. Similar to the measurements performed at HERA and LEP, one could monitor the production of $pp \to pp\mu^+\mu^-$ initiated by $\gamma\gamma$ collisions [142, 143]. This has the benefit of being a well-controlled QED calculation when the muons are high pseudorapidity, low $p_T(\mu)$ and low $m_{\mu\mu}$, with a theoretical cross-section precision achievable of less than 1%. On the other hand, the ATLAS muon system does not provide coverage in the forward region, and constraining the allowed pseudorapidity of the muons acts to lower the cross-section and inflate theoretical uncertainties as the pure QED contribution starts to suffer from the complexity of modelling protons that may break apart in the scattering. The $W \to \ell\nu$ process offers the most significant electroweak cross-section at the LHC, about 10 times larger than that of $Z \to \ell^+\ell^-$, but suffers from a significant background contribution, bringing sizeable systematic uncertainties. In addition, the $W \to \ell\nu$ process is not self-calibrating like the $Z \to \ell^+\ell^-$ process and instead relies on external inputs for correcting detector efficiencies.

Theoretical predictions of the $Z \to \ell^+\ell^-$ cross-section are currently limited by uncertainties in the modelling of PDFs, as can be seen by the calculation performed in Ref. [144], where a prediction was made at NNLO QCD accuracy obtained with the FEWZ 3.1.b2 framework [145] using the CT18ANNLO proton PDF [146] to give $\sigma_{\text{theory}} = 1970$ pb with a PDF uncertainty of 3.5% at 90% CL. Experimental measures can achieve statistical and systematic uncertainties below 1% but are currently limited by the luminosity uncertainty. This can be seen in the fiducial cross-section measurements of $\sigma^{fid.}_{Z\to e^+e^-}$ and $\sigma^{fid.}_{Z\to\mu^+\mu^-}$ performed by ATLAS [50] at $\sqrt{s} = 7\,\text{TeV}$, $\sqrt{s} = 8\,\text{TeV}$ and $\sqrt{s} = 13\,\text{TeV}$ resulting in $451 \pm 0.1\%(\text{stat.}) \pm 0.3\%(\text{syst.}) \pm 0.6\%(\text{beam}) \pm 1.8\%(\text{lumi.})$ pb, $506 \pm 0.1\%(\text{stat.}) \pm 0.6\%(\text{syst.}) \pm 0.6\%(\text{beam}) \pm 1.9\%(\text{lumi.})$ pb and $777 \pm 0.1\%(\text{stat.}) \pm 0.4\%(\text{syst.}) \pm 0.7\%(\text{beam}) \pm 2.1\%(\text{lumi.})$ pb respectively. It is therefore clear that monitoring $Z \to \ell^+\ell^-$ cannot currently be used to provide an absolute estimate any better than the current ATLAS baseline luminosity. With the absense of a precise cross-section however the monitoring of $Z \to \ell^+\ell^-$ events can still prove useful for the relative monitoring of luminosity estimates. Some useful cases are:

- Offering a VdM scan-independent measure of the relative time-dependence, contributing to the long term stability studies in the baseline luminosity estimate (Section 4.4.2).
- Transport of other luminosity estimates between different data taking periods.
- Comparisons of luminosity between the ATLAS and CMS experiments, which is not achievable with hardware specific estimates such as LUCID or track counting.

This chapter will discuss the methodology and results for Run-2 luminosity monitoring using the Z-counting method reported in Ref. [144] to which I contributed.

First will be a discussion of the methodology for luminosity measurement over a single Luminosity Block. Then the results for time-dependence and $\langle\mu\rangle$-dependence compared to the ATLAS

baseline luminosity will be shown over a single LHC fill and the full Run-2 data taking period. An additional study of statistical biases when Z-counting rates are low is also presented.

7.2 Z-Counting Methodology

The Z-counting methodology can be condensed into a single formula that describes how to derive the luminosity estimate for a single luminosity block (LB) from the raw number of reconstructed Z-bosons $N_{Z\to\ell^+\ell^-}$ in the electron and muon channels:

$$\mathcal{L}_{Z\to\ell^+\ell^-}(LB) = \frac{N_{Z\to\ell^+\ell^-}(LB)\cdot(1-f_{\text{bkg}})}{\sigma_{\text{theory}}\times A^{\text{MC}}_{Z\to\ell^+\ell^-}\cdot\varepsilon^{\text{T\&P}}_{Z\to\ell^+\ell^-}(LB)\cdot F^{\text{MC}}_{Z\to\ell^+\ell^-}(\langle\mu\rangle)\cdot t(LB)}. \tag{7.2}$$

Here, each term highlights whether it varies per LB, varies with the LBs corresponding pileup, or is a constant. The definitions of these terms are as follows:

- $N_{Z\to\ell^+\ell^-}(LB)$ is the number of raw selected $Z\to\ell^+\ell^-$ events per LB, details on the selection in each channel are summarised in Section 7.2.1.
- f_{bkg} is the fraction of background events in the signal region, taken as $f_{\text{bkg}} = 0.005$ for both $Z\to e^+e^-$ and $Z\to\mu^+\mu^-$ channels. Backgrounds originate from diboson and $t\bar{t}$ production and this value is taken from Monte Carlo studies performed in [147]. The contribution from multijet events to f_{bkg} is approximately 0.0005 [147], and is not relevant.
- σ_{theory} is the inclusive $Z\to\ell^+\ell^-$ cross-section. Choices for this paramater were discussed in Section 7.1 however all results presented in this chapter do not depend on this quanitity due to normalisation of Z-counting to the ATLAS baseline luminosity or cancellation of the term when evaluating the $Z\to e^+e^-$ and $Z\to\mu^+\mu^-$ ratio.
- $A^{\text{MC}}_{Z\to\ell^+\ell^-}$ is an acceptance factor correcting the inclusive cross-section σ_{theory} to the fiducial phase space defined by the kinematic criteria in the raw selection. Details on this are provided in Section 7.2.4.
- $\varepsilon^{\text{T\&P}}_{Z\to\ell^+\ell^-}(LB)$ is the event trigger and reconstruction efficiency obtained per LB from the data-driven tag-and-probe procedure discussed in Section 7.2.3.
- $F^{MC}_{Z\to\ell^+\ell^-}(\langle\mu\rangle)$ is a pileup $\langle\mu\rangle$ dependent correction factor derived from Monte Carl. This corrects for efficiencies not probed in the the tag-and-probe procedure. It is discussed in Section 7.2.4.
- $t(LB)$ is the live-time of the luminosity block in seconds. Typically this is 60 seconds and it includes corrections for trigger and data acquisition deadtime effects.

The procedure here is implemented for monitoring of both electrons and muon channels $Z\to\ell^+\ell^- = Z\to e^+e^-, Z\to\mu^+\mu^-$.

Selection criteria	Electron channel	Muon channel
Track-vertex association	$\lvert z_0 \sin(\theta)\rvert < 0.5$ mm	$\lvert z_0 \sin(\theta)\rvert < 0.5$ mm
	$\lvert d_0\rvert/\sigma(d_0) < 5$	$\lvert d_0\rvert/\sigma(d_0) < 3$
Identification	LHMedium	Medium, ID+MS combined muon
Isolation	LooseTrackOnly	LooseTrackOnly
Transverse momentum	$p_{\mathrm{T}}^{e} > 27$ GeV	$p_{\mathrm{T}}^{\mu} > 27$ GeV
Pseudorapidity	$0 < \lvert\eta^{e}\rvert < 1.37$ OR $1.52 < \lvert\eta^{e}\rvert < 2.4$	$0 < \lvert\eta^{\mu}\rvert < 2.4$
No. of Leptons	$N_e = 2$	$N_\mu = 2$
Trigger Requirement	1 or 2 Electrons Pass	1 or 2 Muons Pass
Opposite Charge	$1e^+$,$1e^-$	$1\mu^+$,$1\mu^-$
Invariant mass	$66 < m_{e^+e^-} < 116$ GeV	$66 < m_{\mu^+\mu^-} < 116$ GeV

Table 7.1: Overview of selection criteria, where each criterion is applied to a single lepton and two oppositely charged leptons of the same flavour are required to form a Z-boson candidate, with invariant mass in the range $66\,\mathrm{GeV} < m_{\ell^+\ell^-} < 116\,\mathrm{GeV}$. The fiducial phase space is flavour-specific and determined by the invariant mass, η^{ℓ} and p_{T}^{ℓ} requirements.

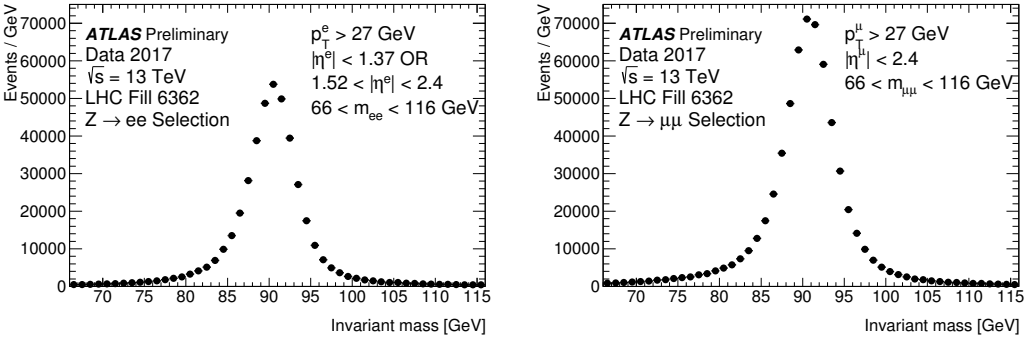

Figure 7.1: The raw selected $Z \to e^+e^-$ and $Z \to \mu^+\mu^-$ events after all selection criteria are applied from the full 2017 LHC fill 6362. Ref. [144].

7.2.1 Event Selection

The Z-counting framework is integrated into the ATLAS offline data-quality monitoring workflow that processes the full set of recorded physics data after initial calibration. Exactly two electrons or two muons with opposing electric charges must be present, and at least one of the selected leptons is required to have triggered the event. The di-lepton mass is restricted to the range $66 < m_{\ell^+\ell^-} < 116\,\mathrm{GeV}$ to select events from the Z-resonance. Mass distributions for selected $Z \to e^+e^-$ and $Z \to \mu^+\mu^-$ events integrated over an example 2017 high-μ LHC fill are shown in Figure 7.1, where a very clear peak is is observed centred on the Z-boson mass of 91.2 GeV. Histograms showing the raw event counts per LB for both $Z \to e^+e^-$ and $Z \to \mu^+\mu^-$ selections for all high-μ Run-2 LBs are shown in Figure 7.2. The raw event counts are of the order of ≈ 100 with, on average, more events reconstructed in the $Z \to \mu^+\mu^-$ selection.

7.2.2 Luminosity Block Selection

The results documented in this chapter use the full high-$\langle\mu\rangle$ Run-2 dataset with all luminosity blocks where ATLAS was in full data-taking configuration and passes the GRL. The live time

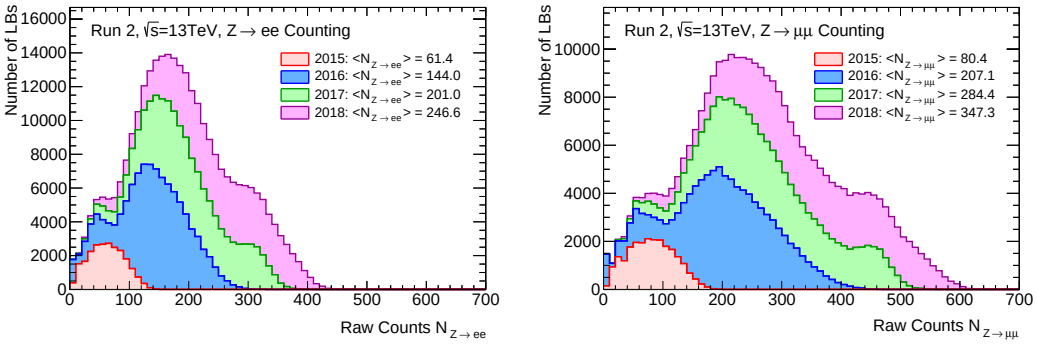

Figure 7.2: Stacked histogram showing the distribution of raw counts N_Z recorded per-LB for both the electron and muon channels for each Run 2 LB passing the GRL. The mean for each year is annotated in the plot.

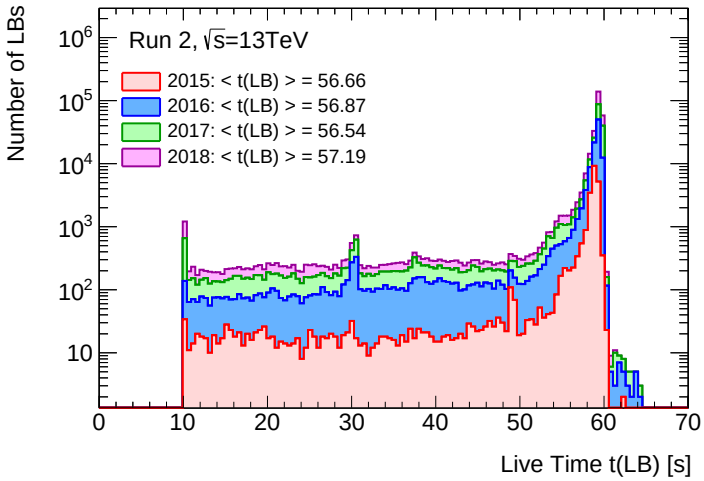

Figure 7.3: The live time $t(LB)$ for all successfully selected luminosity blocks. A requirement of $t(LB) > 10s$ is applied for Z-counting analysis, explaining the sharp drop at 10s.

Selection	**2015**	**2016**	**2017**	**2018**
All LBs	52032 (100.00)%	124702 (100.00)%	130703 (100.00)%	142352 (100.00%)
Pass GRL	23892 (45.92)%	95894 (76.90)%	89890 (68.77)%	93639 (65.78%)
$t(lb) > 10$s	22856 (43.93)%	91176 (73.12)%	86480 (66.17)%	91663 (64.39%)
$N_{Z\to ee} > 0$ and $N_{Z\to\mu\mu} > 0$	22849 (43.91)%	91080 (73.04)%	86465 (66.15)%	91663 (64.39%)
$\sum t(lb) > 40$ minutes	22687 (43.60)%	90843 (72.85)%	86138 (65.90)%	91457 (64.25%)

Table 7.2: A cut-flow table for Luminosity Block selection in Z-counting luminosity analysis. "All LBs" referrs to all high-$\langle\mu\rangle$ luminosity blocks. The selection $\sum t(lb) > 40$ minutes is applied only for time-dependent per-fill plots.

$t(LB)$ is typically 60 s; however, additional corrections for trigger and data acquisition dead-time effects can cause this to be notably lower as shown in Figure 7.3. Luminosity blocks with live time shorter than 10 s are removed and at least one reconstructed event for both $Z \to e^+e^-$ and $Z \to \mu^+\mu^-$ channels is required to ensure all calculations can be performed. Finally, in the time-dependent per-fill plots only fills with at least 40m of live time are considered. Table 7.2 shows the impact of each of these selections on the number of selected luminosity blocks.

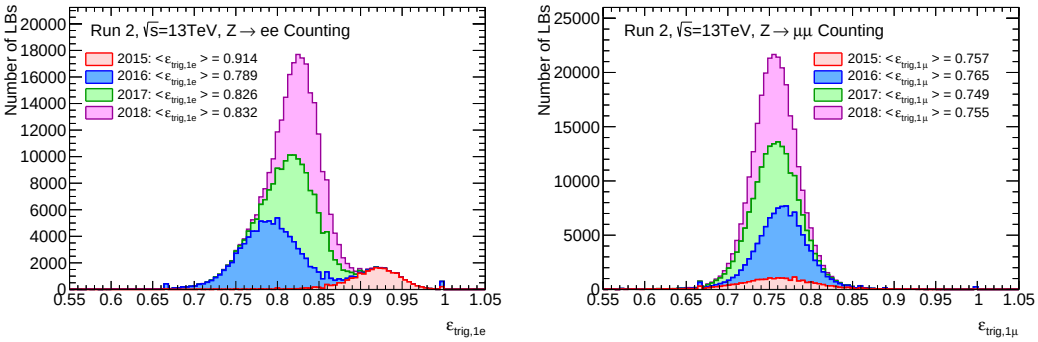

Figure 7.4: The distribution of single-lepton trigger efficiencies $\varepsilon_{\text{trig},1e}$ (left) and $\varepsilon_{\text{trig},1\mu}$ (right) calculated for each high-$\langle\mu\rangle$ luminosity block considered in this analysis.

7.2.3 Data-driven Efficiency Estimation

A critical component of the Z-counting method is the in-situ determination of time-dependent per-LB efficiencies, which is accomplished by employing a tag-and-probe estimation. The tag-and-probe method conveniently utilises the selected Z-boson candidates themselves and minimises dependency on external information. The efficiencies calculated by this method are single-lepton reconstruction and trigger efficiencies for both electrons and muons, which are then combined into an event-level efficiency to reflect the efficiency of $Z \to e^+e^-$ and $Z \to \mu^+\mu^-$ selection.

Single-lepton Trigger Efficiency

The single-lepton trigger efficiency is an estimate of what fraction of "good leptons" successfully pass the relevant single-lepton trigger. The single-lepton trigger efficiency $\varepsilon_{\text{trig},1\ell}$ takes the same form for both electrons and muons and is given by

$$\varepsilon_{\text{trig},1\ell} = \frac{1}{\frac{N_1}{2N_2} + 1}, \tag{7.3}$$

where N_1 is the number of events with exactly one lepton passing the trigger and N_2 is the number of events where both leptons successfully pass the trigger. An event-level trigger efficiency is then determined by,

$$\varepsilon_{\text{trig,event}} = (1 - (1 - \varepsilon_{\text{trig},1\ell})^2) \tag{7.4}$$

The distribution of $\varepsilon_{\text{trig},1e}$ and $\varepsilon_{\text{trig},1\mu}$ obtained for each Run-2 luminosity block is shown in Figure 7.4. Electrons are typically more efficient than muons due to the limited geometric coverage in the MS. Throughout Run-2 $\varepsilon_{\text{trig},1\mu}$ appears stable, but electrons tend to display more variability with a drop going from 2015 to 2016 and a slight increase moving to 2017 and 2018 caused by ongoing work to improve the efficiency of the electron triggers.

Tag Selection Criteria	Electron Channel	Muon Channel
Transverse momentum	nominal	nominal
Impact parameter	nominal	nominal
Identification	LHTight	nominal
Single lepton trigger	matched	matched

Table 7.3: Modified selection criteria defining the 'tag' lepton per channel where 'nominal' refers to the signal selection listed in Table 7.1. All other signal selection criteria remain unchanged.

	Electron Channel	Muon Channel
Minimum Probe Criteria		
Object	Cluster loosely matched to ID track	ID track
Transverse momentum	$p_{\mathrm{T}}^{e} > 27\,\mathrm{GeV}$	$p_{\mathrm{T}}^{\mu} > 27\,\mathrm{GeV}$
Pseudorapidity	$\lvert\eta^{e}\rvert < 1.37$ or $1.52 < \lvert\eta^{e}\rvert < 2.4$	$\lvert\eta^{\mu}\rvert < 2.4$
Impact parameter	—	$\lvert z_0 \sin\theta\rvert < 2$ mm
Passed Probe		
Requirement	nominal ID, impact parameter, isolation	matched to combined muon passing nominal cuts with looser $p_{\mathrm{T}}^{\mu} > 21.6\,\mathrm{GeV}$

Table 7.4: Selection criteria defining the 'probe' lepton for electron and muon channels.

Single-lepton Reconstruction Efficiency

The single-lepton reconstruction efficiency is estimated by the tag-and-probe method. It is the efficiency for a loose selection object (the probe) to be successfully identified as a "good" lepton. Loose selection on the probe object gives more sensitivity to the full efficiency of "good" lepton reconstruction. However, in data this leads to a substantial selection of fake probe objects originating from QCD processes instead of genuine $Z \to \ell\ell$ leptons, which necessitates a background subtraction evaluation in the efficiency calculation. The generalised formula for single-lepton reconstruction efficiency is,

$$\varepsilon_{\mathrm{reco},1\ell} = \frac{N_{\mathrm{pass}}^{\mathrm{OS}} - N_{\mathrm{pass}}^{\mathrm{bkg}}}{N_{\mathrm{pass}}^{\mathrm{OS}} + N_{\mathrm{fail}}^{\mathrm{OS}} - N_{\mathrm{total}}^{\mathrm{bkg}}}, \tag{7.5}$$

where $N_{\mathrm{pass}}^{\mathrm{OS}}$ ($N_{\mathrm{fail}}^{\mathrm{OS}}$) are the number of opposite-sign (OS) (as opposted to the same-sign (SS) mentioned later) charge tag-and-probe pairs, where the probe object passes (fails) the "good" lepton selection and $N_{\mathrm{pass}}^{\mathrm{bkg}}$ ($N_{\mathrm{total}}^{\mathrm{bkg}}$) are estimates of the background contribution in the numerator (denominator).

A summary of the tag (probe) selections is given in Table 7.3 and Table 7.4. A brief description of the selections for each channel's tag object and probe object, and the background estimation methods, is now provided. For a selected $Z \to \ell^{+}\ell^{-}$ candidate event, each lepton is alternated as a tag and as a probe.

Electron Reconstruction Efficiency The electron reconstruction efficiency is based on the method used for Electron Identification in the Egamma group [133]. A tag electron is required to pass the nominal electron selection with the additional requirements that it satisfies the tight identification criteria and match an electron that has succesfully passed the trigger Table 7.3. The probe objects are electron container objects, clusters of energy in the EM calorimeter that

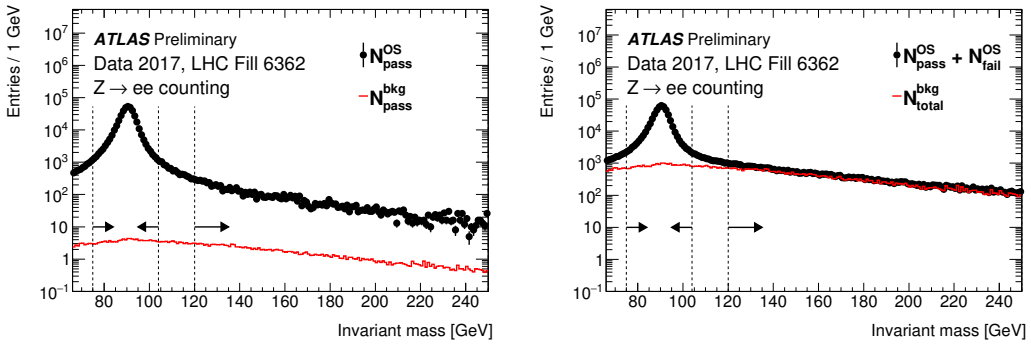

Figure 7.5: The left plot visualises the numerator of Equation 7.5 for di-electron tag-probe pairs where the probe is succesful reconstructed (black points) compared to the scaled background contribution (red). The right plot visualises the denominator of Equation 7.5 for all di-electron tag-probe pairs (black points) compared to the scaled background contribution (red). The vertical dashed lines illustrate the "peak" and "tail" ranges for the electron template method as shown in Equation 7.6. This data was recorded from pp collisions at $\sqrt{s} = 13\,\text{TeV}$ in LHC fill 6362 on November 4th, 2017. Uncertainties are statisitcal contributions only. Ref. [144].

are loosely matched to an ID track with some loose kinematic requirements as shown in Table 7.4. The full electron channel reconstruction efficiency formula is:

$$\varepsilon_{\text{reco,1e}} = \frac{N^{\text{OS}}_{\text{peak,pass}} - N^{\text{OS}}_{\text{peak,template}} \cdot \frac{N^{\text{SS}}_{\text{tail,pass}}}{N^{\text{SS}}_{\text{tail,template}}}}{N^{\text{OS}}_{\text{peak,pass}} + N^{\text{OS}}_{\text{peak,fail}} - N^{\text{OS}}_{\text{peak,template}} \cdot \frac{N^{\text{OS}}_{\text{tail,fail}}}{N^{\text{OS}}_{\text{tail,template}}}}. \tag{7.6}$$

To minimise background contamination, the efficiency is estimated in a tight window of tag-probe invariant mass of $75 < m_{\text{tag,probe}} < 105\,\text{GeV}$, denoted as the *peak* region. Probes that are successfully matched to a corresponding "good" electron are counted as $N^{\text{OS}}_{\text{pass}}$ and probes that cannot be matched are counted as $N^{\text{OS}}_{\text{fail}}$. Background estimation uses a "template" method where a separate selection is performed with inverted isolation and identification requirements on the probe, tracking both opposite-sign and same-sign tag-probe pairs. This template is normalised in a high-mass "tail" region $120 < m_{\text{tag,probe}} < 250\,\text{GeV}$ and the full background yields are obtained by then integrating the normalised yield in the "peak" region. Estimating $N^{\text{bkg}}_{\text{pass}}$ is accomplished using opposite-sign template pairs $N^{\text{OS}}_{\text{template}}$ normalised by $N^{\text{SS}}_{\text{tail,pass}}/N^{\text{SS}}_{\text{tail,template}}$. Estimating $N^{\text{bkg}}_{\text{total}}$ is similarly accomplished using opposite-sign template pairs $N^{\text{OS}}_{\text{template}}$ but normalised by $N^{\text{OS}}_{\text{tail,fail}}/N^{\text{OS}}_{\text{tail,template}}$ instead.

Plots comparing $N^{\text{bkg}}_{\text{pass}}$ and $N^{\text{bkg}}_{\text{total}}$ to the selected count yields are shown in Figure 7.5 where the integrated statistics of a full LHC fill has been used. $N^{\text{bkg}}_{\text{pass}}$ is small compared to $N^{\text{OS}}_{\text{pass}}$ but $N^{\text{bkg}}_{\text{total}}$ shows the same shape and normalisation as $N^{\text{OS}}_{\text{pass}} + N^{\text{OS}}_{\text{fail}}$ in the "tail" region. The remaining contribution of $N^{\text{bkg}}_{\text{total}}$ in the "peak" region is much more significant than for $N^{\text{bkg}}_{\text{pass}}$.

Muon Reconstruction Efficiency For muon reconstruction efficiency, the tag muon must pass the "good" muon selection, including the additional requirement of a match to a muon that has passed the trigger. The probe objects are inner detector tracks with identical kinematic selection to a "good" muon, but a looser longitudinal impact parameter criteria of $|z_0 \sin(\theta)| < 2$

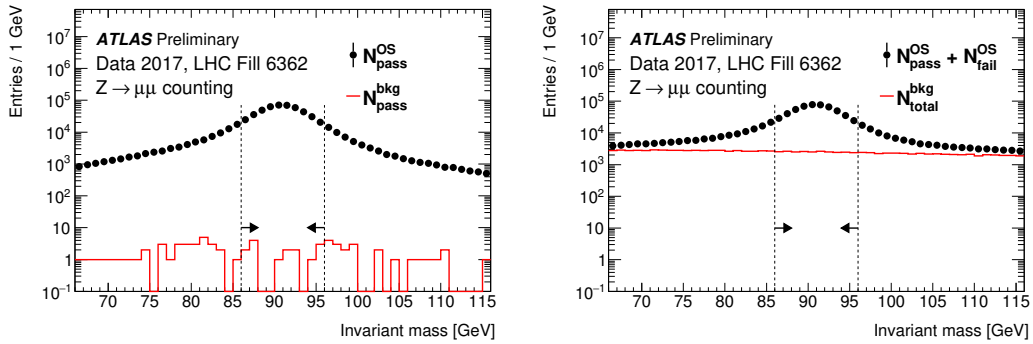

Figure 7.6: The left plot visualises the numerator of Equation 7.5 for di-muon tag-probe pairs where the probe is succesful reconstructed (black points) compared to the scaled background contribution (red). The right plot visualises the denominator of Equation 7.5 for all di-muon tag-probe pairs (black points) compared to the scaled background contribution (red). The vertical dashed lines illustrate the tight "peak" region in the window 86 GeV $< m_{\mu\mu} <$ 96 GeV used for the muon tag-and-probe method as shown in Equation 7.7. This data was recorded from pp collisions at $\sqrt{s}$ = 13 TeV in LHC fill 6362 on November 4th, 2017. Uncertainties are statisitcal contributions only. Ref. [144].

mm. A probe pass is evaluated by searching for a combined muon passing "good" selection that was reconstructed using the probe inner-detector track, and a failed probe cannot be matched. A looser requirement of $p_T^{\mu} > 21.6$ GeV on the tested combined muons was applied to avoid folding esolution effects into the efficiency calculations, such that ID tracks at 27.1 GeV forming a 26.9 GeV combined muon are still flagged as being reconstructed. The full muon channel reconstruction efficiency formula is:

$$\varepsilon_{\text{reco},1\mu} = \frac{N^{\text{OS}}_{\text{pass}} - N^{\text{SS}}_{\text{pass}}}{N^{\text{OS}}_{\text{pass}} - N^{\text{SS}}_{\text{pass}} + N^{\text{OS}}_{\text{fail}} - N^{\text{SS}}_{\text{fail}}}. \tag{7.7}$$

The terms $N^{\text{OS}}_{\text{pass}}$ and $N^{\text{OS}}_{\text{fail}}$ are evaluated using same-sign tag-probe pairs that pass and fail, respectively. The assumption that background events for the opposite-sign selection will be distributed identically to the same-sign selection has also been used by the muon performance group [136]. To minimise background contamination the efficiency is estimated in a tight window of tag-probe invariant mass of 86 $< m_{\text{tag,probe}} <$ 96 GeV. Background contributions $N^{\text{bkg}}_{\text{pass}}$ and $N^{\text{bkg}}_{\text{total}}$ are evaluated using the tag-and-probe yields from same-sign selection $N^{\text{bkg}}_{\text{pass}} = N^{\text{SS}}_{\text{pass}}$ and $N^{\text{bkg}}_{\text{total}} = N^{\text{SS}}_{\text{pass}} + N^{\text{SS}}_{\text{fail}}$ respectively.

Plots comparing $N^{\text{bkg}}_{\text{pass}}$ and $N^{\text{bkg}}_{\text{total}}$ to the selected count yields are shown in Figure 7.6, where the integrated statistics of a full LHC fill has been used. $N^{\text{bkg}}_{\text{pass}}$ is negligible compared to $N^{\text{OS}}_{\text{pass}}$ but $N^{\text{bkg}}_{\text{total}}$ becomes significant compared to $N^{\text{OS}}_{\text{pass}} + N^{\text{OS}}_{\text{fail}}$ outside of the "peak" region. The contribution of $N^{\text{bkg}}_{\text{total}}$ in the "peak" region is much more significant than for $N^{\text{bkg}}_{\text{pass}}$.

Reconstruction Efficiency Distributions The distribution of $\varepsilon_{\text{reco},1e}$ and $\varepsilon_{\text{reco},1\mu}$ obtained for each Run-2 luminosity block is shown in Figure 7.7. Both electrons and muons display good stability with only a small 1-3% level trend over the years. This slight drop corresponds to the increasing pileup conditions of each year. A slightly higher efficiency is observed for muons because of the tighter requirements applied in the MediumLH electron selection. The origin of

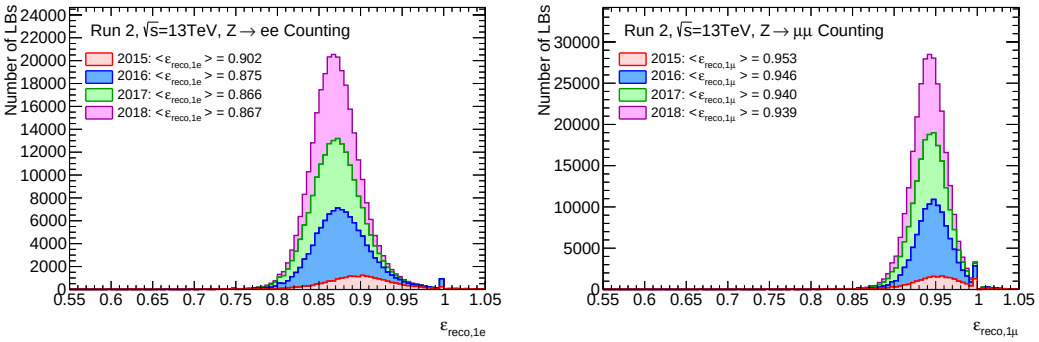

Figure 7.7: The distribution of single-lepton reconstruction efficiencies $\varepsilon_{\text{reco},1e}$ (left) and $\varepsilon_{\text{reco},1\mu}$ (right) calculated for each high-$\langle\mu\rangle$ luminosity block considered in this analysis.

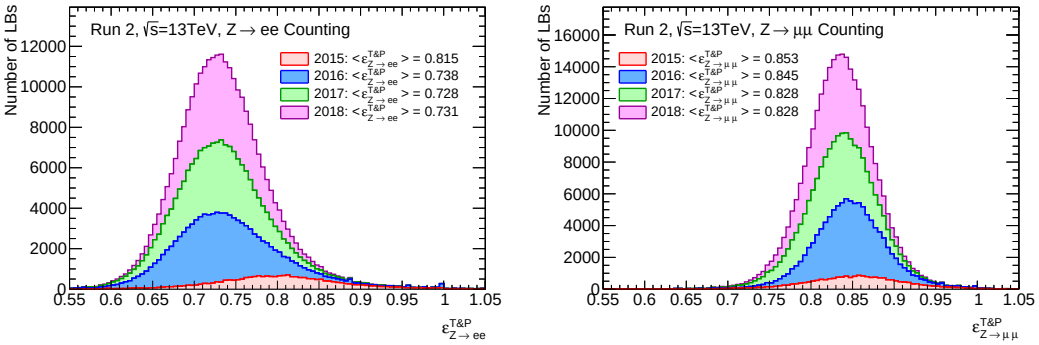

Figure 7.8: The distribution of combined event-level efficiencies $\varepsilon^{\text{T\&P}}_{Z\to e^+e^-}$ (left) and $\varepsilon^{\text{T\&P}}_{Z\to\mu^+\mu^-}$ (right) calculated for each high-$\langle\mu\rangle$ luminosity block considered in this analysis.

the small bumps observed at 1.0 is discussed in Section 7.2.3.

Event-Level Efficiency

For a $Z \to \ell^+\ell^-$ event the two lepton efficiencies are combined into an event-level efficiency of the form,

$$\varepsilon^{\text{T\&P}}_{Z\to\ell^+\ell^-} = (1 - (1 - \varepsilon_{\text{trig},1\ell})^2) \times \varepsilon^2_{\text{reco},1\ell} \tag{7.8}$$

that considers two "good" reconstructed leptons and at least one triggered lepton. This efficiency is then used to correct the raw counts $N_{Z\to\ell^+\ell^-}(LB)$ as in Equation 7.2. The uncertainty on $\varepsilon^{\text{T\&P}}_{Z\to\ell^+\ell^-}$ is obtained using uncertainty propagation and the Poisson uncertainties on each statistical count in the determination of $\varepsilon_{\text{reco},1\ell}$ and $\varepsilon_{\text{trig},1\ell}$. An overview of all uncertainty formulas can be found in Appendix B.1.

The distribution of $\varepsilon^{\text{T\&P}}_{Z\to e^+e^-}$ and $\varepsilon^{\text{T\&P}}_{Z\to\mu^+\mu^-}$ obtained for each Run-2 luminosity block is shown in Figure 7.8. These display a broader distribution than the individual single-lepton efficiencies. The time variability caused by the electron trigger efficiency also propagates to the combined efficiency.

Default Type	2015	2016	2017	2018
Use Previous LB $\varepsilon_{\text{trig},1e}$	168 (1.58%)	476 (3.05%)	115 (0.57%)	91 (0.42%)
Use Previous LB $\varepsilon_{\text{trig},1\mu}$	84 (0.79%)	295 (1.89%)	84 (0.41%)	77 (0.35%)
Use Previous LB $\varepsilon_{\text{reco},1e}$	1 (0.01%)	49 (0.31%)	1 (0.00%)	0 (0.00%)
Use Previous LB $\varepsilon_{\text{reco},1\mu}$	218 (2.06%)	612 (3.92%)	67 (0.33%)	47 (0.22%)
Unity $\varepsilon_{\text{trig},1e}$	208 (1.96%)	385 (2.47%)	1 (0.00%)	4 (0.02%)
Unity $\varepsilon_{\text{trig},1\mu}$	10 (0.09%)	230 (1.47%)	1 (0.00%)	1 (0.00%)
Unity $\varepsilon_{\text{reco},1e}$	12 (0.11%)	237 (1.52%)	0 (0.00%)	1 (0.00%)
Unity $\varepsilon_{\text{reco},1\mu}$	1288 (12.15%)	1446 (9.27%)	208 (1.02%)	121 (0.56%)

Table 7.5: The number of edge-case luminosity blocks where either the previous GRL passing luminosity block efficiency is propagated forward, or the calculation comes out to unity. The table shows the number of luminosity blocks with each given defaulting type and the relative fraction for each year of Run-2 data taking.

Edge-Case Efficiency Calculations

A few edge-cases exist in the efficiency formulae where the calculation breaks down mathematically or the results are not useful. These cases are:

- **Zero-Division:** Due to the background subtraction in the reconstruction efficiency calculations, it is possible to obtain a denominator of zero, leading to an undefined estimate. The efficiency is taken from the previous GRL passing luminosity block in these cases
- **No Passed Probes:** For the trigger efficiency, it is possible to only record events with a single trigger ($N_2 = 0$), which causes the efficiency to come out as zero. The efficiency is taken from the previous GRL passing luminosity block in these cases.
- **No Failed Probes:** It is possible for there to be zero failed probes or zero events with a single triggering lepton ($N_1 = 0$), which causes the efficiency to come out as unity. In this case, the efficiency is set to 1.0 with an uncertainty of ±1.0.

The frequency of each of these edge-cases is shown in Table 7.5. For most cases, the frequency is below 3% in 2015 and 2016 and below 0.5% in 2017 and 2018. The most frequent case occurs for "No Failed Probes" in the $\varepsilon_{\text{reco},1\mu}$ estimation. This occurs for 12.15% of LBs in 2015. As this case is given a conservative uncertainty and the remaining cases are so infrequent, it is not expected that these effects are significant. It does, however, hint that improvements could be made to better facilitate LBs with small event counts, as discussed in Section 7.4.

7.2.4 MC Correction Factor

The closure of the tag-and-probe procedure described in 7.2.3 can be directly tested using Monte Carlo $Z/\gamma^* \to \ell^+\ell^-$ signal samples where losses of events in the full ATLAS detector simulation can be independently calculated using the fraction of all generated events successfully reconstructed. If non-closure is observed in Monte Carlo, it is assumed non-closure also occurs

in data, motivating a correction to be applied to event-level efficiencies calculated on data. This correction is derived as a function of pileup $F^{\mathrm{MC}}(\langle\mu\rangle)$ and is defined by,

$$F^{\mathrm{MC}}(\langle\mu\rangle) = \frac{N^{\mathrm{reco,MC}}_{Z\to\ell^+\ell^-}(\langle\mu\rangle)}{N^{\mathrm{true,nocut,MC}}_{Z\to\ell^+\ell^-}(\langle\mu\rangle)} \times \frac{1}{A^{\mathrm{MC}} \cdot \varepsilon^{\mathrm{T\&P,MC}}_{Z\to\ell^+\ell^-}(\langle\mu\rangle)}, \tag{7.9}$$

where all quantities are based on the MC events generated in a narrow range of the pileup parameter $\langle\mu\rangle$:

- $N^{\mathrm{reco,MC}}_{Z\to\ell^+\ell^-}(\langle\mu\rangle)$ is the number of reconstructed MC events ('reco') which pass the nominal event selection requirements outlined in Section 7.2.1.
- $N^{\mathrm{true,nocut,MC}}_{Z\to\ell^+\ell^-}(\langle\mu\rangle)$ is the number of generated Z boson MC events ('true') without any selection ('nocut').
- $\varepsilon^{\mathrm{T\&P,MC}}_{Z\to\ell^+\ell^-}(\langle\mu\rangle)$ is derived by repeating the tag-and-probe (T&P) procedure using reconstructed MC events.
- A^{MC} is the fiducial acceptance, calculated using leptons originating from true Z bosons as described in Section 7.2.4.

The correction was formulated in this way as it was more convenient to obtain $N^{\mathrm{reco,fiducial,MC}}_{Z\to\ell^+\ell^-}$ and $N^{\mathrm{true,nocut,MC}}_{Z\to\ell^+\ell^-}$ in the framework. This necessitates the introduction of an acceptance factor A^{MC}, which is an identical factor to the A^{MC} found in the luminosity calculation in Eq. 7.2. The correction for acceptance losses actually originates from the fraction of reconstructed events, which can be seen as the product $A\varepsilon$ of a 'pure' phase space acceptance A and an event-level efficiency ε.

$$A\varepsilon(\langle\mu\rangle) = \frac{N^{\mathrm{reco,fiducial,MC}}_{Z\to\ell^+\ell^-}(\langle\mu\rangle)}{N^{\mathrm{true,nocut,MC}}_{Z\to\ell^+\ell^-}(\langle\mu\rangle)}, \tag{7.10}$$

$$\text{thus giving} \quad F^{\mathrm{MC}}(\langle\mu\rangle) = \frac{A\varepsilon(\langle\mu\rangle)}{A^{\mathrm{MC}} \cdot \varepsilon^{\mathrm{T\&P,MC}}_{Z\to\ell^+\ell^-}(\langle\mu\rangle)}. \tag{7.11}$$

It cannot be assumed that the two "factors" can be resolved, and $\varepsilon^{\mathrm{T\&P}}_{Z\to\ell^+\ell^-}$ may not capture all efficiency losses in the full detector simulation, which means one cannot necessarily expect $F^{\mathrm{MC}}(\langle\mu\rangle) = 1$ in practice.

The following results are obtained using the simulated $Z/\gamma^* \to e^+e^-$ and $Z/\gamma^* \to \mu^+\mu^-$ Powheg+Pythia8 AZNLO (see Section 3.4.3) signal samples. These samples have full detector simulation with detector conditions modelled specifically for each data taking year.

QED Dressing	$A_{Z\to\mu\mu}$	$A_{Z\to ee}$
Born leptons	0.3469 ± 0.0002	0.3072 ± 0.0002
Bare leptons	**0.3326 ± 0.0002**	0.2829 ± 0.0002
Dressed leptons	0.3384 ± 0.0002	**0.2996 ± 0.0002**

Table 7.6: A table of calculated A^{MC} values using both $Z \to ee$ and $Z \to \mu\mu$ MC signal samples. The results for Born, Bare and Dressed lepton dressing used in the numerator are shown, and in bold are the values used for the correction factor derivations. Uncertainties reflect the statistics from 5 million sampled events.

Acceptance Factors

The acceptance factor A^{MC} is defined using only truth-level quantities from the Powheg+Pythia8 AZNLO simulated sample. It is calculated using:

$$A^{\mathrm{MC}} = \frac{N^{\mathrm{true,fiducial,MC}}_{Z\to\ell^+\ell^-}}{N^{\mathrm{true,nocut,MC}}_{Z\to\ell^+\ell^-}}, \tag{7.12}$$

where

- $N^{\mathrm{true,fiducial,MC}}_{Z\to\ell^+\ell^-}$ is the number of generated opposite-sign events with kinematic selections $p_T(\ell) > 27\,\mathrm{GeV}$, $|\eta| < 2.4$, with additional removal of electrons in the range $1.37 < |\eta| < 1.52$, and $66 < m_{\ell^+\ell^-} < 116\,\mathrm{GeV}$.
- $N^{\mathrm{true,nocut,MC}}_{Z\to\ell^+\ell^-}$ is the number of generated events in the simulation, which for the ATLAS Powheg sample consists of events with Born lepton pair masses of $m_{\ell^+\ell^-} > 60\,\mathrm{GeV}$.

A choice is needed on exactly what lepton dressing (Section 3.4.4) definition is used for the truth-level kinematics. This choice is arbitrary due to the cancellation of A^{MC} when propagated to the full luminosity equation. Nonetheless, if a unity correction $F^{\mathrm{MC}}(\langle\mu\rangle)$ is desired, then the chosen kinematics should best describe the state of the lepton that the detector subsystem is exposed to. The full table of $\sqrt{s} = 13\,\mathrm{TeV}$ acceptances with various QED kinematics is provided in Table 7.6. Electrons were chosen with "dressed" kinematics as the collinear photon radiation typically ends up in the same calorimeter cluster or in a satellite cluster during the electron reconstruction. Muons were selected with "bare" kinematics as the ID and MS can only measure the charged particle track.

Monte Carlo Correction Factor Results

The pileup-dependent MC correction factors $F^{\mathrm{MC}}(\langle\mu\rangle)$ are derived separately for both $Z \to e^+e^-$ and $Z \to \mu^+\mu^-$ channels, and a separate correction is derived for each year (2015, 2016, 2017 and 2018) with a pileup profile generated over a larger range than that observed in data. The $\langle\mu\rangle$ dependence of $F^{\mathrm{MC}}(\langle\mu\rangle)$ is parameterised with a second-order polynomial for each derived correction. A summary plot showing each year's polynomial fit is shown in Figure 7.9 where an excellent agreement to less than 0.1% is observed between each year. The $Z \to \mu^+\mu^-$

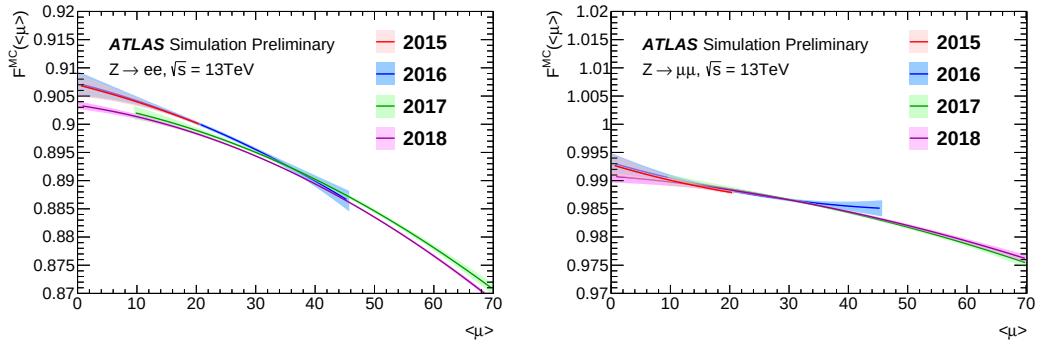

Figure 7.9: $Z \to e^+e^-$ and $Z \to \mu^+\mu^-$ pileup dependent MC correction factors $F^{\mathrm{MC}}(\langle\mu\rangle)$ derived for each year of data (2015, 2016, 2017 and 2018) produced using the dedicated Monte Carlo campaigns. The lines show second-order polynomial fits to the correction factor for the corresponding $\langle\mu\rangle$ range per year, with bands indicating the fit statistical uncertainty. The behaviour of the fits for the 2016 samples, at the low and high ends of the pileup range, is due the limited MC statistics and affects only a very small fraction of the data. Ref. [144].

correction factors are within 0.9%-2.5% of unity in the pileup range $10 < \langle\mu\rangle < 70$ studied in the Run-2 analysis. With a small $\langle\mu\rangle$ dependence and an average offset of 1%, the muon efficiency calculation does an excellent job of estimating the full efficiency loss. The $Z \to e^+e^-$ correction factors lie approximately 10% below unity, which implies that there are sizeable detector efficiencies beyond those outlined electron efficiency calculation can capture. The $\langle\mu\rangle$ dependence is stronger for $Z \to e^+e^-$ than for $Z \to \mu^+\mu^-$, but is still mild, with approximately a 2% gradient in the region $20 < \langle\mu\rangle < 50$. The corrections are all derived over a range that covers the data taken in that given year, except for a small 0.05% of 2017 data taken below $\langle\mu\rangle < 10$ from which the correction factor used is extrapolated via the fitted polynomial. The individual derivations and the corresponding comparisons of $A\varepsilon(\langle\mu\rangle)$ and $A^{\mathrm{MC}} \cdot \varepsilon^{\mathrm{T\&P,MC}}_{Z\to\ell^+\ell^-}(\langle\mu\rangle)$ are shown in Appendix B.3.

The non-zero gradients and global offsets of $F^{\mathrm{MC}}(\langle\mu\rangle) < 1.0$ imply that not all efficiencies are being measured in the Z-counting tag-and-probe procedure. These effects include the efficiency to reconstruct the ID track as a muon, the efficiency for an electron to have a reconstructed cluster associated with an ID track, and the efficiency for an electron charge to be correctly measured. In addition, applying a tighter mass window during the tag-and-probe compared to the event selection will bias the estimated tag-and-probe efficiency upwards.

7.3 Z-Counting Results

7.3.1 Luminosity Calculations

Before showing the Run-2 Z-counting results, a quick overview is given for each calculation performed to convert the single-LB $\mathcal{L}_{Z\to e^+e^-}(LB)$ and $\mathcal{L}_{Z\to\mu^+\mu^-}(LB)$ into the presented Run-2 Z-counting results.

Instantaneous Luminosity Averaging An averaging of instantaneous luminosity over 20LBs is used to improve the sizeable single-LB uncertainties and better highlight trends. A time-weighted average is used:

$$\mathcal{L}_{Z\to\ell^+\ell^-}(NLBs) = \frac{\sum_{LB}^{NLBs} \mathcal{L}_{Z\to\ell^+\ell^-}(LB)\cdot t(LB)}{\sum_{LB}^{NLBs} t(LB)}, \tag{7.13}$$

where $\mathcal{L}_{Z\to\ell^+\ell^-}(LB)$ is a single-LB Z-counting luminosity estimate, $NLBs$ is the number of combined single-LB luminosities and $t(LB)$ is the duration of each LB.

Summing Integrated Luminosity Similarly the summed integrated luminosity is evaluated by,

$$\mathcal{L}_{int,Z\to\mu^+\mu^-}(NLBs) = \sum_{LB}^{NLBs} \mathcal{L}_{Z\to\ell^+\ell^-}(LB)\cdot t(LB), \tag{7.14}$$

Efficiency Averaging For visualisation purposes the average reconstruction, trigger and event efficiencies are calculated over 20 luminosity blocks (denoted 20LB) intervals and in bins of pileup, though these averages are not used for any luminosity calculation. These are evaluated with an uncertainty weighted average:

$$\varepsilon(NLBs) = \frac{\sum_{LB}^{NLBs} \frac{\varepsilon(LB)}{\delta^2_{\varepsilon(LB)}}}{\sum_{LB}^{NLBs} \frac{1}{\delta^2_{\varepsilon(LB)}}}, \tag{7.15}$$

where $\varepsilon(LB)$ and $\delta_{\varepsilon(LB)}$ are, respectively, a per-LB efficiency and the corresponding uncertainty.

Electron-Muon Channel Combination A linear average is used to average $\mathcal{L}_{Z\to e^+e^-}(LB)$ and $\mathcal{L}_{Z\to\mu^+\mu^-}(LB)$ for each individual LB:

$$\mathcal{L}_{Z\to\ell^+\ell^-}(LB) = \frac{\mathcal{L}_{Z\to e^+e^-}(LB) + \mathcal{L}_{Z\to\mu^+\mu^-}(LB)}{2}. \tag{7.16}$$

Normalisation to Baseline ATLAS Luminosity The normalisation of Z-counting to the baseline ATLAS luminosity is used to cancel common effects from the Z-counting estimate such as the large uncertainty on the cross-section. It is accomplished by scaling all Z-counting measurements by the ratio of integrated luminosity by each methodology over a certain data-taking period, either a single LHC fill, a year, or the full Run-2. The correction is defined by:

$$\mathcal{L}^{\text{normalised}}_{Z\to\ell^+\ell^-}(LB) = \mathcal{L}_{Z\to\ell^+\ell^-}(LB)\cdot\frac{\mathcal{L}_{int,ATLAS}(NLBs)}{\mathcal{L}_{int,Z\to\ell^+\ell^-}(NLBs)}, \tag{7.17}$$

where $\mathcal{L}_{int,Z\to\ell^+\ell^-}(NLBs)$ and $\mathcal{L}_{int,ATLAS}(NLBs)$ are the integrated luminosities using the Z-counting methodology and the baseline ATLAS luminosity. This normalisation is defined independently for $\mathcal{L}_{Z\to e^+e^-}(LB)$, $\mathcal{L}_{Z\to\mu^+\mu^-}(LB)$ and the combined $\mathcal{L}_{Z\to\ell^+\ell^-}(LB)$.

Data-taking period	LHC fill	Date	Luminosity [pb^{-1}]	Average pileup $\langle\mu\rangle$
2015	4485	11/10/15	163.5	15.1
2016	4985	03/06/16	313.0	21.8
2017	6362	04/11/17	725.3	39.9
2018	7144	09/09/18	416.8	37.5

Table 7.7: Information about the selected LHC fills used for illustrating the Z-counting methodology for each of the Run-2 data-taking periods. The luminosity and pileup parameter values are taken from Ref. [109].

68th Percentile Bands The agreement between two luminosity estimates as a function of time or pileup $\langle\mu\rangle$ is given by the ratio of the two estimates. The spread is a measure of stability and is defined as the smallest interval around the median containing 68% of the ratios. Such an estimate is similar to a standard deviation but is less influenced when a small number of outliers are present.

7.3.2 Z-counting Results in a Typical LHC Fill

First, each stage of the Z-counting method is illustrated using ATLAS data taken in a typical LHC fill. The data-taking conditions significantly differ year to year, so an example LHC fill from each year was studied in detail. The conditions for each of the studied LHC fills are summarised in Table 7.7. The features observed in these studies are common between each fill and year, so only the 2017 LHC fill 6362 is shown here, with the remaining fills found in Appendix B.2. The data-driven single-lepton trigger and reconstruction efficiencies are shown in Figure 7.10 as a function of 20LB periods (individual LBs averaged over 20 sequential LB windows). The measured efficiencies are in the range 70%-95% and have a notable time dependence. There are consistently lower efficiencies at the beginning of the fill where $\langle\mu\rangle$ was larger and higher efficiencies towards the end where $\langle\mu\rangle$ was smaller. These results illustrate that the data-driven efficiencies reflect the time evolution of the data-taking conditions. For instance, the small dip in the muon trigger efficiency between LBs 920 and 1000 in Figure 7.10 corresponds to a known small loss, during this period, in the coverage of the barrel muon trigger.

The ratio of normalised Z-counting luminosity compared to the baseline ATLAS luminosity is also taken over 20LB as shown in Figure 7.11. The stability is taken to be the 68th percentile band to be 2%, reflecting the statistical precision on the 20LB groups, and shows no significant time-dependent trends against the baseline luminosity estimate. This highlights the excellent ability of both $\mathcal{L}_{Z\to e^+e^-}$ and $\mathcal{L}_{Z\to\mu^+\mu^-}$ methods to calculate a luminosity proportional to existing luminosity measurement in ATLAS.

After calculating the Z-counting luminosity for each LB, the ratio of the two estimates $\mathcal{L}_{Z\to e^+e^-}/\mathcal{L}_{Z\to\mu^+\mu^-}$ is taken in groups of 20LBs as shown in Figure 7.12. The ratio is stable over time with a mean of 0.993, illustrating that the channels show some consistent dependence. Agreement between the channels is not a trivial result as the two methods deal with very different physics objects

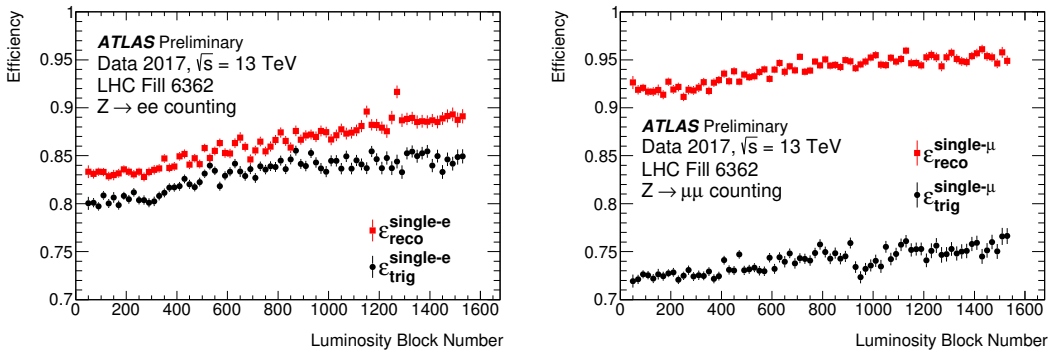

Figure 7.10: Time-dependence (top) and pileup-dependence (bottom) of the data-driven reconstruction and trigger efficiencies for both single electrons (left) and muons (right). This shows results for a single LHC fill (6362) on November 4th 2017. The luminosity block dependent efficiencies are averaged in blocks of 20 luminosity blocks. Uncertainties are statistical components only. Ref. [144].

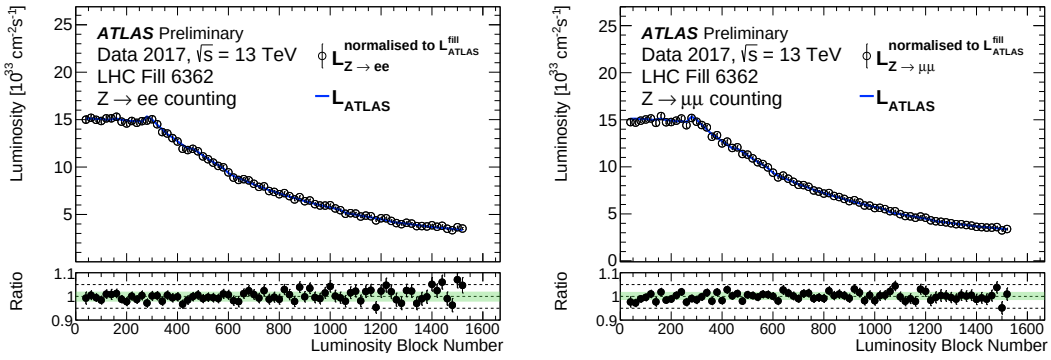

Figure 7.11: The time-dependence of the instantaneous luminosity determined for $Z \to e^+e^-$ and $Z \to \mu^+\mu^-$ luminosity measurement (open circles), the ATLAS-preferred luminosity (blue lines) and the corresponding ratio (full circles). The Z-counting luminosity has been normalised to the corresponding baseline ATLAS luminosity. The respective luminosities have been averaged over blocks of 20 luminosity blocks. This shows results for a single LHC fill (6362) on November 4th 2017. Uncertainties are statistical components only and the green bands contain 68% of all points centred around the mean. Ref. [144].

and employ different selections and methodologies. This offset of 0.7% is also of the same order as the systematic uncertainty encountered in previous experimental cross-section measurements [50]. These systematic uncertainties have not yet been estimated for Z-counting. The stability of the $\mathcal{L}_{Z\to e^+e^-}/\mathcal{L}_{Z\to\mu^+\mu^-}$ is taken to be the 68th percentile band, which was 2%, reflecting the statistical precision of the 20LB groups. No additional systematic trends are visible in the time-dependence.

7.3.3 Run-2 Time and Pileup Dependence of $\mathcal{L}_{Z\to e^+e^-}/\mathcal{L}_{Z\to\mu^+\mu^-}$

Table 7.8 shows the mean and 68% bands for the time-dependence and $\langle\mu\rangle$-dependence of $\mathcal{L}_{Z\to e^+e^-}/\mathcal{L}_{Z\to\mu^+\mu^-}$ over the given data-taking periods (2015, 2016, 2017, 2018 and Run-2). Excellent consistency is observed between the the mean of $\mathcal{L}_{Z\to e^+e^-}/\mathcal{L}_{Z\to\mu^+\mu^-}$ for both time-dependence and $\langle\mu\rangle$-dependence, with values around 0.992-0.993 observed for all years and across the full Run-2 data. The 68% bands reflect the statistical uncertainties for each year

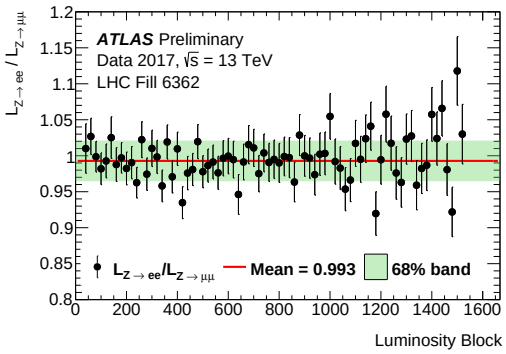

Figure 7.12: Luminosity block dependence of the ratio of instantaneous luminosities determined from $Z \to e^+e^-$ and $Z \to \mu^+\mu^-$ counting. The respective luminosities have been averaged over blocks of 20 luminosity blocks. The red line indicates the mean obtained from a fit to a constant. This shows results for a single LHC fill (6362) on November 4th 2017. Uncertainties are statistical components only, and the green band contains at least 68% of points centred around the mean. Ref. [144].

	$\mathcal{L}_{Z\to e^+e^-}/\mathcal{L}_{Z\to\mu^+\mu^-}$			
	Time dependence		**Pileup dependence**	
Data-taking period	Mean	Spread	Mean	Spread
2015	0.993	0.011	0.9934	0.0066
2016	0.992	0.007	0.9924	0.0017
2017	0.993	0.005	0.9926	0.0027
2018	0.992	0.004	0.9918	0.0018
Run 2	0.992	0.006	0.9923	0.0015

Table 7.8: Summary of the mean and spread (68% of all points centred around the mean) of the $\mathcal{L}_{Z\to e^+e^-}/\mathcal{L}_{Z\to\mu^+\mu^-}$ ratio for each of the Run-2 data-taking periods, and for the full dataset as a function of time and pileup.

	Time dependence			**Pileup dependence**		
Data-taking period	$\mathcal{L}_{Z\to e^+e^-}/\mathcal{L}_{ATLAS}$	$\mathcal{L}_{Z\to\mu^+\mu^-}/\mathcal{L}_{ATLAS}$	$\mathcal{L}_{Z\to\ell^+\ell^-}/\mathcal{L}_{ATLAS}$	$\mathcal{L}_{Z\to e^+e^-}/\mathcal{L}_{ATLAS}$	$\mathcal{L}_{Z\to\mu^+\mu^-}/\mathcal{L}_{ATLAS}$	$\mathcal{L}_{Z\to\ell^+\ell^-}/\mathcal{L}_{ATLAS}$
2015	0.008	0.008	0.007	0.0040	0.0035	0.0040
2016	0.006	0.006	0.005	0.0028	0.0022	0.0024
2017	0.005	0.005	0.004	0.0021	0.0022	0.0017
2018	0.005	0.004	0.004	0.0014	0.0011	0.0011
Run 2	0.008	0.008	0.008	–	–	–

Table 7.9: Summary of the spread (68% of all points centred around unity) of the $\mathcal{L}_{Z\to e^+e^-}/\mathcal{L}_{ATLAS}$, $\mathcal{L}_{Z\to\mu^+\mu^-}/\mathcal{L}_{ATLAS}$ and $\mathcal{L}_{Z\to\ell^+\ell^-}/\mathcal{L}_{ATLAS}$ ratio for each of the Run-2 data-taking periods as a function of time and pileup, and as a function of time for the full Run-2 dataset.

with a time-dependent spread of 1.1% observed in 2015 and a spread of 0.4% in 2018. The $\langle\mu\rangle$-dependence displays similar features with the full Run-2 having a spread of 0.15% showing the excellent control of $\mathcal{L}_{Z\to e^+e^-}/\mathcal{L}_{Z\to\mu^+\mu^-}$ under all Run-2 data taking conditions. Figure 7.13 and Figure 7.14 show the independence of the ratio $\mathcal{L}_{Z\to e^+e^-}/\mathcal{L}_{Z\to\mu^+\mu^-}$ with respect to time and $\langle\mu\rangle$, respectively, when using the full Run-2 data set.

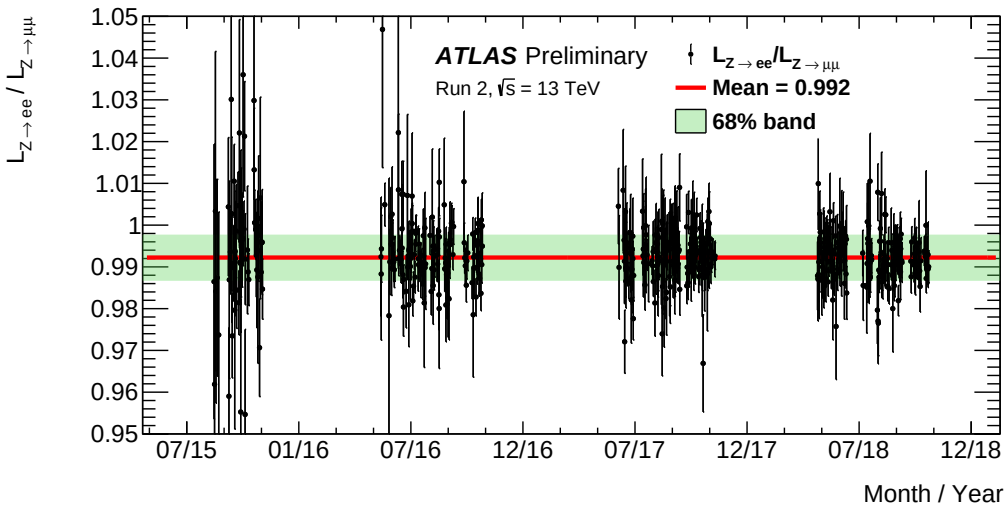

Figure 7.13: Ratio of the integrated luminosities obtained from the $Z \to e^+e^-$ and $Z \to \mu^+\mu^-$ channels per LHC fill ($\mathcal{L}_{Z\to e^+e^-}/\mathcal{L}_{Z\to\mu^+\mu^-}$) for the whole Run-2 data-taking period. Only ATLAS runs with a minimum length of 40 minutes are included and error bars show the statistical uncertainties only. The red line indicates the mean obtained from a fit to a constant. The statistical error on the Run-2 averaged $\mathcal{L}_{Z\to e^+e^-}/\mathcal{L}_{Z\to\mu^+\mu^-}$ ratio is negligible. The green band contains 68% of all points centred around the mean. Ref. [144].

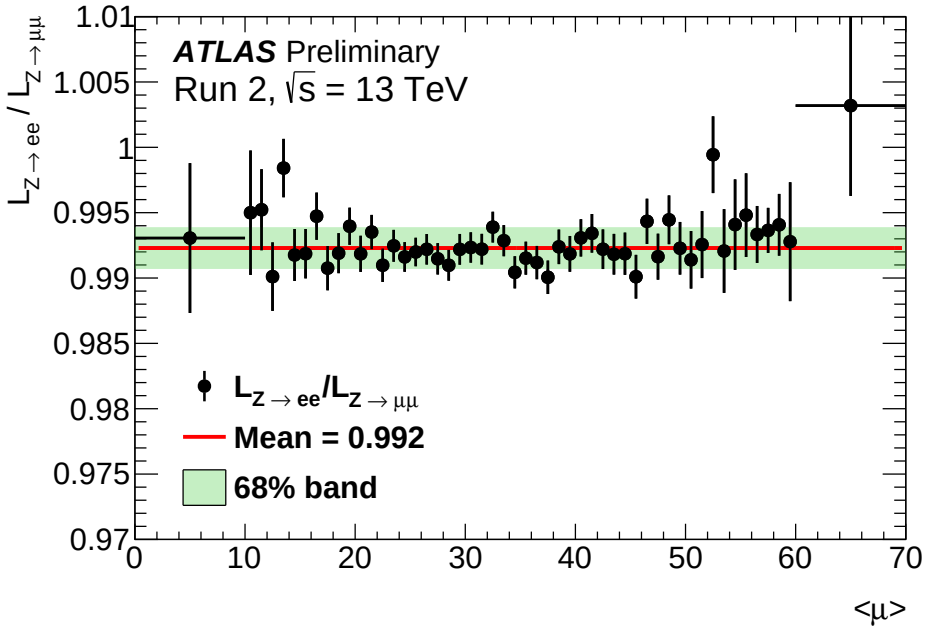

Figure 7.14: The ratio of the integrated luminosities obtained from the $Z \to e^+e^-$ and $Z \to \mu^+\mu^-$ channels ($\mathcal{L}_{Z\to e^+e^-}/\mathcal{L}_{Z\to\mu^+\mu^-}$) for the full Run-2 data-taking period. The x-axis represents the bunch averaged pileup parameter $\langle\mu\rangle$. The error bars show the statistical uncertainties only. The green band contains 68% of all points centred around the mean. Ref. [144].

7.3.4 Time and Pileup Dependence of $\mathcal{L}_{Z\to\ell^+\ell^-}/\mathcal{L}_{ATLAS}$

The excellent stability observed in the ratio $\mathcal{L}_{Z\to e^+e^-}/\mathcal{L}_{Z\to\mu^+\mu^-}$ motivates the use of the averaged $\mathcal{L}_{Z\to\ell^+\ell^-}$ result for comparison with $\mathcal{L}_{ATLAS}$. This reduces the statistical uncertainty on the Z-counting estimate to better highlight any trends against $\mathcal{L}_{ATLAS}$. The normalisation of

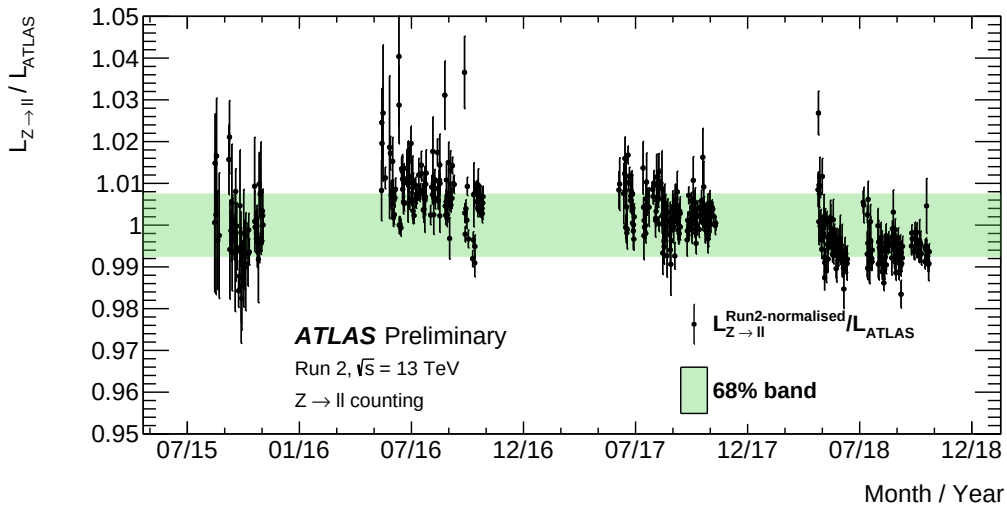

Figure 7.15: The ratio of the integrated, combined Z-counting and baseline ATLAS luminosities per LHC fill taken from pp collisions at $\sqrt{s} = 13$ TeV for the full Run-2 data-taking period. The combined Z-counting luminosity is normalised to the baseline ATLAS luminosity integrated over the Run-2 data-taking period [109]. The x-axis represents the date when the fill started. Only ATLAS runs with a minimum length of 40 minutes are included. The error bars show statistical uncertainties only. The green bands contain 68% of all points centred around the mean. Ref. [144].

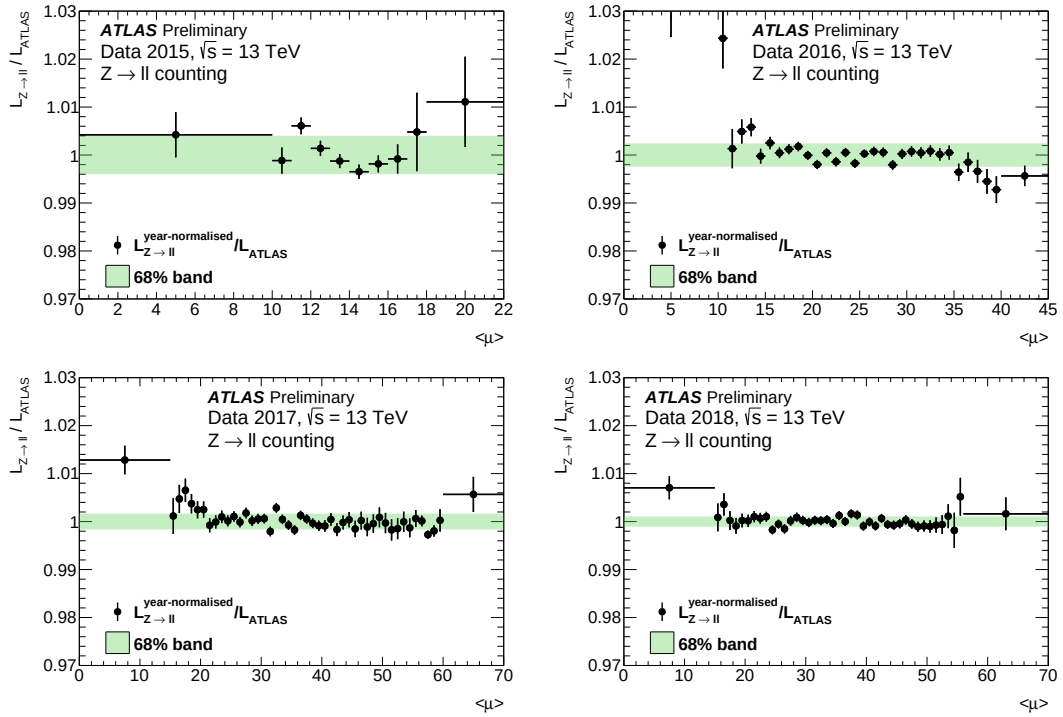

Figure 7.16: The ratio of the integrated, combined Z-counting and baseline ATLAS luminosities per LHC fill taken from pp collisions at $\sqrt{s} = 13$ TeV for data taken in 2015, 2016, 2017 and 2018. The combined Z-counting luminosity is normalised to the baseline ATLAS luminosity integrated over the Run-2 data-taking period [109]. The x-axis represents the bunch averaged pileup parameter $\langle\mu\rangle$. Only ATLAS runs with a minimum length of 40 minutes are included. The error bars show statistical uncertainties only. The green bands contain 68% of all points centred around the mean. Ref. [144].

Z-counting to the baseline ATLAS luminosity results in this ratio being close to unity by construction; however, the 68% band and ratio plots can still provide insight into discrepancies

between the measurements. Table 7.9 shows the 68% bands for the time-dependence and $\langle\mu\rangle$-dependence of $\mathcal{L}_{Z\to e^+e^-}/\mathcal{L}_{ATLAS}$, $\mathcal{L}_{Z\to\mu^+\mu^-}/\mathcal{L}_{ATLAS}$ and $\mathcal{L}_{Z\to\ell^+\ell^-}/\mathcal{L}_{ATLAS}$ over a given data-taking period (2015, 2016, 2017, 2018 and Run-2). Similar trends are observed for the individual channels. The spread observed for each year is either comparable or improved compared to $\mathcal{L}_{Z\to e^+e^-}/\mathcal{L}_{Z\to\mu^+\mu^-}$ due to the ATLAS luminosity having negligible statistical uncertainty. One exception is the spread of the time-dependency evaluated using the full Run-2 data, which is comparatively larger than the spreads of the individual years. The origin of this can be observed in Figure 7.15 which shows the time-dependency over the Run-2 data-taking period. Significant deviations from unity are observed of -0.4% in 2015, +0.6% in 2016, +0.2% in 2017 and -0.5% in 2018. Figure 7.16 shows the $\langle\mu\rangle$-dependence for each individual year. These show excellent stability in the range $\langle\mu\rangle > 10$, though small 0.5-3% offsets are observed for $\langle\mu\rangle > 10$ in all years.

The time-dependent deviations observed are within the uncorrelated year-by-year uncertainties on the baseline ATLAS luminosity [109], which are: 1.3% for 2015/2016, 1.3% for 2017 and 1.0% in 2018. As these trends are visible in $\mathcal{L}_{Z\to\ell^+\ell^-}/\mathcal{L}_{ATLAS}$ but not in $\mathcal{L}_{Z\to e^+e^-}/\mathcal{L}_{Z\to\mu^+\mu^-}$, it is good evidence that the Z-counting method can provide strong constraints and provide improvements on the year-dependent calibrations in the baseline ATLAS luminosity.

7.4 Z-counting Statistical Bias Study

The main limitation of the Z-counting method are the counting rates that lead to non-negligible statistical uncertainties. This can introduce problems such as the edge-case LBs discussed in Section 7.2.3, where raw event counts can be small enough that the normal approximation of uncertainty propagation is not valid, and hence the efficiency and luminosity estimators used may display a statistical bias when the raw count numbers are low. This motivated a study comparing Z-counting results obtained from summing individual LBs to a result obtained by integrating over many LBs.

7.4.1 Toy Study

In this section a simplified toy model of the Z-counting method is constructed to help investigate the possibility of statistical bias in the terms of Equation 7.2. This simplification removes all factors except for the raw reconstructed counts $N^{\text{toy}}_{Z\to\ell^+\ell^-}$, and the event-level efficiency calculated assuming only efficiency losses from a trigger-like source, the expression becomes:

$$\mathcal{L}^{\text{toy}}_{Z\to\ell^+\ell^-} = \frac{N^{\text{toy}}_{Z\to\ell^+\ell^-}}{\left(1-(1-\varepsilon^{\text{toy}}_{\text{trig},1\ell})^2\right)}, \tag{7.18}$$

where all terms are evaluated for a given toy experiment. In the absence of scaling factors and other efficiency sources, the luminosity evaluated here is equivalent to the efficiency corrected counts, or the number of Z-boson events before any efficiency losses.

A given toy experiment is performed with two specified inputs, the true number of generated events $N^{\text{true}}_{Z\to\ell^+\ell^-}$ and the true single lepton trigger efficiency $\varepsilon^{\text{true}}_{\text{trig},1\ell}$. From these quantities, toy estimates for single lepton trigger efficiency $\varepsilon^{\text{toy}}_{\text{trig},1\ell}$ and luminosity $\mathcal{L}^{\text{toy}}_{Z\to\ell^+\ell^-}$ are evaluated using the following procedure:

1. Generate $N^{\text{true}}_{Z\to\ell^+\ell^-}$ Z-boson events.
2. For each generated event, a test of two leptons against a true efficiency $\varepsilon^{\text{true}}_{\text{trig},1\ell}$ is simulated by sampling two random numbers r_1, r_2 from a uniform distribution between 0 and 1, and treating $r_{1,2} < \varepsilon^{\text{true}}_{\text{trig},1\ell}$ as a successful trigger.
3. Count how many events have one and two triggered leptons, N_1 and N_2 respectively, and calculated the toy efficiency estimate $\varepsilon^{\text{toy}}_{\text{trig},1\ell}$.
4. Calculate the number of reconstructed events from $N^{\text{toy}}_{Z\to\ell^+\ell^-} = N_1 + N_2$.
5. Calculate the toy luminosity estimate $\mathcal{L}^{\text{toy}}_{Z\to\ell^+\ell^-}$ as in Equation 7.18.

The estimated $\varepsilon^{\text{toy}}_{\text{trig},1\ell}$ and $\mathcal{L}^{\text{toy}}_{Z\to\ell^+\ell^-}$ can then be compared to the corresponding true values. The bias on the efficiency estimate can be evaluated by,

$$\text{Bias}_{Efficiency} = \frac{1}{N_{\text{toys}}} \sum_{toy}^{N_{\text{toys}}} \frac{\varepsilon^{\text{toy}}_{\text{trig},1\ell}}{\varepsilon^{\text{true}}_{\text{trig},1\ell}}, \tag{7.19}$$

and the bias on the luminosity estimate is calculated by,

$$\text{Bias}_{Luminosity} = \frac{1}{N_{\text{toys}}} \sum_{toy}^{N_{\text{toys}}} \frac{\mathcal{L}^{\text{toy}}_{Z\to\ell^+\ell^-}}{\mathcal{L}^{\text{true}}_{Z\to\ell^+\ell^-}}. \tag{7.20}$$

Here, unity is expected for an unbiased estimate. A scan of the efficiency and luminosity bias as a function of $N^{\text{true}}_{Z\to\ell^+\ell^-}$ is shown in Figure 7.17. The efficiency is on average underestimated compared to the true value, with a 0.5-1% bias when $N^{\text{true}}_{Z\to\ell^+\ell^-} < 100$ and a less than per mille bias when $N^{\text{true}}_{Z\to\ell^+\ell^-} > 500$ with a trend of approaching unity as $N^{\text{true}}_{Z\to\ell^+\ell^-}$ increases. This trend propagates inversely to the luminosity with an amplified effect, with a 1-2% bias overestimation when $N^{\text{true}}_{Z\to\ell^+\ell^-} < 100$ with the same trend towards unity as $N^{\text{true}}_{Z\to\ell^+\ell^-}$ increases. The sampled distribution of $\varepsilon^{\text{toy}}_{\text{trig},1\ell}$ and $\mathcal{L}^{\text{toy}}_{Z\to\ell^+\ell^-}$ as compared to their true values is shown in Figure 7.18 for $N^{\text{true}}_{Z\to\ell^+\ell^-} = 20, 100, 1000$. For a low number of $N^{\text{true}}_{Z\to\ell^+\ell^-}$ events, the resulting distributions do not appear continuous as there are finite combinations of integer counts of N_1 and N_2. As $N^{\text{true}}_{Z\to\ell^+\ell^-}$ increases, the distribution becomes smoother and the spread around 1.0 becomes smaller. It is also seen, for $N^{\text{true}}_{Z\to\ell^+\ell^-} = 20$, that the distribution is not symmetric and has a tail below unity, which explains the observed bias.

7.4.2 Correcting Z-counting Estimates for Low Event Count Periods

The simple toy model provides evidence that a statistical bias exists using just the trigger efficiency formula and that this bias is emphasised when the event counts are low. As the

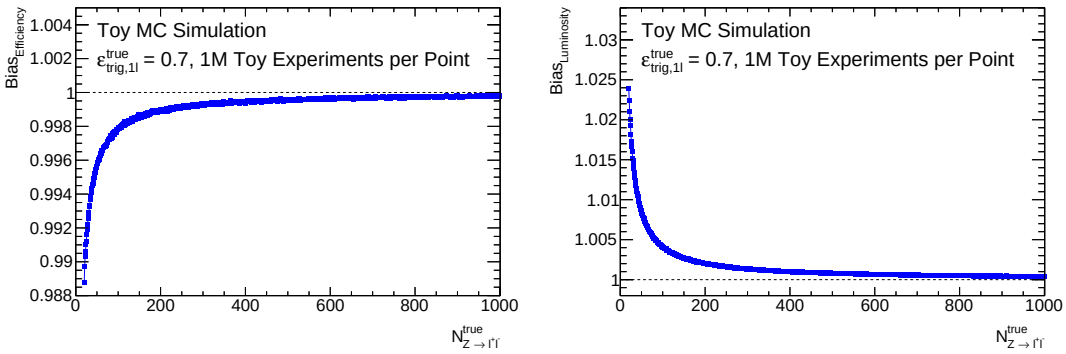

Figure 7.17: The bias of estimated $\varepsilon^{toy}_{trig,1\ell}$ and $\mathcal{L}^{toy}_{Z\to\ell^+\ell^-}$ as a function of $N^{true}_{Z\to\ell^+\ell^-}$ with integer steps between 20 and 1000. The average for each point is evaluated from 1 million independent toy experiments.

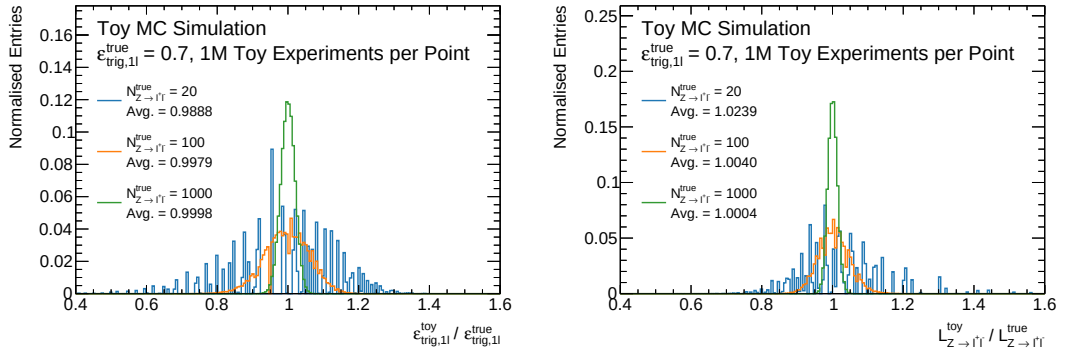

Figure 7.18: The distribution of estimated $\varepsilon^{toy}_{trig,1\ell}$ and $\mathcal{L}^{toy}_{Z\to\ell^+\ell^-}$ compared to the true quantities $\varepsilon^{true}_{trig,1\ell}$ and $\mathcal{L}^{true}_{Z\to\ell^+\ell^-}$ respectively, evaluated with 1 million independent toy experiments for each $N^{true}_{Z\to\ell^+\ell^-} = 20, 100, 1000$.

Z-counting formulae are more complex due to background subtraction terms and a combination of independent reconstruction and trigger efficiencies, it is important to study the impact of this bias on the 20LB binned, the LHC fill binned, and $\langle\mu\rangle$-binned Z-counting estimates. A summary is given of the possible solutions for correcting this bias:

- **Unbiased Estimator:** Deriving an unbiased estimator could be accomplished by utilising a toy model to perform a maximum-likelihood fit for a given set of true parameters to yield the observed quantities: reconstructed counts $N_{Z\to\ell^+\ell^-}(LB)$ and the associated tag-and-probe counts. This is feasible for the trigger efficiency component, but the background contamination in the reconstruction efficiencies would require a much more detailed model. This would also require significant computation time requiring thousands of multidimensional parameter scans, one per LB, for just a single LHC fill.

- **Bias Correction:** Use full-detector Monte Carlo to model the bias as a function of true or reconstructed quantities, for example $N^{true}_{Z\to\ell^+\ell^-}$ and $\varepsilon^{true}_{Z\to\ell^+\ell-}$ or $N_{Z\to\ell^+\ell^-}(LB)$ and $\varepsilon^{T\&P}_{Z\to\ell^+\ell-}(LB)$, then correct the estimated per-LB luminosity estimates by the corresponding bias factor. This method does not account for time-dependent fluctuations in the detector efficiencies, which can occur in data.

- **Aggregated Data:** Group many individual LBs together, increasing the total event

counts, and calculate a single luminosity estimate for the group. This requires definition of *aggregation functions* that dictate how each variable should be merged, for example *sum mean*, *time-weighted mean* etc.

The aggregated data method is the simplest to implement and is also the safest choice as it essentially avoids low event count calculations altogether. The remaining sections will study the impact of using the aggregated data method.

Grouping Luminosity Blocks

The aggregated data method requires LBs to be grouped, but some care is required on how these groups are defined. Due to the non-linearity of the pileup dependent correction factor $F^{MC}_{Z\to\ell^+\ell^-}(\langle\mu\rangle)$, only LBs with similar $\langle\mu\rangle$ conditions should be merged. With this in mind, two grouping methods are introduced:

- **LB Grouping:** Group Sequential LBs together with a constant step size (e.g. 20LB). Generally, LBs close to each other share similar conditions, so this is well motivated. Time-dependent trends exist over a full LHC-fill, however, so this grouping should be kept as small as possible to avoid complications from the low-statistics bias.
- **$\langle\mu\rangle$ Grouping:** Group LBs into bins of $\langle\mu\rangle$, which directly ensures that the merged LBs are taken under similar $\langle\mu\rangle$ conditions. This is performed for each LHC fill independently.

Naturally, per-fill integrated luminosity can still be obtained by summing the results of each group, similar to summing individual LBs.

Aggregation Functions

Aggregation functions describe how a given quantity should be merged when grouping multiple LBs. The raw counts, the tag-and-probe counts and the live time combine using a linear sum. The merging of $\langle\mu\rangle$ is accomplished instead by aggregating the $F^{MC}_{Z\to\ell^+\ell^-}(\langle\mu\rangle)$ term. This is accomplished by the use of a luminosity weighted correction factor defined by,

$$F^{MC,\text{aggregated}}_{Z\to\ell^+\ell^-}(\langle\mu\rangle) = \frac{\sum_{LB}^{NLBs} \mathcal{L}_{\text{int,ATLAS}}(LB) F^{MC}_{Z\to\ell^+\ell^-}(\langle\mu\rangle, LB)}{\sum_{LB}^{NLBs} \mathcal{L}_{\text{int,ATLAS}}(LB)}, \tag{7.21}$$

where $F^{MC}_{Z\to\ell^+\ell^-}(\langle\mu\rangle, LB)$ is evaluated for each individual LB and averaged with the official integrated luminosity estimate used as the weight $\mathcal{L}_{\text{int,ATLAS}}(LB)$. This could be done iteratively using the per-LB Z-counting luminosities, however for simplicity, the official luminosity was used for this study. As the two grouping methods lead to similar values of $\langle\mu\rangle$ being merged, it is not expected that this will have a large impact.

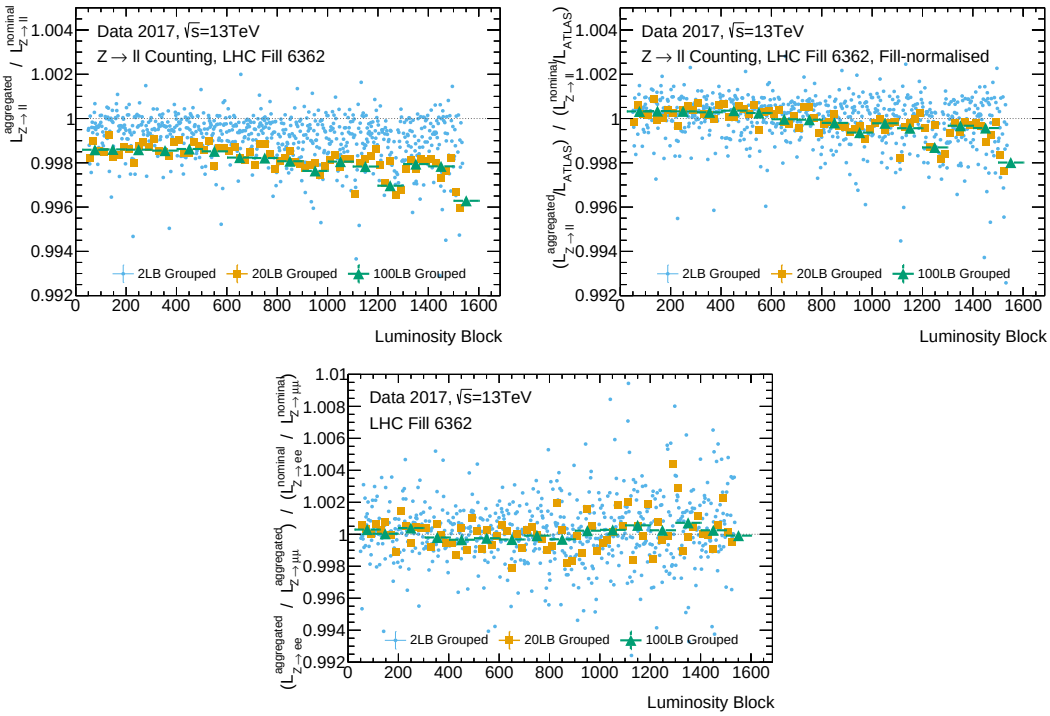

Figure 7.19: Ratio plots comparing the relative difference between "aggregated" Z-counting luminosity estimates to the "nominal" single-LB estimate for various choices of luminosity block grouping (2LB, 20LB, 100LB). The x-axis represents the luminosity block number.

7.4.3 Aggregated Data Results

All results shown in this section compare the ratio of an "aggregated" Z-counting luminosity to the sum of single-LB Z-counting estimates, denoted "nominal", calculated using the same group of LBs. The ratio of the two estimates can be interpreted directly as a correction to the single-LB estimates presented in the previous section.

Aggregated Z-counting for a Typical LHC Fill

The results in Figure 7.19 show the impact of aggregation for the 2017 LHC fill 6362 with various choices for LB grouping 2LB, 20LB and 100LB. The absolute luminosity $\mathcal{L}_{Z\to\ell^+\ell^-}$ shows a 0.1-0.3% bias in the 20LB and 100LB groupings when comparing the aggregated and nominal methods. The 2LB grouping shows no significant difference from those performed with one LB, implying that it is not sufficient to remove the bias. The bias displays only small dependence as the fill progresses, leading to a very small trend of about 0.1% across the fill. The impact on $\mathcal{L}_{Z\to\ell^+\ell^-}$ when normalised to $\mathcal{L}_{ATLAS}$ is mostly less significant, with a +0.05% bias at the start of the fill and -0.05% bias at the end. When comparing $\mathcal{L}_{Z\to e^+e^-}/\mathcal{L}_{Z\to\mu^+\mu^-}$ between aggregated and nominal, there is no obvious discrepancy, implying that the impact of aggregation is similar for both $\mathcal{L}_{Z\to e^+e^-}$ and $\mathcal{L}_{Z\to\mu^+\mu^-}$.

The 20LB method was selected to study the full Run-2 data as it displayed a significant difference from the nominal method and a negligible difference from the larger 100LB grouping.

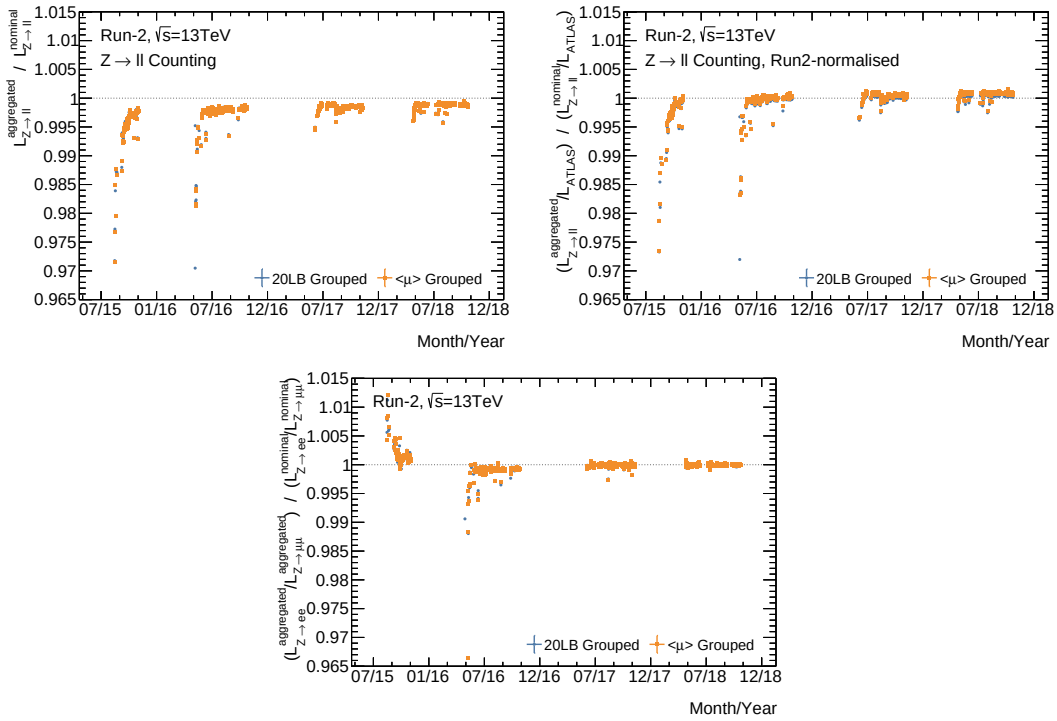

Figure 7.20: Ratio plots comparing the relative difference between "aggregated" Z-counting luminosity estimates to the "nominal" single-LB estimate for per-fill integrated luminosity estimates using the full Run-2 dataset. Two grouping methods are shown: the 20LB grouping and pileup binned grouping. The x-axis represents the date when the fill started. Only ATLAS runs with a minimum length of 40 minutes are included.

In addition, the 20LB grouping was also preferable as it matches the granularity used for the single fill studies in Section 7.3.2.

Aggregated Z-counting for Run-2

The results in Figure 7.20 and Figure 7.21, respectively, show the per-fill time-dependent and $\langle\mu\rangle$-dependent impact of aggregation on $\mathcal{L}_{Z\to\ell^+\ell^-}$ over the full Run-2 data period. The time-dependent plots show fill-integrated luminosities using the 20LB and $\langle\mu\rangle$ grouping schemes with excellent agreement between the two. The $\langle\mu\rangle$-dependent plots, by definition, can only integrate the per-fill $\langle\mu\rangle$ grouped luminosities. The offset observed for absolute luminosity estimate is a mostly consistent offset of 0.1-0.2% in all fills in 2017 and 2018, where $\langle\mu\rangle$ was large. These results are in agreement with the previously studied 2017 fill. The 2015 and 2016 contain some sizeable 0.4-3.0% offsets at the beginning of each year of data-taking, which correspond to special low-luminosity conditions used as data-taking first started. The remaining fills in 2015-2016 are slightly lower than in 2017 and 2018, with a 0.2-0.4% offset due to the lower $\langle\mu\rangle$ used in these runs. The bins $\langle\mu\rangle < 10$ and $\langle\mu\rangle > 60$ are subject to statistical fluctuations due to the small fraction of LBs populating these regions. The bins in the range $10 < \langle\mu\rangle < 60$ are well-populated and display smooth trends. A similar trend is observed with the time-dependent plots, where both channels display a 0.1-0.2% offset which decreases as $\langle\mu\rangle$ increases. After performing Run-2 normalisation, the aggregated results are stable compared to the nominal

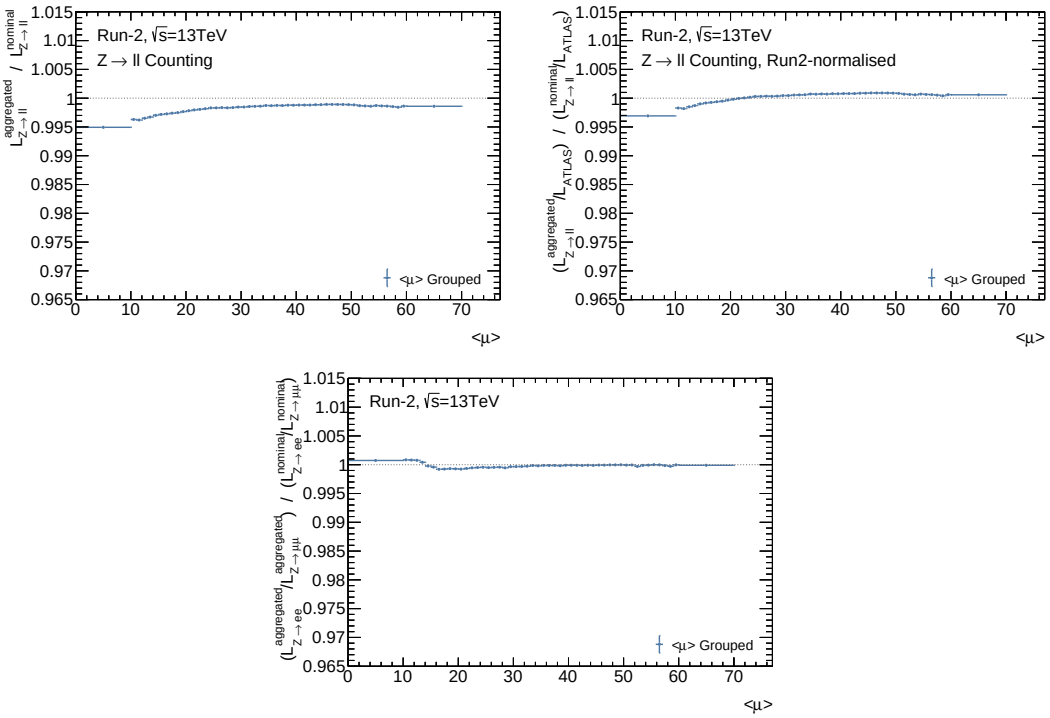

Figure 7.21: Ratio plots comparing the relative difference between "aggregated" Z-counting luminosity estimates to the "nominal" single-LB estimate for pileup-binned integrated luminosity estimates using the full Run-2 dataset.

results, with a ratio of less than 0.1% and only the noted low-luminosity fills showing a sizeable difference.

Comparing the aggregated and nominal $\mathcal{L}_{Z\to e^+e^-}/\mathcal{L}_{Z\to\mu^+\mu^-}$ values shows they are mostly consistent, with divergences seen for most fills of less than 0.1%. The noted low-luminosity fills in 2015 and 2016 display as much as 1% disagreement on the $\mathcal{L}_{Z\to e^+e^-}/\mathcal{L}_{Z\to\mu^+\mu^-}$ ratio, however, implying this discrepancy is stronger in one of the channels than the other. Interestingly the offset on the $\mathcal{L}_{Z\to e^+e^-}/\mathcal{L}_{Z\to\mu^+\mu^-}$ ratio appears to be an increase in 2015 and a decrease in 2016. The likely explanation is the change in electron triggers, as in 2015, the electron trigger efficiency was much higher about 90%, compared to the roughly 80% observed in the rest of Run-2, which allows for more statistics to be recorded, minimising the impact of 2015 low-luminosity conditions compared to similar conditions in the rest of Run-2. This feature is visible on the $\langle\mu\rangle$ dependent $\mathcal{L}_{Z\to e^+e^-}/\mathcal{L}_{Z\to\mu^+\mu^-}$ plot as most data below $\langle\mu\rangle < 20$ originate from 2015.

These results can be interpreted directly as corrections to the stability plots presented in Section 7.3. As most of the corrections are less than 0.1% after normalisation, they do not invalidate any of the conclusions already made. However, this correction would reduce some of the outliers, most notably the fills early in 2015 and 2016, and correct some of the minor trends.

In summary, additional care should be taken when using Z-counting in low-luminosity and low-pileup conditions. As future luminosity measurement at ATLAS approaches a precision of 1% or lower, the treatment of these permille effects will become relevant.

8 Drell–Yan Triple-differential Cross-section Measurement

8.1 Overview and Motivations

Measurements of Drell-Yan cross-sections provide precises test of perturbative Quantum Chromodynamics (QCD), offer sensitivity to parameterisations of the parton distribution functions (PDFs) and sensitivity to electroweak parameters such as the electroweak mixing angle.

This chapter presents the full analysis chain for the measurement of 3D differential Drell-Yan cross-sections in the ee and $\mu\mu$ channels using 256.8 pb^{-1} of $\sqrt{s}$ =5.02 TeV data and 335.2 fb^{-1}of $\sqrt{s}$ =13 TeV data collected by ATLAS in low-μ pp collisions. These measurements will supersede the previous $\sqrt{s}$ = 5.02 TeV measurement as the dataset is ten times larger and will be the first differential cross-section measurement at $\sqrt{s}$ =13 TeV. These measurement are expected to produce the most precise total cross-section measurement due to the reduced uncertainty on the luminosity determination of 1.6% (1.5%) for the 5.02 TeV(13 TeV) dataset respectively [112]. The $p_T(\ell) > 15$ GeV thresholds on the low-μ triggers provide increased fiducial acceptance around the Z-mass resonance as well as allowing measurement of low-mass regions of phase space. These measurements are performed in wide intervals of dilepton invariant mass, $m_{\ell\ell}$, between 40 GeV and 500 GeV, in bins of dilepton rapidity $|y_{\ell\ell}|$ up to 2.4 and in bins of the cosine of the production angle measured in the Collins-Soper frame $\cos\theta^*_{CS}$.

First, there is a discussion of the data and simulated MC samples used in Section 8.5. There is then a discussion of the fiducial volume and measurement binning scheme in Section 8.3, and the selection of leptons and events in Section 8.4. The data-driven estimate of the multijet background is discussed in Section 8.5. The unfolding procedure and the treatment of experimental uncertainties are discussed in Section 8.6 and Section 8.7 respectively. Finally, a discussion of the unfolded results, the combination of electron and muon channels and a discussion of the integrated fiducial cross-sections is provided in Section 8.8.1.

8.2 Data and Simulated Event Samples

The data used for this analysis consist of the special $\sqrt{s}$ = 5.02 TeV and $\sqrt{s}$ = 13 TeV low-μ datasets collected in 2017 and 2018, as described in Section 4.5.1. Only data taken during stable beam conditions with fully operational detector systems are used, as defined by the luminosity

Process	Data set	Generator	$(\sigma_{\text{theory}}\cdot\text{BR})\times\epsilon_{\text{filter}}$ [nb]	Uncertainty [%]
$Z/\gamma^* \to ee$ ($m_{ee} > 60\,\text{GeV}$)	361106	Powheg+Pythia8	0.6600×1.025	5%
$Z/\gamma^* \to \mu\mu$ ($m_{\mu\mu} > 60\,\text{GeV}$)	361107	Powheg+Pythia8	0.6600×1.025	5%
$Z/\gamma^* \to \tau\tau$ ($m_{\tau\tau} > 60\,\text{GeV}$)	361108	Powheg+Pythia8	0.6600×1.025	5%
$Z/\gamma^* \to ee$ ($10\,\text{GeV} < m_{ee} < 60\,\text{GeV}$)	361665	Powheg+Pythia8	3.15×0.304	5%
$Z/\gamma^* \to \mu\mu$ ($10\,\text{GeV} < m_{\mu\mu} < 60\,\text{GeV}$)	361667	Powheg+Pythia8	3.15×0.312	5%
$Z/\gamma^* \to \tau\tau$ ($10\,\text{GeV} < m_{\tau\tau} < 60\,\text{GeV}$)	361669	Powheg+Pythia8	3.15×0.015	5%
$WZ(\ell\ell\ell^-\nu\text{SF})$	361064	Sherpa 2.1	0.0005324	10%
$WZ(\ell\ell\ell^-\nu\text{OF})$	361065	Sherpa 2.1	0.001041	10%
$WZ(\ell\ell\ell^+\nu\text{SF})$	361066	Sherpa 2.1	0.0008433	10%
$WZ(\ell\ell\ell^+\nu\text{OF})$	361067	Sherpa 2.1	0.001633	10%
$WW(2\ell 2\nu)$	361068	Sherpa 2.1	0.003356	10%
$WW(q\bar{q}\ell\nu)$	361091	Sherpa 2.1	0.006059	10%
$WW(\ell\nu q\bar{q})$	361092	Sherpa 2.1	0.006082	10%
$WZ(\ell\nu q\bar{q})$	361093	Sherpa 2.1	0.002503	10%
$WZ(q\bar{q}\ell\ell)$	361094	Sherpa 2.1	0.0007518	10%
$ZZ(q\bar{q}\ell\ell)$	361096	Sherpa 2.1	0.003789×0.148	10%
$t\bar{t}$	410470	Powheg+Pythia8	0.06890×0.544	7%
$t(\text{s}-\text{chan.}t)$	410644	Powheg+Pythia8	0.0005400	10%
$t(\text{s}-\text{chan.}\bar{t})$	410645	Powheg+Pythia8	0.0002751	10%
Wt	410646	Powheg+Pythia8	0.002990	10%
$W\bar{t}$	410647	Powheg+Pythia8	0.002983	10%
$t(\text{t}-\text{chan.}t)$	410658	Powheg+Pythia8	0.005414	10%
$t(\text{t}-\text{chan.}\bar{t})$	410659	Powheg+Pythia8	0.002682	10%
$\gamma\gamma \to ee$ ($20\,\text{GeV} < m_{ee} < 60\,\text{GeV}$)	364834	Pythia8	0.023×0.498	50%
$\gamma\gamma \to \mu\mu$ ($20\,\text{GeV} < m_{\mu\mu} < 60\,\text{GeV}$)	364841	Pythia8	0.022×0.512	50%
$\gamma\gamma \to \tau\tau$ ($20\,\text{GeV} < m_{\tau\tau} < 60\,\text{GeV}$)	363284	Pythia8	0.017×0.01	50%
$\gamma\gamma \to ee$ ($60\,\text{GeV} < m_{ee} < 200\,\text{GeV}$)	364835	Pythia8	0.002×0.698	50%
$\gamma\gamma \to \mu\mu$ ($60\,\text{GeV} < m_{\mu\mu} < 200\,\text{GeV}$)	364842	Pythia8	0.002×0.71	50%
$\gamma\gamma \to \tau\tau$ ($60\,\text{GeV} < m_{\tau\tau} < 200\,\text{GeV}$)	363285	Pythia8	0.001×0.038	50%
$\gamma\gamma \to ee$ ($200\,\text{GeV} < m_{ee} < 600\,\text{GeV}$)	364836	Pythia8	0.0016×0.794	50%
$\gamma\gamma \to \mu\mu$ ($200\,\text{GeV} < m_{\mu\mu} < 600\,\text{GeV}$)	364843	Pythia8	0.0016×0.802	50%
$\gamma\gamma \to \tau\tau$ ($200\,\text{GeV} < m_{\tau\tau} < 600\,\text{GeV}$)	363286	Pythia8	0.0013×0.065	50%

Table 8.1: Monte Carlo samples at $\sqrt{s} = 5.02\text{TeV}$. Given is a short description of the process, the ATLAS MC sample number, the MC generator(s), the used value of the higher order cross section times the branching tratio and filter efficiencies $(\sigma_{\text{theory}}\cdot\text{BR})\times\epsilon_{\text{filter}}$ (where the absence of the $\times$ symbol indicates $\epsilon_{\text{filter}} = 1$) and the uncertainty applied on the sample normalisation. The filter efficiency for $Z/\gamma^* \to \ell\ell$ ($m_{\ell\ell} > 60\,\text{GeV}$) is greater than 1.0 as it corrects for the fact that the theory cross-section used was calculated using $66\,\text{GeV} < m_{\ell\ell} < 116\,\text{GeV}$.

blocks passing the GRL. This provides an integrated luminosity of $\mathcal{L}_{int} = 256.8\text{pb}^{-1}(1.5\%)$ at $\sqrt{s} = 5.02\,\text{TeV}$ and $\mathcal{L}_{int} = 335.1\text{pb}^{-1}(1.6\%)$ at $\sqrt{s} = 13\,\text{TeV}$.

The signal process, $Z/\gamma^* \to ee$ and $Z/\gamma^* \to \mu\mu$, was modelled using Powheg+Pythia8 AZNLO samples as described in Section 3.4.3. The $Z/\gamma^* \to \tau\tau$ background is modelled using the same simulation as the signal samples but with τ leptons in the final state, with modelling of both leptonic and hadronic decays. Top-quark pair-production $t\bar{t}$ as well as single-top production (Wt, t-channel, s-channel) are generated with Powheg+Pythia. Di-bosons production of $VV, V = W, Z$ are simulated with Sherpa for all decay channels with at least one real lepton in the final state. Photon induced di-lepton processes in the electron, muon and τ channels are simulated by Pythia.

All Monte Carlo samples are processed using the same analysis chain. Analysis histograms are filled using with the generator-level weights w provided by the simulation. Samples are

Process	Data set	Generator	$(\sigma_{\text{theory}}\cdot\text{BR}) \times \epsilon_{\text{filter}}$ [nb]	Uncertainty [%]
$Z/\gamma^* \to ee$ ($m_{ee} > 60$ GeV)	361106	Powheg+Pythia8	1.910×1.025	5%
$Z/\gamma^* \to \mu\mu$ ($m_{\mu\mu} > 60$ GeV)	361107	Powheg+Pythia8	1.910×1.025	5%
$Z/\gamma^* \to \tau\tau$ ($m_{\tau^+\tau^-} > 60$ GeV)	361108	Powheg+Pythia8	1.910×1.025	5%
$Z/\gamma^* \to ee$ (10 GeV $< m_{ee} <$ 60 GeV)	361665	Powheg+Pythia8	6.62×0.266	5%
$Z/\gamma^* \to \mu\mu$ (10 GeV $< m_{\mu\mu} <$ 60 GeV)	361667	Powheg+Pythia8	6.62×0.274	5%
$Z/\gamma^* \to \tau\tau$ (10 GeV $< m_{\tau\tau} <$ 60 GeV)	361669	Powheg+Pythia8	6.62×0.015	5%
$ZZ(q\bar{q}\ell\ell)$	363356	Sherpa 2.2.1	0.01556×0.141	10%
$WZ(q\bar{q}\ell\ell)$	363358	Sherpa 2.2.1	0.003433	10%
$WW(q\bar{q}\ell\nu)$	363359	Sherpa 2.2.1	0.02472	10%
$WW(\ell\nu q\bar{q})$	363360	Sherpa 2.2.1	0.02472	10%
$WZ(\ell\nu q\bar{q})$	363489	Sherpa 2.2.1	0.01142	10%
$ZZ(4\ell)$	364250	Sherpa 2.2.2	0.001252	10%
$WZ(3\ell\nu)$	364253	Sherpa 2.2.2	0.004583	10%
$WW(2\ell 2\nu)$	364254	Sherpa 2.2.2	0.01250	10%
$WZ(\ell 3\nu)$	364255	Sherpa 2.2.2	0.003235	10%
Wt	410013	Powheg+Pythia8	0.03582	10%
$W\bar{t}$	410014	Powheg+Pythia8	0.03399	10%
$t\bar{t}$ (nominal)	410470	Powheg+Pythia8	0.8318×0.544	7%
$\gamma\gamma \to ee$ (18 GeV $< m_{ee} <$ 60 GeV)	363672	Pythia8	0.01749×0.116	50%
$\gamma\gamma \to \mu\mu$ (18 GeV $< m_{\mu\mu} <$ 60 GeV)	363676	Pythia8	0.01748×0.265	50%
$\gamma\gamma \to \tau\tau$ (18 GeV $< m_{\tau\tau} <$ 60 GeV)	363680	Pythia8	0.01426×0.011	50%
$\gamma\gamma \to ee$ (60 GeV $< m_{ee} <$ 200 GeV)	363673	Pythia8	0.00179×0.314	50%
$\gamma\gamma \to \mu\mu$ (60 GeV $< m_{\mu\mu} <$ 200 GeV)	363677	Pythia8	0.00179×0.342	50%
$\gamma\gamma \to \tau\tau$ (60 GeV $< m_{\tau\tau} <$ 200 GeV)	363681	Pythia8	0.00163×0.032	50%
$\gamma\gamma \to ee$ (200 GeV $< m_{ee} <$ 600 GeV)	363674	Pythia8	0.0×0.00013	50%
$\gamma\gamma \to \mu\mu$ (200 GeV $< m_{\mu\mu} <$ 600 GeV)	363678	Pythia8	0.00014×0.382	50%
$\gamma\gamma \to \tau\tau$ (200 GeV $< m_{\tau\tau} <$ 600 GeV)	363682	Pythia8	0.00014×0.05	50%

Table 8.2: Monte Carlo samples at $\sqrt{s} = 13$TeV. Given is a short description of the process, the ATLAS MC sample number, the MC generator(s), the used value of the higher order cross section times the branching tratio and filter efficiencies $(\sigma_{\text{theory}}\cdot\text{BR}) \times \epsilon_{\text{filter}}$ (where the absence of the $\times$ symbol indicates $\epsilon_{\text{filter}} = 1$) and the uncertainty applied on the sample normalisation. The filter efficiency for $Z/\gamma^* \to \ell\ell$ ($m_{\ell\ell} > 60$ GeV) is greater than 1.0 as it also corrects for the fact that the theory cross-section used was calculated using 66 GeV $< m_{\ell\ell} <$ 116 GeV.

normalised to the data luminosity using the factor:

$$SF = \frac{\sigma_{\text{theory}} \times BR \times \epsilon_{\text{filter}} \times \mathcal{L}_{int}}{\sum_i^{N_{\text{events}}} w_i} \tag{8.1}$$

where $\sigma_{\text{theory}} \times BR$ is the theoretical cross-section of the process with the decay channel branching ratio factored in, ϵ_{filter} is the generator-level filter efficiency, $\mathcal{L}_{int}$ is the integrated luminosity corresponding to the data sample and w_i are the generator-level weights for each generated event. A summary of these factors for each sample used in this analysis is provided in Table 8.1 and Table 8.2.

8.3 Measurement Strategy

8.3.1 Fiducial Volume Definition

This measurement will report a three-dimensional differential cross-section of the neutral current Drell-Yan process with leptonic decays $Z \to \ell\ell$ where $\ell = e, \mu$. The the fiducial volume of the

measurement should be close to the experimental kinematic requirements. The "truth"-level lepton kinematics within the measurement volume are defined by:

- Lepton Transverse Momentum : $p_T^\ell > 15\,\text{GeV}$
- Lepton Rapidity : $|\eta^\ell| < 2.5$
- Invariant Mass : $40\,\text{GeV} < m_{\ell\ell} < 500\,\text{GeV}$

where the leptons here correspond to Born level QED kinematics. A slight preference was given to choosing $|\eta^\ell| < 2.5$ over $|\eta^\ell| < 2.4$ to avoid subtraction of events with selected electrons in the region $|\eta^e| > 2.4$, however it should be noted that this choice introduces a small extrapolation for the muon channel due to the requirement $|\eta^\mu| < 2.4$.

8.3.2 Binning Motivations

At leading order, Drell-Yan kinematics are simple and can be used to illustrate how fiducial selections on the final state leptons can introduce constraints on the allowed phase space. The formulae displayed here follow the definitions outlined in Ref. [148].

Some relevant expressions are:

$$p_1^+ p_2^- - p_1^- p_2^+ = p_{T,1}(\ell) p_{T,2}(\ell) \sinh(\Delta y_{\ell\ell}) \tag{8.2}$$

and

$$m_{\ell\ell}^2 + (p_T^{\ell\ell})^2 = (p_{T,1}(\ell))^2 + (p_{T,2}(\ell))^2 + p_{T,1}(\ell) p_{T,2}(\ell) \cosh(\Delta y_{\ell\ell}) \tag{8.3}$$

where $\Delta y_{\ell\ell}$ is the difference between the lepton rapidities $y_{\ell,1}$ and $y_{\ell,2}$. At leading order, the di-lepton system is produced back-to-back with $p_{T,1}(\ell) = p_{T,2}(\ell) = p_T(\ell)$ and hence zero di-lepton transverse momentum $(p_T^{\ell\ell})^2 = 0$. An expression for $\cos(\theta_{CS}^*)$ can hence be derived from Equation 3.11 as

$$\cos(\theta_{CS}^*) = \frac{\sinh(\Delta y_{\ell\ell})}{1 + \cosh(\Delta y_{\ell\ell})}, \tag{8.4}$$

which is symmetric with respect to the sign of $\Delta y_{\ell\ell}$.

Experimental measurements usually require a fiducial selection to account for experimental geometry, often requiring a maximum lepton rapidity. With a maximum allowed rapidity of $|y_\ell^{\text{max}}|$, and noting that the di-lepton rapidity is the average of the single-lepton rapidities

$$y_{\ell\ell} = \frac{y_\ell^1 + y_\ell^2}{2}, \tag{8.5}$$

the greatest value of $\Delta y_{\ell\ell}$ permitted is $2(y_\ell^{\text{max}} - |y_{\ell\ell}|)$, leading to the constraint,

$$\cos(\theta_{CS}^*) \leq \frac{\sinh\left(2(y_\ell^{\text{max}} - |y_{\ell\ell}|)\right)}{1 + \cosh\left(2(y_\ell^{\text{max}} - |y_{\ell\ell}|)\right)}. \tag{8.6}$$

This defines an allowed boundary in $|y_{\ell\ell}|, \cos(\theta_{CS}^*)$ space at leading order.

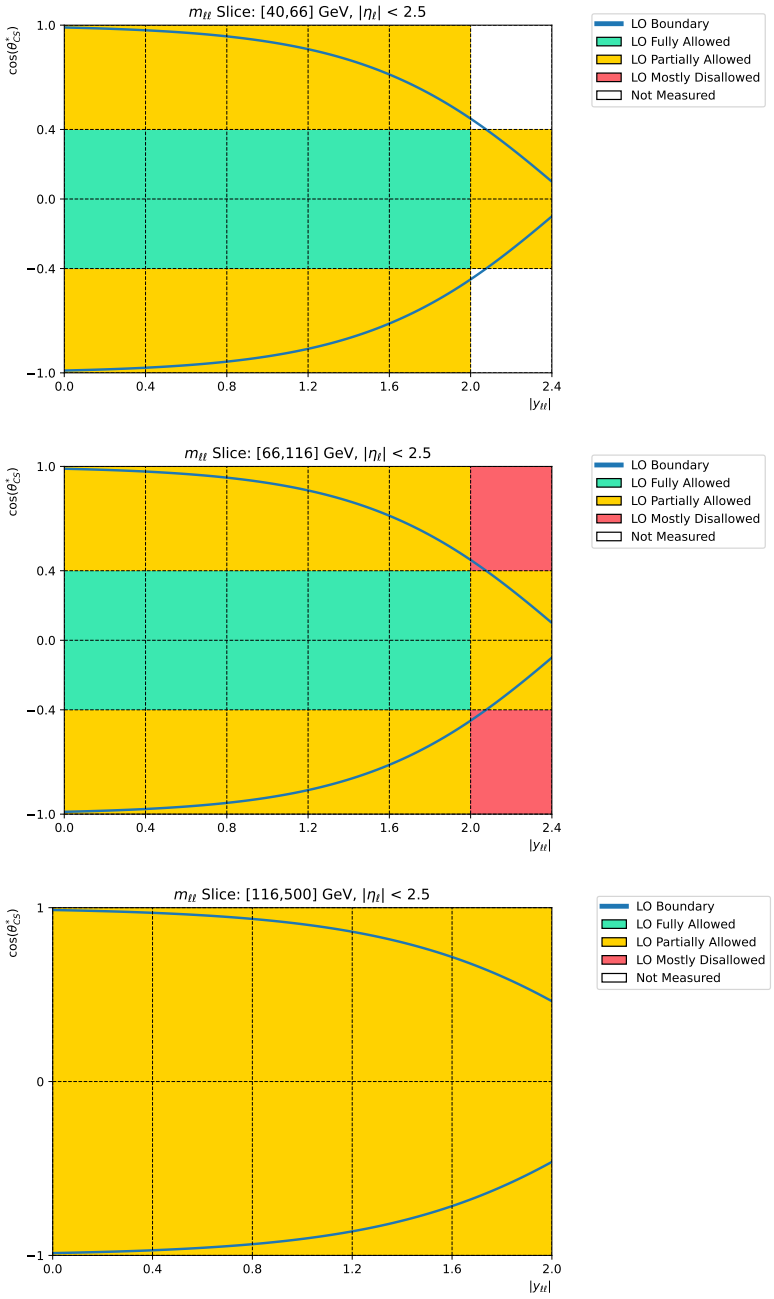

Figure 8.1: The overlay of the LO forbidden region when analysing with a 3D binning in $m_{\ell\ell}$, $y_{\ell\ell}$ and $\cos(\theta^*_{CS})$. The binning shown is the binning used in the cross-section analysis detailed in Section 8.

Beyond leading-order, the assumptions that $p_T^{\ell\ell} = 0$ and that the lab-frame leptons are back-to-back no longer hold. The effect of higher-order corrections is largely to smooth above the boundary so it becomes a gradual transition [148]. Proper understanding of this requires accurate modelling of $p_T^{\ell\ell}$ which also introduces dependence on both $m_{\ell\ell}$ and $\sqrt{s}$.

8.3.3 Analysis Bins

The differential binning for this measurement is defined in di-lepton mass $m_{\ell\ell}$, absolute di-lepton rapidity $|y_{\ell\ell}|$ and $\cos(\theta^*_{CS})$. The bin edges are decided taking account of the theoretical

motivations for slicing in $\cos(\theta^*_{CS})$, but with the additional constraint that each bin contains enough events at the reconstructed level to ensure statistical uncertainties are in the Gaussian limit. The same binning scheme is used at both $\sqrt{s} = 5.02\,\text{TeV}$ and $\sqrt{s} = 13\,\text{TeV}$ and is defined by:

- $m_{\ell\ell}$ binning:
  - low-mass bin $m_{\ell\ell} \in [40\,\text{GeV}, 66\,\text{GeV}]$
  - central-mass bin $m_{\ell\ell} \in [66\,\text{GeV}, 116\,\text{GeV}]$
  - high-mass bin $m_{\ell\ell} \in [116\,\text{GeV}, 500\,\text{GeV}]$
- $\cos(\theta^*_{CS})$ binning:
  - low-mass: 4 bins $\cos(\theta^*_{CS}) \in [-1.0, -0.4],\ [-0.4, 0.0],\ [0.0, 0.4],\ [0.4, 1.0]$.
  - central-mass: 4 bins $\cos(\theta^*_{CS}) \in [-1.0, -0.4],\ [-0.4, 0.0],\ [0.0, 0.4],\ [0.4, 1.0]$.
  - high-mass: 2 bins $\cos(\theta^*_{CS}) \in [-1.0, 0.0],\ [0.0, 1.0]$.
- $|y_{\ell\ell}|$ binning (all bins are of width $\Delta|y_{\ell\ell}| = 0.4$):
  - central-mass: 6 bins $|y_{\ell\ell}| \in [0.0, 2.4]$.
  - low-mass & 6 bins $|\cos(\theta^*_{CS})| < 0.4 : |y_{\ell\ell}| \in [0.0, 2.4]$.
  - low-mass & 5 bins $|\cos(\theta^*_{CS})| > 0.4 : |y_{\ell\ell}| \in [0.0, 2.0]$.
  - high-mass : 5 bins $|y_{\ell\ell}| \in [0.0, 2.0]$.

Figure 8.1 categorises each bin as "fully allowed", "partially allowed", or "mostly disallowed" with LO kinematics. Also highlighted is the boundary defined by Equation 8.6. This shows that a good separation of bins "fully allowed" and "partially allowed" has been made for the low-mass and central-mass slices. The high-mass slice could not be split in $\cos(\theta^*_{CS})$ due to the small selected sample size, so no "fully allowed" bins have been isolated. The central-mass bin also measures two extreme bins with a negligible fraction within the LO boundary. These bins are assigned the "mostly disallowed" category.

8.3.4 Unravelled Binning Scheme

An unravelled binning scheme was defined to track bin boundaries and correlations between bins easily. The unravelled binning scheme concatenates the $|y_{\ell\ell}|$ distribution from each $m_{\ell\ell}$–$\cos(\theta^*_{CS})$ slice into a single 1D distribution. The mapping of each 3D bin to the 1D unravelled binning scheme is shown in Table 8.3. The final results for this analysis will be reported in their respective slices, but the intermediate plots will use histograms defined with the unravelled binning scheme to reduce the number of required plots.

Unfolding measurements allow the possibility of using separate binning schemes for both the truth-level and reconstructed-level distributions, with the only requirement being that the

Bin No.	$m_{\ell\ell}$ [GeV]	$cos(\theta^*_{CS})$	$\lvert y_{\ell\ell}\rvert$	Bin No.	$m_{\ell\ell}$ [GeV]	$cos(\theta^*_{CS})$	$\lvert y_{\ell\ell}\rvert$	Bin No.	$m_{\ell\ell}$ [GeV]	$cos(\theta^*_{CS})$	$\lvert y_{\ell\ell}\rvert$
1	[40, 66]	[−1.0, −0.4]	[0.0, 0.4]	23	[66, 116]	[−1.0, −0.4]	[0.0, 0.4]	47	[116, 500]	[−1.0, 0.0]	[0.0, 0.4]
2	[40, 66]	[−1.0, −0.4]	[0.4, 0.8]	24	[66, 116]	[−1.0, −0.4]	[0.4, 0.8]	48	[116, 500]	[−1.0, 0.0]	[0.4, 0.8]
3	[40, 66]	[−1.0, −0.4]	[0.8, 1.2]	25	[66, 116]	[−1.0, −0.4]	[0.8, 1.2]	49	[116, 500]	[−1.0, 0.0]	[0.8, 1.2]
4	[40, 66]	[−1.0, −0.4]	[1.2, 1.6]	26	[66, 116]	[−1.0, −0.4]	[1.2, 1.6]	50	[116, 500]	[−1.0, 0.0]	[1.2, 1.6]
5	[40, 66]	[−1.0, −0.4]	[1.6, 2.0]	27	[66, 116]	[−1.0, −0.4]	[1.6, 2.0]	51	[116, 500]	[−1.0, 0.0]	[1.6, 2.0]
6	[40, 66]	[−0.4, 0.0]	[0.0, 0.4]	28	[66, 116]	[−1.0, −0.4]	[2.0, 2.4]	52	[116, 500]	[0.0, 1.0]	[0.0, 0.4]
7	[40, 66]	[−0.4, 0.0]	[0.4, 0.8]	29	[66, 116]	[−0.4, 0.0]	[0.0, 0.4]	53	[116, 500]	[0.0, 1.0]	[0.4, 0.8]
8	[40, 66]	[−0.4, 0.0]	[0.8, 1.2]	30	[66, 116]	[−0.4, 0.0]	[0.4, 0.8]	54	[116, 500]	[0.0, 1.0]	[0.8, 1.2]
9	[40, 66]	[−0.4, 0.0]	[1.2, 1.6]	31	[66, 116]	[−0.4, 0.0]	[0.8, 1.2]	55	[116, 500]	[0.0, 1.0]	[1.2, 1.6]
10	[40, 66]	[−0.4, 0.0]	[1.6, 2.0]	32	[66, 116]	[−0.4, 0.0]	[1.2, 1.6]	56	[116, 500]	[0.0, 1.0]	[1.6, 2.0]
11	[40, 66]	[−0.4, 0.0]	[2.0, 2.4]	33	[66, 116]	[−0.4, 0.0]	[1.6, 2.0]				
12	[40, 66]	[0.0, 0.4]	[0.0, 0.4]	34	[66, 116]	[−0.4, 0.0]	[2.0, 2.4]				
13	[40, 66]	[0.0, 0.4]	[0.4, 0.8]	35	[66, 116]	[0.0, 0.4]	[0.0, 0.4]				
14	[40, 66]	[0.0, 0.4]	[0.8, 1.2]	36	[66, 116]	[0.0, 0.4]	[0.4, 0.8]				
15	[40, 66]	[0.0, 0.4]	[1.2, 1.6]	37	[66, 116]	[0.0, 0.4]	[0.8, 1.2]				
16	[40, 66]	[0.0, 0.4]	[1.6, 2.0]	38	[66, 116]	[0.0, 0.4]	[1.2, 1.6]				
17	[40, 66]	[0.0, 0.4]	[2.0, 2.4]	39	[66, 116]	[0.0, 0.4]	[1.6, 2.0]				
18	[40, 66]	[0.4, 1.0]	[0.0, 0.4]	40	[66, 116]	[0.0, 0.4]	[2.0, 2.4]				
19	[40, 66]	[0.4, 1.0]	[0.4, 0.8]	41	[66, 116]	[0.4, 1.0]	[0.0, 0.4]				
20	[40, 66]	[0.4, 1.0]	[0.8, 1.2]	42	[66, 116]	[0.4, 1.0]	[0.4, 0.8]				
21	[40, 66]	[0.4, 1.0]	[1.2, 1.6]	43	[66, 116]	[0.4, 1.0]	[0.8, 1.2]				
22	[40, 66]	[0.4, 1.0]	[1.6, 2.0]	44	[66, 116]	[0.4, 1.0]	[1.2, 1.6]				
				45	[66, 116]	[0.4, 1.0]	[1.6, 2.0]				
				46	[66, 116]	[0.4, 1.0]	[2.0, 2.4]				

Table 8.3: The unfolding binning scheme used in this analysis. This table shows the 56 analysis bins and the relationship to the unfolding binning scheme.

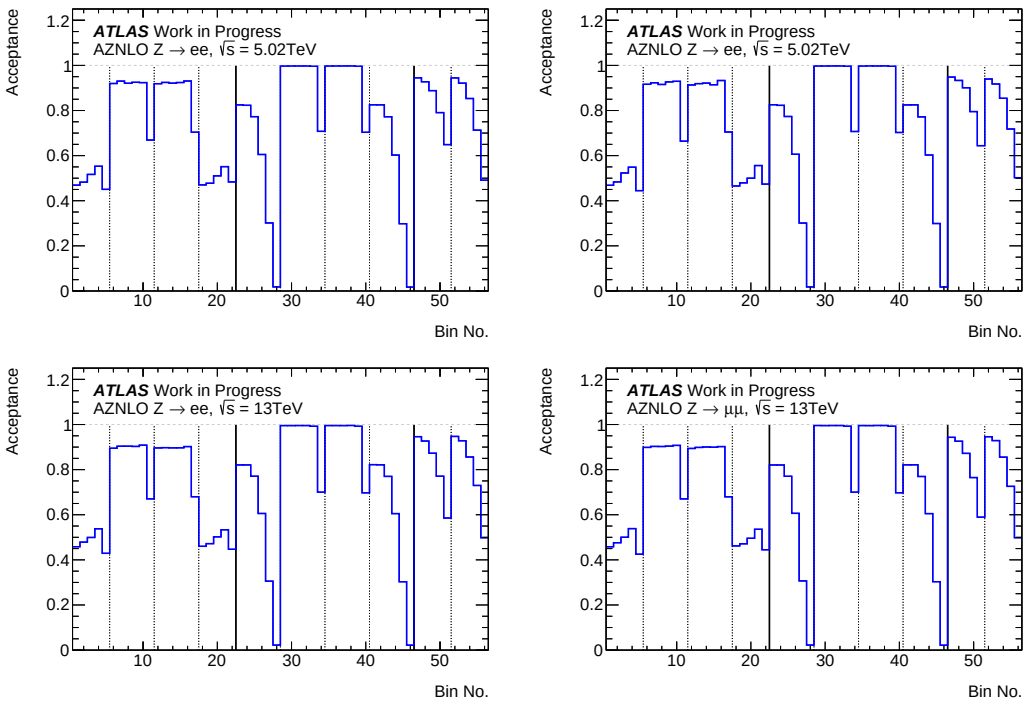

Figure 8.2: The fiducial acceptance given by with the ATLAS Powheg+Pythia8 signal sample for the unravelled binning scheme.

reconstructed-level binning does not use fewer bins than the truth-level binning. The same unravelled binning scheme is used for both reconstructed-level and truth-level for this analysis.

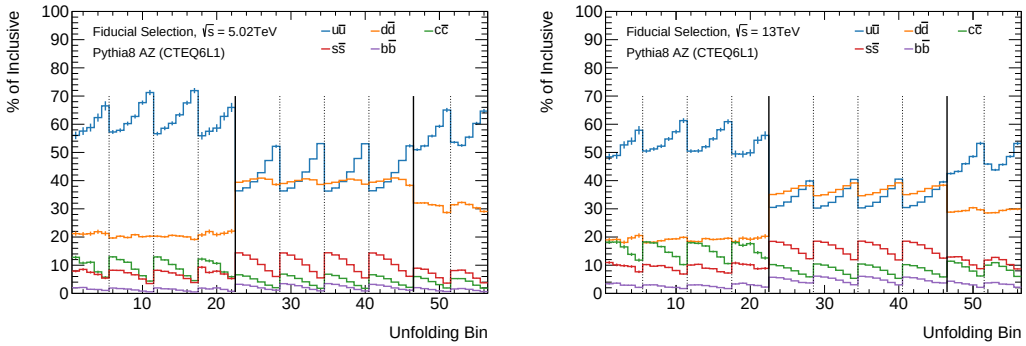

Figure 8.3: The $\sqrt{s} = 5.02\,\text{TeV}$ and $\sqrt{s} = 13\,\text{TeV}$ relative contribution of each quark-quark initial state in each unfolding bin. These results are obtained at born-level and are simulated using Pythia8 with the AZ tune (CTEQ6L1). Uncertainties reflect the statistical uncertainty on the generated sample.

8.3.5 Binning Features

For comparison with theoretical predictions, it is beneficial for measured bins to have high fiducial acceptance as low fiducial acceptance bins have increased dependency on the modelling of η^{ℓ} and $p_T(\ell)$. The differential binning in $\cos(\theta^*_{CS})$ allows isolation of high-acceptance bins dominated by events with high $p_T(\ell)$ and low $|y_{\ell\ell}|$, which are far from the fiducial volume boundaries. The acceptance is quantified using:

$$A_i = \frac{N^{\text{true,fiducial,MC}}_{Z/\gamma^* \to \ell\ell, i}}{N^{\text{true,nocut,MC}}_{Z/\gamma^* \to \ell\ell, i}} \tag{8.7}$$

where $N^{\text{true,nocut,MC}}_{Z/\gamma^* \to \ell\ell, i}$ is the number of true events within the kinematic boundaries of bin i, and $N^{\text{true,fiducial,MC}}_{Z/\gamma^* \to \ell\ell, i}$ is the number of true events that additionally pass the fiducial selections on $p_T(\ell)$ and low $|y_{\ell\ell}|$. Figure 8.2 shows the fiducial acceptance modelled using Powheg+Pythia8 for $Z/\gamma^* \to ee$ and $Z/\gamma^* \to \mu\mu$ production at both $\sqrt{s} = 5.02\,\text{TeV}$ and $\sqrt{s} = 13\,\text{TeV}$ using Born-level kinematics. These plots show that bins with $|\cos(\theta^*_{CS})| < 0.4$ have acceptance close to 100% while bins with $|\cos(\theta^*_{CS})| > 0.4$ have lower acceptance. The low-mass slice yields slightly lower acceptances than the central-mass slice due to events having lower $p_T(\ell)$. These are less frequently selected due the $p_T(\ell) > 15\,\text{GeV}$ requirement. The high-mass slice does not have binning in $|\cos(\theta^*_{CS})| < 0.4$ and therefore does not benefit from the separation of low-acceptance and high-acceptance regions.

The differential binning in $m_{\ell\ell}$ and $|y_{\ell\ell}|$ also provides sensitivity to events produced by different initial state $q\bar{q}$ pairs which allows the data to be used in future PDF fits. This is demonstrated in Figure 8.3 where the Pythia8 AZ tune (PDF set CTEQ6L1) has been used to show the relative contribution of each initial state to the total inclusive cross-section. These plots show that the fraction of events in the central-mass bins have greater contributions from $d\bar{d}$ initial states than the low-mass and high-mass slices, the fraction of $s\bar{s}$ and $c\bar{c}$ initial states is in the range 10-20% at $\sqrt{s} = 13\,\text{TeV}$, with stronger $s\bar{s}$ production in the central-mass bins and stronger $c\bar{c}$ production in the low-mass bins. Trends of 10-15% in the relative fractions can be observed as a function of $|y_{\ell\ell}|$ in most $m_{\ell\ell}$ and $\cos(\theta^*_{CS})$ slices.

Selection criteria	$Z \to ee$ channel	$Z \to \mu\mu$ channel
Track-vertex association	$\lvert z_0 \sin(\theta)\rvert < 0.5$ mm	$\lvert z_0 \sin(\theta)\rvert < 0.5$ mm
	$\lvert d_0\rvert/\sigma(d_0) < 5$	$\lvert d_0\rvert/\sigma(d_0) < 3$
Identification	Pass MediumLH	Pass Medium
Isolation	`ptvarcone20/pt` < 0.1	`ptvarcone20/pt` < 0.1
Transverse momentum	$p_{\mathrm{T}}^{e} > 15$ GeV	$p_{\mathrm{T}}^{\mu} > 15$ GeV
Pseudorapidity	$0 < \lvert\eta^{e}\rvert < 1.37$ or $1.52 < \lvert\eta^{e}\rvert < 2.47$	$0 < \lvert\eta^{\mu}\rvert < 2.4$
No. of leptons	$N_e = 2$	$N_\mu = 2$
1 or 2 triggered leptons	`HLT_e15_lhloose_nod0_L1EM12`	`HLT_mu14`
Opposite sign charge	$1e^+$,$1e^-$	$1\mu^+$,$1\mu^-$
Invariant mass	40 GeV $< m_{e^+e^-} <$ 500 GeV	40 GeV $< m_{\mu^+\mu^-} <$ 500 GeV

Table 8.4: Overview of lepton object requirements and the dilepton selections used in this analysis for both electron and muon channels.

8.4 Analysis Selection

In this analysis, the $Z \to ee$ and $Z \to \mu\mu$ channels are studied, requiring a definition of electron and muon objects and a di-lepton selection to minimise background contamination. This section describes these object selection criteria, summarised in Table 8.4.

Electrons and muons are selected with $p_T(e) > 15$ GeV and $p_T(\mu) > 15$ GeV respectively to utilise the lower $p_T(\ell)$ thresholds of the low-μ triggers. Electrons are selected with $|\eta^e| < 2.47$ excluding candidates in the detector crack region of $1.37 < |\eta^e| < 1.52$ and muons are selected with $|\eta^\mu| < 2.4$. Electrons and muons are selected with the MediumLH and Medium identification working points, respectively, and are both required to pass the isolation criteria of `ptvarcone20/pt` < 0.1. For electrons, the requirements on impact parameters are $|z_0 \sin(\theta)| < 0.5$ mm and $|d_0|/\sigma(d_0) < 5$ and for muons the requirements are $|z_0 \sin(\theta)| < 0.5$ mm and $|d_0|/\sigma(d_0) < 3$. Before selection, both electrons and muons undergo the calibrations described in Section 6 which apply to both data and MC.

Selection of $Z \to \ell\ell$ events required exactly two opposite-sign electron candidates for $Z \to e^+e^-$ and exactly two opposite-sign muon candidates for $Z \to \mu^+\mu^-$. At least one of the selected electrons (muons) is required to have passed the corresponding trigger, `HLT_e15_lhloose_nod0_L1EM12` and `HLT_mu14`. The invariant mass of the di-lepton system is required to be $m_{\ell^+\ell^-} > 40$ GeV to avoid the large acceptance losses that occur as the invariant mass approaches $m_{\ell^+\ell^-} \approx 2 \times p_T(\ell)$. The upper limit on invariant mass was $m_{\ell^+\ell^-} < 500$ GeV above which there are few events. Events selected in the MC are weighted by the corresponding di-lepton scale factors described in Section 6.3.

Figure 8.4 and Figure 8.5 shows control plots for the selected events at reconstructed level binned in $m_{\ell\ell}$ and in the unravelled binning scheme, respectively. Appendix C.2 shows control plots for the electron and muon kinematics (transverse momentum $p_T(\ell)$, pseudorapidity η^ℓ, azimuthal angle ϕ_ℓ) and di-lepton distributions (di-lepton rapidity $y_{\ell\ell}$ and di-lepton $\cos(\theta^*_{CS})$). With the exception of the invariant mass plot, these plots are separated into events with low-mass, central-mass and high-mass slices. The sum of expected signal and all background contributions

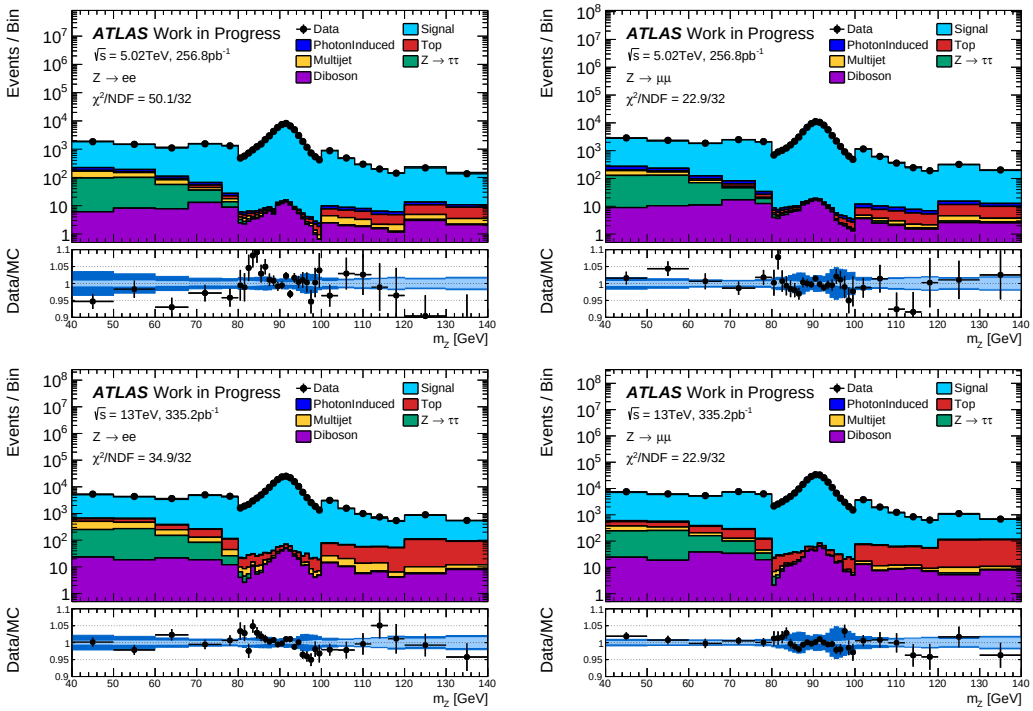

Figure 8.4: Control plots showing the agreement between data (black points) and MC (that has been normalised by integral to the data) for the di-lepton invariant mass for $Z \to ee$ and $Z \to \mu\mu$ selections at both $\sqrt{s} = 5.02\,\text{TeV}$ and $\sqrt{s} = 13\,\text{TeV}$. The χ^2/NDF shown in each plot is calculated between the data and normalised MC using statistical and systematic uncertainties where the χ^2 and NDF terms have been kept separate.

has been normalised to the data, so these plots are meant to provide a shape comparison and at this stage are insensitive to any global normalisation differences. Each distribution has a χ^2/NDF estimated between the normalised MC and data, including statistical uncertainties and the bin to bin correlations from experimental systematic uncertainties (excluding luminosity). These are not required to be in good agreement as there is an absence of modelling uncertainties on the Powheg+Pythia8 AZNLO prediction. Nonetheless, the agreement between data and MC is satisfactory with most $\sqrt{s} = 5.02\,\text{TeV}$ distributions having χ^2/NDF close to unity and $\sqrt{s} = 13\,\text{TeV}$ displaying a few distributions with χ^2/NDF slightly larger than unity.

8.5 Data-Driven Multijet Background Estimate

Multijet background contributions originate from events where one or both leptons originate from the semileptonic decay of heavy-flavour hadrons. This process cannot be estimated with Monte Carlo, and hence a data-driven method is used to obtain both the shape and normalisation of this background. This section describes the derivation of a multijet enriched selection to be used as a shape template and the derivation of normalisation factors required to scale the template yield to match the the signal selection.

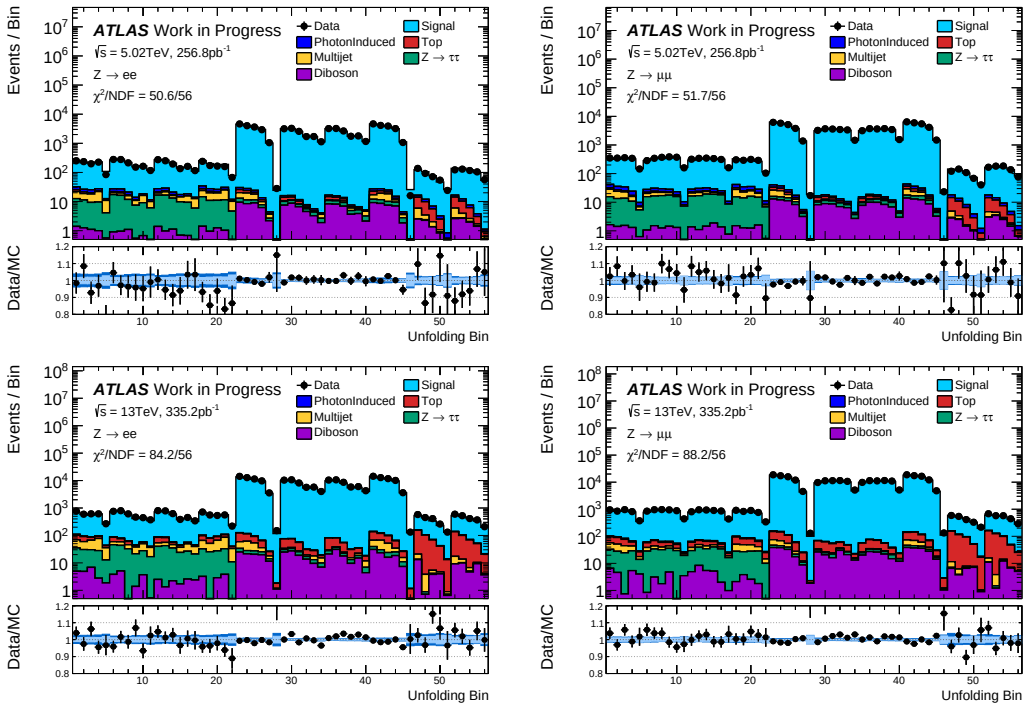

Figure 8.5: Control plots showing the agreement between data (black points) and MC (that has been normalised by integral to the data) for the unravelled binning scheme for $Z \to ee$ and $Z \to \mu\mu$ selections at both $\sqrt{s} = 5.02\,\text{TeV}$ and $\sqrt{s} = 13\,\text{TeV}$. The χ^2/NDF shown in each plot is calculated between the data and normalised MC using statistical and systematic uncertainties where the χ^2 and NDF terms have been kept separate.

Selection criteria	$Z \to ee$ **channel**	$Z \to \mu\mu$ **channel**
Track-vertex association	$\lvert z_0 \sin\theta\rvert < 0.5$ mm	$\lvert z_0 \sin\theta\rvert < 0.5$ mm
	$\lvert d_0\rvert/\sigma(d_0) < 5$	No $\lvert d_0\rvert/\sigma(d_0)$ Requirement
Identification	Pass Loose, Fail MediumLH	Pass Medium
Isolation	`ptvarcone20/pt` < 1.0	`ptvarcone20/pt` < 1.0
Transverse momentum	$p_{\text{T}}^{e} > 15\,\text{GeV}$	$p_{\text{T}}^{\mu} > 15\,\text{GeV}$
Pseudorapidity	$0 < \lvert\eta^{e}\rvert < 1.37$ or $1.52 < \lvert\eta^{e}\rvert < 2.47$	$0 < \lvert\eta^{\mu}\rvert < 2.4$
No. of leptons	$N_e = 2$	$N_\mu = 2$
1 or 2 triggered leptons	`HLT_e15_lhloose_nod0_L1EM12`	`HLT_mu14`
Same sign charge	$1e^+$,$1e^+$ or $1e^-$,$1e^-$	$1\mu^+$,$1\mu^+$ or $1\mu^-$,$1\mu^-$
Invariant mass	$40 < m_{e^+e^-} < 500\,\text{GeV}$	$40 < m_{\mu^+\mu^-} < 500\,\text{GeV}$

Table 8.5: Overview of the selection criteria used to obtain multijet enriched template distributions in the ee and $\mu\mu$ channels.

8.5.1 Template Selection

The purpose of the template selection is to obtain a sample enriched with multijet events containing little contribution from signal or other electroweak processes with two isolated leptons. The template selection criteria are described in Table 8.5. As the nominal selection is constructed to select signal events, the template selection should contain no events that are shared with the signal selection. Furthermore, the templates are required to have identical kinematic and trigger requirements to the nominal selection. The orthogonality of the templates

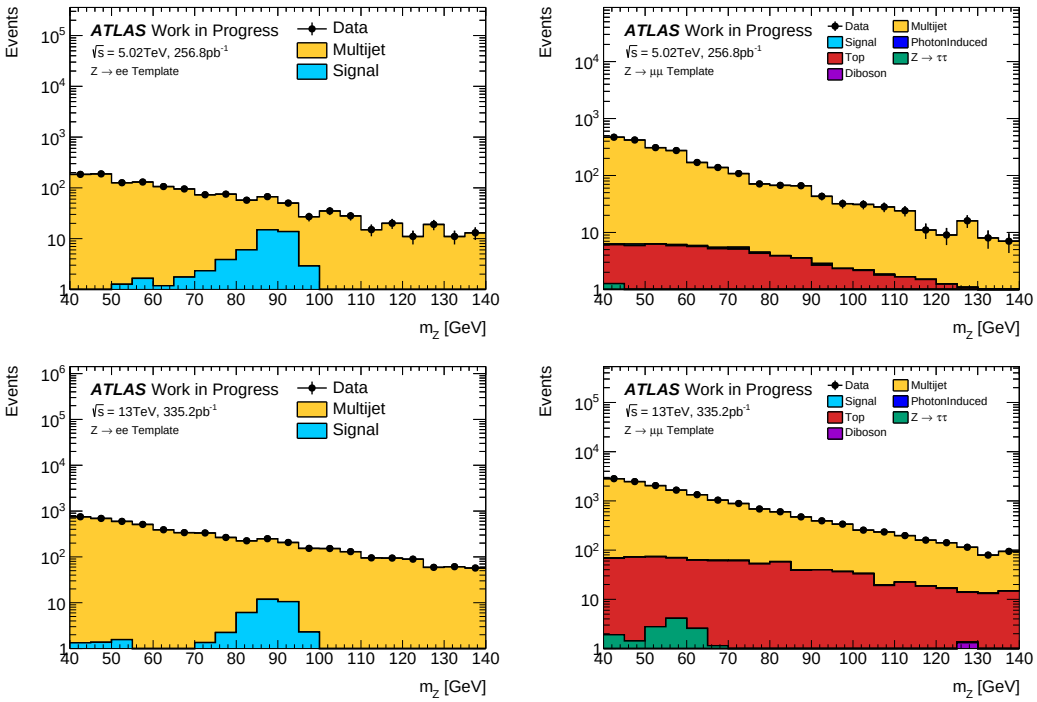

Figure 8.6: Invariant mass distributions for each channel at both $\sqrt{s} = 5.02\,\text{TeV}$ and $\sqrt{s} = 13\,\text{TeV}$ for events selected with the template selection (Table 8.5). The multijet template is derived from the data with small MC contributions subtracted.

arise from the requirement of same-sign di-lepton pairs for both channels as well as further differences in lepton quality criteria. These details are clarified below:

- $Z \to ee$ Template Selection
  - Same-sign electrons: Discrimination from signal events.
  - Pass Loose ID, Fail MediumLH ID: Discrimination of signal events and improved selection of fake electron events.
  - `ptvarcone20/pt` < 1.0: Improved selection of fake electron events while removing events that have vastly different isolations to the nominal selection.
- $Z \to \mu\mu$ Template Selection
  - Same-sign muons: Discrimination from signal events.
  - `ptvarcone20/pt` < 1.0: Improved selection of fake muon events while removing events that have vastly different isolations to the nominal selection.
  - No $|d_0|/\sigma(d_0)$ Requirement: Relaxing this cut from the nominal $|d_0|/\sigma(d_0) < 3$ yields an increase of template statistics by a factor of about $\times 4$ while retaining consistent template shape.

These selections are constructed to minimise signal and electroweak contributions; however, the contributions will still exist and should be subtracted to obtain pure templates. This small contamination is evaluated using Monte Carlo simulation scaled to the luminosity by,

$$N_{\text{template}} = N_{\text{Data}} - N_{\text{MC,EW}} - N_{\text{MC,Signal}} \tag{8.8}$$

Figure 8.6 shows the invariant mass distributions for the template selections. The resulting templates show no peak around the Z mass resonance of about 90.2 GeV, indicating the contamination is negligible or correctly accounted for, and instead display a smooth shape with an increasing background at low mass. The $Z \to \mu\mu$ channel has both electroweak and signal contributions and $N_{\text{MC,EW}}$ contributions are observed to be negligible compared to N_{Data} in the low-mass region, where the multijet contribution is expected to be largest. For technical reasons the $N_{\text{MC,EW}}$ term for the $Z \to ee$ template was neglected, however this is expected to have minimal impact.

Note on Same Sign $\cos(\theta^*_{CS})$ The definition of $\cos(\theta^*_{CS})$ requires the separation of the negative and positive leptons, but by selecting same-sign events, this is no longer possible. So instead, an assumption is made that opposite sign multijet events will be symmetric in charge and thus share the same shape as the same sign selection. This technicality is resolved using a random number generator and assigning the highest p^{ℓ}_{T} to be the negative lepton with a 50% probability.

8.5.2 Template Normalisation

As the templates are constructed with different selection requirements, it is expected that further normalisation is required to provide a multijet estimate for the nominal selection. This was accomplished in two steps with an identical methodology for both $Z \to ee$ and $Z \to \mu\mu$. To avoid large statistical fluctuations, these factors could not be derived independently in each analysis bin. The factors were derived by grouping bins in slices of $m_{\ell\ell}$ and $\cos(\theta^*_{CS})$ to ensure similar kinematics events share the same normalisation factors. The four groupings used are:

- $m_{\ell\ell} = [40\,\text{GeV}, 66\,\text{GeV}] + |\cos(\theta^*_{CS})| < 0.4$
- $m_{\ell\ell} = [40\,\text{GeV}, 66\,\text{GeV}] + |\cos(\theta^*_{CS})| > 0.4$
- $m_{\ell\ell} = [66\,\text{GeV}, 116\,\text{GeV}]$
- $m_{\ell\ell} = [116\,\text{GeV}, 500\,\text{GeV}]$

A set of normalisation factors is then derived for each group, at each energy, for each channel, resulting in 12 sets of normalisation factors. The procedure will be demonstrated only for $\sqrt{s} = 13\,\text{TeV}$ in the $m_{\ell\ell} = [40\,\text{GeV}, 66\,\text{GeV}] + |\cos(\theta^*_{CS})| < 0.4$ slice, as this is where the multijet contribution is the largest fractional contribution compared to data. Figures for the remaining slices can be found in Appendix C.3.

Three separate selections are used for the derivation of the multijet background, defined as,

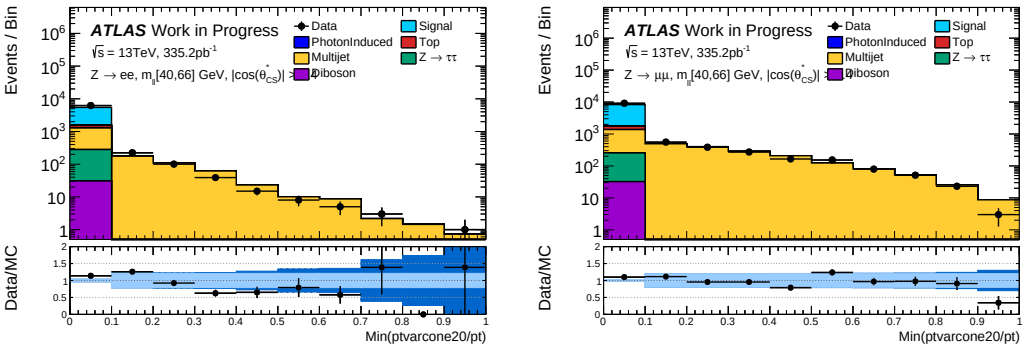

Figure 8.7: The `Min(ptvarcone20/pt)` distribution at $\sqrt{s} = 13\,\text{TeV}$ for the $Z \to ee$ and $Z \to \mu\mu$ selections in the $m_{\ell\ell} = [40\,\text{GeV}, 66\,\text{GeV}] + |\cos(\theta^*_{CS})| < 0.4$ slice. The selected events are in the `NominalLooseIsolation` selection and the multijet template has been normalised by just the $S_{control}$ factor to the region `Min(ptvarcone20/pt)` > 0.1. The ratio panel is the absolute ratio of data and MC where the light band reflects the systematic uncertainty on the multijet estimate and the darker band includes the template statistics.

- `Nominal` : The nominal selection used in the analysis described in 8.4.
- `Template` : The selections described in 8.5.1
- `NominalLooseIsolation` : The nominal selection used in this analysis but with the isolation requirement loosened to `ptvarcone20/pt` < 1.0 to match the template selection.

Step1: Normalising the Template in the Nominal Selection with Loosened Isolation The first normalisation factor $S_{control}$ is defined to correct for the differences in the selected objects between the `Nominal` selection and `Template` selection. To derive this factor, the nominal selection was re-ran with the same loosened isolation criteria of `ptvarcone20/pt` < 1.0 as the template, the `NominalLooseIsolation` selection. A control region is then defined by `Min(ptvarcone20/pt)` > 0.1, where `Min(ptvarcone20/pt)` is the minimum `ptvarcone20/pt` for both leptons. This control region contains no events from the nominal selection and strongly discriminates between selected events and the modelled Monte Carlo. The $S_{control}$ factor is then defined by taking the ratio of yields in the control region between the `NominalLooseIsolation` and `Template` selections:

$$S_{control} = \frac{N_{\texttt{NominalLooseIsolation,Min(ptvarcone20/pt)>0.1}}}{N_{\texttt{Template,Min(ptvarcone20/pt)>0.1}}} \tag{8.9}$$

The `Min(ptvarcone20/pt)` distributions for the example $\sqrt{s} = 13\,\text{TeV}$ selections are shown in Figure 8.7 where the templates have been normalised by the $S_{control}$ factors.

Step 2: Estimating the Isolation Efficiency of the Multijet Sample The second scale factor $S_{isolation}$ corrects the multijet estimate to that expected with the nominal isolation requirement of `ptvarcone20/pt` < 0.1. This is obtained using the `Max(ptvarcone20/pt)` variable, the maximum of `ptvarcone20/pt` for both leptons. All events in the nominal selection satisfy

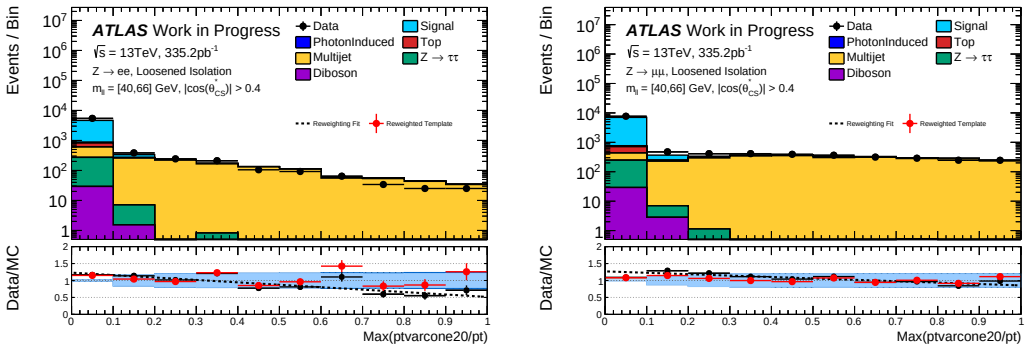

Figure 8.8: The `Max(ptvarcone20/pt)` distribution at $\sqrt{s} = 13\,\text{TeV}$ for the $Z \to ee$ and $Z \to \mu\mu$ selections in the $m_{\ell\ell} = [40\,\text{GeV}, 66\,\text{GeV}] + |\cos(\theta^*_{CS})| < 0.4$ slice. The selected events satisfy the `NominalLooseIsolation` selection and the multijet template has been normalised by just the $S_{control}$ factor to the region `Min(ptvarcone20/pt)` > 0.1. The ratio panel shows the absolute ratio of data and MC with the nominal template selection, the 1st order polynomial fit to the ratio, and the absolute ratio of data and MC with the reweighted template selection. The light band reflects systematic uncertainty on the multijet estimate and the darker band includes the template statistics.

`Max(ptvarcone20/pt)` < 0.1 and events with `Max(ptvarcone20/pt)` > 0.1 fail the nominal isolation requirement. $S_{isolation}$ is defined via:

$$S_{isolation} = \frac{N_{\texttt{Template,Max(ptvarcone20/pt)<0.1}}}{N_{\texttt{Template,Max(ptvarcone20/pt)<1.0}}} \tag{8.10}$$

Comparing data and Monte Carlo in the `NominalLooseIsolation` selection for the `Max(ptvarcone20/pt)` distribution reveals some tension in shape, which would affect the evaluation of $S_{isolation}$. To account for this a reweighting procedure was derived by fitting a straight line (constant term p_0 and gradient term p_1) to the Data/MC ratio for `Max(ptvarcone20/pt)` > 0.2 where the contribution is dominated by multijet events. After obtaining the best fit, the distribution is then reweighted bin-by-bin by the inverse of the fitted polynomial via:

$$N_{\texttt{Reweighted Template,Max(ptvarcone20/pt)}} = \frac{1}{p_0 + p_1(\text{bincentre})} \times N_{\texttt{Template,Max(ptvarcone20/pt)}}. \tag{8.11}$$

An alternative $S_{isolation}$ factor ($S_{isolation,rw}$), is then derived using the reweighted `Max(ptvarcone20/pt)` defined by:

$$S_{isolation,rw} = \frac{N_{\texttt{Reweighted Template,Max(ptvarcone20/pt)<0.1}}}{N_{\texttt{Reweighted Template,Max(ptvarcone20/pt)<1.0}}}. \tag{8.12}$$

The `Max(ptvarcone20/pt)` distributions for the example $\sqrt{s} = 13\,\text{TeV}$ selections are shown in Figure 8.8 where the template has been normalised by the $S_{control}$ factor to the region `Min(ptvarcone20/pt)` > 0.1. These plots show the agreement between the normalised template and data before and after the reweighting procedure. The corresponding 1st order polynomial fits are also shown.

Energy $\sqrt{s}$	Channel	Slice	$S_{control}$	$S_{isolation}$	p_0	p_1	$S_{isolation,rw}$	S_{total}	% Unc.
5.02 TeV	$Z \to ee$	40 GeV $< m_{\ell\ell} <$ 66 GeV & $\lvert\cos(\theta^*_{CS})\rvert < 0.4$	0.65 ± 0.13	0.332 ± 0.016	0.67 ± 0.35	-1.27 ± 0.96	0.59 ± 0.22	0.38 ± 0.13	(34.2)%
5.02 TeV	$Z \to ee$	40 GeV $< m_{\ell\ell} <$ 66 GeV & $\lvert\cos(\theta^*_{CS})\rvert > 0.4$	0.659 ± 0.099	0.2670 ± 0.0096	0.62 ± 0.19	-1.17 ± 0.46	0.533 ± 0.074	0.35 ± 0.10	(28.6)%
5.02 TeV	$Z \to ee$	66 GeV $< m_{\ell\ell} <$ 116 GeV	0.230 ± 0.054	0.296 ± 0.012	0.34 ± 0.37	-0.2 ± 1.1	0.40 ± 0.36	0.093 ± 0.036	(38.7)%
5.02 TeV	$Z \to ee$	116 GeV $< m_{\ell\ell} <$ 500 GeV	0.138 ± 0.074	0.392 ± 0.024	1.0* ± 0	0.0* ± 0	0.42 ± 0.34	0.058 ± 0.046	(79.3)%
5.02 TeV	$Z \to \mu\mu$	40 GeV $< m_{\ell\ell} <$ 66 GeV & $\lvert\cos(\theta^*_{CS})\rvert < 0.4$	1.043 ± 0.075	0.0427 ± 0.0024	0.928 ± 0.096	-0.97 ± 0.11	0.0883 ± 0.0025	0.092 ± 0.021	(22.8)%
5.02 TeV	$Z \to \mu\mu$	40 GeV $< m_{\ell\ell} <$ 66 GeV & $\lvert\cos(\theta^*_{CS})\rvert > 0.4$	1.168 ± 0.066	0.0747 ± 0.0024	0.796 ± 0.062	-0.842 ± 0.076	0.1416 ± 0.0029	0.165 ± 0.036	(21.8)%
5.02 TeV	$Z \to \mu\mu$	66 GeV $< m_{\ell\ell} <$ 116 GeV	1.160 ± 0.085	0.0325 ± 0.0023	0.97 ± 0.10	-1.04 ± 0.12	0.0731 ± 0.0020	0.085 ± 0.019	(22.4)%
5.02 TeV	$Z \to \mu\mu$	116 GeV $< m_{\ell\ell} <$ 500 GeV	1.23 ± 0.25	0.0572 ± 0.0087	0.41 ± 0.34	-0.39 ± 0.63	0.13 ± 0.16	0.154 ± 0.055	(35.7)%
13 TeV	$Z \to ee$	40 GeV $< m_{\ell\ell} <$ 66 GeV & $\lvert\cos(\theta^*_{CS})\rvert < 0.4$	0.743 ± 0.068	0.2590 ± 0.0061	0.478 ± 0.076	-0.64 ± 0.15	0.400 ± 0.023	0.298 ± 0.071	(23.8)%
13 TeV	$Z \to ee$	40 GeV $< m_{\ell\ell} <$ 66 GeV & $\lvert\cos(\theta^*_{CS})\rvert > 0.4$	0.721 ± 0.048	0.2376 ± 0.0042	0.347 ± 0.045	-0.460 ± 0.078	0.377 ± 0.013	0.272 ± 0.060	(22.1)%
13 TeV	$Z \to ee$	66 GeV $< m_{\ell\ell} <$ 116 GeV	0.300 ± 0.028	0.2994 ± 0.0053	0.370 ± 0.095	-0.61 ± 0.22	0.506 ± 0.056	0.152 ± 0.037	(24.3)%
13 TeV	$Z \to ee$	116 GeV $< m_{\ell\ell} <$ 500 GeV	0.087 ± 0.025	0.3200 ± 0.0082	1.03 ± 0.93	-2.5 ± 3.1	0.93 ± 0.65	0.081 ± 0.037	(45.7)%
13 TeV	$Z \to \mu\mu$	40 GeV $< m_{\ell\ell} <$ 66 GeV & $\lvert\cos(\theta^*_{CS})\rvert < 0.4$	0.399 ± 0.015	0.0510 ± 0.0011	1.250 ± 0.064	-1.355 ± 0.075	0.1156 ± 0.0016	0.0461 ± 0.0095	(20.6)%
13 TeV	$Z \to \mu\mu$	40 GeV $< m_{\ell\ell} <$ 66 GeV & $\lvert\cos(\theta^*_{CS})\rvert > 0.4$	0.421 ± 0.012	0.06644 ± 0.00091	1.122 ± 0.045	-1.216 ± 0.056	0.1413 ± 0.0017	0.060 ± 0.012	(20.0)%
13 TeV	$Z \to \mu\mu$	66 GeV $< m_{\ell\ell} <$ 116 GeV	0.402 ± 0.014	0.0520 ± 0.0010	1.202 ± 0.064	-1.354 ± 0.081	0.1285 ± 0.0023	0.052 ± 0.011	(21.2)%
13 TeV	$Z \to \mu\mu$	116 GeV $< m_{\ell\ell} <$ 500 GeV	0.371 ± 0.029	0.0467 ± 0.0023	1.08 ± 0.14	-1.17 ± 0.19	0.1103 ± 0.0070	0.0409 ± 0.0093	(22.7)%

Table 8.6: Summary of the multijet background normalisation factors derived in categories of energy, channel, mass and $|\cos(\theta^*_{CS})|$. The relative uncertainty is shown only for $S_{control}$. * A single polynomial fit failed to minimise due to limited statistics, in this case p_0, p_1 was set to 1.0, 0.0.

Step3: Total Normalisation The full correction required to scale the template to the nominal selection is defined as,

$$S_{total} = S_{control} \times S_{isolation,rw} \tag{8.13}$$

Summary of Factors

The normalisation factors $S_{control}$, $S_{isolation}$, $S_{isolation,rw}$ and S_{total} as well as the fitted p_0 and p_1 coefficients are summarised in Table 8.6 for each $m_{\ell\ell} - |\cos(\theta^*_{CS})|$ group. Consistency is observed between same-channel estimates for $\sqrt{s} = 5.02$ TeV and $\sqrt{s} = 13$ TeV, however, the normalisation factors for $Z \to ee$ and $Z \to \mu\mu$ are significantly different. This is not unexpected due to the differing template selections.

8.5.3 Multijet Shape Comparisons

Comparisons of the multijet estimates for each energy and channel are shown in Figure 8.9 where it is shown that multijet contribution is largest in the low-mass region with a larger contribution relative to data in the $Z \to ee$ channel. The multijet shape is found to be very similar for a given final state ($Z \to ee$ and $Z \to \mu\mu$) when compared between $\sqrt{s} = 5.02$ TeV and $\sqrt{s} = 13$ TeV. Similar shape is observed in $\cos(\theta^*_{CS})$ with a differing shape observed for $y_{\ell\ell}$.

8.5.4 Multijet Uncertainties

Template Statistics The statistical uncertainties on the selected templates can be significant in certain bins, notably in the electron channel and the high-mass bins. The statistical component is combined with the background Monte Carlo statistics and is propagated through the unfolding algorithm via Gaussian toy variations.

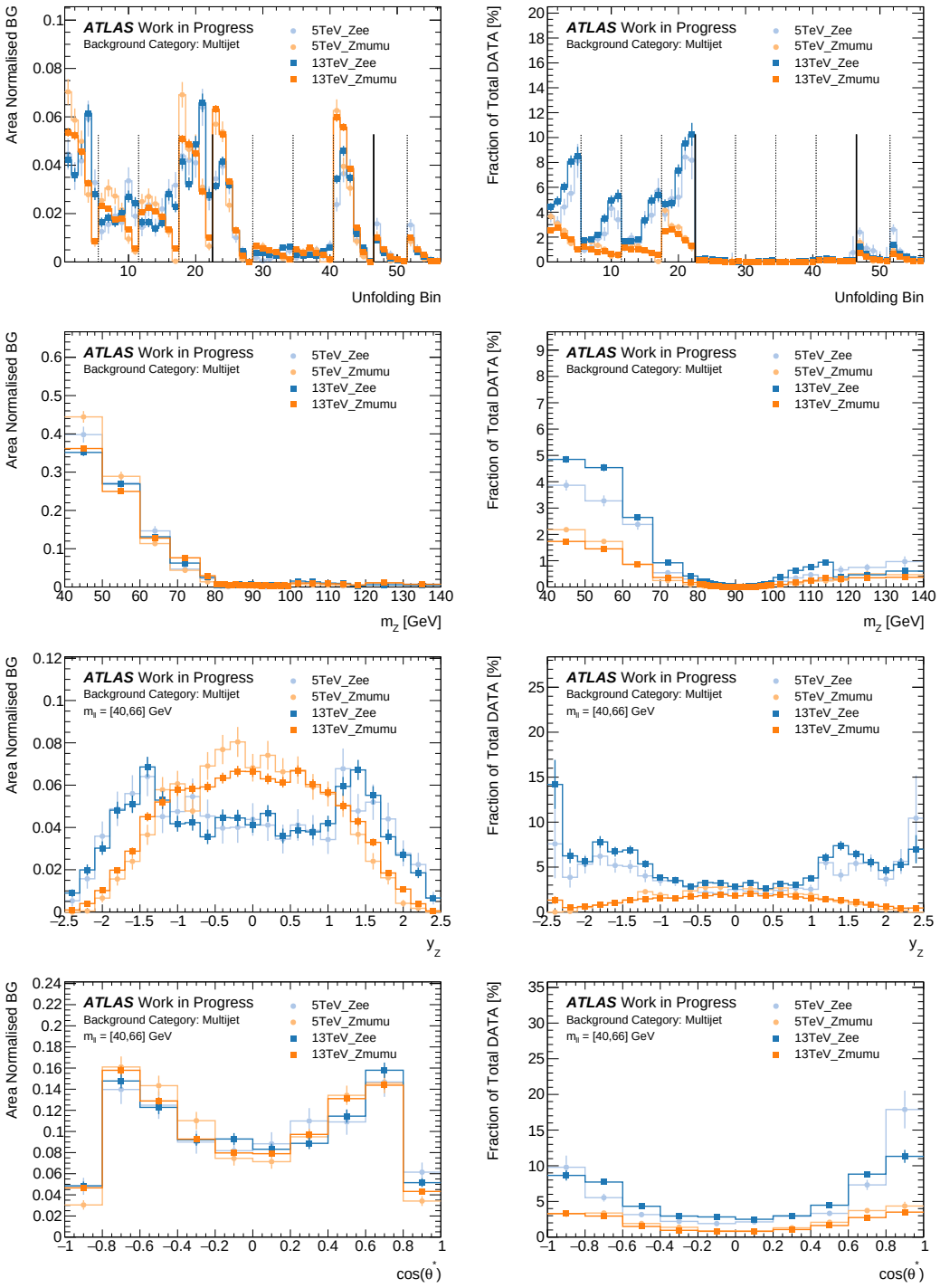

Figure 8.9: Comparisons of Multijet background shape for the unravelled binning scheme, $m_{\ell\ell}$, low-mass $y_{\ell\ell}$ and low-mass $\cos(\theta^*_{CS})$ distributions at both $\sqrt{s} = 5.02\,\text{TeV}$ and $\sqrt{s} = 13\,\text{TeV}$ for both the $Z \to ee$ and $Z \to \mu\mu$ channels. Shown on the left is a shape comparison where the distributions are normalised by area. Shown on the right is a comparison of the relative fraction of multijet to selected events in data. Bin uncertainties only reflect the uncertainty on the multijet template.

Correlated Systematics The uncertainty on $S_{control}$ is calculated with uncertainty propagation using the uncertainties on both terms. This is largely dominated by the limited statistics when selecting the `NominalLooseIsolation` events inside the control region $N_{\texttt{NominalLooseIsolation,Min(ptvarcone20/pt)>0.1}}$. This uncertainty is propagated through the unfolding algorithm as a correlated source on the

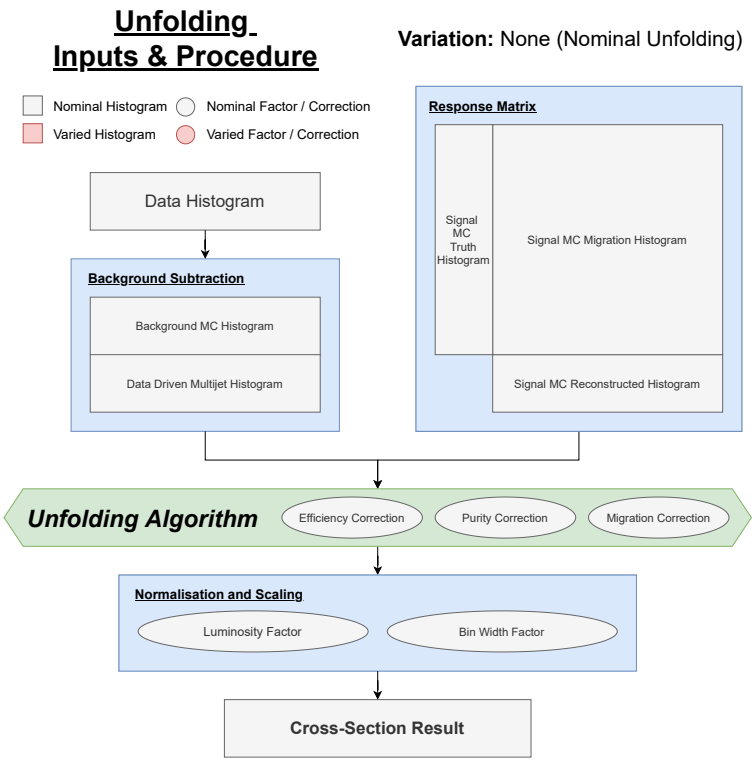

Figure 8.10: Diagram showing the steps to convert the input histograms through the unfolding framework and into a final cross-section result. This shows the nominal unfolding procedure where all histograms and factors take their nominal value.

Multijet normalisation.

The straight line fit in the derivation of $S_{isolation,rw}$ produces uncertainties on the coefficients p_0 and p_1. These are propagated to $S_{isolation,rw}$ using toy 1σ fluctuations on the fitted coefficients (this maintains any correlation between the fitted coefficients). The uncertainty on $S_{isolation,rw}$ is taken from the standard deviation of $S_{isolation,rw,toy}$.

Limitations A few limitations exist in this estimation which are not expected to have a significant impact. A conservative systematic of 20% is applied to all multijet estimates to cover these missing ingredients.

- The electroweak background contributions for the $Z \to ee$ were not processed and not accounted for when calculating the template.
- Subtraction of signal MC introduces a small circular dependency on the normalisation of the signal. This is only important for the central-mass slice where the fraction of multijet events compared to the selected events data is below 0.1%.

8.6 Unfolding Strategy

After running the analysis selection on samples for data, signal MC and background MC, the outputs are interfaced with the unfolding library *RooUnfold* [149]. The cross-section is obtained by taking the steps:

1. Subtract background (MC modelled and multijet) from data.
2. Produce a *RooUnfoldResponse* object using signal MC requiring three inputs: 1D reconstructed selection histogram, 1D truth selection histogram, 2D reconstructed and truth selection migration histogram.
3. The background-subtracted data and *RooUnfoldResponse* object is passed through an unfolding algorithm, where the efficiency, migration and purity corrections are applied within the algorithm.
4. Apply the luminosity and bin width factors to the unfolded result.

These steps are shown schematically in Figure 8.10. A more detailed explanation of what unfolding is doing will now be provided.

8.6.1 Unfolding Corrections

Unfolding is the correction of a reconstructed measured distribution into the true underlying distribution. These corrections are all performed within an unfolding algorithm, but the corrections can be thought of as correcting three distinct issues:

Bin Efficiency The unfolding efficiency correction accounts for losses of events within the true fiducial volume that were not succesfully reconstructed. Mathematically, the unfolding efficiency ϵ_j in a given truth bin j is defined as:

$$\epsilon_j \equiv \frac{N_j^{\text{reco\&truth}}}{N_j^{\text{truth}}} \tag{8.14}$$

where $N_j^{\text{reco\&truth}}$ is the number of events in a given truth bin j passing both reconstructed-level ("reco") and fiducial truth-level ("truth") selections compared to the number of events selected in bin j just passing the truth selection N_j^{truth}. This is largely driven by detector inefficiencies where the detector misses one or both leptons. This also extends to losses due to discrepancies in kinematic acceptance between "truth" and "reco". For this analysis, this occurs for electrons that fall within the crack region $1.37 < |\eta^e| < 1.52$ and muons in the region $2.4 < |\eta^\mu| < 2.5$. Figure 8.11 shows the the unfolding bin efficiencies for this analysis. The $Z \to \mu\mu$ channel at both energies has unfolding efficiency in most bins of $\epsilon_j \approx 80\%$. The $Z \to ee$ channel at both energies has a lower unfolding efficiency in most bins of $\epsilon_j \approx 60\%$.

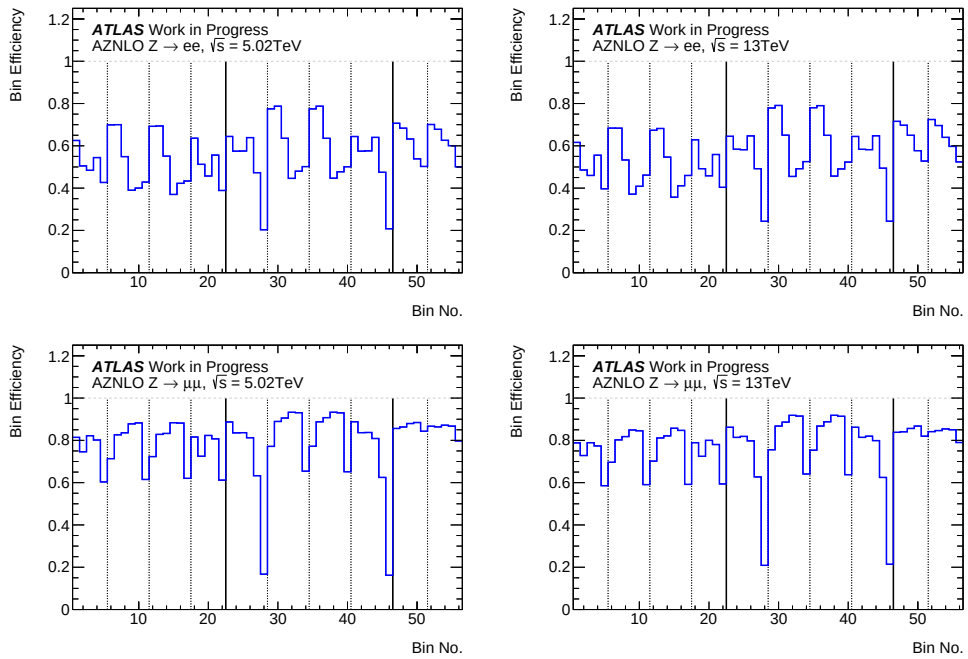

Figure 8.11: Bin Efficiency (Equation 8.14) in the unravelled binning scheme for the $Z \to ee$ channel (top) and the $Z \to \mu\mu$ channel (bottom) as modelled by the detector reconstruction with all calibrations included.

Bin Migrations The unfolding migration correction accounts for events that are reconstructed in a different "reco" bin to their corresponding "truth" bin. Migrations can be visualised as a matrix M_{ij}, defined by filling a 2-dimensional histogram for all events that pass both reconstructed-level and truth-level selections with the events reconstructed value on the x-axis at bin i and truth value on the y-axis at bin j:

$$M_{ij} \equiv N_{ij}^{\text{reco\&truth}} \tag{8.15}$$

If no bin-bin migrations are present, this matrix is completely diagonal; however, the off-diagonal bins are populated if there are bin-bin migrations. This is driven by the smearing of particle kinematics originating from limited detector resolution. Figure 8.12 shows the unfolding bin-bin migrations for this analysis. The matrix is mostly diagonal with some smaller linear structures visible between slices of mass and $\cos(\theta^*_{CS})$ originating from events close to the boundaries. One larger source of migration that is more difficult to spot in the figure is the migration between bin 23 and bin 41 or between bin 41 and bin 23. These are events very close to $y_{ll} = 0$ at truth-level which are reconstructed with the wrong sign of y_{ll}. This produces a sign flip in the reconstructed $\cos(\theta^*_{CS})$.

Bin Purity The unfolding purity correction accounts for events that are reconstructed in a bin, but originate outside the true fiducial volume. The bin purity in a given reconstructed bin i is defined as:

$$p_i \equiv \frac{N_i^{\text{reco\&truth}}}{N_i^{\text{reco}}} \tag{8.16}$$

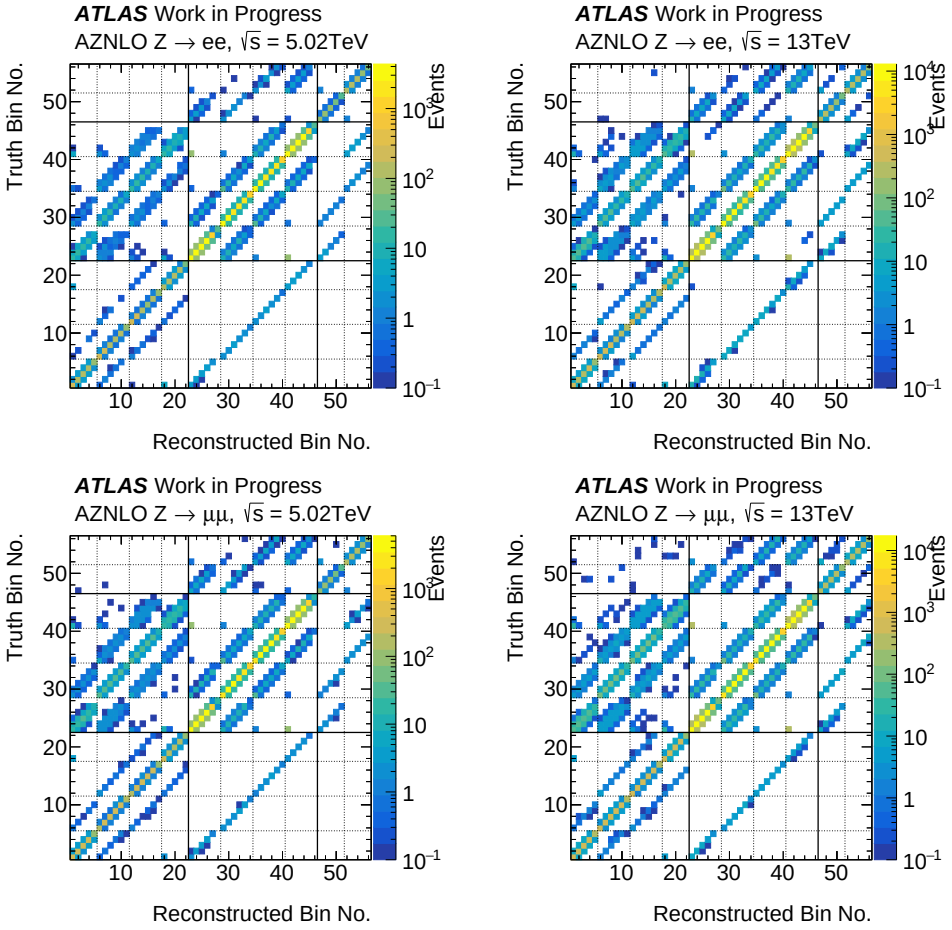

Figure 8.12: Bin-Bin migration matrices (Equation 8.15) in the unravelled binning scheme for the $Z \to ee$ channel (top) and the $Z \to \mu\mu$ channel (bottom) as modelled with Powheg AZNLO. The z-axis shows MC normalised by luminosity.

where $N_i^{\text{reco\&truth}}$ is the number of reconstructed events in bin i passing both reconstructed-level and truth-level selections compared to the number of events in the reconstructed-level bin N_i^{reco}. These are typically events that at truth-level lie close to, but outside of, a kinematic requirement on the selection. Figure 8.13 shows the unfolding bin purity for this analysis. The purity is unity in the central-mass and high-mass slices, with a slight drop at low-mass showing more of an impact for $Z \to ee$ than $Z \to \mu\mu$ at low-mass. It is likely this originates from events with one or both leptons just below $p_T(\ell) < 15\,\text{GeV}$ that migrate into the low-mass selection result.

8.6.2 RooUnfold and Unfolding Algorithms

The unfolding performed in this analysis uses the dedicated unfolding library *RooUnfold* that contains implementations for multiple unfolding algorithms. All algorithms in *RooUnfold* require three histograms as input:

- N_i^{reco} : Reconstructed distribution for events passing the experimental selection.
- N_j^{truth} : Underlying truth distribution for events passing the truth selection

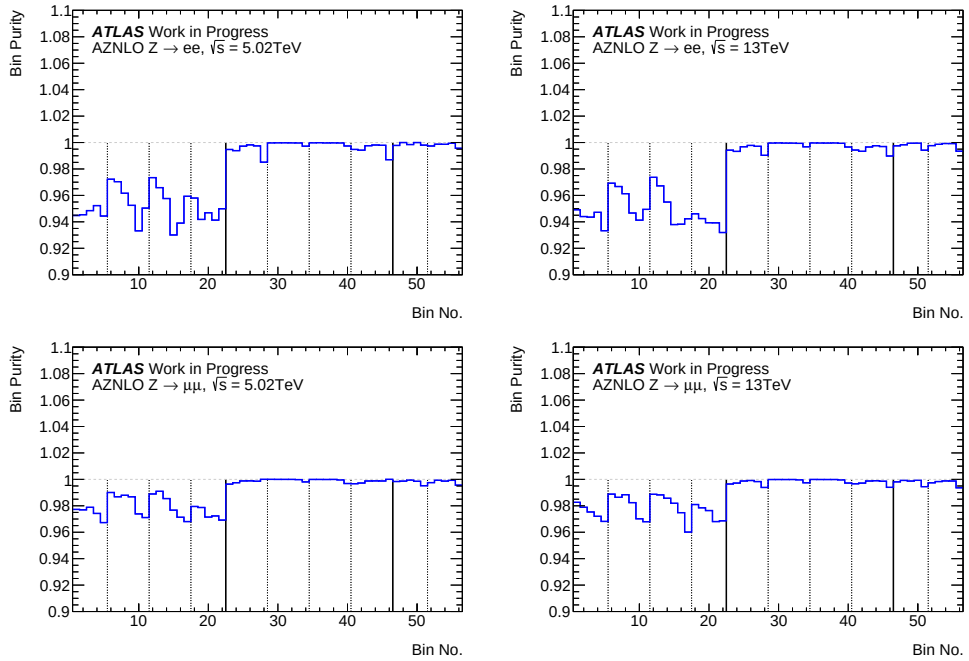

Figure 8.13: Bin Purity (Equation 8.16) in the unravelled binning scheme for the $Z \to ee$ channel (top) and the $Z \to \mu\mu$ channel (bottom) as modelled with Powheg AZNLO.

- M_{ij} : The migration matrix for events passing both the reconstruction and truth selections.

These can be used to calculate the purity and efficiency corrections, as well as the response matrix R_{ij}. The response matrix R_{ij} is defined as the conditional probability to reconstruct an event in bin i, given that at truth-level, it was in bin j:

$$R_{ij} = \epsilon_j M_{ij}^{normalised} = P(\text{reconstructed in } i|\text{truth in } j). \tag{8.17}$$

Note that

$$\epsilon_j = \sum_{i=1} R_{ij} = P(\text{reconstructed in any bin}|\text{truth in } j). \tag{8.18}$$

The data we measure is assumed to arise by combining the response matrix with the truth distribution, applying a purity correction, and including background processes. This is written symbolically as:

$$D_i = \left(\sum_j R_{ij} T_j \right) / p_i + B_i \tag{8.19}$$

where T is the true underlying distribution obtained after fiducial cuts; R_{ij} is the response matrix estimated using signal MC. D and B are the observed distribution in data and the sum of all background contributions, respectively, obtained after reconstructed-level cuts, and p_i is the purity correction as modelled by signal MC. As T_j is the quantity to be measured, this equation is reverted in the unfolding procedure and determines the best estimate of the underlying distribution through:

$$\tilde{U}_j = \sum_i U_{ij}(D_i - B_i) * p_i. \tag{8.20}$$

Here $\tilde{U}_j$ is the unfolded spectrum, which is an estimate of the underlying distribution T; and U_{ij} symbolically represents the unfolding transformation. The background-subtracted data distribution $D_i - B_i$ is corrected by the purity p_i.

Several algorithms exist to obtain U_{ij} and p_i in *RooUnfold*. This analysis uses D'Agostini iterative unfolding [150], as implemented in the *RooUnfoldBayes* class, but two simpler unfoldings (*RooUnfoldBinByBin* and *RooUnfoldInvert*) are also used for comparison.

Bin-By-Bin Unfolding

This unfolding procedure derives a factor for each analysis bin using signal MC:

- $C_i = T_i/r_i$ where T_i is the number of MC events in bin i and r_i is the number of reconstructed MC events in bin i.
- $U_i = C_i \times (D_i - B_i) \times p_i$; the factors are multipled in each bin. The RooUnfold implementation *RooUnfoldBinByBin* also includes the purity correction.

Bin-by-bin unfolding does not account for migrations which potentially introduces model dependence, especially when migrations are sizeable.

Matrix Inversion Unfolding

This unfolding procedure simply inverts the response matrix R_{ij} in place of the unfolding transformation U_{ij} from Equation 8.20. The RooUnfold implementation *RooUnfoldInvert* also includes the purity correction. This method generally struggles when bin to bin migrations are sizeable, leading to oscillations caused by statistical fluctuations of the inputs and often needs a more complex regularisation process to control the output uncertainties. This often relies on assuming some level of smoothness for the distribution, which is not possible for the artificial unfolding bins employed in this analysis.

D'Agostini Iterative Unfolding

This method uses the definition of the response matrix as a conditional probability as a way to introduce Bayes rule and rewrites the symbolic unfolding formula as:

$$\tilde{U}_j = \frac{1}{\epsilon_j} \sum_i P(\text{truth in } j|\text{reconstructed in } i) \times (D_i - B_i) * p_i \tag{8.21}$$

where the term ϵ_j is included for normalisation. Following Bayes' theorem, the term $P(\text{truth in } j|\text{reconstructed in } i)$ can be rewritten as

$$P(\text{truth in } j|\text{reconstructed in } i) = \frac{P(\text{reconstructed in } i|\text{truth in } j)P(\text{truth in } j)}{P(\text{reconstructed in } i)} \tag{8.22}$$

and by translating some of these probabilities back into elements of the response matrix

$$P(\text{truth in } j|\text{reconstructed in } i) = \frac{R_{ji}P(\text{truth in } j)}{\sum_k R_{ki}P(\text{truth in } k)}. \tag{8.23}$$

This depends only on only two inputs, the response matrix which is obtained from MC, and a set of prior probabilities $P(\text{truth in } k)$ for each bin (the loop k just loops over all bins in the analysis). An initial prior is required to start the unfolding, and is taken as the true distribution from the fraction of events T_j per bin j to the total events as modelled in the signal MC:

$$P^{\text{iter}=0}(\text{truth in } j) = N_j^{truth} / \sum_k N_k^{truth}. \tag{8.24}$$

The algorithm is then iterated α times, where the prior for the next step is defined using the fraction of the unfolded result $\tilde{U}_j$ from bin j to the integral of all unfolded bins, as taken from the result of the previous iteration:

$$P^{\text{iter}=\alpha>0}(\text{truth in } j) = \tilde{U}_j^{\alpha-1} / \sum_k \tilde{U}_k^{\alpha-1} \tag{8.25}$$

The result is expected to converge after a few iterations if the MC is reasonably close to the true distribution. The reliance on a prior provided by the MC must be tracked with an estimate of bias uncertainty.

This method is commonly used in ATLAS. Overall, the algorithm has multiple advantages:

- Computationally fast, which is useful when 1000s of independent unfoldings are needed for uncertainty propagation.
- Does not require the distribution to be smooth, so it will not struggle with artificial binning schemes with sharp rises as in this analysis.
- The number of iterations is easy to control and understandable and does not rely on a definition of smoothness.

8.6.3 Cross-Section Calculation

The unfolded distribution $\tilde{U}_j$ is a measure of the number of Born-level fiducial events produced. To convert this into a differential cross-section, the corrected event counts are divided by the luminosity and bin width:

$$\frac{\mathrm{d}^3\sigma^{fid.}}{\mathrm{d}m_{\ell\ell}\mathrm{d}\cos(\theta^*_{CS})\mathrm{d}|y_{\ell\ell}|} = \tilde{U}_j \frac{1}{\mathcal{L}_{\text{int}}\Delta_j m_{\ell\ell}\Delta_j \cos(\theta^*_{CS})\Delta_j|y_{\ell\ell}|} \tag{8.26}$$

where $\mathcal{L}_{\text{int}}$ is the integrated luminosity of the corresponding dataset. The factors $\Delta_j m_{\ell\ell}$, $\Delta_j \cos(\theta^*_{CS})$ and $\Delta_j|y_{\ell\ell}|$ correspond to the bin width in each dimension of the binning scheme. This is consistently $\Delta_j|y_{\ell\ell}| = 0.4$ for all absolute rapidity bins. The mass bin widths in this

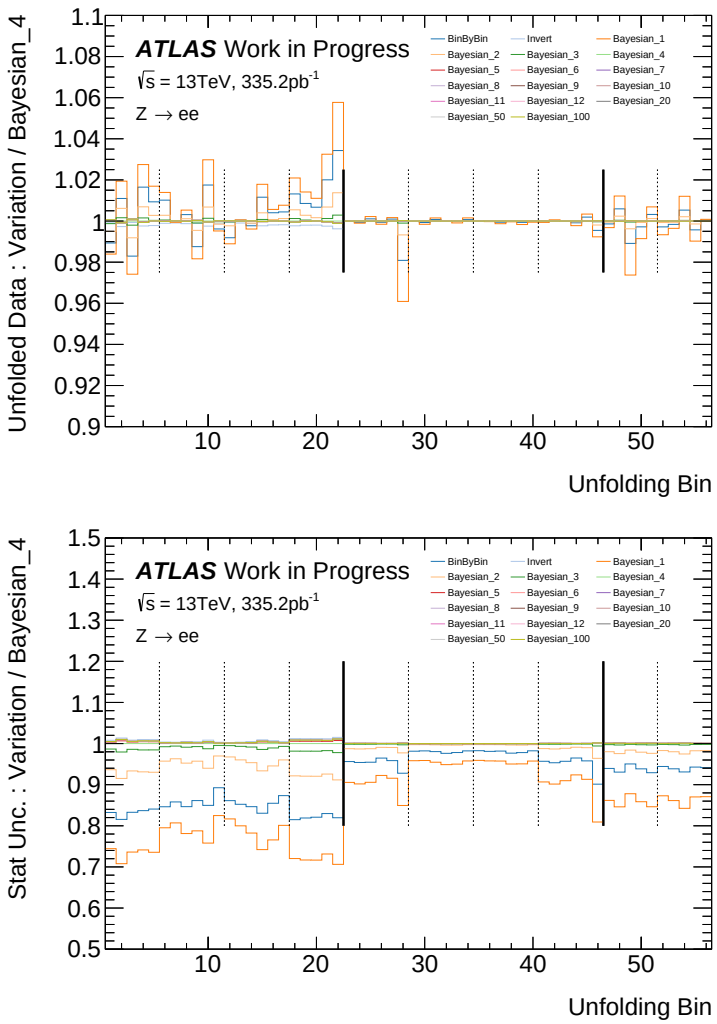

Figure 8.14: The variation in unfolded $\sqrt{s} = 13\,\text{TeV}$ $Z \to ee$ cross-section result (top) and statistical uncertainty (bottom) for a range of unfolding iterations compared to the 4th iteration. In addition, the results for bin-by-bin unfolding and matrix inversion are also shown.

analysis are $\Delta_j m_{\ell\ell} = 26\,\text{GeV}, 50\,\text{GeV}, 384\,\text{GeV}$ corresponding to their slice. The $\cos(\theta^*_{CS})$ bins are $\Delta_j \cos(\theta^*_{CS}) = 0.6, 0.4, 1.0$ also depending on the corresponding slice.

8.6.4 Optimisation of Number of Iterations

In this analysis, the optimal number of unfolding iterations is chosen based on the requirement that at least two iterations have occurred to utilise the iterative nature of the algorithm appropriately. Furthermore, the optimal number of iterations should be when the result has stabilised and the uncertainties do not display large fluctuations.

Figure 8.14 shows the $\sqrt{s} = 13\,\text{TeV}$ $Z \to ee$ unfolded cross-section and the corresponding statistical uncertainty (Section 8.7) for various iterations, the bin-by-bin method and the matrix inversion method. The results are shown relative to the fourth iteration, which was selected as the nominal number of iterations. Similar results were observed for $Z \to \mu\mu$ and at $\sqrt{s} = 5.02\,\text{TeV}$, so the 4th iteration is used for both energies and both channels. Iterations before the fourth

display differences of 1-2% compared to the 4th in the unfolded cross-section and 10-30% in the statistical uncertainty. Similar results are also observed for the bin-by-bin method. Iterations beyond the fourth display no significant change implying stability of the result. The stabilised result also shows good consistency with the matrix inversion method.

8.7 Uncertainties and Bias Estimate

This section describes how various types of uncertainty are propagated through the unfolding, showing the differing treatment of statistical and systematic uncertainties. A summary of the systematic uncertainties considered in this analysis is then provided. Finally, a derivation of the unfolding bias uncertainty is discussed.

8.7.1 Uncertainty Propagation

Statistical Uncertainties Statistical uncertainties for the data and signal MC are propagated through the unfolding using the bootstrap resampling method [151]. Instead of traditional statistical resampling, the Poisson bootstrap approximation is used whereby many pseudo experiments N_{bs} are run in parallel and each event is selected w times according to a Poisson distribution of mean $\lambda = 1$, or rather is assigned an event weight of

$$w = \mathcal{P}(\lambda = 1) \tag{8.27}$$

where $\mathcal{P}(\lambda = 1)$ is the randomly sampled value from the Poisson distribution. To mimic traditional resampling, the sum of sampled bootstrap weights in each pseudo experiment should equal the sum of events, which only approaches validity when the total number of events is large ($n > 100$), which is valid for this analysis. The benefit of using bootstrap toy weights over traditional Poisson fluctuations of bin contents is that the correlations between multiple histogram fills can be easily tracked. This is important for the signal MC where various histograms are required to build the response matrix and will share statistical fluctuations. To adequately evaluate uncertainties it is advised that $N_{bs} > 100$. To adequately evaluate covariances it is advised that $N_{bs} > 1000$.

Data Statistics Data statistical uncertainties result from fluctuations in the observed spectrum D. These are propagated using bootstrap weights as a separate unfolding for each of the N_{bs} pseudo experiments. For each pseudo-experiment sample α, the unfolded spectrum is

$$\tilde{U}_j = \sum_i U_{ij}(D_i^\alpha - B_i) * p_i \tag{8.28}$$

As the data statistical uncertainty is the dominant source of uncertainty in this analysis, the number of pseudo experiments was set to be large with $N_{bs} = 10000$.

MC Statistics The limited signal MC statistics will affect the evaluation of the response matrix and hence corrections in the unfolding procedure. These are propagated using bootstrap weights as a separate unfolding for N_{bs} variations, ensuring that for each MC event, the truth selection and reconstructed selection share the same bootstrap weight. For each pseudo variation of the signal sample α, the unfolded spectrum is

$$\tilde{U}_j^{\alpha} = \sum_i U_{ij}^{\alpha}(D_i - B_i) * p_i^{\alpha} \tag{8.29}$$

The number of pseudo experiments for the signal MC was set to be $N_{bs} = 1000$, which was enough to resolve correlations adequately but did not require unachievable computational time.

Background Statistics Limited precision in background MC and the multijet template is propagated to the background subtraction term B. As this was computationally expensive for a minor uncertainty source, this was not propagated with full bootstrap variations and instead used N_{gauss} Gaussian variations. Here, the bin content of the background contribution is varied using a Gaussian fluctuation around the bin centre, using the combined background statistical uncertainties as the standard deviation. For each pseudo variation of the signal sample α, the unfolded spectrum is

$$\tilde{U}_j^{\alpha} = \sum_i U_{ij}(D_i - B_i^{\alpha}) * p_i \tag{8.30}$$

The number of Gaussian variations was set to be large, $N_{gauss} = 10000$, as these variations do not require complete processing of events.

Statistical Uncertainty Calculation The statisitcal bin to bin covariance for (X =Data, MC, background) on the unfolded results is evaluated through

$$C_{kl}^{stat,X} = \frac{1}{N_{toy} - 1} \sum_{\alpha=1}^{N_{toy}} (\tilde{U}_k^{\alpha} - \langle \tilde{U} \rangle_k)\,(\tilde{U}_l^{\alpha} - \langle \tilde{U} \rangle_l), \tag{8.31}$$

where N_{toy} is the number of bootstrap variations N_{bs} or the number of Gaussian variations N_{gauss}. The uncertainty from statistical sources in each bin is obtained from the diagonal elements via

$$\delta \tilde{U}_k^{\,stat,X} = \sqrt{C_{kk}^{stat,X}}. \tag{8.32}$$

Systematic Uncertainties for Signal Samples These systematic variations affect the signal MC (scale factors, calibration) which will change the response matrix. For each systematic variation of the signal sample a, the unfolded spectrum is

$$\tilde{U}_j^{a} = \sum_i U_{ij}^{a}(D_i - B_i) * p_i^{a}. \tag{8.33}$$

Systematic Uncertainties for Background Samples These systematic variations affect the backgrounds (background cross-section uncertainties, $t\bar{t}$ modelling, multijet uncertainties) and will change the background term B. For each systematic variation of the background contribution a, the unfolded spectrum is

$$\tilde{U}_j^a = \sum_i U_{ij}(D_i - B_i^a) * p_i \tag{8.34}$$

Uncertainty and Covariance Calculation Most of these variations have a corresponding 1-sigma *up* and *down* variation, the uncertainty on the unfolded spectrum $\delta\tilde{U}_k^a$ is calculated as half the difference between *up* and *down*, ensuring *up* is the first term to maintain the correct sign.

$$\delta\tilde{U}_k^a = \frac{1}{2}(\tilde{U}_k^{a,up} - \tilde{U}_k^{a,down}) \tag{8.35}$$

Some uncertainties have no corresponding *up* and *down* variation, and in this case the uncertainty is calculated as the difference from the nominal result.

$$\delta\tilde{U}_k^a = (\tilde{U}_k^a - \tilde{U}_k^{\text{Nom}}). \tag{8.36}$$

These uncertainties are treated as fully correlated sources across all bins, and the bin-bin covariance between bins k and l is calculated via

$$C_{kl}^a = \delta\tilde{U}_k^a \, \delta\tilde{U}_l^a. \tag{8.37}$$

Luminosity Uncertainty The luminosity uncertainty is propagated simultaneously in two steps of the calculation. First in the normalisation of MC backgrounds

$$\tilde{U}_j^{\text{lumi}} = \sum_i U_{ij}(D_i - B_i^{\text{lumi}}) * p_i, \tag{8.38}$$

and also in the final normalisation in the cross-section calculation

$$\frac{\mathrm{d}^3\sigma^{fid.,\text{lumi}}}{\mathrm{d}m_{\ell\ell}\mathrm{d}\cos(\theta^*_{CS})\mathrm{d}|y_{\ell\ell}|} = \tilde{U}_j^{\text{lumi}} \frac{1}{\mathcal{L}_{\text{int}}^{lumivar}\Delta_j m_{\ell\ell}\Delta_j \cos(\theta^*_{CS})\Delta_j|y_{\ell\ell}|}. \tag{8.39}$$

The uncertainty is calculated as the difference between half of the *up* and *down* variations via

$$\delta\tilde{U}_k^{\text{lumi}} = \frac{1}{2}(\tilde{U}_k^{\text{lumi,up}} - \tilde{U}_k^{\text{lumi,down}}), \tag{8.40}$$

and is treated as a fully correlated source of uncertainty, with the bin-bin covariance between bins k and l is calculated via

$$C_{kl}^{\text{lumi}} = \delta\tilde{U}_k^{\text{lumi}} \, \delta\tilde{U}_l^{\text{lumi}} \tag{8.41}$$

Combination of Uncertainties

The total covariance matrix is given by summing the individual covariance matrices:

$$C_{kl}^{tot} = C_{kl}^{stat,Data} + C_{kl}^{stat,MC} + C_{kl}^{stat,BG} + C_{kl}^{\text{lumi}} + \sum_{a} C_{kl}^{a} \tag{8.42}$$

where a runs over all sources of systematic uncertainty. The covariance corresponding to a given category of sources of uncertainty can be calculated by restricting a accordingly. Individual bin uncertainties can again be obtained from the diagonal elements via:

$$\delta\tilde{U}_k^{\,tot} = \sqrt{C_{kk}^{tot}} \tag{8.43}$$

8.7.2 Sources of Systematic Uncertainty

An overview of all systematic uncertainty sources in this analysis and the various contributions to each source is now provided:

- **Electron Calibration:** These correspond to the high-μ and low-μ electron calibration as described in Section 6.1. These consist of 60 nuisance parameters taken from the High-μ electron calibration, and 24 uncorrelated variations for both α and c' which are varied for each bin in the Low-μ electron calibration.
- **Muon Calibration:** These correspond to the high-μ muon calibration and Sagitta bias correction as described in Section 6.2. These consist of: 3 nuisance parameters, taken from the High-μ muon calibration, 48 uncorrelated variations for the muon sagitta bias correction bin uncertainties, and a single correlated uncertainty on the muon sagitta bias correction.
- **Electron SFs:** These correspond to uncertainties on the electron scale factor maps as described in Section 6.3.
  - **Electron Trigger SFs:** 5 correlated sources and 264 uncorrelated sources.
  - **Electron Reconstruction SFs:** 8 correlated sources and 264 uncorrelated sources.
  - **Electron Identification SFs:** 15 correlated sources and 286 uncorrelated sources.
  - **Electron Isolation SFs:** 3 correlated sources and 242 uncorrelated sources.
- **Muon SFs:** These correspond to uncertainties on the muon scale factor maps as described in Section 6.3.
  - **Muon Trigger SFs:** 3 correlated sources and 310 uncorrelated sources.
  - **Muon Reconstruction SFs:** 9 correlated sources and 322 uncorrelated sources.
  - **Muon TTVA SFs:** 5 correlated sources and 24 uncorrelated sources.

  - **Muon Isolation SFs:** 7 correlated sources and 416 uncorrelated sources.

- **Background Modelling:** These correspond to variations in the background subtraction.
  - **Cross-Section Normalisation:** The normalisation on each MC sample is varied by the theoretical uncertainty assigned in Table 8.1 and Table 8.2.
  - **Multijet Uncertainties:** Variations on the multijet normalisation as discussed in Section 8.5.4.
  - **$t\bar{t}$ Modelling Uncertainties:** Uncertainty propagated only for $\sqrt{s} = 13\,\text{TeV}$. This probes the difference in $t\bar{t}$ modelling when using an additional sample modelled using Powheg+Herwig7 and an additional Powheg+Pythia8 sample with varied tune parameters.
- **Luminosity Uncertainty:** The uncertainty on the luminosity is 1.6% (1.5%) for the 5.02 TeV(13 TeV) datasets, respectively.
- **Bias Uncertainty:** This uncertainty covers the dependency of the unfolded result on the signal sample modelling used in the unfolding. This includes checking various generators with various PDF sets. The evaluation of the bias uncertainty is discussed in Section 8.7.3.

8.7.3 Bias Uncertainty

Unfolding should be insensitive to the underlying physics distribution. However, in practice, the result and the theoretical extrapolation are not entirely separable. For iterative bayesian unfolding, this is clear from the dependence on some prior, but this more generally applies to all algorithms, as the unfolding corrections have dependencies on the truth modelling. This is strongest for the efficiency correction for regions where acceptance extrapolation is sizeable and events close to the fiducial cuts where slightly different modelling can change the purity. Significant bias uncertainty is only expected for unfolding analyses with large bin to bin migrations, which are not observed for this analysis.

Bias is evaluated here by constructing the response matrix using reweighted signal samples and passing the nominal reconstructed level Powheg+Pythia8 through the unfolding algorithm (with zero background subtraction). The unfolded result is then compared to the nominal truth level Powheg+Pythia8 result. Variations of the signal simulation were modelled with truth-level reweightings of Powheg+Pythia8 in $p_T(Z)$ (Z-boson transverse momentum) and $y_{\ell\ell}$ (labelled "PTYRew"), reweightings of the A_i coefficients [152] of Powheg+Pythia8 (labelled "AiRew") and combinations of both reweightings. Truth-level predictions available for $p_T(V)$ and $y_{\ell\ell}$ reweighting were:

- DYTURBO [153] (CT14)
- Powheg+Herwig7 (CT18)
- Powheg+Pythia8 (NNPDF3.0)

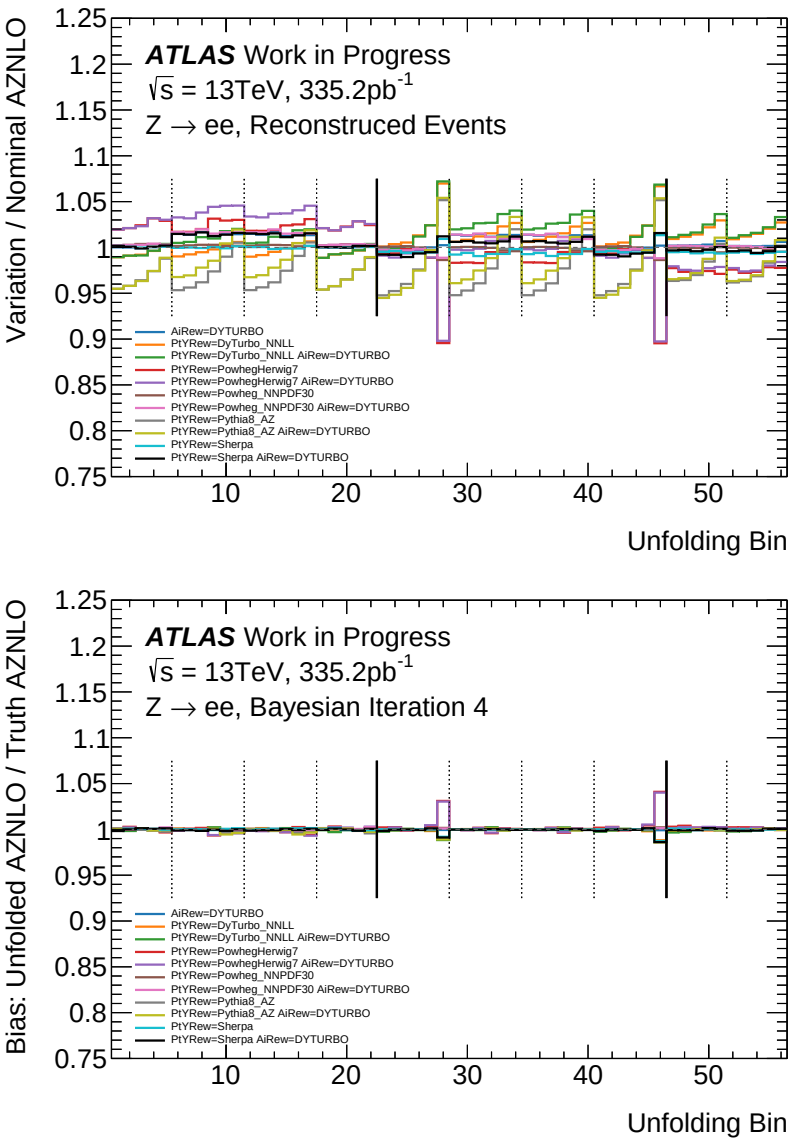

Figure 8.15: Shown are the variations used for estimating bias uncertainty compared to the nominal Powheg+Pythia8 are reconstructed level and the difference in unfolded Powheg+Pythia8 after (with Bayesian 4th iteration) unfolding with response matrix defined by each variation. These results are obtained from the $\sqrt{s} = 13\,\text{TeV}$ $Z \to ee$ channel MC. Similar results are observed for the other unfoldings.

- Pythia8 AZ (CTEQ6L1)
- Sherpa (NNPDF3.0 NNLO)

where the corresponding PDF set for each prediction has been labelled.

What is important is that a sizeable spread of values is observed at reconstructed level. The exact technical details of what causes these differences are not strictly needed for the study. Figure 8.15 shows the impact of the $\sqrt{s} = 13\,\text{TeV}$ variations at the reconstructed level as well as the variation of unfolded Powheg+Pythia8 compared to true Powheg+Pythia8. The reconstructed level variations show a spread of up to 10% in $|y_{\ell\ell}|$ bins in some slices with an average of about 4% over all bins. The variation in unfolded Powheg+Pythia8 for fourth

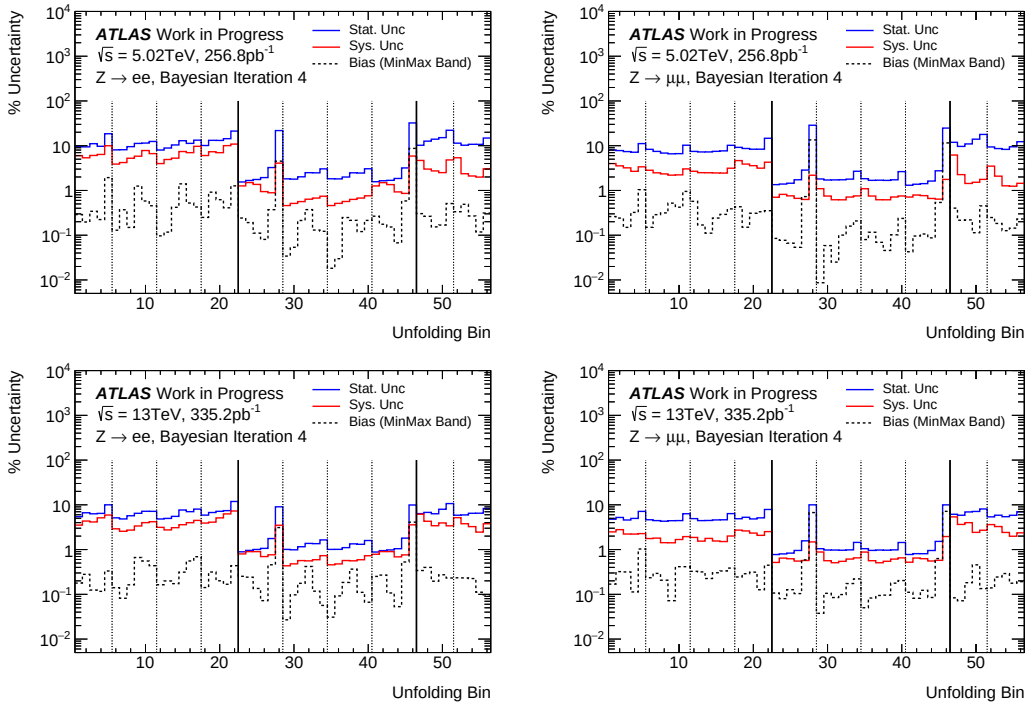

Figure 8.16: The bias uncertainties compared with the total statistical and systematic uncertainties. Shown for the $Z \to ee$ and $Z \to \mu\mu$ channels at $\sqrt{s} = 5.02\,\text{TeV}$ channels.

iteration bayesian unfolding (the final selected algorithm) is shown to be considerably smaller in most bins, with larger contributions only appearing in the high $|y_{\ell\ell}|$, $\cos(\theta^*_{CS})$ bins where the spread at reconstructed level is also largest.

The spread of unfolded Powheg+Pythia8 compared to true Powheg+Pythia8 is measured using an envelope (denoted "MinMax" band). This is a conservative estimate defined by the maximum deviation from the true distribution, considering derivations both above and below. In Figure 8.16 the bias uncertainty is compared to the total statistical and systematic uncertainties in each channel. The bias uncertainty is shown to be negligible except for in high $|y_{\ell\ell}|$, $\cos(\theta^*_{CS})$ bins, where it nevertheless is still below the statistical uncertainty.

8.8 Results

This section presents the unfolded cross-section results with a qualitative discussion of their agreement with Powheg+Pythia8 AZNLO. The electron and muon channel combination is then presented, before giving a quantitative discussion of their agreement with Powheg+Pythia8 AZNLO. Finally, the inclusive fiducial cross-section results are presented.

8.8.1 Unfolded Cross-Section Result

Figure 8.17 and Figure 8.18, respectively, show the unfolded differential cross-section compared to Powheg+Pythia8 AZNLO and the relative uncertainty breakdown for $Z \to ee$ and $Z \to \mu\mu$

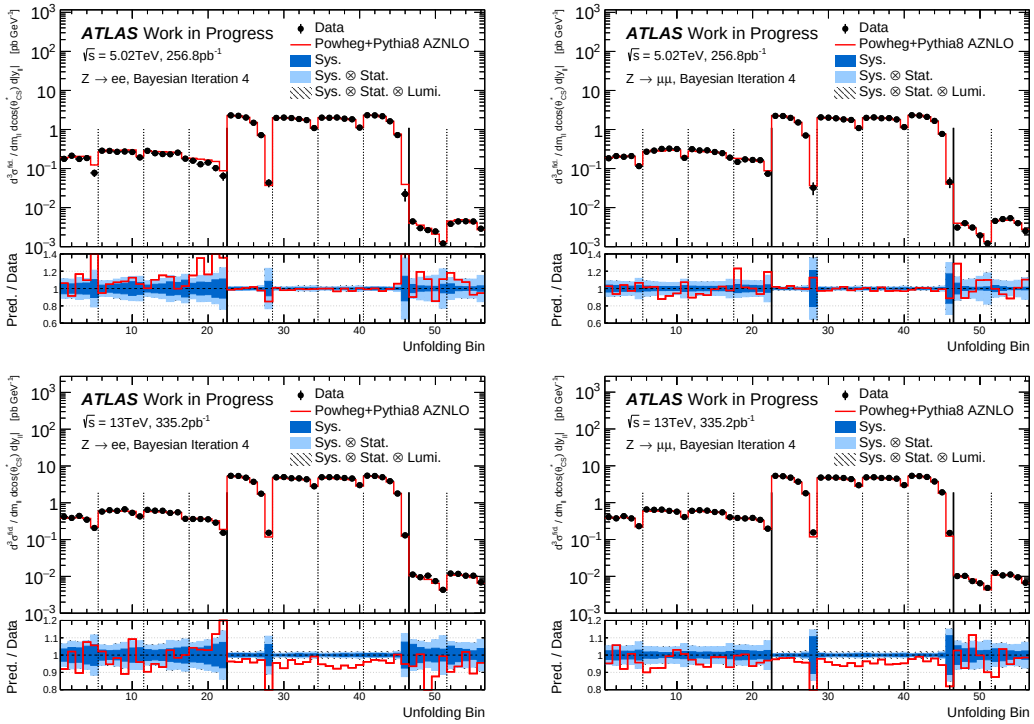

Figure 8.17: The unfolded differential cross-section results in the unravelled binning scheme compared to Powheg+Pythia8 AZNLO. $Z \to ee$ (left) and $Z \to \mu\mu$ (right) at $\sqrt{s} = 5.02$ TeV (top) and $\sqrt{s} = 13$ TeV (bottom).

channels at $\sqrt{s} = 5.02$ TeV and $\sqrt{s} = 13$ TeV. The results can be found tabulated in Appendix C.4.

The data statistical uncertainties in the central-mass slice are of the order of about 1% and 2% at $\sqrt{s} = 5.02$ TeV and $\sqrt{s} = 13$ TeV respectively with the exception of the bins at $|\cos(\theta^*_{CS})| > 0.4$ and $2.0 < |y_{\ell\ell}| < 2.4$ which have statistical uncertainties > 10%. In the central-mass slice, the luminosity uncertainty is comparable to the statistical uncertainty for $\sqrt{s} = 5.02$ TeV and is the dominant uncertainty at $\sqrt{s} = 13$ TeV. In the central-mass slice the uncertainty from the electron SFs is comparable to the statisitcal uncertainty in some bins with $|\cos(\theta^*_{CS})| > 0.4$. The uncertainty from muon SFs is well below the statitstical uncertainty. Uncertainty for the low-mass and high-mass slices are dominated by the data statistical uncertainty with about 10% and 5% uncertainties for $\sqrt{s} = 5.02$ TeV and $\sqrt{s} = 13$ TeV respectively. The next largest uncertainty is from the background modelling uncertainty, which is largely multijet uncertainty for low-mass bins and $t\bar{t}$ modelling uncertainty for the $\sqrt{s} = 13$ TeV high-mass bins.

The unfolded results at $\sqrt{s} = 5.02$ TeV show good agreement with Powheg+Pythia8 AZNLO with fluctuations comparable to the size of the uncertainties. The unfolded results at $\sqrt{s} = 13$ TeV show a consistent offset compared to Powheg+Pythia8 which is significant in the central-mass region.

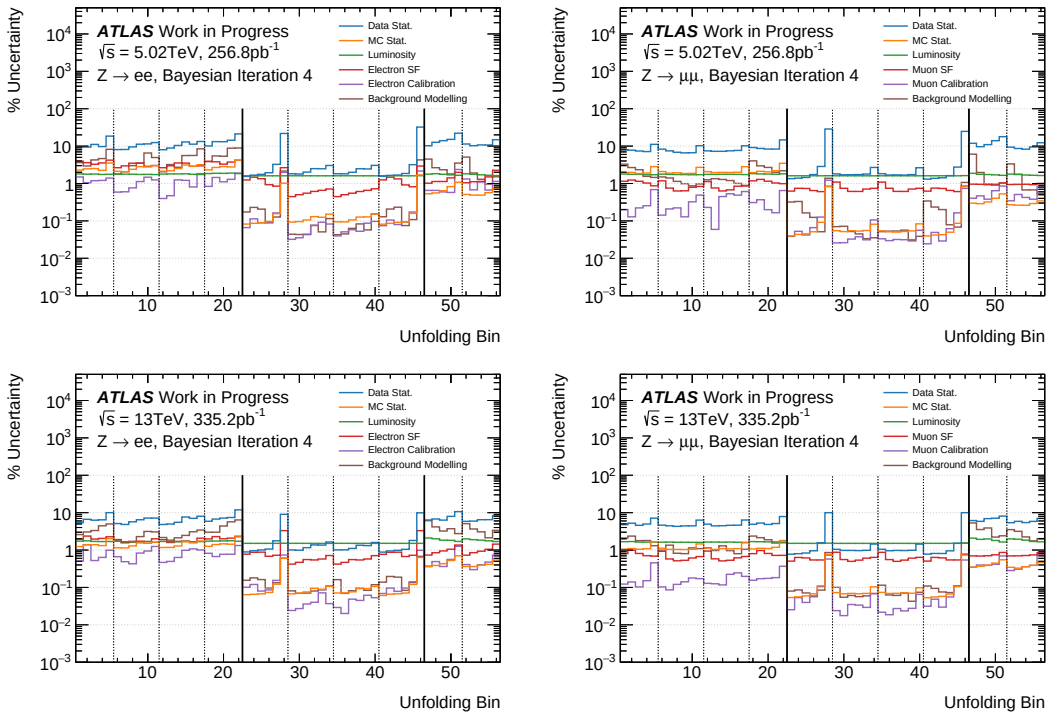

Figure 8.18: Uncertainty breakdown of the unfolded differential cross-section in the unravelled binning scheme. $Z \to ee$ (left) and $Z \to \mu\mu$ (right) at $\sqrt{s} = 5.02\,\text{TeV}$ (top) and $\sqrt{s} = 13\,\text{TeV}$ (bottom).

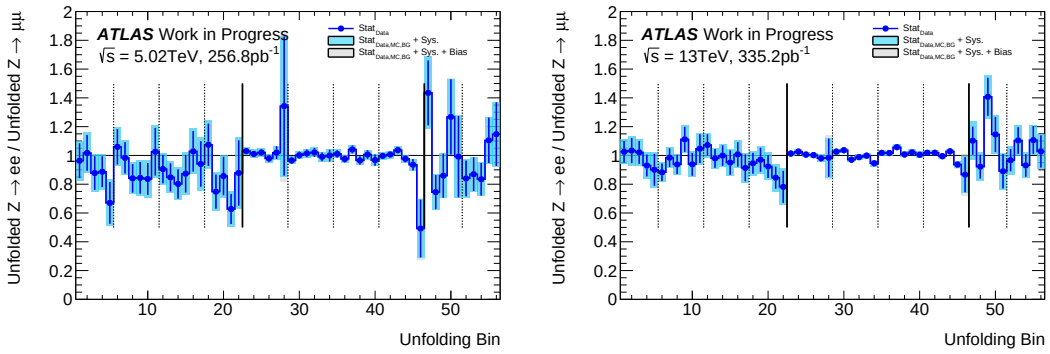

Figure 8.19: Ratio of unfolded differential cross-section between $Z \to ee$ and $Z \to \mu\mu$ in the unravelled binning scheme at $\sqrt{s} = 5.02\,\text{TeV}$ (left) and $\sqrt{s} = 13\,\text{TeV}$ (right).

8.8.2 Channel Compatibility

Figure 8.19 shows the ratio of $Z \to ee$ and $Z \to \mu\mu$ unfolded results. Good agreement is observed between the channels in the central-mass and high-mass slices within uncertainties and where the uncertainties are small the ratio is observed to be unity within $\approx 5\%$. The low-mass slices display small trends at $\sqrt{s} = 5\,\text{TeV}$ however as there is also an increase in systematic uncertainty this is not necessarily problematic.

8.8.3 Channel Combination

Lepton universality suggests the Born-level cross-section results in the $Z \to ee$ and $Z \to \mu\mu$ will be identical distributed. With this in mind, a combined $Z \to \ell\ell$ average is calculated to improve the precision of the measurement. The combination is performed using the HERAverager [154] tool, which allows the combination of the measurement with consideration of the correlated systematic uncertainties that are shared between the measurements. For this analysis, most uncertainties are not correlated between channels, but the exceptions are the cross-section normalisation, the $t\bar{t}$ modelling uncertainties and the luminosity uncertainty.

The combination procedure is based on the the minimisation of the χ^2 function defined as:

$$\chi^2(\vec{m}, \vec{b}) = \sum_{e}^{N_e} \sum_{i}^{N_M} \frac{\left(m_i - \mu_{e,i} - \sum_j^{N_S} \Gamma^i_{j,e} b_j\right)^2}{\Delta^2_{i,e}} \times w_{i,e} + \sum_{j}^{N_S} b_j^2 \tag{8.44}$$

where:

- $\vec{m}$ is a vector of averaged values in each of the N_M analysis bins i. To be obtained from χ^2 minimisation.
- $\vec{b}$ is a vector of length N_S nuisance parameters b_j corresponding to each source of systematic uncertainty.
- N_e is the number of experiments (in this case $N_e = 2$ for $Z \to ee$ and $Z \to \mu\mu$).
- $\mu_{i,e}$ is the measured value for bin i in measurement e
- $\Gamma^i_{j,e}$ is the absolute correlated systematic uncertainty. It is equal to zero if the measurement in bin i in experiment e is insensitive to the source of systematic error j.
- $\Delta^2_{i,e}$ is the total uncorrelated uncertainty for bin i in measurement e. In this case it is the quadratic sum of the statistical uncertainties.
- $w_{i,e}$ is equal to 1 if measurement e contributes to a measurement at point i otherwise it is set to zero.

The averaged result is then produced by minimising the χ^2 function:

$$\frac{\partial \chi^2(\vec{m}, \vec{b})}{\partial \vec{m}} = 0 \tag{8.45}$$

Figure 8.20 shows the comparison of $Z \to ee$ and $Z \to \mu\mu$ to the averaged $Z \to \ell\ell$ result. The smaller statistical uncertainties in the $Z \to \mu\mu$ channel and larger systematic uncertainties on $Z \to ee$ (notably in the low-mass bins) result in the $Z \to \ell\ell$ result being closer to the $Z \to \mu\mu$ channel. The minimised χ^2/NDF values are:

- $\sqrt{s} = 5.02\,\text{TeV}$: $\chi^2/NDF = 52.9/56$ (p-value = 0.60)
- $\sqrt{s} = 13\,\text{TeV}$: $\chi^2/NDF = 78.9/56$ (p-value = 0.02)

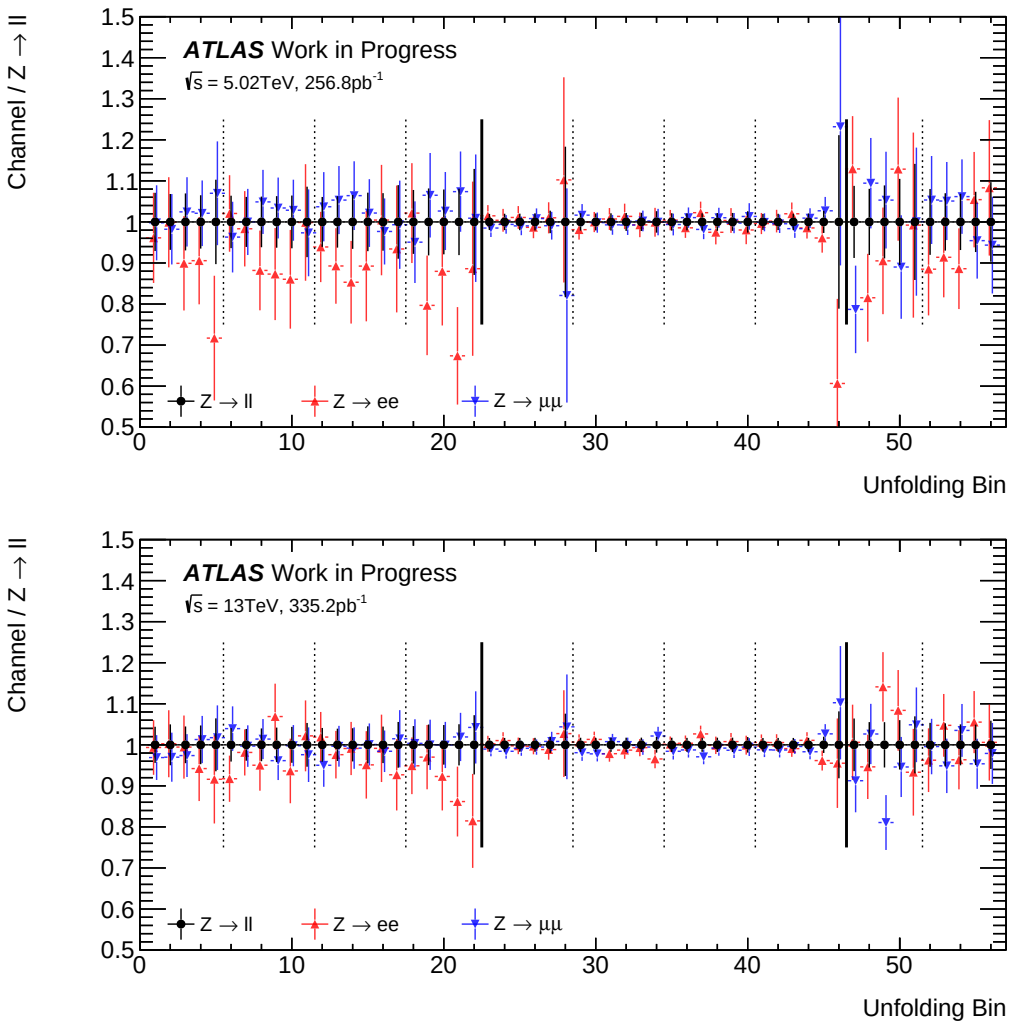

Figure 8.20: Plots showing the $Z \to ee$ and $Z \to \mu\mu$ unfolded Born-level cross-sections compared to the combined lepton result $Z \to \ell\ell$.

The $\sqrt{s} = 5.02$ TeV results yield a χ^2/NDF close to 1.0 whereas the value at $\sqrt{s} = 13$ TeV is about 1.4. The $\sqrt{s} = 13$ TeV results have sizeable contributions from systematic uncertainty sources which suggests there may be an under-estimation of systematic uncertainties by 10-20% in magnitude or an issue in the correlation model. The statistical uncertainties in the $\sqrt{s} = 5.02$ TeV results are much more dominant, so the impact of under-estimation of systematic uncertainties is dampened.

8.8.4 Combined Channel Cross-Section Results

Figure 8.21 and Figure 8.22 show the comparison of the combined Born-level differential cross-section to Powheg+Pythia8 AZNLO in each slice of ($m_{\ell\ell}$,cos($\theta*_{CS}$)) at $\sqrt{s} = 5.02$ TeV and $\sqrt{s} = 13$ TeV respectively. The χ^2/NDF is evaluated for each slice using all experimental uncertainties and the corresponding bin to bin correlations without any theoretical uncertainties on the Powheg+Pythia8 AZNLO prediction. Excellent agreement is observed for all slices at $\sqrt{s} = 5.02$ TeV with χ^2/NDF close to 1.0. Good agreement is observed for $\sqrt{s} = 13$ TeV the

low-mass and high-mass slices which have χ^2/NDF compatible with 1.0, but worse agreement is seen in the the central-mass slices where the χ^2/NDF is significantly larger than 1.0. This is also observed for the χ^2/NDF evaluated across all bins. These are:

- $\sqrt{s}$ = 5.02 TeV: χ^2/NDF = 42.4/56 (p-value = 0.91).
- $\sqrt{s}$ = 13 TeV: χ^2/NDF = 115.9/56 (p-value <0.00001).

8.8.5 Integrated Fiducial Cross-Section Results

To produce an integrated fiducial cross-section measurement, the differential cross-section is intergated over all 3D bins within a certain mass bin. This involves multiplying the differential cross-section by the bin width factor:

$$\sigma^{\text{fid.}} = \sum_{i}^{N_{\text{bins}}} \sigma^{\text{3D,bin}=i} \times \Delta_i. \tag{8.46}$$

Here N_{bins} is the number of bins at the given mass slice and $\Delta_i = \Delta_i m_{\ell\ell} \Delta_i \cos(\theta^*_{CS}) \Delta_i |y_{\ell\ell}|$ is the product of the bin dimensions for bin i. The phase space for these fiducial cross-section measurements is defined by both the phase space discussed in Section 8.3 and the boundaries in $m_{\ell\ell}$, $|y_{\ell\ell}|$ and $\cos(\theta^*_{CS})$ that define the 3D bins. The integrated fiducial cross-sections are summarised in Table 8.7. The results show that the central-mass estimates are dominated by their luminosity uncertainty. The low-mass and high-mass estimates have statistical and systematic uncertainties comparable in size to the luminosity uncertainty. The central-mass fiducial cross-sections are slightly larger than previous fiducial measurements: $\sigma^{\text{fid.}}$ = 374.5 ± 0.9%(stat.) ± 1.0%(syst.) ± 1.9%(lumi.) pb [47] and $\sigma^{\text{fid.}}$ = 777 ± 0.1%(stat.) ± 0.4%(syst.) ± 0.7%(beam) ± 2.1%(lumi.) pb [50] at $\sqrt{s}$ = 5.02 TeV and $\sqrt{s}$ = 13 TeV respectively. These measurements have different phase-space with $p_T(\ell) > 20$ GeV, $|y_{\ell\ell}| < 2.5$ and $p_T(\ell) > 25$ GeV, $|y_{\ell\ell}| < 2.5$ at $\sqrt{s}$ = 5.02 TeV and $\sqrt{s}$ = 13 TeV respectively. Nonetheless, this shows the magnitude of these integrated fiducial cross-sections is comparable and that at $\sqrt{s}$ = 13 TeV the choice of $p_T(\ell) > 15$ GeV sizeably increses the fiducial cross-section.

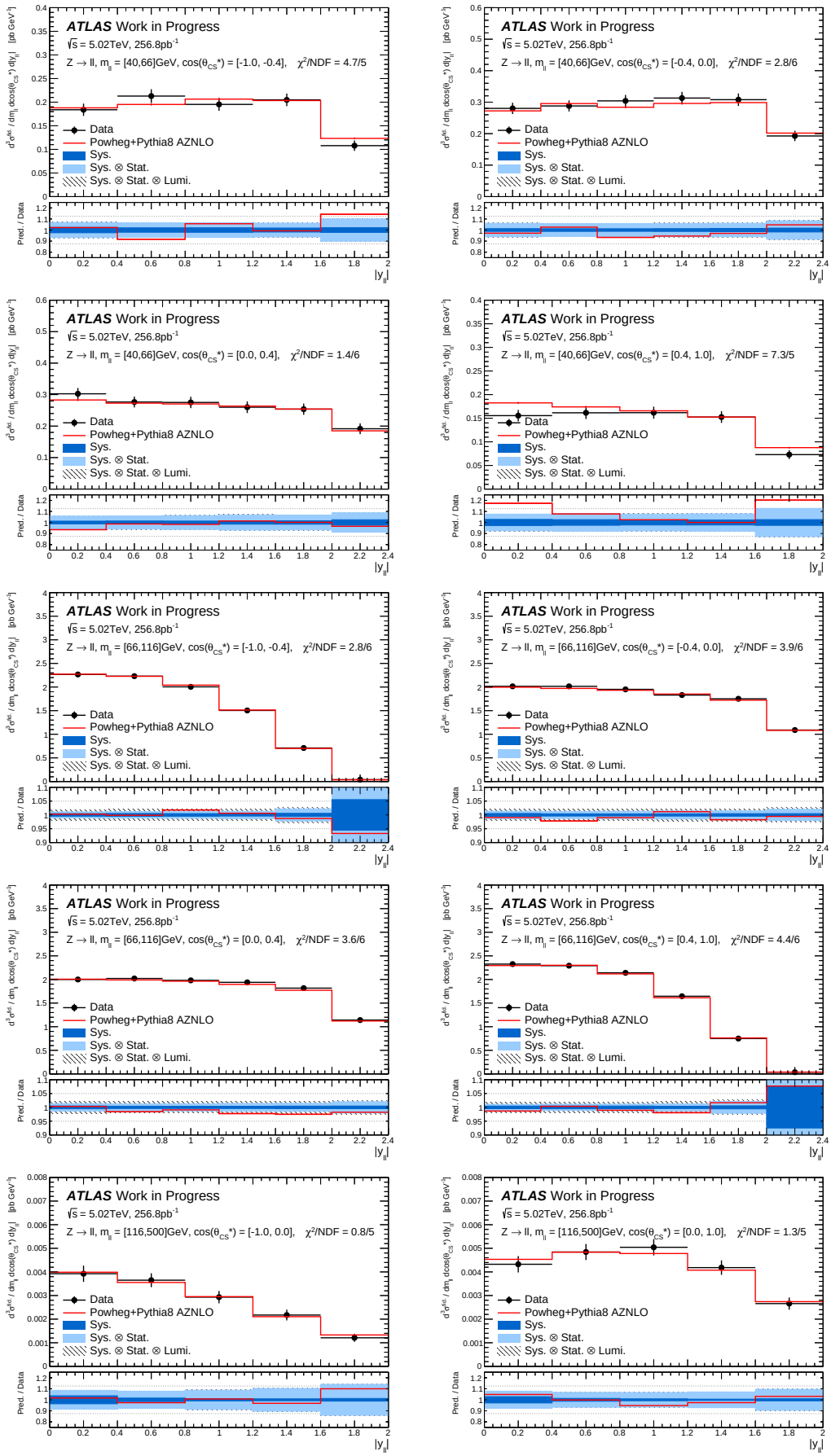

Figure 8.21: Shown are results for the combined Born-level cross-section for $\sqrt{s} = 5.02\,\text{TeV}$. These are the $|y_{\ell\ell}|$ distributions for each $m_{\ell\ell}$ and $\cos(\theta^*_{CS})$ slice.

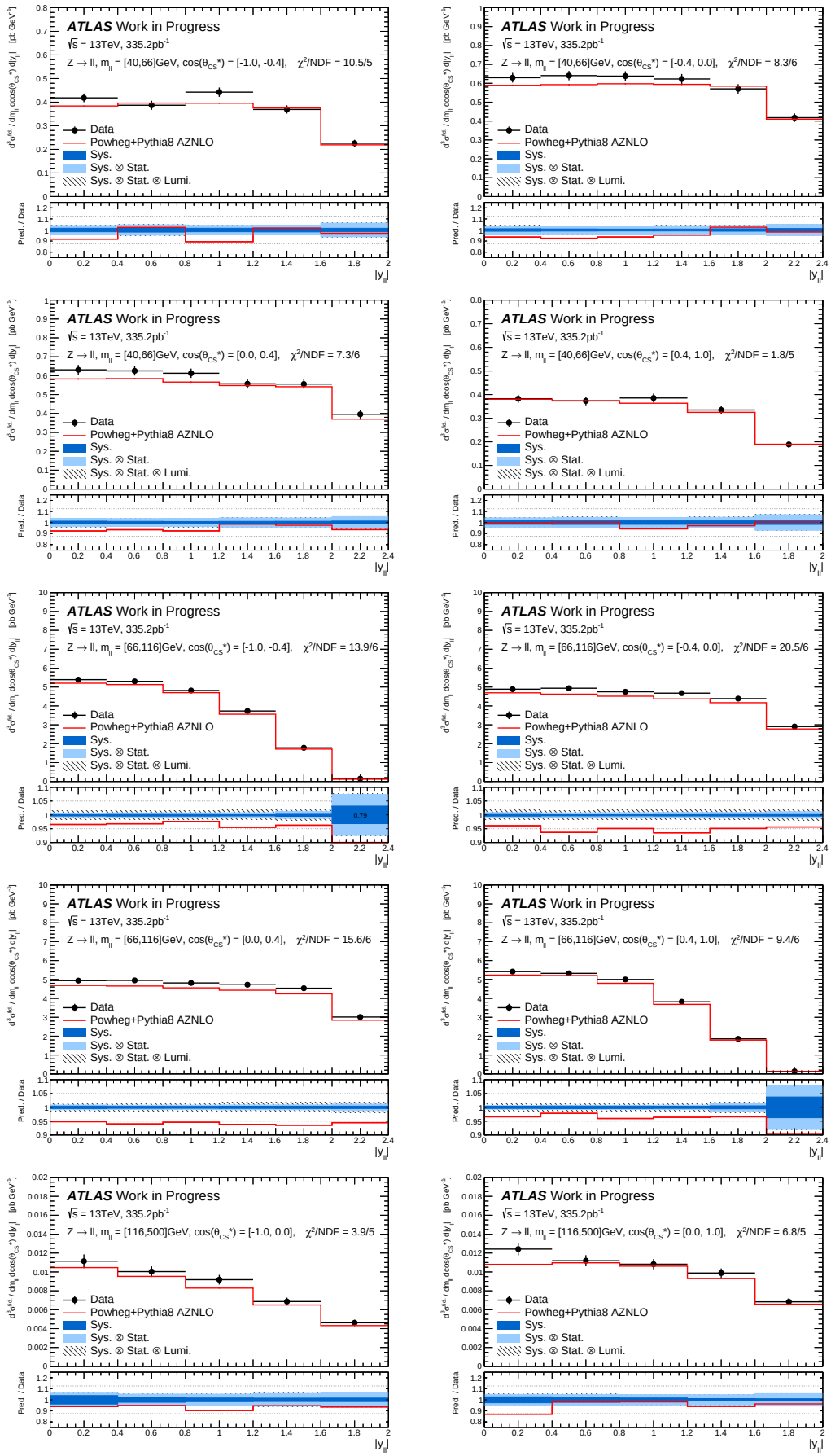

Figure 8.22: Shown are results for the combined Born-level cross-section for $\sqrt{s} = 13\,\text{TeV}$. These are the $|y_{\ell\ell}|$ distributions for each $m_{\ell\ell}$ and $\cos(\theta^*_{CS})$ slice.

	$\sigma^{\text{fid.}}$ [pb]	± stat.(%)	± sys.(%)	± lumi.(%)
$\sqrt{s}$ = 5.02 TeV 40 GeV < $m_{\ell\ell}$ < 66 GeV	23.54	0.34 (1.4%)	0.43 (1.8%)	0.42 (1.8%)
$\sqrt{s}$ = 5.02 TeV 66 GeV < $m_{\ell\ell}$ < 116 GeV	387.7	1.1 (0.3%)	2.0 (0.5%)	6.2 (1.6%)
$\sqrt{s}$ = 5.02 TeV 116 GeV < $m_{\ell\ell}$ < 500 GeV	5.367	0.14 (2.5%)	0.091 (1.7%)	0.094 (1.7%)
$\sqrt{s}$ = 13 TeV 40 GeV < $m_{\ell\ell}$ < 66 GeV	50.58	0.44 (0.9%)	0.68 (1.4%)	0.82 (1.6%)
$\sqrt{s}$ = 13 TeV 66 GeV < $m_{\ell\ell}$ < 116 GeV	940.8	1.5 (0.2%)	4.2 (0.4%)	14 (1.5%)
$\sqrt{s}$ = 13 TeV 116 GeV < $m_{\ell\ell}$ < 500 GeV	14.28	0.22 (1.5%)	0.30 (2.1%)	0.27 (1.9%)

Table 8.7: Fiducial integrated cross-section results for $\sqrt{s}$ = 5.02 TeV and $\sqrt{s}$ = 13 TeV $Z \to \ell\ell$ production in the three analysis mass-slices 40 GeV < $m_{\ell\ell}$ < 66 GeV, 66 GeV < $m_{\ell\ell}$ < 116 GeV and 116 GeV < $m_{\ell\ell}$ < 500 GeV. These results are calculated by merging the individual bins of the combined lepton differential cross-section results.

9 Summary

This thesis presented two analyses involving Drell-Yan production using ATLAS Run-2 pp collision data and gave an overview of the necessary theoretical and experimental background behind the measurements.

Chapter 6 presented the the derivation of muon trigger efficiency scale factors at both $\sqrt{s} = 5.02\,\text{TeV}$ and $\sqrt{s} = 13\,\text{TeV}$. The dependence of the corrections on η^{μ} was observed in 1D before devising a 2D scale factor map that lines up with the calorimeter bins used by electrons and to allow measurement below $p_T(\mu) = 20\,\text{GeV}$.

Chapter 7 presented the new Z-counting method for luminosity monitoring at ATLAS by counting $Z \to ee$ and $Z \to \mu\mu$ events, which is a self-calibrating measurement of luminosity independent of Van der Meer scans. Studies were shown of individual LHC fills as well as the full $\sqrt{s} = 13\,\text{TeV}$ high-μ Run-2 dataset. Residual corrections determined from Monte Carlo were determined to have a dependence on pileup of 2-3% with a difference of 10% in magnitude between $Z \to ee$ and $Z \to \mu\mu$. The validity of these corrections was shown through the excellent stability of $Z \to ee$ and $Z \to \mu\mu$ vs pileup (time) of 0.6% (1.5%). The use of Z-counting as a relative luminometer was shown with comparisons of $Z \to \ell\ell$ to the baseline ATLAS luminosity, where year-dependent trends were observed with a 1% difference between 2016 and 2018. Finally, the statistical bias on the Z-counting absolute luminosity was shown to be as large as 2% for low luminosity data-taking conditions and 0.1-0.3% for most Run-2 data-taking. After normalisation, this impact is well below 0.1%. As the LHC ramps up for Run-3 and the future holds a push to high-μ conditions with the HL-LHC, it is clear that Z-Counting will offer invaluable insight for future luminosity studies at ATLAS as a relative luminometer. Its use as an absolute luminometer relies on improvements to the process cross-section either from improved PDF modelling or from dedicated precision experimental measurements.

Chapter 8 presented the triple-differential Drell-Yan cross-section measurements in $m_{\ell\ell}$, $|y_{\ell\ell}|$ and $\cos(\theta^*_{CS})$ using the special low-μ datasets from 2017 and 2018, constituting 256.8 pb^{-1} at $\sqrt{s} = 5.02\,\text{TeV}$ and 335.2 pb^{-1} at $\sqrt{s} = 13\,\text{TeV}$. Care was taken to produce an analysis binning that best utilises the available data. The full analysis chain of the measurement was performed with a data-driven estimate of the mulitjet background, all experimental uncertainties and an optimisation of the unfolding. The unfolded cross-sections were shown to have statistical uncertainties in the range of 5-15% in the low-mass and high-mass bins and in the range of 0.5-2% in the central-mass bins. Statistical uncertainties are the limiting uncertainties for all low-mass and high-mass bins, whereas, in the central-mass bins, luminosity and systematic uncertainties are similar. A combination between electron and muon channels was performed

showing excellent compatibility at $\sqrt{s} = 5.02\,\text{TeV}$ with worse agreement at $\sqrt{s} = 13\,\text{TeV}$. The combined results were compared to Powheg+Pythia8 AZNLO where good compatibility was observed at $\sqrt{s} = 5.02\,\text{TeV}$ with worse agreement observed at $\sqrt{s} = 13\,\text{TeV}$. Integrated fiducial cross-sections were obtained from the combined differential results, where it was observed that the uncertainty on the central-mass cross-sections was dominated by luminosity uncertainty, showing their potential to be the most precise Drell-Yan cross-section measurements. The low-mass and high-mass cross-sections was observed to have statistical and systematic uncertainties of comparable magnitude. Future work on this analysis will focus on interpretation of these results, such as studying the constraining power of the data in PDF fits and comparing it to higher-order predictions.

Appendix

A Low-μ Analysis Lepton Scale Factor

This section shows the scale factor maps for used in the low-*mu* analyses.

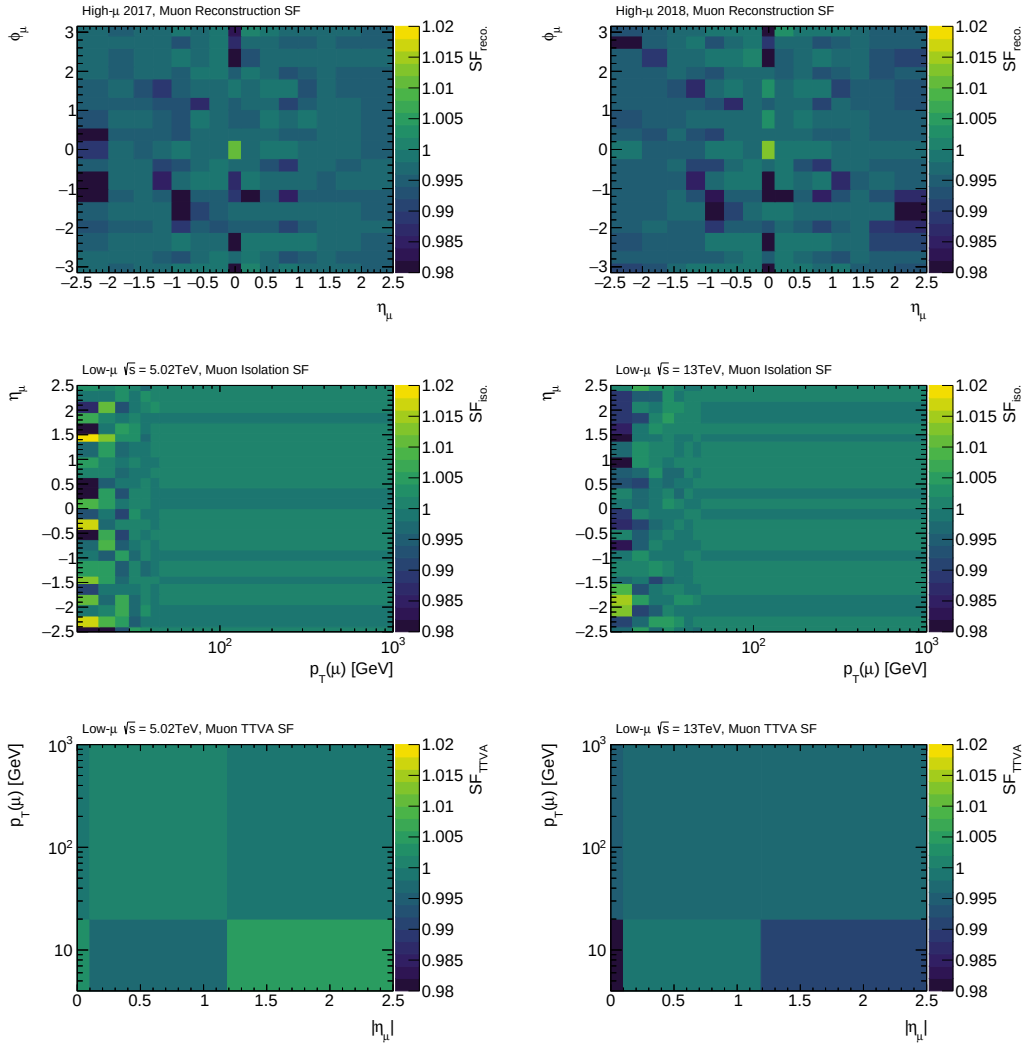

Figure A.1: Single-Muon Reconstruction (row 1), Isolation (row 2) and TTVA (row 3) scale factors used for low-μ analysis. The Reconstruction scale factors are derived for 2017 and 2018 respectively. Isolation and TTVA are derived for $\sqrt{s} = 5.02\,\text{TeV}$ and $\sqrt{s} = 13\,\text{TeV}$, [135].

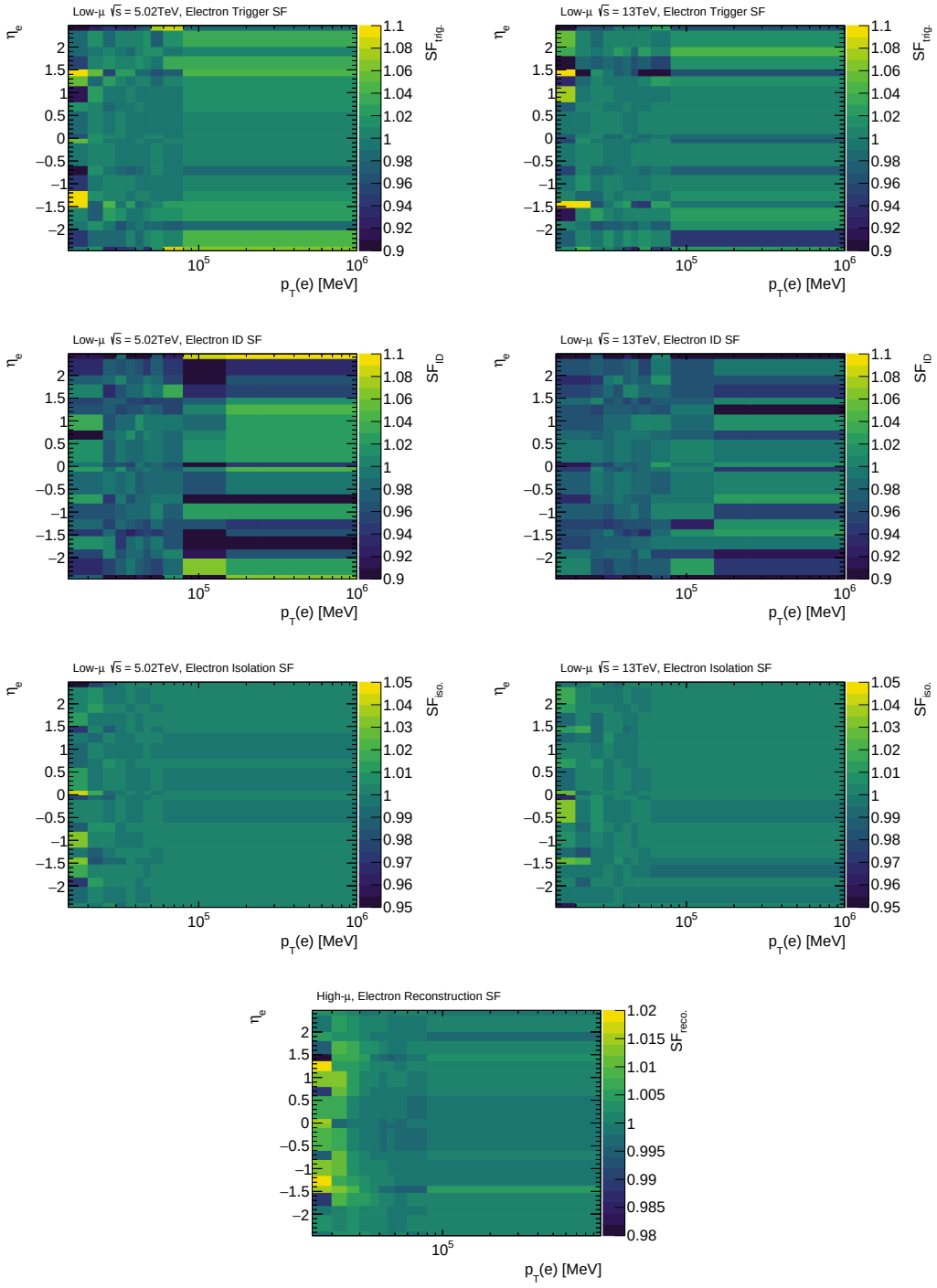

Figure A.2: Single-Electron Trigger (row 1), Identification (row 2), Isolation (row 3) scale factors used for low-μ analysis at both $\sqrt{s} = 5.02\,\text{TeV}$ and $\sqrt{s} = 13\,\text{TeV}$. The Reconstruction (row 4) scale factor map is used for both $\sqrt{s} = 5.02\,\text{TeV}$ and $\sqrt{s} = 13\,\text{TeV}$. Values taken from Ref. [134].

B Additional Z-Counting Material

B.1 Uncertainty Calculations

The uncertainty calculations used for Z-counting propagate the statistical components of both the raw event selection and tag-and-probe selections. The formulae are based on gaussian uncertainty propagation rules, assuming the high-statistics limit of Poisson distributions with a symmetric gaussian of standard deviation of = $\sqrt{N}$ used for modelling the uncertainty on each count. The following formulae assume zero correlation between terms.

The uncertainty calculation performed for single-LB luminosity estimate is:

$$\delta_{\mathcal{L}_{Z\to\ell^+\ell^-}(LB)} = \frac{(1-f_{\text{bkg}})}{\sigma_{\text{theory}} \times A^{\text{MC}}_{Z\to\ell^+\ell-} F^{\text{MC}}_{Z\to\ell^+\ell-}(\langle\mu\rangle)\cdot t(LB)} \cdot \sqrt{\left(\frac{\delta_{N_{Z\to\ell^+\ell^-}(LB)}}{\varepsilon^{\text{T\&P}}_{Z\to\ell^+\ell-}(LB)}\right)^2 + \left(\frac{N_{Z\to\ell^+\ell^-}(LB)\cdot\delta_{\varepsilon^{\text{T\&P}}_{Z\to\ell^+\ell-}(LB)}}{(\varepsilon^{\text{T\&P}}_{Z\to\ell^+\ell-}(LB))^2}\right)^2} \tag{B.1}$$

The efficiency calculations contain many parameters, increasing the complexity of the efficiency calculation. These expressions were derived with software and verified by hand. The most complex is the electron reconstruction efficieincy uncertainty:

$$\begin{aligned}
\delta^2_{\varepsilon_{\text{reco},1e}} = {} & \frac{\delta^2_{N^{\text{OS}}_{\text{tail,fail}}} N^{\text{OS},2}_{\text{peak,template}} N^{\text{OS},2}_{\text{tail,template}} \left(N^{\text{OS}}_{\text{peak,pass}} N^{\text{SS}}_{\text{tail,template}} - N^{\text{SS}}_{\text{tail,pass}} N^{\text{OS}}_{\text{peak,template}}\right)^2}{N^{\text{SS},2}_{\text{tail,template}} \left(N^{\text{OS}}_{\text{tail,fail}} N^{\text{OS}}_{\text{peak,template}} - N^{\text{OS}}_{\text{tail,template}} \left(N^{\text{OS}}_{\text{peak,pass}} + N^{\text{OS}}_{\text{peak,fail}}\right)\right)^4} \\
& + \frac{\delta^2_{N^{\text{OS}}_{\text{peak,template}}} N^{\text{OS},2}_{\text{tail,template}} \left(N^{\text{OS}}_{\text{peak,pass}} N^{\text{SS}}_{\text{tail,pass}} N^{\text{OS}}_{\text{tail,template}} - N^{\text{OS}}_{\text{peak,pass}} N^{\text{OS}}_{\text{tail,fail}} N^{\text{SS}}_{\text{tail,template}} + N^{\text{SS}}_{\text{tail,pass}} N^{\text{OS}}_{\text{peak,fail}} N^{\text{OS}}_{\text{tail,template}}\right)^2}{N^{\text{SS},2}_{\text{tail,template}} \left(N^{\text{OS}}_{\text{peak,pass}} N^{\text{OS}}_{\text{tail,template}} + N^{\text{OS}}_{\text{peak,fail}} N^{\text{OS}}_{\text{tail,template}} - N^{\text{OS}}_{\text{tail,fail}} N^{\text{OS}}_{\text{peak,template}}\right)^4} \\
& + \frac{\delta^2_{N^{\text{OS}}_{\text{tail,template}}} N^{\text{OS},2}_{\text{tail,fail}} N^{\text{OS},2}_{\text{peak,template}} \left(N^{\text{OS}}_{\text{peak,pass}} N^{\text{SS}}_{\text{tail,template}} - N^{\text{SS}}_{\text{tail,pass}} N^{\text{OS}}_{\text{peak,template}}\right)^2}{N^{\text{SS},2}_{\text{tail,template}} \left(N^{\text{OS}}_{\text{tail,fail}} N^{\text{OS}}_{\text{peak,template}} - N^{\text{OS}}_{\text{tail,template}} \left(N^{\text{OS}}_{\text{peak,pass}} + N^{\text{OS}}_{\text{peak,fail}}\right)\right)^4} \\
& + \frac{\delta^2_{N^{\text{OS}}_{\text{peak,fail}}} N^{\text{OS},4}_{\text{tail,template}} \left(N^{\text{OS}}_{\text{peak,pass}} N^{\text{SS}}_{\text{tail,template}} - N^{\text{SS}}_{\text{tail,pass}} N^{\text{OS}}_{\text{peak,template}}\right)^2}{N^{\text{SS},2}_{\text{tail,template}} \left(N^{\text{OS}}_{\text{tail,fail}} N^{\text{OS}}_{\text{peak,template}} - N^{\text{OS}}_{\text{tail,template}} \left(N^{\text{OS}}_{\text{peak,pass}} + N^{\text{OS}}_{\text{peak,fail}}\right)\right)^4} \\
& + \frac{\delta^2_{N^{\text{SS}}_{\text{tail,pass}}} N^{\text{OS},2}_{\text{peak,template}} N^{\text{OS},2}_{\text{tail,template}}}{N^{\text{SS},2}_{\text{tail,template}} \left(N^{\text{OS}}_{\text{tail,fail}} N^{\text{OS}}_{\text{peak,template}} - N^{\text{OS}}_{\text{tail,template}} \left(N^{\text{OS}}_{\text{peak,pass}} + N^{\text{OS}}_{\text{peak,fail}}\right)\right)^2} \\
& + \frac{\delta^2_{N^{\text{OS}}_{\text{peak,pass}}} N^{\text{OS},2}_{\text{tail,template}} \left(N^{\text{SS}}_{\text{tail,pass}} N^{\text{OS}}_{\text{peak,template}} N^{\text{OS}}_{\text{tail,template}} + N^{\text{OS}}_{\text{peak,fail}} N^{\text{OS}}_{\text{tail,template}} N^{\text{SS}}_{\text{tail,template}} - N^{\text{OS}}_{\text{tail,fail}} N^{\text{OS}}_{\text{peak,template}} N^{\text{SS}}_{\text{tail,template}}\right)^2}{N^{\text{SS},2}_{\text{tail,template}} \left(N^{\text{OS}}_{\text{peak,pass}} N^{\text{OS}}_{\text{tail,template}} + N^{\text{OS}}_{\text{peak,fail}} N^{\text{OS}}_{\text{tail,template}} - N^{\text{OS}}_{\text{tail,fail}} N^{\text{OS}}_{\text{peak,template}}\right)^4} \\
& + \frac{\delta^2_{N^{\text{SS}}_{\text{tail,template}}} N^{\text{SS},2}_{\text{tail,pass}} N^{\text{OS},2}_{\text{peak,template}} N^{\text{OS},2}_{\text{tail,template}}}{N^{\text{SS},4}_{\text{tail,template}} \left(N^{\text{OS}}_{\text{tail,fail}} N^{\text{OS}}_{\text{peak,template}} - N^{\text{OS}}_{\text{tail,template}} \left(N^{\text{OS}}_{\text{peak,pass}} + N^{\text{OS}}_{\text{peak,fail}}\right)\right)^2}
\end{aligned} \tag{B.2}$$

The muon reconstruction efficieincy uncertainty is:

$$\delta_{\varepsilon_{\text{reco},1\mu}} = \sqrt{\frac{\left(\delta^2_{N^{\text{OS}}_{\text{pass}}} + \delta^2_{N^{\text{SS}}_{\text{pass}}}\right)\left(N^{\text{OS}}_{\text{fail}} - N^{\text{SS}}_{\text{fail}}\right)^2 + \left(\delta^2_{N^{\text{OS}}_{\text{fail}}} + \delta^2_{N^{\text{SS}}_{\text{fail}}}\right)\left(N^{\text{OS}}_{\text{pass}} - N^{\text{SS}}_{\text{pass}}\right)^2}{\left(N^{\text{OS}}_{\text{pass}} - N^{\text{SS}}_{\text{pass}} + N^{\text{OS}}_{\text{fail}} - N^{\text{SS}}_{\text{fail}}\right)^4}} \tag{B.3}$$

The trigger efficiency uncertainty is:

$$\delta_{\varepsilon_{\text{trig},1\ell}} = \varepsilon^2_{\text{trig},1\ell}\sqrt{\left(\frac{\delta_{N_1}}{2N_2}\right)^2 + \left(\frac{N_1\delta_{N_2}}{2N_2^2}\right)^2} \tag{B.4}$$

The combined event-level efficiency is:

$$\delta_{\varepsilon^{\text{T\&P}}_{Z\to\ell^+\ell^-}} = \sqrt{(2\varepsilon^2_{\text{reco},1\ell}(1-\varepsilon_{\text{trig},1\ell})\delta_{\varepsilon_{\text{trig},1\ell}})^2 + (2\varepsilon_{\text{reco},1\ell}(1-(1-\varepsilon_{\text{trig},1\ell})^2)\delta_{\varepsilon_{\text{reco},1\ell}})^2} \tag{B.5}$$

The following formula describes the uncertainty calculation for channel combination

$$\delta_{\mathcal{L}_{Z\to\ell^+\ell^-}(LB)} = \frac{1}{2}\sqrt{(\delta_{\mathcal{L}_{Z\to e^+e^-}(LB)}) + (\delta_{\mathcal{L}_{Z\to\mu^+\mu^-}(LB)})^2} \tag{B.6}$$

The following formula describes the uncertainty calculation when combining integrated luminosity from multiple luminosity blocks.

$$\delta_{\mathcal{L}_{\text{int},Z\to\ell^+\ell^-}(NLB)s} = \sqrt{\sum_{LB}^{NLBs}\left(t(LB)\cdot\delta_{\mathcal{L}_{Z\to\ell^+\ell^-}(LB)}\right)} \tag{B.7}$$

B.2 Additional Z-Counting Fills

This section shows plots for the 2015, 2016 and 2018 LHC Fills studied [144] and discussed along side the 2017 example fill in Section 7.3.

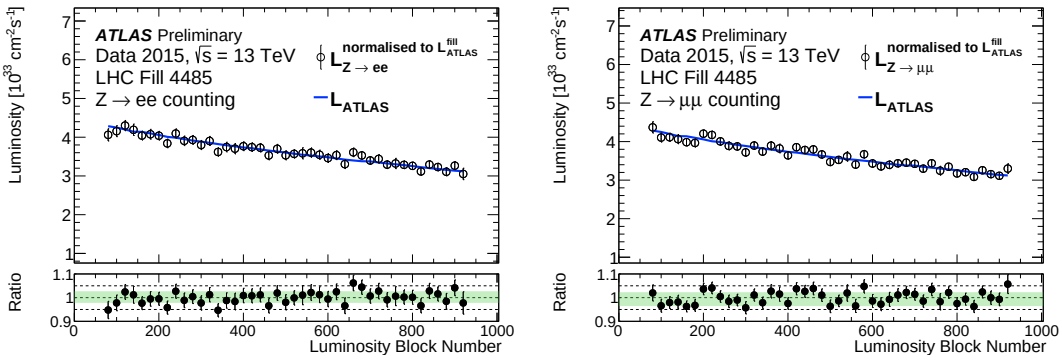

Figure B.1: The time-dependence of the instantaneous luminosity determined for $Z \to e^+e^-$ and $Z \to \mu^+\mu^-$ luminosity measurement (open circles), the ATLAS-preferred luminosity (blue lines) and the corresponding ratio (full circles). The Z-counting luminosity has been normalised to the corresponding baseline ATLAS luminosity. The respective luminosities have been averaged over blocks of 20 luminosity blocks. This shows results for a single LHC fill (4485) on October 11th 2015. Uncertainties are statistical components only and the green bands contain 68% of all points centred around the mean. Ref. [144].

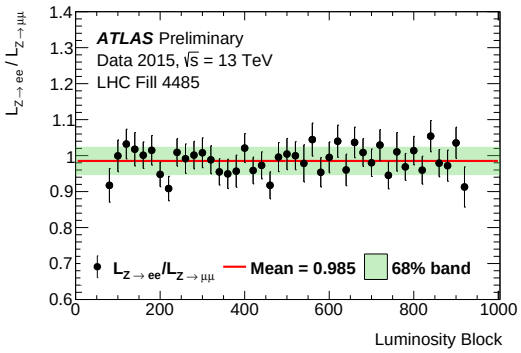

Figure B.2: Luminosity block dependence of the ratio of instantaneous luminosities determined from $Z \to e^+e^-$ and $Z \to \mu^+\mu^-$ counting. The respective luminosities have been averaged over blocks of 20 luminosity blocks. The red line indicates the mean obtained from a fit to a constant. This shows results for a single LHC fill (4485) on October 11th 2015. Uncertainties are statistical components only and the green band contains at least 68% of points centred around the mean. Ref. [144].

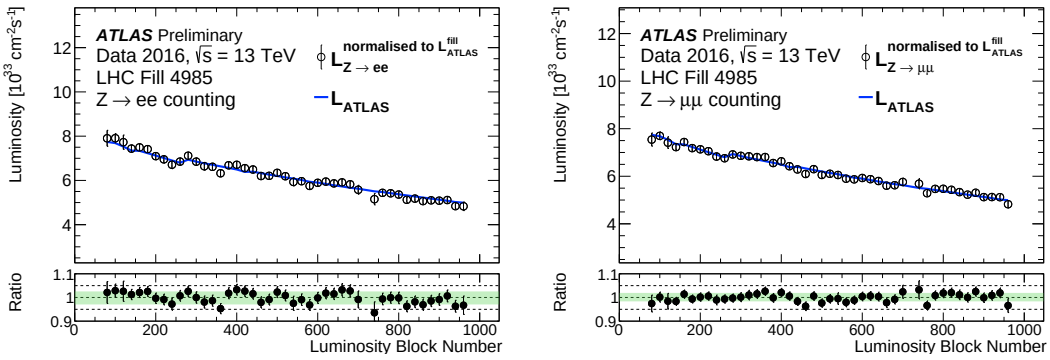

Figure B.3: The time-dependence of the instantaneous luminosity determined for $Z \to e^+e^-$ and $Z \to \mu^+\mu^-$ luminosity measurement (open circles), the ATLAS-preferred luminosity (blue lines) and the corresponding ratio (full circles). The Z-counting luminosity has been normalised to the corresponding baseline ATLAS luminosity. The respective luminosities have been averaged over blocks of 20 luminosity blocks. This shows results for a single LHC fill (4985) on June 3rd 2016. Uncertainties are statistical components only and the green bands contain 68% of all points centred around the mean. Ref. [144].

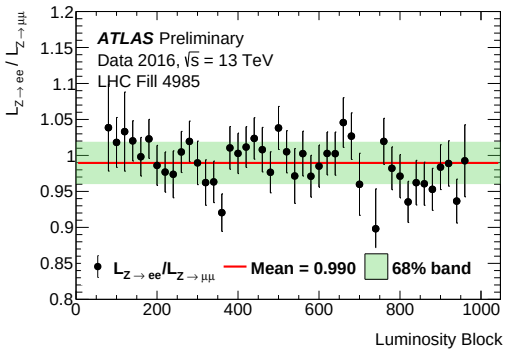

Figure B.4: Luminosity block dependence of the ratio of instantaneous luminosities determined from $Z \to e^+e^-$ and $Z \to \mu^+\mu^-$ counting. The respective luminosities have been averaged over blocks of 20 luminosity blocks. The red line indicates the mean obtained from a fit to a constant. This shows results for a single LHC fill (4985) on June 3rd 2016. Uncertainties are statistical components only and the green band contains at least 68% of points centred around the mean.

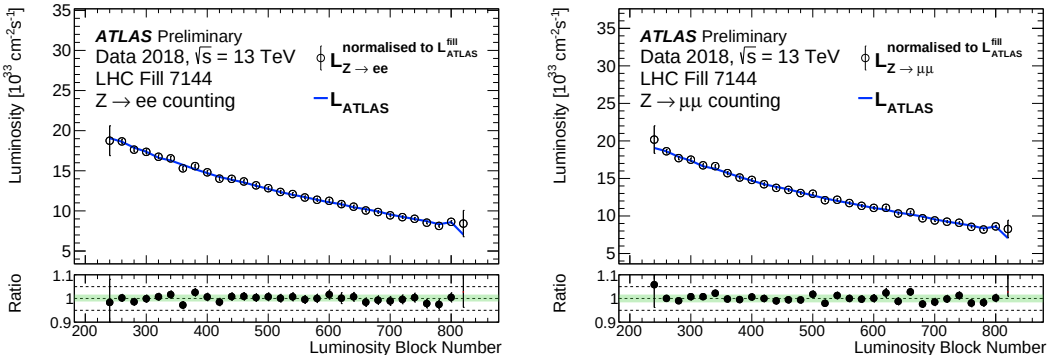

Figure B.5: The time-dependence of the instantaneous luminosity determined for $Z \to e^+e^-$ and $Z \to \mu^+\mu^-$ luminosity measurement (open circles), the ATLAS-preferred luminosity (blue lines) and the corresponding ratio (full circles). The Z-counting luminosity has been normalised to the corresponding baseline ATLAS luminosity. The respective luminosities have been averaged over blocks of 20 luminosity blocks. This shows results for a single LHC fill (7144) on September 9th 2018. Uncertainties are statistical components only and the green bands contain 68% of all points centred around the mean. Ref. [144].

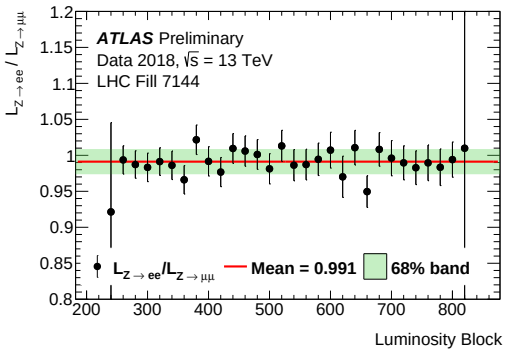

Figure B.6: Luminosity block dependence of the ratio of instantaneous luminosities determined from $Z \to e^+e^-$ and $Z \to \mu^+\mu^-$ counting. The respective luminosities have been averaged over blocks of 20 luminosity blocks. The red line indicates the mean obtained from a fit to a constant. This shows results for a single LHC fill (7144) on September 9th 2018. Uncertainties are statistical components only and the green band contains at least 68% of points centred around the mean. Ref. [144].

B.3 Pileup Dependent MC Correction Factors

This section shows the derivation of the Monte Carlo correction factors $F^{MC}_{Z\to\ell^+\ell^-}(\langle\mu\rangle)$ for $Z \to ee$ and $Z \to \mu\mu$ using samples simulated with the conditions of each operational year in Run-2. Each plot shows the corresponding 2nd order polynomial fit to the ratio and the corresponding coefficients p_0, p_1 and p_2.

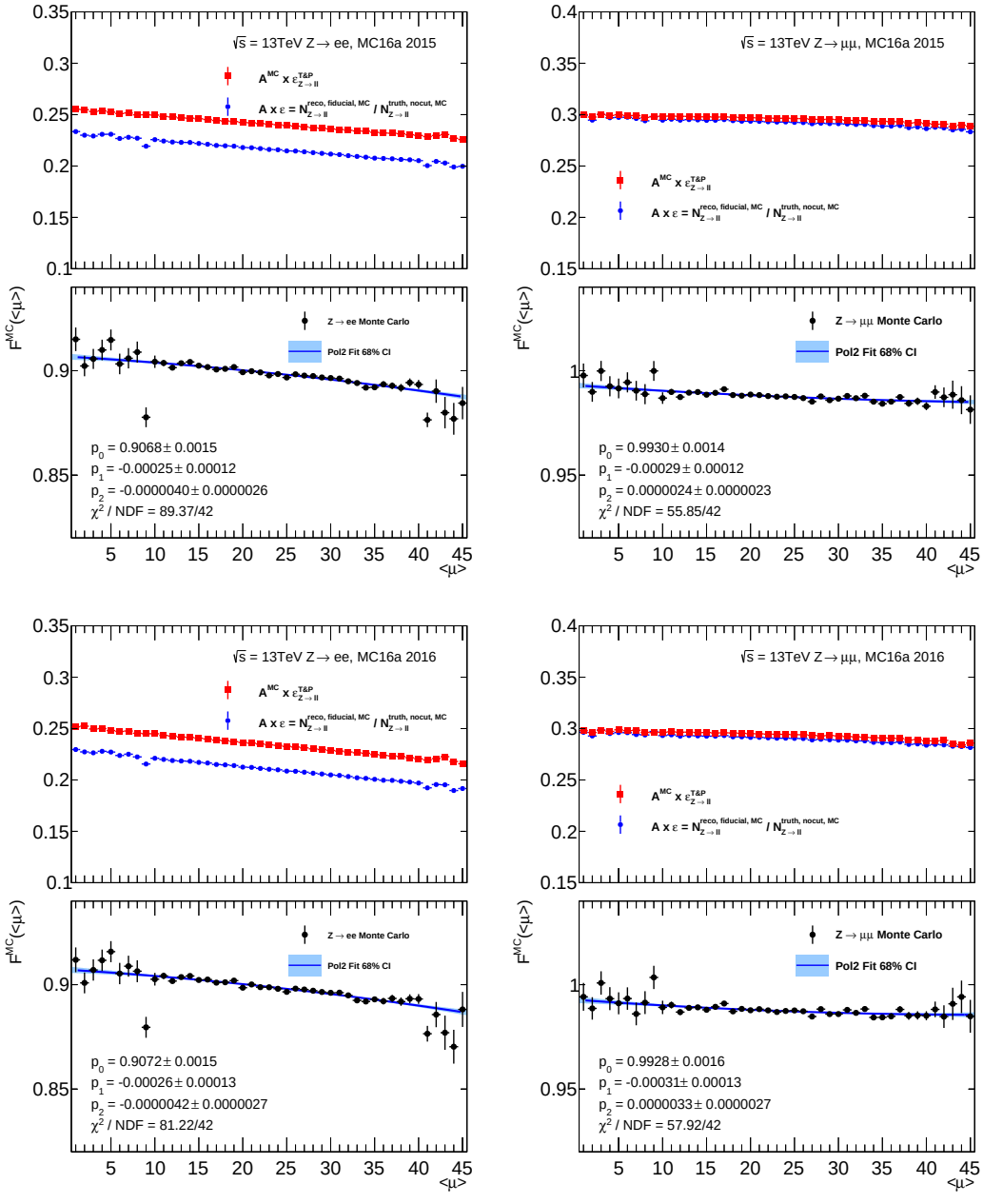

Figure B.7: The Monte Carlo points used to derive the pileup dependent correction factor, and the pol2 fits performed for 2015 and 2016 in each channel. The plots show the polynomial terms and their uncertainties, as well as the χ^2/NDF of the fit.

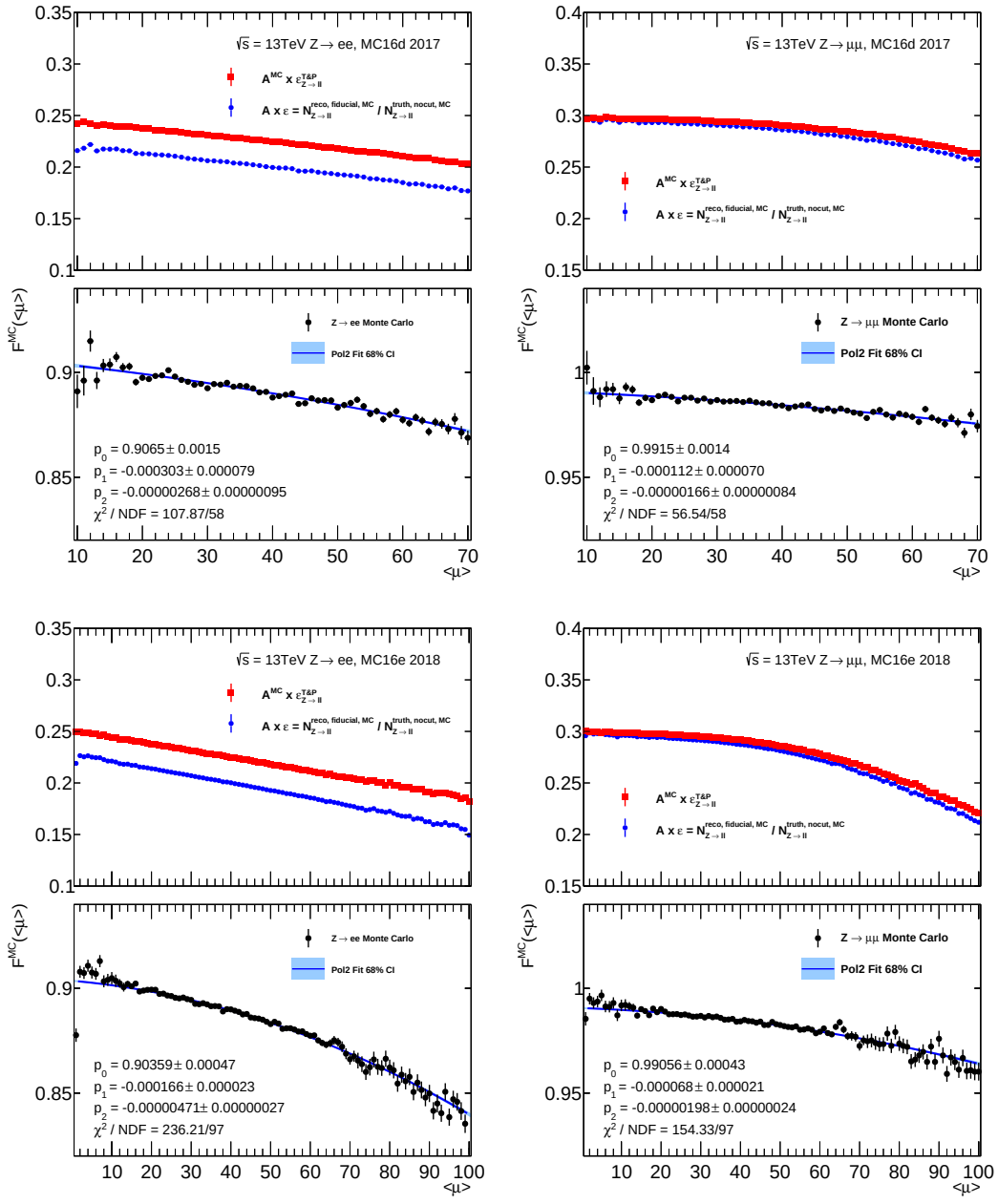

Figure B.8: The Monte Carlo points used to derive the pileup dependent correction factor, and the pol2 fits performed for 2017 and 2018 in each channel. The plots show the polynomial terms and their uncertainties, as well as the χ^2/NDF of the fit.

C Low-μ Analysis Cross-Section Cut Flows

C.1 Low-μ Analysis Cross-Section Cut Flows

A summary of cut-flows, tables showing the yield in data, signal and the background contributions after each selection. Yields are shown to two significant figures of their corresponding statistical uncertainty (systematics not included). Multijet is only evaluated for the final selection and others are left blank, uncertainty reflects the template statistics only.

Cut	Data	Signal			$Z \to \tau\tau$			Top			Diboson			Photon			Multijet		
No Cut	7434	5124	±	20	331.6	±	3.1	57.87	±	0.55	35.5	±	1.0	136.5	±	1.3		-	
Two Electrons	7416	5115	±	20	331.4	±	3.1	56.98	±	0.54	33.39	±	0.98	136.4	±	1.3		-	
Pass Trigger (1 or 2 Electrons)	7116	4849	±	20	322.9	±	3.0	56.26	±	0.54	32.76	±	0.97	118.7	±	1.2		-	
Both Pass Isolation	5530	4738	±	20	315.3	±	3.0	40.58	±	0.44	29.21	±	0.90	116.7	±	1.2		-	
$\|\eta\| < 2.47$	5509	4726	±	20	314.6	±	3.0	40.55	±	0.44	29.17	±	0.90	116.4	±	1.2		-	
$\|\eta\| < 1.37$ & $\|\eta\| > 1.52$	5458	4687	±	19	312.3	±	3.0	40.24	±	0.44	28.90	±	0.90	115.6	±	1.2		-	
$p_T^e > 15$ GeV	4222	3828	±	18	220.9	±	2.5	31.37	±	0.38	21.67	±	0.77	90.7	±	1.0		-	
Opposite Sign e^+e^-	4118	3787	±	18	218.7	±	2.5	29.61	±	0.37	19.95	±	0.75	90.1	±	1.0	142.0	±	5.3

Table C.1: $\sqrt{s} = 5.02$TeV cut-flow table for the $m_{\ell\ell} = [40, 66]$ GeV selection in the $Z \to ee$ channel.

Cut	Data	Signal			$Z \to \tau\tau$			Top			Diboson			Photon			Multijet		
No Cut	64366	63423	±	41	47.3	±	1.2	67.70	±	0.57	157.3	±	3.7	51.42	±	0.27		-	
Two Electrons	64319	63378	±	41	47.2	±	1.2	66.61	±	0.57	149.8	±	3.4	51.40	±	0.27		-	
Pass Trigger (1 or 2 Electrons)	63993	62919	±	41	46.9	±	1.1	66.24	±	0.57	149.3	±	3.4	48.99	±	0.26		-	
Both Pass Isolation	63117	62430	±	41	46.4	±	1.1	55.95	±	0.51	146.4	±	3.2	48.56	±	0.26		-	
$\|\eta\| < 2.47$	62913	62255	±	41	46.3	±	1.1	55.85	±	0.51	146.2	±	3.2	48.41	±	0.26		-	
$\|\eta\| < 1.37$ & $\|\eta\| > 1.52$	62324	61692	±	41	45.7	±	1.1	55.41	±	0.50	145.0	±	3.2	47.96	±	0.26		-	
$p_T^e > 15$ GeV	60941	60340	±	40	43.1	±	1.1	50.44	±	0.48	138.4	±	3.2	44.89	±	0.25		-	
Opposite Sign e^+e^-	60286	59583	±	40	42.7	±	1.1	48.54	±	0.47	134.7	±	3.2	44.49	±	0.25	56.0	±	2.2

Table C.2: $\sqrt{s} = 5.02$TeV cut-flow table for the $m_{\ell\ell} = [66, 116]$ GeV selection in the $Z \to ee$ channel.

Cut	Data	Signal			$Z \to \tau\tau$			Top			Diboson			Photon			Multijet		
No Cut	1095	923.0	±	5.0	1.12	±	0.17	44.19	±	0.45	21.15	±	0.80	14.72	±	0.13		-	
Two Electrons	1089	922.1	±	5.0	1.12	±	0.17	43.39	±	0.44	18.66	±	0.77	14.71	±	0.13		-	
Pass Trigger (1 or 2 Electrons)	1074	920.1	±	5.0	1.12	±	0.17	43.29	±	0.44	18.63	±	0.77	14.60	±	0.13		-	
Both Pass Isolation	994	916.2	±	4.9	1.06	±	0.17	41.76	±	0.43	18.47	±	0.76	14.54	±	0.13		-	
$\|\eta\| < 2.47$	992	913.6	±	4.9	1.06	±	0.17	41.68	±	0.43	18.37	±	0.76	14.49	±	0.13		-	
$\|\eta\| < 1.37$ & $\|\eta\| > 1.52$	984	904.7	±	4.9	1.04	±	0.17	41.27	±	0.43	18.19	±	0.76	14.34	±	0.13		-	
$p_T^e > 15$ GeV	964	899.2	±	4.9	0.98	±	0.16	40.55	±	0.43	17.76	±	0.75	14.14	±	0.13		-	
Opposite Sign e^+e^-	936	881.4	±	4.8	0.95	±	0.16	39.49	±	0.42	16.47	±	0.73	13.91	±	0.13	10.4	±	1.2

Table C.3: $\sqrt{s} = 5.02$TeV cut-flow table for the $m_{\ell\ell} = [116, 500]$ GeV selection in the $Z \to ee$ channel.

Cut	Data	Signal			$Z \to \tau\tau$			Top			Diboson			Photon			Multijet		
No Cut	24808	14069	±	31	901.8	±	8.3	684	±	16	82	±	10	114.26	±	0.32		-	
Two Electrons	24719	14038	±	31	901.3	±	8.3	677	±	16	78	±	10	114.19	±	0.32		-	
Pass Trigger (1 or 2 Electrons)	24412	13360	±	30	879.5	±	8.2	667	±	16	77	±	10	102.91	±	0.31		-	
Both Pass Isolation	17038	12910	±	30	848.3	±	8.1	500	±	14	72.0	±	9.8	101.17	±	0.30		-	
$\|\eta\| < 2.47$	16988	12888	±	30	846.8	±	8.1	499	±	14	72.0	±	9.8	101.01	±	0.30		-	
$\|\eta\| < 1.37$ & $\|\eta\| > 1.52$	16890	12816	±	30	842.2	±	8.0	495	±	14	71.9	±	9.8	100.49	±	0.30		-	
$p_T^e > 15$ GeV	12540	10234	±	27	588.2	±	6.7	391	±	12	63.4	±	8.6	79.23	±	0.27		-	
Opposite Sign e^+e^-	12218	10129	±	26	581.4	±	6.6	372	±	12	58.0	±	8.5	78.70	±	0.27	533.6	±	9.8

Table C.4: $\sqrt{s} = 13$TeV cut-flow table for the $m_{\ell\ell} = [40, 66]$ GeV selection in the $Z \to ee$ channel.

Cut	Data	Signal			$Z \to \tau\tau$			Top			Diboson			Photon			Multijet		
No Cut	208153	195801	±	95	136.6	±	3.2	917	±	19	460	±	17	60.23	±	0.24	-		
Two Electrons	207956	195628	±	95	136.4	±	3.2	905	±	19	446	±	17	60.17	±	0.24	-		
Pass Trigger (1 or 2 Electrons)	207625	194474	±	94	135.4	±	3.2	900	±	19	445	±	17	58.21	±	0.23	-		
Both Pass Isolation	203108	192247	±	94	131.0	±	3.1	772	±	18	432	±	17	57.67	±	0.23	-		
$\|\eta\| < 2.47$	202750	191907	±	94	130.7	±	3.1	771	±	18	429	±	17	57.53	±	0.23	-		
$\|\eta\| < 1.37$ & $\|\eta\| > 1.52$	201599	190879	±	93	130.1	±	3.1	767	±	18	427	±	17	57.23	±	0.23	-		
$p_T^e > 15$ GeV	196156	186134	±	92	121.4	±	3.0	702	±	17	410	±	17	53.96	±	0.23	-		
Opposite Sign e^+e^-	194090	183891	±	92	119.9	±	3.0	679	±	17	393	±	16	53.42	±	0.22	241.7	±	4.4

Table C.5: $\sqrt{s}$ = 13TeV cut-flow table for the $m_{\ell\ell} = [66, 116]$ GeV selection in the $Z \to ee$ channel.

Cut	Data	Signal			$Z \to \tau\tau$			Top			Diboson			Photon			Multijet		
No Cut	4933	3129	±	12	3.81	±	0.53	748	±	17	80	±	11	30.66	±	0.15	-		
Two Electrons	4899	3123	±	12	3.81	±	0.53	737	±	17	67	±	10	30.63	±	0.15	-		
Pass Trigger (1 or 2 Electrons)	4877	3118	±	12	3.81	±	0.53	736	±	17	66	±	10	30.49	±	0.15	-		
Both Pass Isolation	4420	3100	±	12	3.34	±	0.50	706	±	16	65	±	10	30.36	±	0.15	-		
$\|\eta\| < 2.47$	4402	3095	±	12	3.34	±	0.50	704	±	16	65	±	10	30.28	±	0.15	-		
$\|\eta\| < 1.37$ & $\|\eta\| > 1.52$	4382	3076	±	12	3.34	±	0.50	701	±	16	65	±	10	30.09	±	0.15	-		
$p_T^e > 15$ GeV	4176	3055	±	12	3.08	±	0.48	688	±	16	62	±	10	29.78	±	0.15	-		
Opposite Sign e^+e^-	4051	2994	±	12	2.80	±	0.46	670	±	16	60.4	±	9.9	29.16	±	0.14	26.4	±	1.3

Table C.6: $\sqrt{s}$ = 13TeV cut-flow table for the $m_{\ell\ell} = [116, 500]$ GeV selection in the $Z \to ee$ channel.

Cut	Data	Signal			$Z \to \tau\tau$			Top			Diboson			Photon			Multijet		
No Cut	24808	14069	±	31	901.8	±	8.3	684	±	16	82	±	10	114.26	±	0.32	-		
Two Electrons	24719	14038	±	31	901.3	±	8.3	677	±	16	78	±	10	114.19	±	0.32	-		
Pass Trigger (1 or 2 Electrons)	24412	13360	±	30	879.5	±	8.2	667	±	16	77	±	10	102.91	±	0.31	-		
Both Pass Isolation	17038	12910	±	30	848.3	±	8.1	500	±	14	72.0	±	9.8	101.17	±	0.30	-		
$\|\eta\| < 2.47$	16988	12888	±	30	846.8	±	8.1	499	±	14	72.0	±	9.8	101.01	±	0.30	-		
$\|\eta\| < 1.37$ & $\|\eta\| > 1.52$	16890	12816	±	30	842.2	±	8.0	495	±	14	71.9	±	9.8	100.49	±	0.30	-		
$p_T^e > 15$ GeV	12540	10234	±	27	588.2	±	6.7	391	±	12	63.4	±	8.6	79.23	±	0.27	-		
Opposite Sign e^+e^-	12218	10129	±	26	581.4	±	6.6	372	±	12	58.0	±	8.5	78.70	±	0.27	533.6	±	9.8

Table C.7: $\sqrt{s}$ = 13TeV cut-flow table for the $m_{\ell\ell} = [40, 66]$ GeV selection in the $Z \to ee$ channel.

Cut	Data	Signal			$Z \to \tau\tau$			Top			Diboson			Photon			Multijet		
No Cut	208153	195801	±	95	136.6	±	3.2	917	±	19	460	±	17	60.23	±	0.24	-		
Two Electrons	207956	195628	±	95	136.4	±	3.2	905	±	19	446	±	17	60.17	±	0.24	-		
Pass Trigger (1 or 2 Electrons)	207625	194474	±	94	135.4	±	3.2	900	±	19	445	±	17	58.21	±	0.23	-		
Both Pass Isolation	203108	192247	±	94	131.0	±	3.1	772	±	18	432	±	17	57.67	±	0.23	-		
$\|\eta\| < 2.47$	202750	191907	±	94	130.7	±	3.1	771	±	18	429	±	17	57.53	±	0.23	-		
$\|\eta\| < 1.37$ & $\|\eta\| > 1.52$	201599	190879	±	93	130.1	±	3.1	767	±	18	427	±	17	57.23	±	0.23	-		
$p_T^e > 15$ GeV	196156	186134	±	92	121.4	±	3.0	702	±	17	410	±	17	53.96	±	0.23	-		
Opposite Sign e^+e^-	194090	183891	±	92	119.9	±	3.0	679	±	17	393	±	16	53.42	±	0.22	241.7	±	4.4

Table C.8: $\sqrt{s}$ = 13TeV cut-flow table for the $m_{\ell\ell} = [66, 116]$ GeV selection in the $Z \to ee$ channel.

Cut	Data	Signal			$Z \to \tau\tau$			Top			Diboson			Photon			Multijet		
No Cut	4933	3129	±	12	3.81	±	0.53	748	±	17	80	±	11	30.66	±	0.15	-		
Two Electrons	4899	3123	±	12	3.81	±	0.53	737	±	17	67	±	10	30.63	±	0.15	-		
Pass Trigger (1 or 2 Electrons)	4877	3118	±	12	3.81	±	0.53	736	±	17	66	±	10	30.49	±	0.15	-		
Both Pass Isolation	4420	3100	±	12	3.34	±	0.50	706	±	16	65	±	10	30.36	±	0.15	-		
$\|\eta\| < 2.47$	4402	3095	±	12	3.34	±	0.50	704	±	16	65	±	10	30.28	±	0.15	-		
$\|\eta\| < 1.37$ & $\|\eta\| > 1.52$	4382	3076	±	12	3.34	±	0.50	701	±	16	65	±	10	30.09	±	0.15	-		
$p_T^e > 15$ GeV	4176	3055	±	12	3.08	±	0.48	688	±	16	62	±	10	29.78	±	0.15	-		
Opposite Sign e^+e^-	4051	2994	±	12	2.80	±	0.46	670	±	16	60.4	±	9.9	29.16	±	0.14	26.4	±	1.3

Table C.9: $\sqrt{s}$ = 13TeV cut-flow table for the $m_{\ell\ell} = [116, 500]$ GeV selection in the $Z \to ee$ channel.

Cut	Data	Signal			$Z \to \tau\tau$			Top			Diboson			Photon			Multijet		
No Cut	18336	8705	±	28	466.9	±	3.7	156.83	±	0.93	57.7	±	1.3	228.4	±	1.7	-		
Two Muons	18246	8702	±	28	466.7	±	3.7	150.88	±	0.91	51.8	±	1.2	228.3	±	1.7	-		
Pass Trigger (1 or 2 Muons)	17719	8148	±	27	441.7	±	3.6	141.77	±	0.88	49.0	±	1.1	201.9	±	1.6	-		
Both Pass Isolation	9074	7826	±	26	429.2	±	3.5	51.37	±	0.49	40.0	±	1.0	198.0	±	1.6	-		
$\|\eta\| < 2.4$	8393	7222	±	25	398.7	±	3.4	50.11	±	0.49	37.45	±	0.99	184.3	±	1.5	-		
$p_T^\mu > 15$ GeV	6598	5758	±	23	285.6	±	2.9	38.61	±	0.42	28.75	±	0.87	134.9	±	1.3	-		
Opposite Sign $\mu^+\mu^-$	6541	5757	±	23	285.6	±	2.9	36.49	±	0.40	27.36	±	0.85	134.9	±	1.3	116.1	±	2.9

Table C.10: $\sqrt{s}$ = 5.02TeV cut-flow table for the $m_{\ell\ell} = [40, 66]$ GeV selection in the $Z \to \mu\mu$ channel.

Cut	Data	Signal			$Z \to \tau\tau$			Top			Diboson			Photon			Multijet		
No Cut	97232	97237	±	71	67.0	±	1.4	144.65	±	0.85	243.5	±	2.8	83.26	±	0.35	-		
Two Muons	97114	97194	±	71	67.0	±	1.4	137.58	±	0.83	231.0	±	2.8	83.20	±	0.35	-		
Pass Trigger (1 or 2 Muons)	96722	94112	±	70	64.4	±	1.4	132.34	±	0.81	224.6	±	2.7	77.89	±	0.33	-		
Both Pass Isolation	92956	92856	±	69	62.8	±	1.3	71.09	±	0.57	211.0	±	2.7	76.97	±	0.33	-		
$\|\eta\| < 2.4$	85720	85133	±	66	58.0	±	1.3	68.92	±	0.56	196.8	±	2.5	70.54	±	0.32	-		
$p_T^\mu > 15$ GeV	83375	82606	±	65	54.5	±	1.2	62.95	±	0.53	187.3	±	2.5	63.15	±	0.30	-		
Opposite Sign $\mu^+\mu^-$	83364	82606	±	65	54.5	±	1.2	60.98	±	0.52	185.7	±	2.5	63.15	±	0.30	59.5	±	2.0

Table C.11: $\sqrt{s}$ = 5.02TeV cut-flow table for the $m_{\ell\ell} = [66, 116]$ GeV selection in the $Z \to \mu\mu$ channel.

Cut	Data	Signal			$Z \to \tau\tau$			Top			Diboson			Photon			Multijet		
No Cut	1734	1316.7	±	8.2	1.59	±	0.21	71.48	±	0.58	29.15	±	0.80	22.53	±	0.16	-		
Two Muons	1710	1314.2	±	8.2	1.56	±	0.21	67.44	±	0.56	24.85	±	0.74	22.52	±	0.16	-		
Pass Trigger (1 or 2 Muons)	1694	1278.5	±	8.1	1.50	±	0.20	65.61	±	0.55	24.04	±	0.73	21.68	±	0.16	-		
Both Pass Isolation	1388	1267.3	±	8.1	1.31	±	0.19	51.75	±	0.48	22.68	±	0.71	21.48	±	0.16	-		
$\|\eta\| < 2.4$	1273	1160.7	±	7.7	1.25	±	0.19	49.78	±	0.47	20.55	±	0.66	19.19	±	0.15	-		
$p_T^\mu > 15$ GeV	1260	1153.4	±	7.7	1.22	±	0.18	48.69	±	0.47	20.19	±	0.66	18.81	±	0.15	-		
Opposite Sign $\mu^+\mu^-$	1256	1153.4	±	7.7	1.19	±	0.18	48.11	±	0.46	19.39	±	0.65	18.81	±	0.15	5.43	±	0.78

Table C.12: $\sqrt{s}$ = 5.02TeV cut-flow table for the $m_{\ell\ell} = [116, 500]$ GeV selection in the $Z \to \mu\mu$ channel.

Cut	Data	Signal			$Z \to \tau\tau$			Top			Diboson			Photon			Multijet		
No Cut	54997	23760	±	41	935.1	±	8.5	1539	±	24	132	±	13	189.60	±	0.61	-		
Two Muons	54698	23746	±	41	934.3	±	8.5	1502	±	24	126	±	13	189.52	±	0.61	-		
Pass Trigger (1 or 2 Muons)	52917	22278	±	40	881.6	±	8.3	1427	±	23	119	±	13	170.84	±	0.57	-		
Both Pass Isolation	24866	21107	±	39	841.1	±	8.1	634	±	16	98	±	12	167.49	±	0.57	-		
$\|\eta\| < 2.4$	22900	19390	±	37	775.9	±	7.8	600	±	15	92	±	12	152.59	±	0.54	-		
$p_T^\mu > 15$ GeV	17692	15282	±	33	550.9	±	6.5	480	±	13	74	±	11	114.00	±	0.46	-		
Opposite Sign $\mu^+\mu^-$	17570	15281	±	33	550.4	±	6.5	468	±	13	71	±	11	113.99	±	0.46	256.7	±	2.6

Table C.13: $\sqrt{s}$ = 13TeV cut-flow table for the $m_{\ell\ell} = [40, 66]$ GeV selection in the $Z \to \mu\mu$ channel.

Cut	Data	Signal			$Z \to \tau\tau$			Top			Diboson			Photon			Multijet		
No Cut	307031	293220	±	120	147.5	±	3.4	1621	±	25	707	±	23	96.75	±	0.32	-		
Two Muons	306528	293030	±	120	147.0	±	3.4	1570	±	24	667	±	22	96.68	±	0.32	-		
Pass Trigger (1 or 2 Muons)	304600	283870	±	120	141.5	±	3.3	1503	±	24	643	±	21	91.52	±	0.31	-		
Both Pass Isolation	288443	278620	±	110	135.4	±	3.3	912	±	19	613	±	21	90.18	±	0.31	-		
$\|\eta\| < 2.4$	264623	253870	±	110	123.8	±	3.1	870	±	18	565	±	20	80.99	±	0.29	-		
$p_T^\mu > 15$ GeV	256562	245730	±	110	116.4	±	3.0	797	±	17	541	±	20	73.96	±	0.28	-		
Opposite Sign $\mu^+\mu^-$	256500	245730	±	110	116.4	±	3.0	780	±	17	539	±	20	73.96	±	0.28	171.0	±	1.9

Table C.14: $\sqrt{s}$ = 13TeV cut-flow table for the $m_{\ell\ell} = [66, 116]$ GeV selection in the $Z \to \mu\mu$ channel.

Cut	Data	Signal			$Z \to \tau\tau$			Top			Diboson			Photon			Multijet		
No Cut	7866	4349	±	14	4.51	±	0.58	1148	±	21	109	±	12	46.71	±	0.19	-		
Two Muons	7749	4334	±	14	4.48	±	0.58	1108	±	21	91	±	12	46.64	±	0.19	-		
Pass Trigger (1 or 2 Muons)	7600	4214	±	14	4.36	±	0.58	1075	±	20	86	±	12	45.06	±	0.19	-		
Both Pass Isolation	5423	4163	±	14	3.42	±	0.50	881	±	18	81	±	12	44.60	±	0.19	-		
$\|\eta\| < 2.4$	4903	3774	±	13	2.99	±	0.47	828	±	18	72	±	11	39.23	±	0.18	-		
$p_T^\mu > 15$ GeV	4829	3744	±	13	2.76	±	0.45	811	±	18	68	±	11	38.68	±	0.17	-		
Opposite Sign $\mu^+\mu^-$	4803	3744	±	13	2.75	±	0.45	806	±	18	63	±	11	38.68	±	0.17	16.68	±	0.63

Table C.15: $\sqrt{s}$ = 13TeV cut-flow table for the $m_{\ell\ell} = [116, 500]$ GeV selection in the $Z \to \mu\mu$ channel.

C.2 Low-μ Analysis Cross-Section Control Plots

This section shows various control plots for single-lepton and di-lepton selections categorised into the low-mass, central-mass and high-mass bins used in the analysis. for the low-μ cross-section analysis. For all cases the sum of expected signal and all background contributions has been normalised to the data, so these plots are meant to provide a shape comparison and at this stage are insensitive to any global normalisation differences. The χ^2 is calculated using statistical and systematic uncertainties.

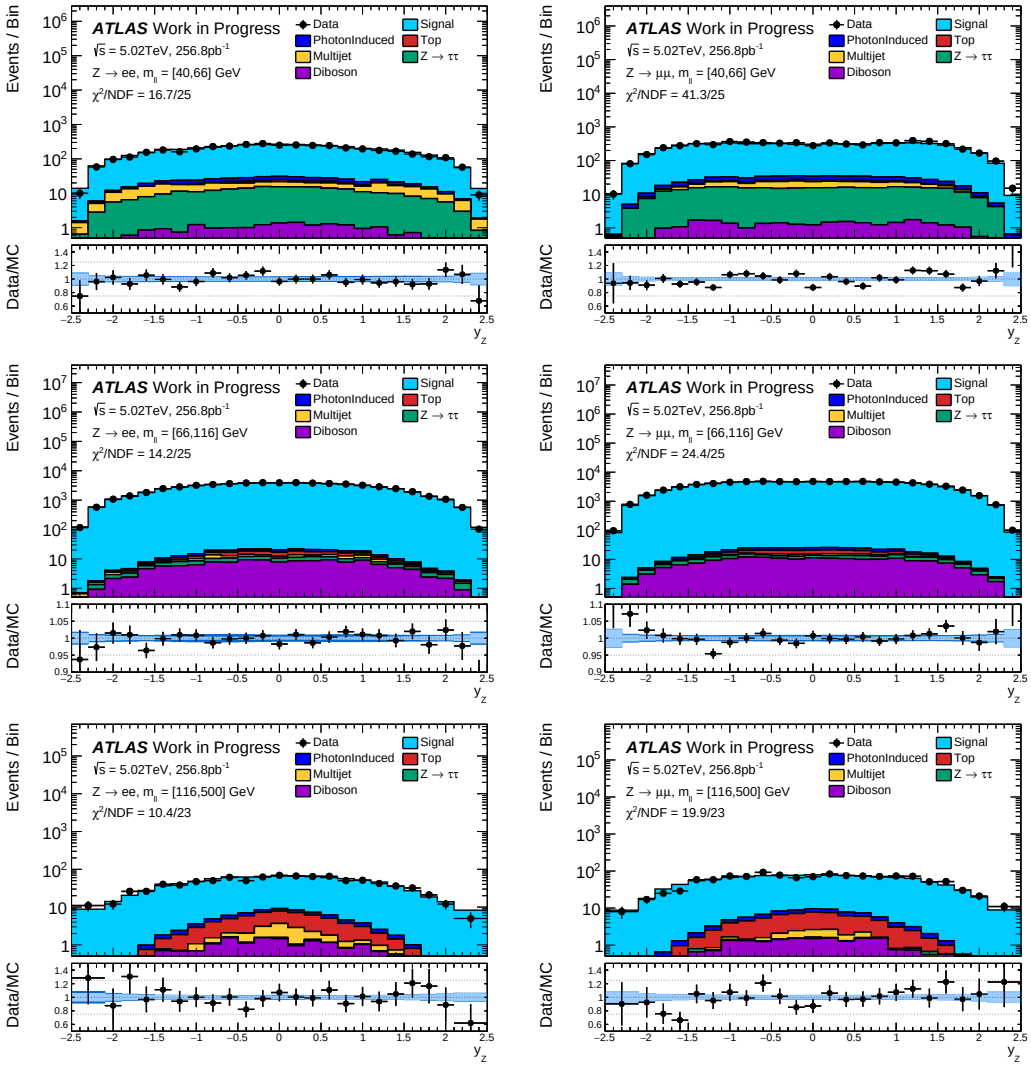

Figure C.1: $\sqrt{s} = 5.02\,\text{TeV}$ di-lepton rapidity $y_{\ell\ell}$ in the low-mass (top), central-mass (middle) and high-mass (bottom) slices for the $Z \to ee$ and $Z \to \mu\mu$ selections

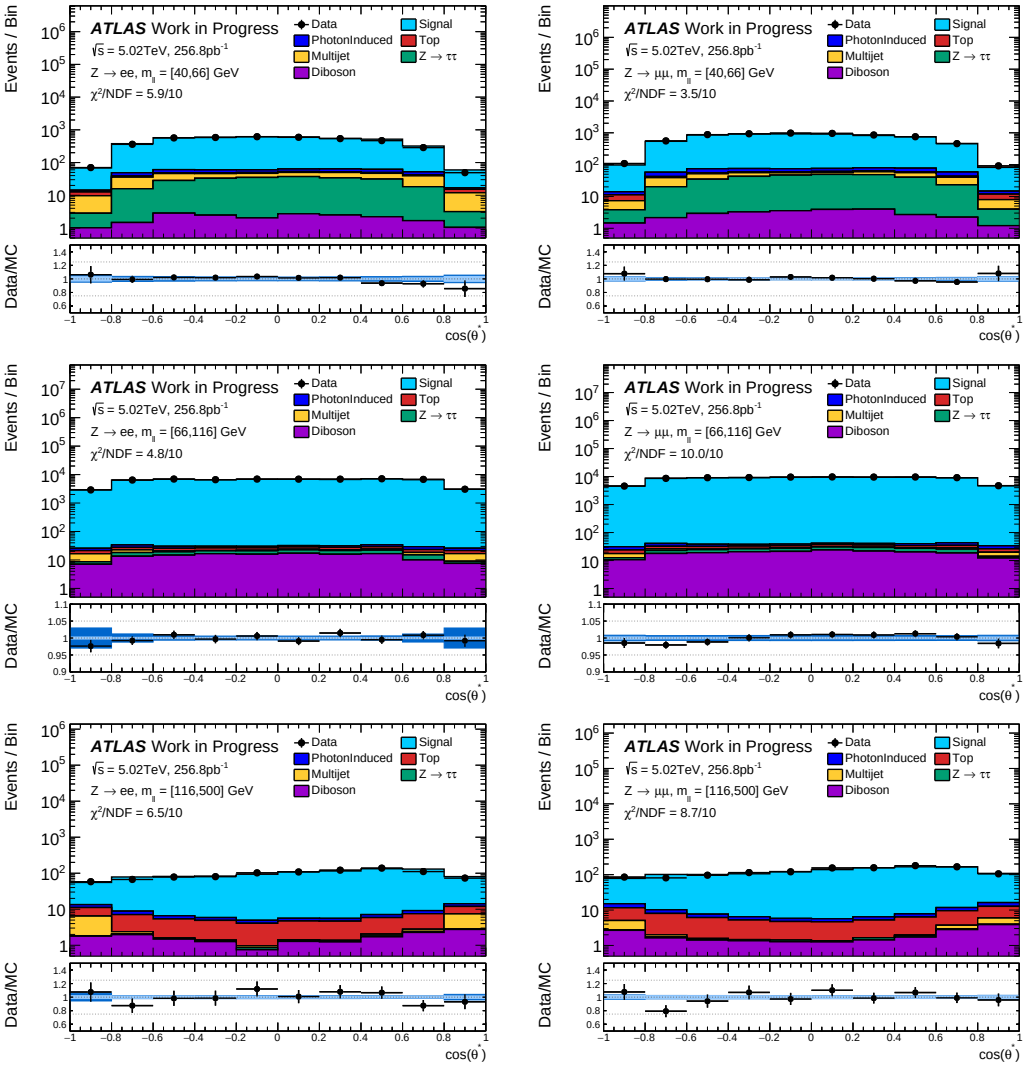

Figure C.2: $\sqrt{s} = 5.02\,\text{TeV}$ $cos(\theta^*)$ in the low-mass (top), central-mass (middle) and high-mass (bottom) slices for the $Z \to ee$ and $Z \to \mu\mu$ selections

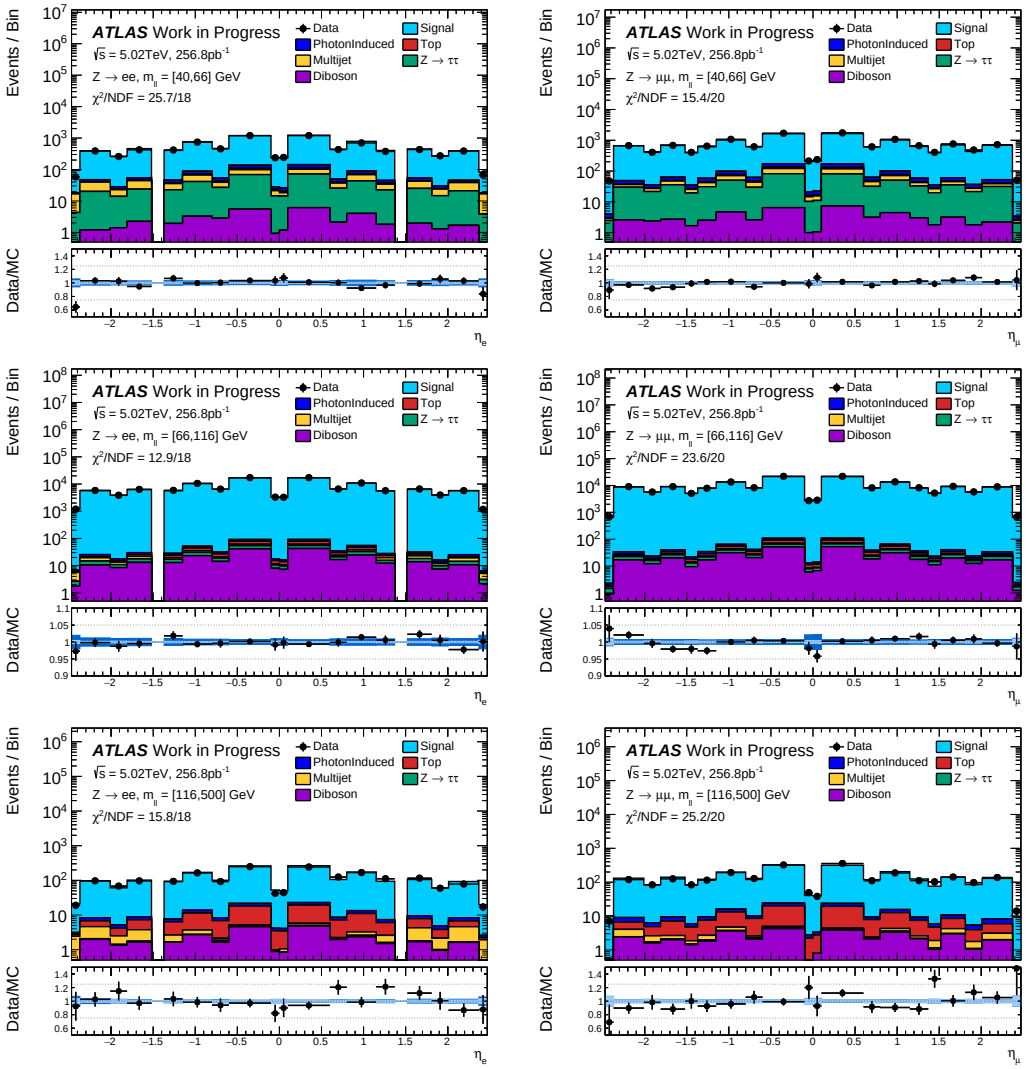

Figure C.3: $\sqrt{s} = 5.02\,\text{TeV}$ lepton pseudorapidity η_ℓ in the low-mass (top), central-mass (middle) and high-mass (bottom) slices for the $Z \to ee$ and $Z \to \mu\mu$ selections

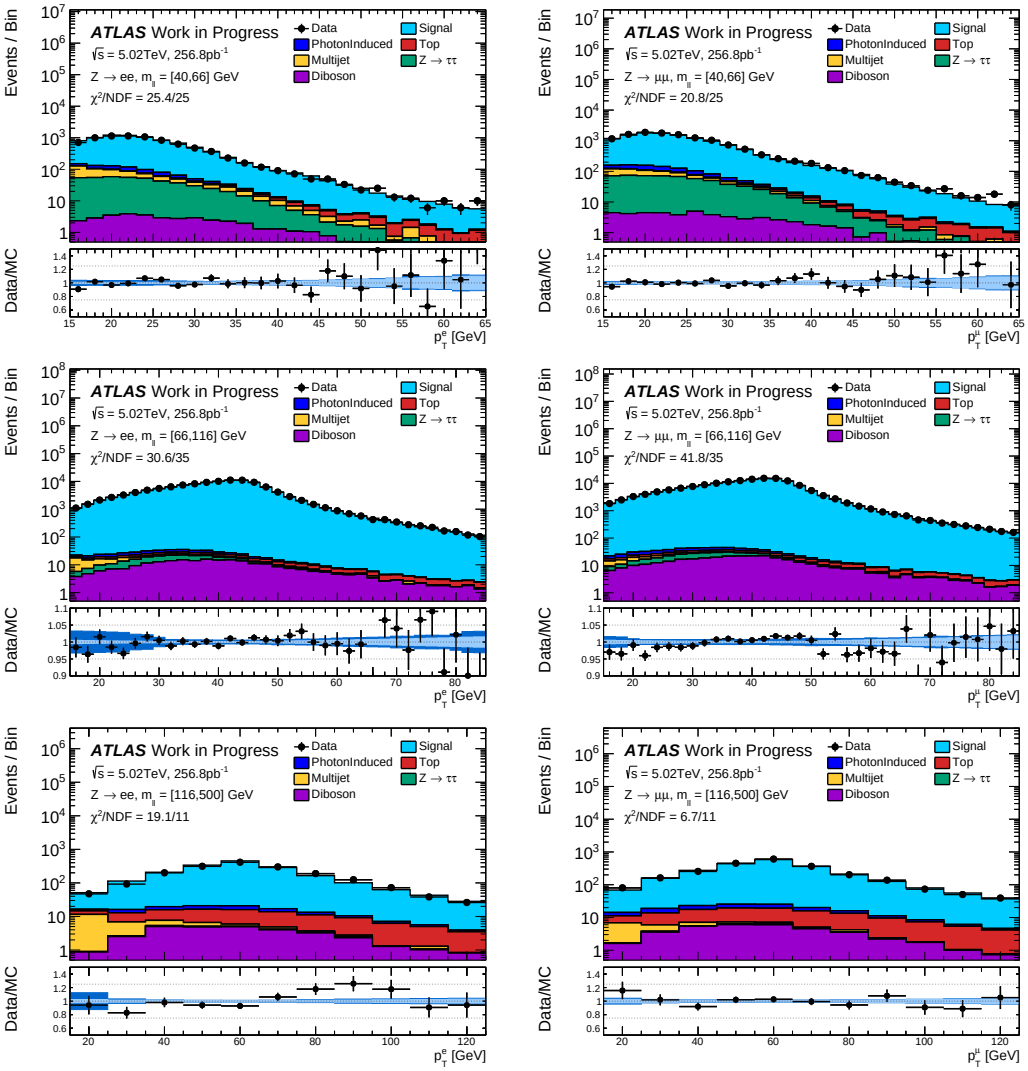

Figure C.4: $\sqrt{s} = 5.02$ TeV lepton transverse momentum $p_{T,\ell}$ in the low-mass (top), central-mass (middle) and high-mass (bottom) slices for the $Z \to ee$ and $Z \to \mu\mu$ selections.

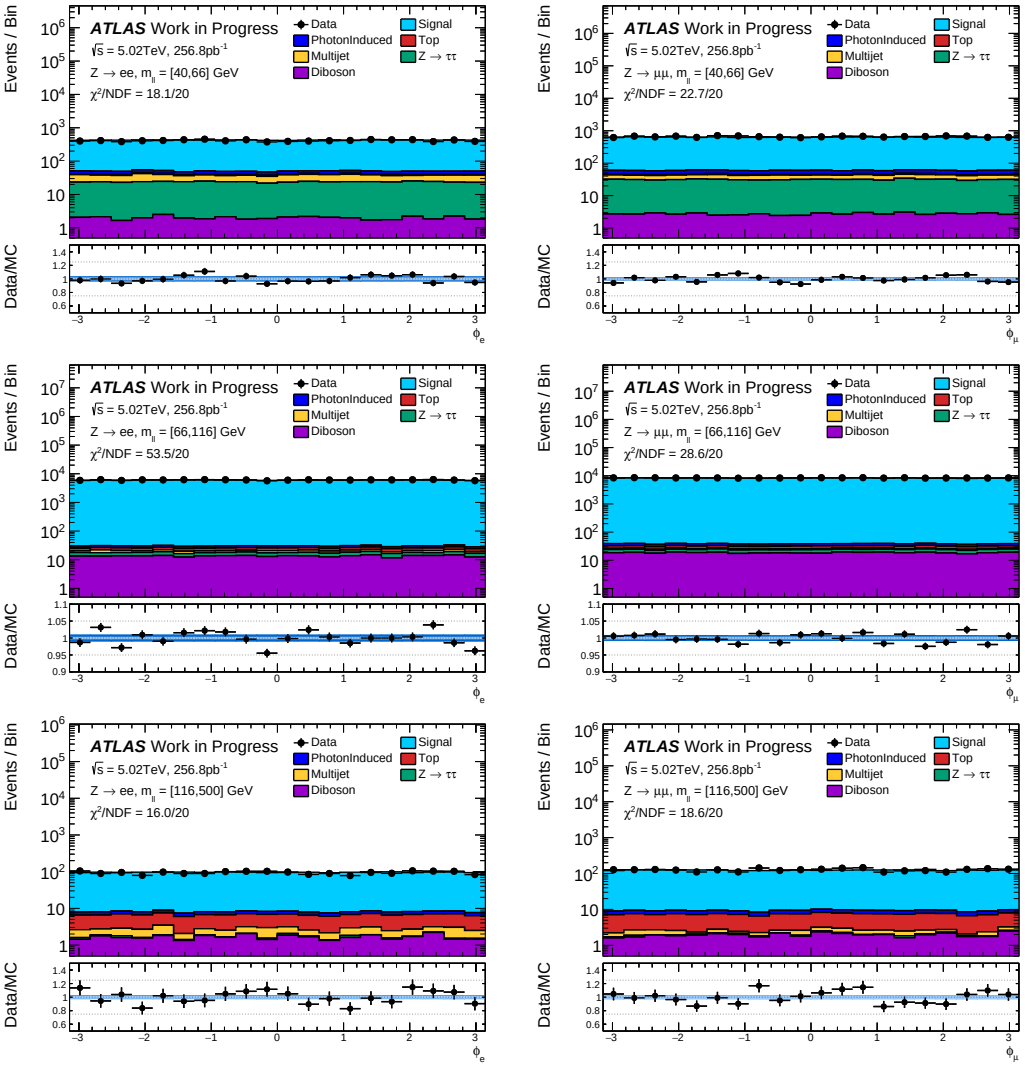

Figure C.5: $\sqrt{s} = 5.02\,\text{TeV}$ azimuthal angle ϕ_ℓ in the low-mass (top), central-mass (middle) and high-mass (bottom) slices for the $Z \to ee$ and $Z \to \mu\mu$ selections

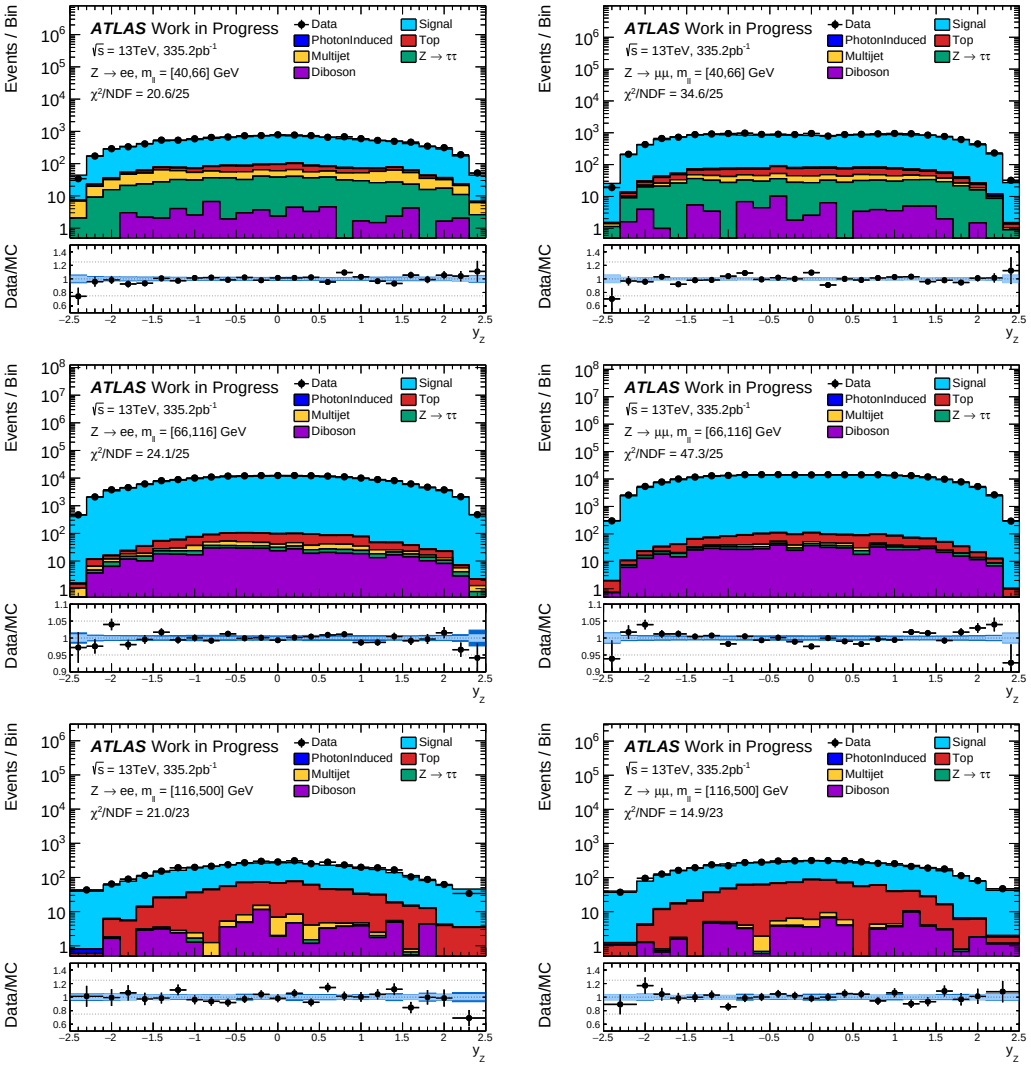

Figure C.6: $\sqrt{s} = 13\,\text{TeV}$ di-lepton rapidity $y_{\ell\ell}$ in the low-mass (top), central-mass (middle) and high-mass (bottom) slices for the $Z \to ee$ and $Z \to \mu\mu$ selections

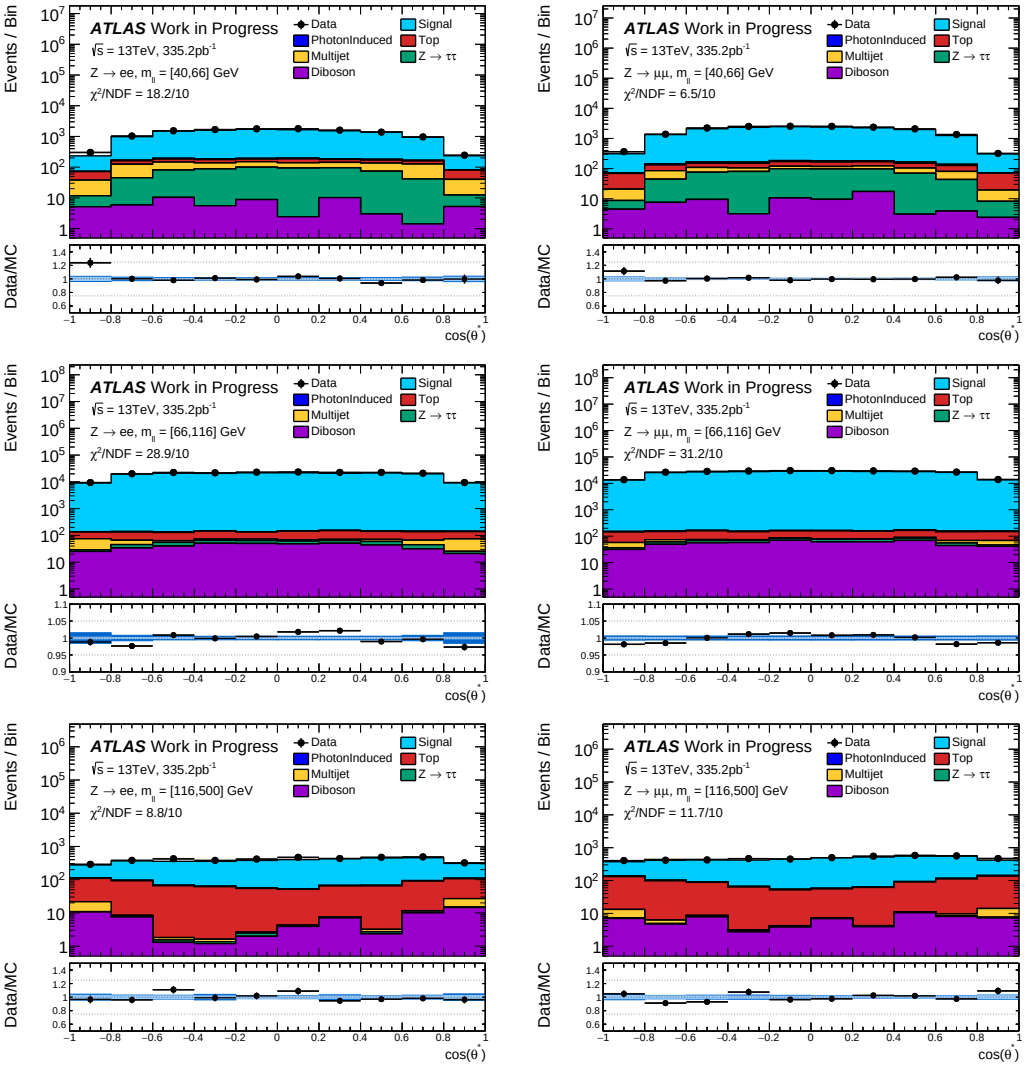

Figure C.7: $\sqrt{s} = 13\,\text{TeV}$ $cos(\theta^*)$ in the low-mass (top), central-mass (middle) and high-mass (bottom) slices for the $Z \to ee$ and $Z \to \mu\mu$ selections

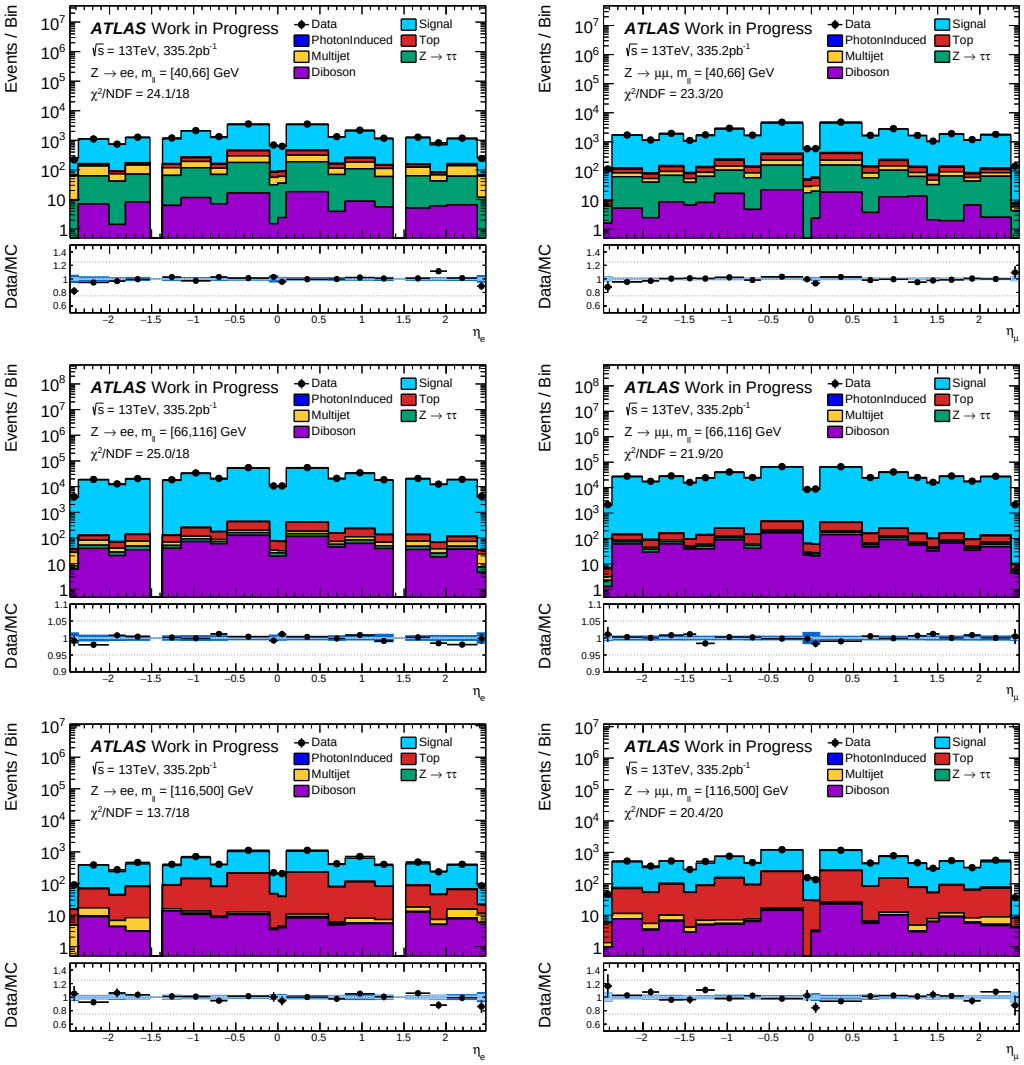

Figure C.8: $\sqrt{s} = 13\,\text{TeV}$ lepton pseudorapidity η_ℓ in the low-mass (top), central-mass (middle) and high-mass (bottom) slices for the $Z \to ee$ and $Z \to \mu\mu$ selections

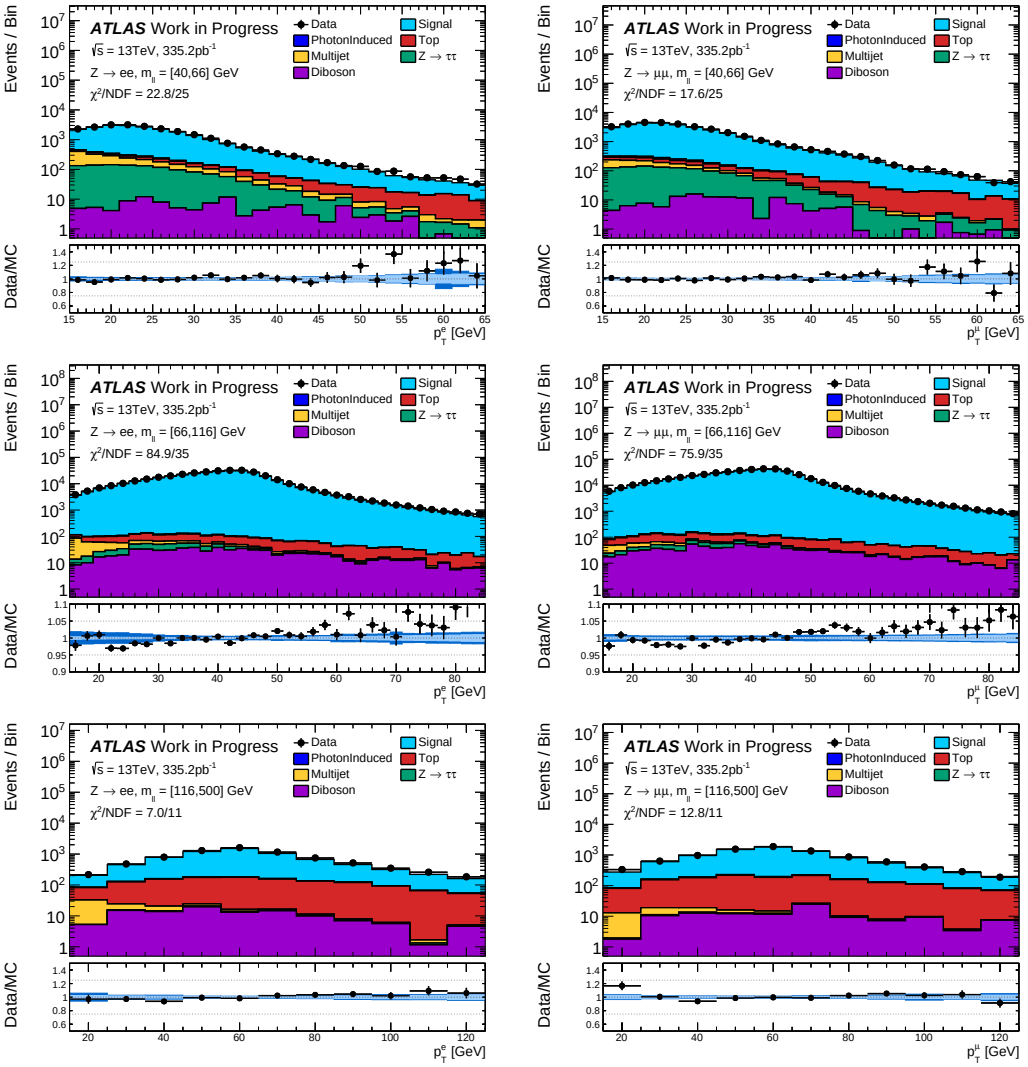

Figure C.9: $\sqrt{s} = 13\,\text{TeV}$ lepton transverse momentum $p_{T,\ell}$ in the low-mass (top), central-mass (middle) and high-mass (bottom) slices for the $Z \to ee$ and $Z \to \mu\mu$ selections

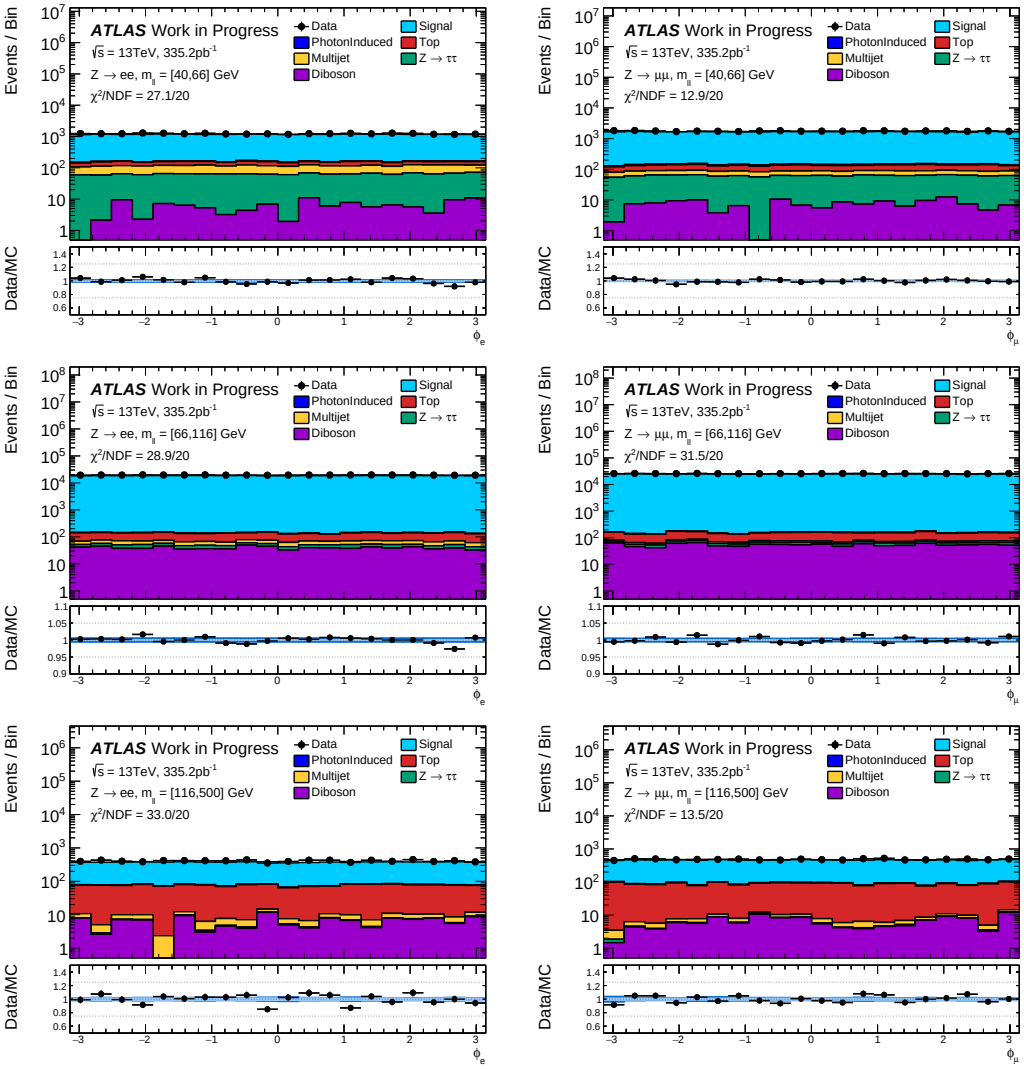

Figure C.10: $\sqrt{s} = 13$ TeV azimuthal angle ϕ_ℓ in the low-mass (top), central-mass (middle) and high-mass (bottom) slices for the $Z \to ee$ and $Z \to \mu\mu$ selections

C.3 Low-μ Multijet Derivation Plots

This section shows the `Min(ptvarcone20/pt)` and `Max(ptvarcone20/pt)` distributions used in the multijet estimation for $\sqrt{s} = 5.02\,\text{TeV}$ and $\sqrt{s} = 13\,\text{TeV}$, excluding the slices shown in Section 8.5.

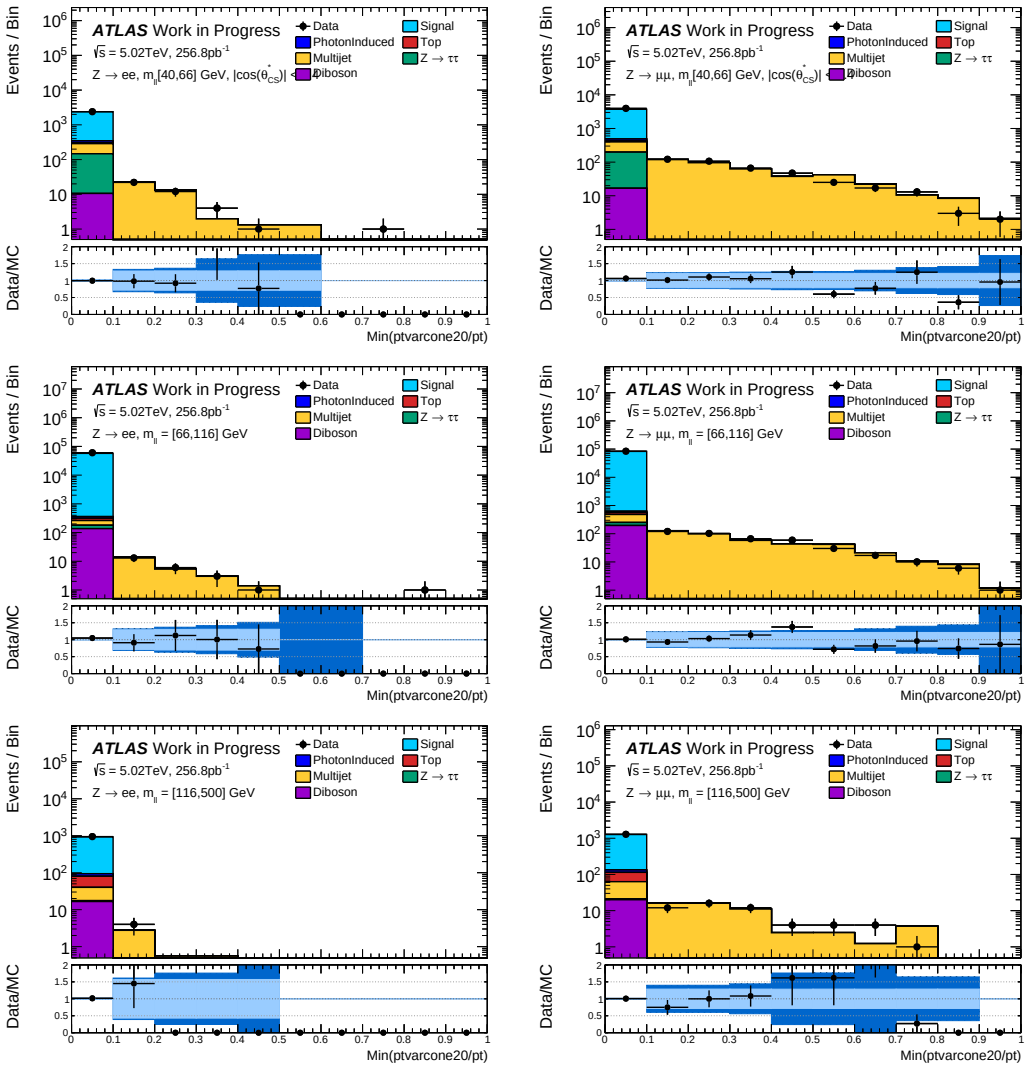

Figure C.11: The `Min(ptvarcone20/pt)` distribution at $\sqrt{s} = 5.02\,\text{TeV}$ for $Z \to ee$ and $Z \to \mu\mu$ selections. The selected events are in the `NominalLooseIsolation` selection and the multijet template has been normalised by just the $S_{control}$ factor to the region `Min(ptvarcone20/pt)` > 0.1. The ratio panel is the absolute ratio of data and MC where the light band reflects systematic uncertainty on the multijet estimate and the darker band includes the template statistics.

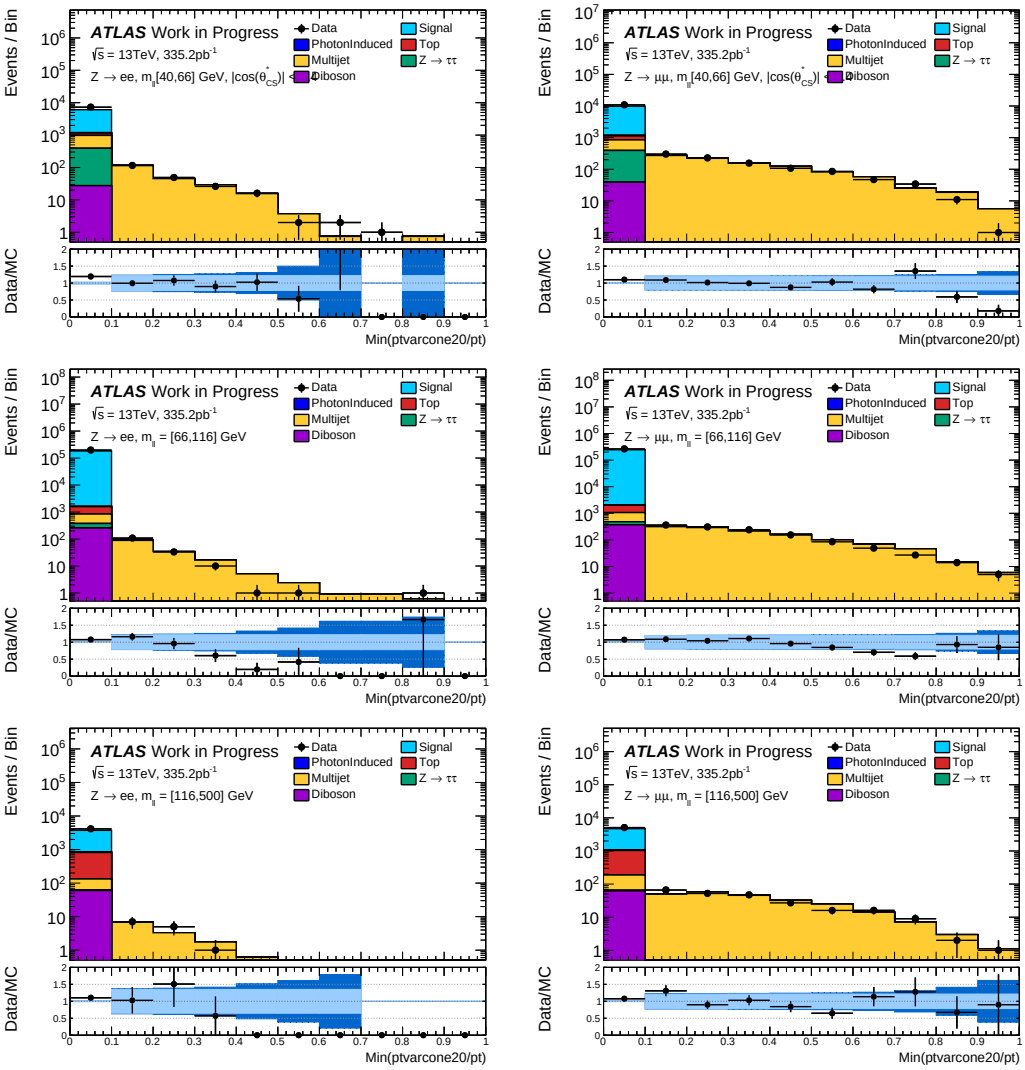

Figure C.12: The `Min(ptvarcone20/pt)` distribution at $\sqrt{s} = 13\,\text{TeV}$ for $Z \to ee$ and $Z \to \mu\mu$ selections. The selected events are in the `NominalLooseIsolation` selection and the multijet template has been normalised by just the $S_{control}$ factor to the region `Min(ptvarcone20/pt)` > 0.1. The ratio panel is the absolute ratio of data and MC where the light band reflects systematic uncertainty on the multijet estimate and the darker band includes the template statistics.

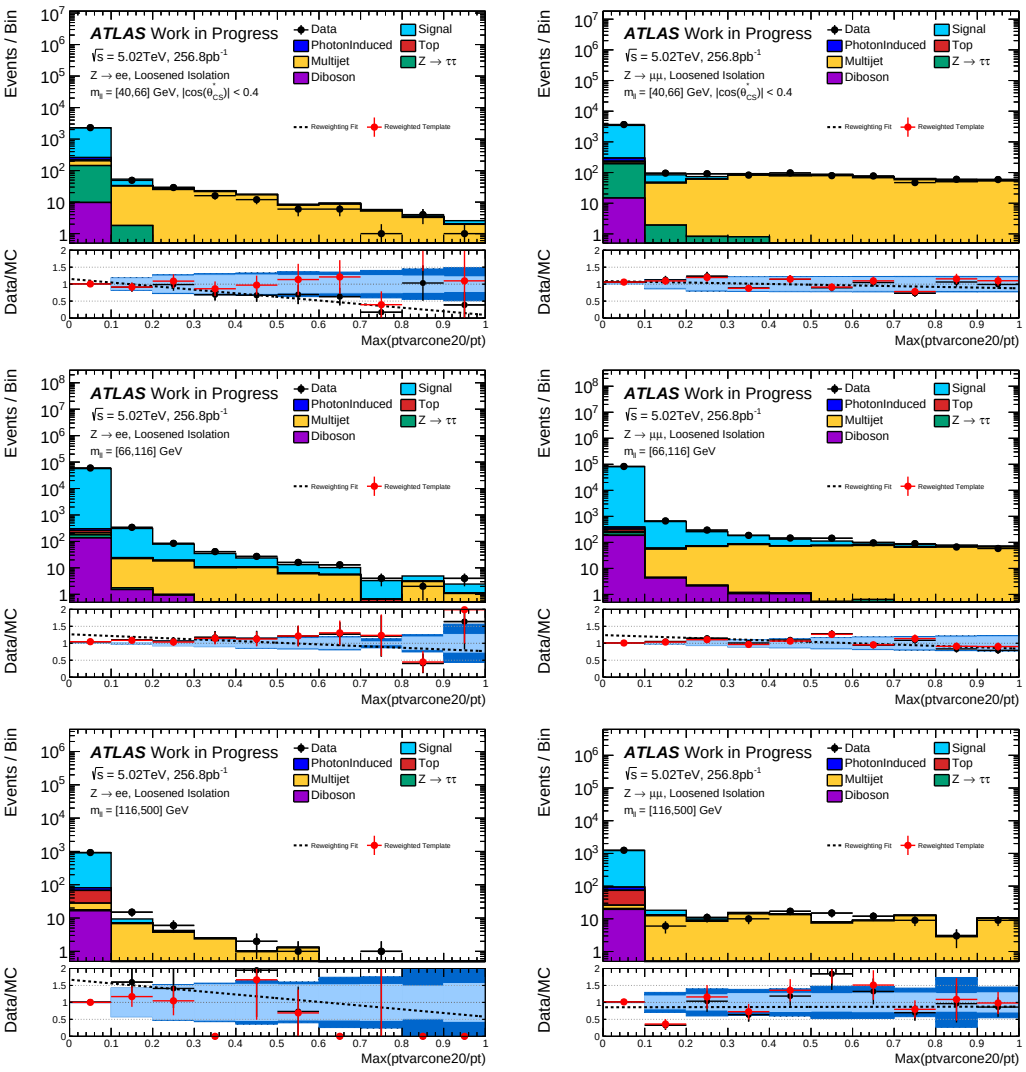

Figure C.13: The `Max(ptvarcone20/pt)` distribution at $\sqrt{s} = 5.02\,\text{TeV}$ for $Z \to ee$ and $Z \to \mu\mu$ selections. The selected events are in the `NominalLooseIsolation` selection and the multijet template has been normalised by just the $S_{control}$ factor to the region `Min(ptvarcone20/pt)` > 0.1. The ratio panel shows the absolute ratio of data and MC with the nominal template selection, the 1st order polynomial fit to the ratio, and the absolute ratio of data and MC with the reweighted template selection. The light band reflects systematic uncertainty on the multijet estimate and the darker band includes the template statistics.

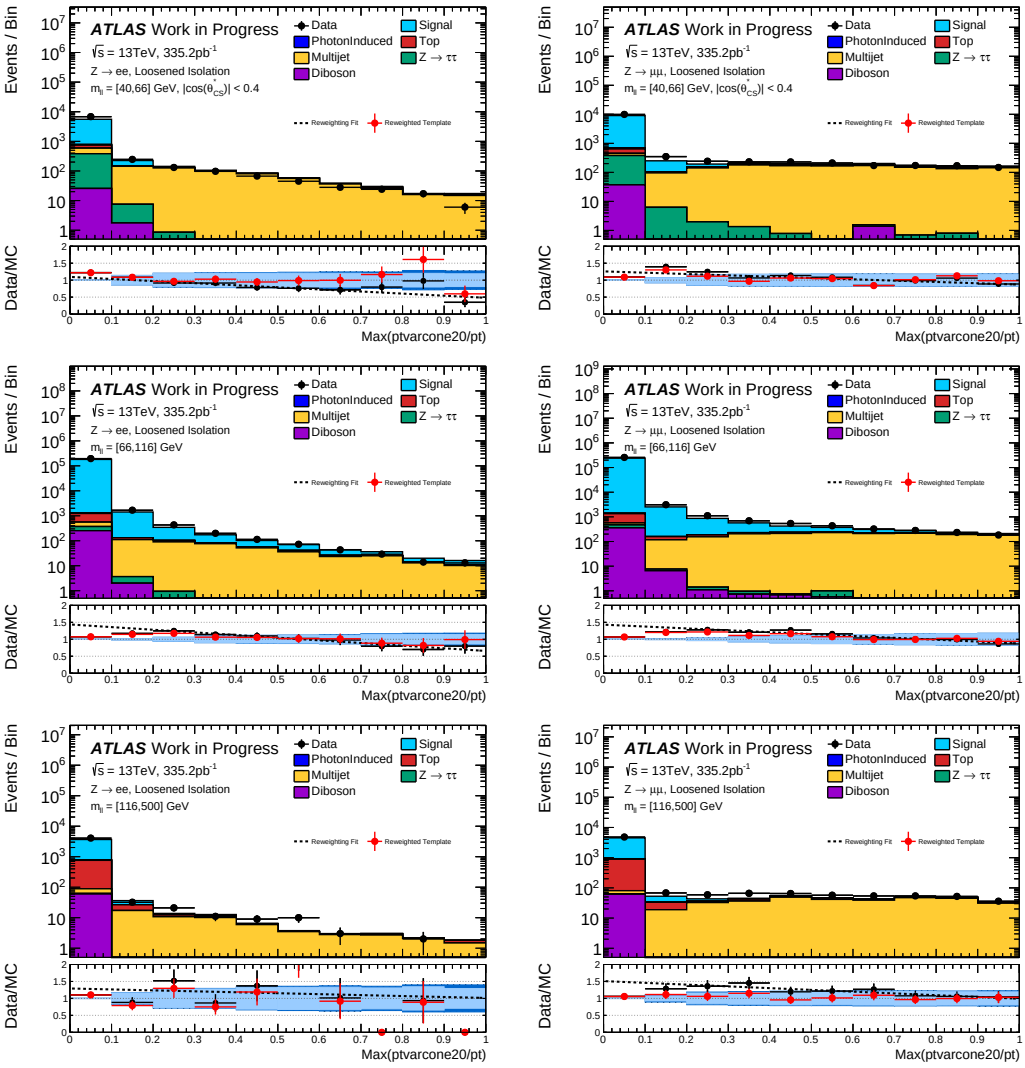

Figure C.14: The `Max(ptvarcone20/pt)` distribution at $\sqrt{s} = 13\,\text{TeV}$ for $Z \to ee$ and $Z \to \mu\mu$ selections. The selected events are in the `NominalLooseIsolation` selection and the multijet template has been normalised by just the $S_{control}$ factor to the region `Min(ptvarcone20/pt)` > 0.1. The ratio panel shows the absolute ratio of data and MC with the nominal template selection, the 1st order polynomial fit to the ratio, and the absolute ratio of data and MC with the reweighted template selection. The light band reflects systematic uncertainty on the multijet estimate and the darker band includes the template statistics.

C.4 Low-μ Analysis Results Tables

Tabulated results for the unfolded born-level differential Drell-Yan cross-section measurements for $Z \to ee$ and $Z \to \mu\mu$ at $\sqrt{s} = 5.02\,\text{TeV}$ and $\sqrt{s} = 13\,\text{TeV}$. All uncertainties are shown as percentages. Uncertainties are defined as:

- Statistical uncertainties are shown for data statistics $\delta^{stat,data}$, signal MC statistics $\delta^{stat,signalMC}$ and background statistics $\delta^{stat,background}$.
- Electron SF uncertainties are shown for each SF type δ^{id}, δ^{reco}, δ^{trig} and δ^{iso}.
- Muon SF uncertainties are shown for δ^{reco}, δ^{trig}, δ^{iso} and δ^{ttva}.
- Muon calibration and Sagitta Bias uncertainties are given by $\delta^{muon,cal}$.
- Electron calibration is separated into the low-μ and high-μ components: $\delta^{low\mu,cal}$ and $\delta^{high\mu,cal}$
- Background modelling uncertainties such as cross-section normalisation, $t\bar{t}$ variations and all multijet uncertainties are given by δ^{bkg}.
- The multijet uncertainties are given by $\delta^{Multijet}$.
- Bias uncertainty is given by δ^{bias}.
- Luminosity uncertainty is given by δ^{lumi}.

Bin No.	$m_{\ell\ell}$ [GeV]	$cos(\theta^*_{CS})$	$\lvert y_{\ell\ell}\rvert$	$\frac{d^3\sigma}{dm_{\ell\ell}dcos(\theta^*_{CS})d\lvert y_{\ell\ell}\rvert}$ [pb/GeV]	$\delta^{stat,data}$ [%]	$\delta^{stat,signalMC}$ [%]	$\delta^{stat,background}$ [%]	δ^{id} [%]	δ^{reco} [%]	δ^{trig} [%]	δ^{iso} [%]	$\delta^{highp_T,cal}$ [%]	$\delta^{lowp_T,cal}$ [%]	δ^{bkg} [%]	$\delta^{Multijet}$ [%]	δ^{bias} [%]	δ^{lumi} [%]
1	[40, 66]	[−1.0, −0.4]	[0.0, 0.4]	0.177	9.6	2.3	1.5	3.7	1.3	0.064	0.46	1.5	0.2	3.3	2.8	0.41	1.8
2	[40, 66]	[−1.0, −0.4]	[0.4, 0.8]	0.213	9.4	2.5	1.4	3.5	0.89	0.052	0.4	1.0	0.27	2.6	2.3	0.32	1.8
3	[40, 66]	[−1.0, −0.4]	[0.8, 1.2]	0.176	11.0	2.5	1.9	3.2	0.75	0.062	0.37	1.1	0.34	3.8	3.4	0.66	1.8
4	[40, 66]	[−1.0, −0.4]	[1.2, 1.6]	0.186	9.7	2.2	1.9	3.4	0.87	0.065	0.38	1.2	0.32	4.2	4.1	0.42	1.7
5	[40, 66]	[−1.0, −0.4]	[1.6, 2.0]	0.077	19.0	3.5	4.3	4.1	0.86	0.11	0.48	1.3	0.55	7.0	6.9	2.8	1.8
6	[40, 66]	[−0.4, 0.0]	[0.0, 0.4]	0.286	8.1	2.1	0.79	2.5	0.78	0.0081	0.34	0.57	0.16	1.6	1.2	0.23	1.8
7	[40, 66]	[−0.4, 0.0]	[0.4, 0.8]	0.283	8.1	2.1	0.85	2.8	0.97	0.014	0.33	0.54	0.27	1.9	1.5	0.5	1.8
8	[40, 66]	[−0.4, 0.0]	[0.8, 1.2]	0.268	9.5	2.4	1.2	3.3	0.99	0.026	0.36	0.72	0.24	2.7	2.5	0.29	1.8
9	[40, 66]	[−0.4, 0.0]	[1.2, 1.6]	0.273	11.0	2.8	1.6	3.4	0.8	0.053	0.3	1.1	0.24	3.2	3.0	1.8	1.7
10	[40, 66]	[−0.4, 0.0]	[1.6, 2.0]	0.265	11.0	2.8	2.2	2.8	0.64	0.056	0.19	1.4	0.32	6.2	6.1	1.2	1.8
11	[40, 66]	[−0.4, 0.0]	[2.0, 2.4]	0.192	12.0	3.0	2.1	2.9	0.58	0.054	0.24	1.1	0.49	4.5	4.4	0.8	1.7
12	[40, 66]	[0.0, 0.4]	[0.0, 0.4]	0.284	8.0	2.1	0.85	2.5	0.79	0.0082	0.34	0.36	0.17	1.9	1.4	0.19	1.8
13	[40, 66]	[0.0, 0.4]	[0.4, 0.8]	0.247	8.9	2.2	1.2	2.8	0.98	0.015	0.34	0.44	0.17	3.0	2.7	0.25	1.8
14	[40, 66]	[0.0, 0.4]	[0.8, 1.2]	0.235	10.0	2.5	1.3	3.4	1.0	0.028	0.37	1.2	0.22	2.4	2.1	0.58	1.8
15	[40, 66]	[0.0, 0.4]	[1.2, 1.6]	0.232	13.0	3.1	2.3	3.4	0.8	0.059	0.31	1.2	0.36	5.1	4.9	2.1	1.8
16	[40, 66]	[0.0, 0.4]	[1.6, 2.0]	0.255	11.0	2.9	2.0	2.8	0.65	0.055	0.19	0.77	0.24	5.3	5.1	0.98	1.8
17	[40, 66]	[0.0, 0.4]	[2.0, 2.4]	0.179	13.0	3.2	2.8	2.9	0.58	0.052	0.25	1.8	0.31	8.0	7.9	0.84	1.7
18	[40, 66]	[0.4, 1.0]	[0.0, 0.4]	0.159	10.0	2.3	1.7	3.6	1.3	0.062	0.46	0.77	0.34	3.5	3.0	0.43	1.8
19	[40, 66]	[0.4, 1.0]	[0.4, 0.8]	0.129	13.0	2.7	2.5	3.7	0.93	0.057	0.44	1.4	0.35	4.9	4.4	1.3	1.9
20	[40, 66]	[0.4, 1.0]	[0.8, 1.2]	0.142	13.0	2.8	2.5	3.2	0.76	0.063	0.38	1.1	0.33	4.7	4.3	0.9	1.9
21	[40, 66]	[0.4, 1.0]	[1.2, 1.6]	0.103	14.0	2.8	3.4	3.6	0.9	0.068	0.41	1.2	0.38	8.1	7.8	0.65	1.9
22	[40, 66]	[0.4, 1.0]	[1.6, 2.0]	0.065	21.0	4.2	5.1	4.1	0.83	0.11	0.53	1.8	0.53	7.3	7.1	1.8	1.8
23	[66, 116]	[−1.0, −0.4]	[0.0, 0.4]	2.300	1.5	0.082	0.029	1.1	0.47	0.015	0.12	0.06	0.027	0.17	0.16	0.4	1.6
24	[66, 116]	[−1.0, −0.4]	[0.4, 0.8]	2.239	1.7	0.086	0.035	1.4	0.49	0.016	0.14	0.11	0.033	0.23	0.22	0.29	1.6
25	[66, 116]	[−1.0, −0.4]	[0.8, 1.2]	2.026	1.8	0.089	0.05	1.2	0.49	0.012	0.13	0.08	0.038	0.2	0.19	0.18	1.6
26	[66, 116]	[−1.0, −0.4]	[1.2, 1.6]	1.484	1.9	0.097	0.032	0.81	0.45	0.0089	0.087	0.083	0.047	0.083	0.073	0.11	1.6
27	[66, 116]	[−1.0, −0.4]	[1.6, 2.0]	0.717	3.3	0.16	0.07	0.72	0.44	0.011	0.075	0.12	0.11	0.11	0.1	0.65	1.6
28	[66, 116]	[−1.0, −0.4]	[2.0, 2.4]	0.0434	22.0	1.0	2.2	2.6	0.57	0.079	0.16	1.0	1.7	0.035	0.022	7.3	1.6
29	[66, 116]	[−0.4, 0.0]	[0.0, 0.4]	1.977	1.8	0.093	0.027	0.25	0.37	0.0045	0.042	0.02	0.025	0.035	0.01	0.052	1.6
30	[66, 116]	[−0.4, 0.0]	[0.4, 0.8]	2.014	1.8	0.096	0.028	0.34	0.37	0.0057	0.033	0.02	0.029	0.033	0.0023	0.079	1.6
31	[66, 116]	[−0.4, 0.0]	[0.8, 1.2]	1.965	2.0	0.11	0.03	0.41	0.37	0.0042	0.035	0.038	0.023	0.031	0.01	0.33	1.6
32	[66, 116]	[−0.4, 0.0]	[1.2, 1.6]	1.855	2.5	0.13	0.061	0.45	0.42	0.0078	0.04	0.061	0.043	0.046	0.035	0.52	1.6
33	[66, 116]	[−0.4, 0.0]	[1.6, 2.0]	1.739	2.5	0.12	0.041	0.43	0.49	0.013	0.032	0.074	0.055	0.03	0.02	0.25	1.6
34	[66, 116]	[−0.4, 0.0]	[2.0, 2.4]	1.089	3.0	0.15	0.067	0.51	0.5	0.02	0.031	0.05	0.066	0.094	0.092	0.21	1.6
35	[66, 116]	[0.0, 0.4]	[0.0, 0.4]	2.009	1.8	0.095	0.026	0.25	0.37	0.0046	0.042	0.033	0.022	0.034	0.01	0.03	1.6
36	[66, 116]	[0.0, 0.4]	[0.4, 0.8]	1.992	1.8	0.094	0.028	0.34	0.37	0.0053	0.033	0.039	0.032	0.035	0.016	0.046	1.6
37	[66, 116]	[0.0, 0.4]	[0.8, 1.2]	2.026	2.0	0.11	0.035	0.41	0.37	0.0041	0.035	0.048	0.033	0.053	0.043	0.38	1.6
38	[66, 116]	[0.0, 0.4]	[1.2, 1.6]	1.891	2.5	0.13	0.044	0.44	0.42	0.0075	0.039	0.039	0.035	0.07	0.065	0.32	1.6
39	[66, 116]	[0.0, 0.4]	[1.6, 2.0]	1.823	2.4	0.13	0.043	0.43	0.49	0.013	0.032	0.063	0.059	0.037	0.029	0.21	1.6
40	[66, 116]	[0.0, 0.4]	[2.0, 2.4]	1.118	3.1	0.15	0.068	0.52	0.5	0.021	0.03	0.07	0.067	0.14	0.14	0.32	1.6
41	[66, 116]	[0.4, 1.0]	[0.0, 0.4]	2.317	1.6	0.082	0.05	1.2	0.47	0.015	0.12	0.066	0.034	0.12	0.11	0.42	1.6
42	[66, 116]	[0.4, 1.0]	[0.4, 0.8]	2.297	1.6	0.086	0.034	1.4	0.49	0.016	0.14	0.098	0.037	0.2	0.2	0.26	1.6
43	[66, 116]	[0.4, 1.0]	[0.8, 1.2]	2.183	1.7	0.091	0.036	1.2	0.49	0.012	0.13	0.074	0.03	0.23	0.22	0.23	1.6
44	[66, 116]	[0.4, 1.0]	[1.2, 1.6]	1.621	1.9	0.093	0.031	0.79	0.45	0.0087	0.085	0.08	0.047	0.068	0.058	0.1	1.6
45	[66, 116]	[0.4, 1.0]	[1.6, 2.0]	0.720	3.2	0.16	0.069	0.69	0.44	0.011	0.072	0.11	0.13	0.084	0.078	0.94	1.6
46	[66, 116]	[0.4, 1.0]	[2.0, 2.4]	0.0222	32.0	1.7	4.2	2.9	0.58	0.069	0.15	1.5	1.6	0.99	0.99	13.0	1.6
47	[116, 500]	[−1.0, 0.0]	[0.0, 0.4]	0.00443	10.0	0.53	0.92	0.94	0.38	0.017	0.055	0.62	0.21	4.4	4.3	0.41	1.8
48	[116, 500]	[−1.0, 0.0]	[0.4, 0.8]	0.00298	13.0	0.56	1.2	1.1	0.39	0.017	0.064	0.6	0.26	2.4	2.0	0.56	1.8
49	[116, 500]	[−1.0, 0.0]	[0.8, 1.2]	0.00265	14.0	0.64	1.4	1.1	0.4	0.012	0.069	0.52	0.29	1.9	1.6	0.29	1.8
50	[116, 500]	[−1.0, 0.0]	[1.2, 1.6]	0.00245	15.0	0.83	1.6	1.3	0.42	0.016	0.066	0.45	0.36	0.82	0.49	0.25	1.7
51	[116, 500]	[−1.0, 0.0]	[1.6, 2.0]	0.00120	22.0	1.1	3.5	1.9	0.48	0.024	0.032	2.3	0.42	0.6	0.026	0.98	1.7
52	[116, 500]	[0.0, 1.0]	[0.0, 0.4]	0.00383	11.0	0.51	1.0	0.97	0.38	0.017	0.055	1.3	0.22	5.0	4.8	0.65	1.8
53	[116, 500]	[0.0, 1.0]	[0.4, 0.8]	0.00443	10.0	0.49	0.85	1.0	0.39	0.017	0.065	0.65	0.19	1.7	1.5	0.78	1.8
54	[116, 500]	[0.0, 1.0]	[0.8, 1.2]	0.00447	11.0	0.49	0.83	1.1	0.41	0.015	0.064	1.1	0.21	1.0	0.77	0.38	1.7
55	[116, 500]	[0.0, 1.0]	[1.2, 1.6]	0.00441	11.0	0.57	0.83	1.4	0.43	0.018	0.048	0.61	0.28	0.49	0.32	0.26	1.7
56	[116, 500]	[0.0, 1.0]	[1.6, 2.0]	0.00288	15.0	0.74	1.5	2.2	0.46	0.026	0.041	1.0	0.5	0.36	0.31	0.56	1.6

Table C.16: The $\sqrt{s} = 5.02\,\text{TeV}$, $Z \to ee$ channel Born-level triple-differential cross-section $\frac{\mathrm{d}^3\sigma}{\mathrm{d}m_{\ell\ell}\mathrm{d}cos(\theta^*_{CS})\mathrm{d}|y_{\ell\ell}|}$. Unfolded results obtained from 4th iteration Bayesian unfolding.

Bin No.	$m_{\ell\ell}$ [GeV]	$cos(\theta^*_{CS})$	$\lvert y_{\ell\ell}\rvert$	$\frac{d^3\sigma}{dm_{\ell\ell}dcos(\theta^*_{CS})d\lvert y_{\ell\ell}\rvert}$ [pb/GeV]	$\delta^{stat,data}$ [%]	$\delta^{stat,signalMC}$ [%]	$\delta^{stat,background}$ [%]	δ^{reco} [%]	δ^{trig} [%]	δ^{iso} [%]	δ^{ttva} [%]	$\delta^{muon,cal}$ [%]	δ^{bkg} [%]	$\delta^{Multi\,jet}$ [%]	δ^{bias} [%]	δ^{lumi} [%]
1	[40, 66]	[−1.0, −0.4]	[0.0, 0.4]	0.184	8.0	1.9	1.0	0.46	0.26	0.53	0.86	0.2	3.1	2.6	0.37	1.8
2	[40, 66]	[−1.0, −0.4]	[0.4, 0.8]	0.209	7.8	2.0	0.89	0.8	0.21	0.47	0.79	0.13	2.5	2.1	0.46	1.8
3	[40, 66]	[−1.0, −0.4]	[0.8, 1.2]	0.200	7.4	1.8	0.8	0.59	0.12	0.47	0.86	0.22	2.2	1.7	0.24	1.8
4	[40, 66]	[−1.0, −0.4]	[1.2, 1.6]	0.209	7.1	1.9	0.6	0.45	0.13	0.47	0.79	0.25	1.4	0.91	0.47	1.7
5	[40, 66]	[−1.0, −0.4]	[1.6, 2.0]	0.115	11.0	2.8	0.84	0.43	0.15	0.42	0.61	0.69	1.2	0.62	1.5	1.7
6	[40, 66]	[−0.4, 0.0]	[0.0, 0.4]	0.270	8.3	2.1	0.53	1.0	0.3	0.41	0.36	0.14	1.4	0.62	0.2	1.8
7	[40, 66]	[−0.4, 0.0]	[0.4, 0.8]	0.288	7.5	1.9	0.46	0.52	0.22	0.3	0.39	0.21	1.3	0.61	0.39	1.8
8	[40, 66]	[−0.4, 0.0]	[0.8, 1.2]	0.319	6.8	1.9	0.39	0.43	0.16	0.27	0.34	0.22	1.1	0.49	0.44	1.7
9	[40, 66]	[−0.4, 0.0]	[1.2, 1.6]	0.324	6.6	1.9	0.36	0.42	0.076	0.25	0.4	0.13	0.92	0.36	0.75	1.7
10	[40, 66]	[−0.4, 0.0]	[1.6, 2.0]	0.317	6.6	1.9	0.31	0.47	0.047	0.29	0.57	0.32	0.81	0.16	0.64	1.7
11	[40, 66]	[−0.4, 0.0]	[2.0, 2.4]	0.188	10.0	2.7	0.52	0.49	0.085	0.39	0.54	0.49	0.83	0.17	1.4	1.7
12	[40, 66]	[0.0, 0.4]	[0.0, 0.4]	0.314	7.5	2.1	0.45	0.95	0.3	0.41	0.35	0.23	1.2	0.52	0.8	1.8
13	[40, 66]	[0.0, 0.4]	[0.4, 0.8]	0.291	7.3	2.0	0.44	0.53	0.23	0.31	0.38	0.059	1.3	0.53	0.27	1.8
14	[40, 66]	[0.0, 0.4]	[0.8, 1.2]	0.293	7.3	2.0	0.44	0.43	0.16	0.27	0.34	0.45	1.2	0.47	0.21	1.8
15	[40, 66]	[0.0, 0.4]	[1.2, 1.6]	0.266	7.5	2.0	0.43	0.41	0.076	0.26	0.46	0.53	1.1	0.36	0.45	1.8
16	[40, 66]	[0.0, 0.4]	[1.6, 2.0]	0.248	7.7	2.0	0.42	0.46	0.045	0.31	0.64	0.49	0.92	0.27	0.56	1.8
17	[40, 66]	[0.0, 0.4]	[2.0, 2.4]	0.190	10.0	2.8	0.48	0.48	0.084	0.4	0.58	0.61	0.75	0.02	0.76	1.7
18	[40, 66]	[0.4, 1.0]	[0.0, 0.4]	0.148	9.2	2.0	1.3	0.47	0.28	0.54	0.89	0.31	3.8	3.2	0.66	1.8
19	[40, 66]	[0.4, 1.0]	[0.4, 0.8]	0.172	8.7	2.1	1.0	0.82	0.23	0.49	0.83	0.37	2.8	2.1	0.26	1.8
20	[40, 66]	[0.4, 1.0]	[0.8, 1.2]	0.166	8.3	2.1	0.94	0.58	0.12	0.49	0.86	0.2	2.5	2.0	0.44	1.8
21	[40, 66]	[0.4, 1.0]	[1.2, 1.6]	0.164	8.4	2.2	0.8	0.45	0.13	0.46	0.79	0.16	1.8	1.3	0.64	1.8
22	[40, 66]	[0.4, 1.0]	[1.6, 2.0]	0.074	15.0	3.5	1.2	0.42	0.15	0.48	0.74	0.65	1.8	0.77	0.65	1.8
23	[66, 116]	[−1.0, −0.4]	[0.0, 0.4]	2.232	1.3	0.04	0.032	0.56	0.08	0.12	0.25	0.039	0.32	0.31	0.12	1.6
24	[66, 116]	[−1.0, −0.4]	[0.4, 0.8]	2.217	1.4	0.043	0.034	0.71	0.059	0.12	0.17	0.053	0.33	0.32	0.16	1.6
25	[66, 116]	[−1.0, −0.4]	[0.8, 1.2]	1.985	1.5	0.045	0.027	0.72	0.11	0.1	0.079	0.042	0.16	0.15	0.13	1.6
26	[66, 116]	[−1.0, −0.4]	[1.2, 1.6]	1.517	1.7	0.051	0.028	0.63	0.1	0.085	0.048	0.066	0.12	0.11	0.12	1.6
27	[66, 116]	[−1.0, −0.4]	[1.6, 2.0]	0.703	2.9	0.091	0.035	0.59	0.12	0.078	0.057	0.13	0.037	0.023	1.1	1.6
28	[66, 116]	[−1.0, −0.4]	[2.0, 2.4]	0.032	29.0	0.83	1.4	0.79	0.17	0.17	0.17	1.2	0.077	0.018	21.0	1.6
29	[66, 116]	[−0.4, 0.0]	[0.0, 0.4]	2.049	1.8	0.055	0.026	1.1	0.13	0.055	0.047	0.026	0.065	0.057	0.013	1.6
30	[66, 116]	[−0.4, 0.0]	[0.4, 0.8]	2.012	1.7	0.052	0.025	0.73	0.12	0.03	0.045	0.026	0.067	0.059	0.1	1.6
31	[66, 116]	[−0.4, 0.0]	[0.8, 1.2]	1.937	1.7	0.054	0.023	0.6	0.096	0.032	0.039	0.033	0.047	0.036	0.039	1.6
32	[66, 116]	[−0.4, 0.0]	[1.2, 1.6]	1.816	1.7	0.053	0.028	0.61	0.041	0.036	0.054	0.038	0.035	0.023	0.15	1.6
33	[66, 116]	[−0.4, 0.0]	[1.6, 2.0]	1.756	1.8	0.055	0.019	0.7	0.026	0.043	0.069	0.031	0.028	0.015	0.23	1.6
34	[66, 116]	[−0.4, 0.0]	[2.0, 2.4]	1.089	2.7	0.081	0.027	0.73	0.11	0.066	0.069	0.11	0.023	0.0019	0.34	1.6
35	[66, 116]	[0.0, 0.4]	[0.0, 0.4]	1.987	1.8	0.054	0.024	1.1	0.13	0.055	0.047	0.033	0.045	0.033	0.11	1.6
36	[66, 116]	[0.0, 0.4]	[0.4, 0.8]	2.042	1.7	0.051	0.022	0.73	0.12	0.03	0.046	0.03	0.048	0.037	0.17	1.6
37	[66, 116]	[0.0, 0.4]	[0.8, 1.2]	1.945	1.7	0.05	0.024	0.6	0.096	0.032	0.039	0.032	0.048	0.037	0.11	1.6
38	[66, 116]	[0.0, 0.4]	[1.2, 1.6]	1.959	1.7	0.052	0.023	0.61	0.042	0.036	0.053	0.031	0.052	0.045	0.074	1.6
39	[66, 116]	[0.0, 0.4]	[1.6, 2.0]	1.812	1.7	0.054	0.017	0.71	0.026	0.043	0.069	0.031	0.024	0.0025	0.16	1.6
40	[66, 116]	[0.0, 0.4]	[2.0, 2.4]	1.156	2.6	0.083	0.03	0.73	0.11	0.066	0.069	0.056	0.024	0.012	0.34	1.6
41	[66, 116]	[0.4, 1.0]	[0.0, 0.4]	2.324	1.3	0.04	0.033	0.56	0.079	0.13	0.24	0.024	0.34	0.33	0.067	1.6
42	[66, 116]	[0.4, 1.0]	[0.4, 0.8]	2.282	1.4	0.042	0.032	0.72	0.059	0.12	0.17	0.049	0.23	0.23	0.17	1.6
43	[66, 116]	[0.4, 1.0]	[0.8, 1.2]	2.106	1.4	0.043	0.028	0.72	0.11	0.099	0.076	0.029	0.2	0.19	0.17	1.6
44	[66, 116]	[0.4, 1.0]	[1.2, 1.6]	1.660	1.6	0.05	0.023	0.64	0.1	0.083	0.048	0.062	0.075	0.067	0.14	1.6
45	[66, 116]	[0.4, 1.0]	[1.6, 2.0]	0.769	2.7	0.086	0.038	0.59	0.12	0.077	0.057	0.16	0.057	0.05	0.79	1.6
46	[66, 116]	[0.4, 1.0]	[2.0, 2.4]	0.045	25.0	0.83	1.1	0.79	0.18	0.18	0.19	0.74	0.068	0.014	17.0	1.6
47	[116, 500]	[−1.0, 0.0]	[0.0, 0.4]	0.00309	12.0	0.3	1.0	0.94	0.16	0.046	0.076	0.4	6.0	5.8	0.66	1.9
48	[116, 500]	[−1.0, 0.0]	[0.4, 0.8]	0.00399	9.6	0.29	0.56	0.94	0.14	0.036	0.046	0.47	1.9	1.6	0.34	1.8
49	[116, 500]	[−1.0, 0.0]	[0.8, 1.2]	0.00309	11.0	0.32	0.47	0.92	0.14	0.031	0.039	0.38	0.85	0.19	0.29	1.7
50	[116, 500]	[−1.0, 0.0]	[1.2, 1.6]	0.00194	14.0	0.4	0.58	0.9	0.093	0.041	0.048	0.64	0.76	0.16	0.19	1.7
51	[116, 500]	[−1.0, 0.0]	[1.6, 2.0]	0.00121	18.0	0.53	0.9	1.0	0.092	0.057	0.065	0.85	0.5	0.065	0.81	1.7
52	[116, 500]	[0.0, 1.0]	[0.0, 0.4]	0.00456	9.4	0.27	0.64	0.92	0.16	0.043	0.065	0.34	3.3	3.1	0.34	1.8
53	[116, 500]	[0.0, 1.0]	[0.4, 0.8]	0.00509	8.6	0.26	0.47	0.94	0.13	0.037	0.041	0.51	1.7	1.5	0.27	1.7
54	[116, 500]	[0.0, 1.0]	[0.8, 1.2]	0.00535	8.3	0.26	0.32	0.95	0.11	0.031	0.039	0.42	0.59	0.33	0.2	1.7
55	[116, 500]	[0.0, 1.0]	[1.2, 1.6]	0.00399	9.5	0.29	0.37	0.92	0.11	0.036	0.046	0.38	0.56	0.41	0.3	1.7
56	[116, 500]	[0.0, 1.0]	[1.6, 2.0]	0.00251	12.0	0.34	0.46	1.0	0.11	0.06	0.063	0.81	0.28	0.047	0.41	1.6

Table C.17: The $\sqrt{s} = 5.02\,\text{TeV}$, $Z \rightarrow \mu\mu$ channel Born-level triple-differential cross-section $\frac{\mathrm{d}^3\sigma}{\mathrm{d}m_{\ell\ell}\mathrm{d}cos(\theta^*_{CS})\mathrm{d}|y_{\ell\ell}|}$. Unfolded results obtained from 4th iteration Bayesian unfolding.

Bin No.	$m_{\ell\ell}$ [GeV]	$cos(\theta^*_{CS})$	$\lvert y_{\ell\ell}\rvert$	$\frac{d^3\sigma}{dm_{\ell\ell}dcos(\theta^*_{CS})d\lvert y_{\ell\ell}\rvert}$ [pb/GeV]	$\delta^{stat,data}$ [%]	$\delta^{stat,signalMC}$ [%]	$\delta^{stat,background}$ [%]	δ^{id} [%]	δ^{reco} [%]	δ^{trig} [%]	δ^{iso} [%]	$\delta^{highp_T,cal}$ [%]	$\delta^{lowp_T,cal}$ [%]	δ^{bkg} [%]	$\delta^{Multijet}$ [%]	δ^{bias} [%]	δ^{lumi} [%]
1	[40, 66]	[−1.0, −0.4]	[0.0, 0.4]	0.416	5.4	1.2	1.2	1.4	1.3	0.045	0.52	0.5	0.11	2.3	2.1	0.31	1.7
2	[40, 66]	[−1.0, −0.4]	[0.4, 0.8]	0.388	6.7	1.4	1.4	2.1	0.9	0.056	0.6	1.4	0.17	2.7	2.4	0.43	1.8
3	[40, 66]	[−1.0, −0.4]	[0.8, 1.2]	0.440	6.3	1.4	1.4	1.7	0.75	0.069	0.65	0.5	0.16	3.0	2.9	0.27	1.7
4	[40, 66]	[−1.0, −0.4]	[1.2, 1.6]	0.348	6.4	1.3	1.5	1.8	0.86	0.05	0.54	0.62	0.15	4.2	4.0	0.25	1.7
5	[40, 66]	[−1.0, −0.4]	[1.6, 2.0]	0.207	10.0	2.0	2.3	2.0	0.81	0.071	0.59	0.96	0.24	4.4	4.3	0.59	1.7
6	[40, 66]	[−0.4, 0.0]	[0.0, 0.4]	0.578	5.1	1.1	0.94	1.7	0.79	0.0095	0.36	0.65	0.13	1.5	0.87	0.28	1.7
7	[40, 66]	[−0.4, 0.0]	[0.4, 0.8]	0.629	4.8	1.1	0.78	1.2	0.94	0.012	0.36	0.48	0.085	1.4	0.89	0.18	1.7
8	[40, 66]	[−0.4, 0.0]	[0.8, 1.2]	0.606	5.7	1.3	0.92	1.3	0.96	0.021	0.42	0.42	0.08	1.3	1.1	0.37	1.7
9	[40, 66]	[−0.4, 0.0]	[1.2, 1.6]	0.666	6.5	1.6	1.1	1.5	0.78	0.044	0.49	0.82	0.13	2.0	1.7	0.96	1.6
10	[40, 66]	[−0.4, 0.0]	[1.6, 2.0]	0.534	7.2	1.5	1.5	1.5	0.64	0.054	0.51	0.93	0.15	2.8	2.7	0.94	1.7
11	[40, 66]	[−0.4, 0.0]	[2.0, 2.4]	0.427	7.1	1.6	1.3	1.9	0.58	0.047	0.43	1.2	0.22	2.8	2.6	0.77	1.6
12	[40, 66]	[0.0, 0.4]	[0.0, 0.4]	0.643	4.8	1.2	0.88	1.7	0.78	0.0093	0.35	0.46	0.093	2.0	0.8	0.27	1.7
13	[40, 66]	[0.0, 0.4]	[0.4, 0.8]	0.610	5.0	1.2	0.9	1.2	0.96	0.013	0.37	0.48	0.12	1.6	0.82	0.33	1.7
14	[40, 66]	[0.0, 0.4]	[0.8, 1.2]	0.607	5.5	1.3	0.79	1.3	0.97	0.021	0.42	0.63	0.1	2.0	0.88	0.32	1.7
15	[40, 66]	[0.0, 0.4]	[1.2, 1.6]	0.530	7.7	1.7	1.3	1.5	0.79	0.045	0.5	0.97	0.16	2.1	1.8	0.49	1.7
16	[40, 66]	[0.0, 0.4]	[1.6, 2.0]	0.551	7.0	1.6	1.4	1.5	0.64	0.054	0.5	1.1	0.15	2.8	2.6	0.89	1.7
17	[40, 66]	[0.0, 0.4]	[2.0, 2.4]	0.367	8.0	1.7	1.7	1.9	0.58	0.049	0.45	0.99	0.17	3.0	2.9	1.0	1.7
18	[40, 66]	[0.4, 1.0]	[0.0, 0.4]	0.363	5.9	1.3	1.3	1.4	1.3	0.046	0.53	0.81	0.13	2.7	2.3	0.22	1.7
19	[40, 66]	[0.4, 1.0]	[0.4, 0.8]	0.362	6.7	1.4	1.4	2.0	0.89	0.055	0.6	0.65	0.16	2.7	2.3	0.58	1.7
20	[40, 66]	[0.4, 1.0]	[0.8, 1.2]	0.356	7.2	1.5	1.8	1.7	0.74	0.069	0.66	0.74	0.2	4.0	3.8	0.3	1.8
21	[40, 66]	[0.4, 1.0]	[1.2, 1.6]	0.288	7.4	1.4	1.9	1.8	0.87	0.052	0.58	0.76	0.13	5.3	5.1	0.42	1.8
22	[40, 66]	[0.4, 1.0]	[1.6, 2.0]	0.154	12.0	2.2	2.8	2.1	0.84	0.074	0.64	1.3	0.21	5.8	5.6	0.77	1.7
23	[66, 116]	[−1.0, −0.4]	[0.0, 0.4]	5.404	0.89	0.064	0.055	0.59	0.47	0.013	0.18	0.099	0.018	0.15	0.11	0.48	1.5
24	[66, 116]	[−1.0, −0.4]	[0.4, 0.8]	5.355	0.96	0.066	0.059	0.69	0.49	0.015	0.22	0.12	0.02	0.17	0.16	0.36	1.5
25	[66, 116]	[−1.0, −0.4]	[0.8, 1.2]	4.804	1.0	0.067	0.06	0.71	0.48	0.011	0.17	0.078	0.018	0.15	0.14	0.19	1.5
26	[66, 116]	[−1.0, −0.4]	[1.2, 1.6]	3.718	1.1	0.073	0.061	0.5	0.45	0.0086	0.11	0.082	0.026	0.075	0.065	0.14	1.5
27	[66, 116]	[−1.0, −0.4]	[1.6, 2.0]	1.764	1.8	0.12	0.1	0.56	0.45	0.012	0.1	0.14	0.066	0.083	0.065	0.65	1.5
28	[66, 116]	[−1.0, −0.4]	[2.0, 2.4]	0.153	9.0	0.6	0.54	3.3	0.56	0.074	0.19	0.66	0.32	0.27	0.0089	5.0	1.5
29	[66, 116]	[−0.4, 0.0]	[0.0, 0.4]	4.919	1.0	0.067	0.06	0.19	0.37	0.0054	0.058	0.021	0.013	0.054	0.015	0.046	1.5
30	[66, 116]	[−0.4, 0.0]	[0.4, 0.8]	5.001	0.99	0.071	0.056	0.29	0.37	0.0052	0.049	0.022	0.016	0.041	0.015	0.14	1.5
31	[66, 116]	[−0.4, 0.0]	[0.8, 1.2]	4.646	1.2	0.076	0.059	0.41	0.37	0.0089	0.055	0.031	0.019	0.039	0.017	0.25	1.5
32	[66, 116]	[−0.4, 0.0]	[1.2, 1.6]	4.615	1.4	0.095	0.06	0.34	0.42	0.0086	0.062	0.03	0.027	0.053	0.023	0.64	1.5
33	[66, 116]	[−0.4, 0.0]	[1.6, 2.0]	4.357	1.4	0.089	0.065	0.29	0.49	0.016	0.059	0.066	0.029	0.057	0.05	0.24	1.5
34	[66, 116]	[−0.4, 0.0]	[2.0, 2.4]	2.807	1.6	0.11	0.066	0.5	0.5	0.024	0.053	0.027	0.025	0.087	0.081	0.12	1.5
35	[66, 116]	[0.0, 0.4]	[0.0, 0.4]	4.947	1.0	0.071	0.058	0.19	0.37	0.0053	0.058	0.026	0.013	0.15	0.012	0.051	1.5
36	[66, 116]	[0.0, 0.4]	[0.4, 0.8]	4.970	1.0	0.071	0.059	0.28	0.37	0.0049	0.049	0.012	0.016	0.036	0.0099	0.14	1.5
37	[66, 116]	[0.0, 0.4]	[0.8, 1.2]	4.943	1.1	0.076	0.056	0.41	0.37	0.0087	0.054	0.045	0.019	0.059	0.015	0.26	1.5
38	[66, 116]	[0.0, 0.4]	[1.2, 1.6]	4.716	1.3	0.093	0.056	0.34	0.42	0.0083	0.062	0.038	0.024	0.078	0.023	0.56	1.5
39	[66, 116]	[0.0, 0.4]	[1.6, 2.0]	4.571	1.3	0.092	0.068	0.29	0.49	0.016	0.059	0.056	0.026	0.049	0.038	0.23	1.5
40	[66, 116]	[0.0, 0.4]	[2.0, 2.4]	3.011	1.6	0.11	0.053	0.5	0.5	0.024	0.053	0.045	0.028	0.11	0.07	0.12	1.5
41	[66, 116]	[0.4, 1.0]	[0.0, 0.4]	5.447	0.88	0.061	0.061	0.58	0.46	0.012	0.18	0.066	0.019	0.12	0.11	0.47	1.5
42	[66, 116]	[0.4, 1.0]	[0.4, 0.8]	5.352	0.95	0.066	0.058	0.69	0.49	0.015	0.23	0.094	0.021	0.19	0.18	0.4	1.5
43	[66, 116]	[0.4, 1.0]	[0.8, 1.2]	4.953	0.98	0.067	0.055	0.71	0.48	0.011	0.17	0.075	0.022	0.18	0.15	0.17	1.5
44	[66, 116]	[0.4, 1.0]	[1.2, 1.6]	3.862	1.0	0.071	0.049	0.49	0.45	0.0084	0.11	0.092	0.027	0.068	0.055	0.12	1.5
45	[66, 116]	[0.4, 1.0]	[1.6, 2.0]	1.785	1.8	0.12	0.082	0.56	0.45	0.011	0.098	0.13	0.063	0.11	0.081	0.75	1.5
46	[66, 116]	[0.4, 1.0]	[2.0, 2.4]	0.130	9.9	0.63	0.63	3.3	0.58	0.083	0.19	0.84	0.51	0.24	0.11	6.6	1.5
47	[116, 500]	[−1.0, 0.0]	[0.0, 0.4]	0.01121	6.4	0.36	2.2	0.63	0.38	0.018	0.064	0.35	0.13	5.7	4.1	0.58	2.1
48	[116, 500]	[−1.0, 0.0]	[0.4, 0.8]	0.00950	6.8	0.39	2.2	0.75	0.39	0.018	0.06	0.48	0.11	3.5	2.0	0.63	2.0
49	[116, 500]	[−1.0, 0.0]	[0.8, 1.2]	0.01047	6.3	0.43	1.7	0.86	0.4	0.016	0.05	0.33	0.14	2.7	0.83	0.3	1.8
50	[116, 500]	[−1.0, 0.0]	[1.2, 1.6]	0.00744	8.0	0.53	2.6	0.96	0.43	0.016	0.036	0.54	0.15	2.7	0.6	0.4	1.8
51	[116, 500]	[−1.0, 0.0]	[1.6, 2.0]	0.00431	11.0	0.7	2.2	1.3	0.47	0.028	0.037	1.2	0.31	1.7	0.33	0.37	1.7
52	[116, 500]	[0.0, 1.0]	[0.0, 0.4]	0.01196	5.9	0.36	1.8	0.62	0.38	0.017	0.063	0.39	0.12	4.7	4.2	0.43	2.0
53	[116, 500]	[0.0, 1.0]	[0.4, 0.8]	0.01172	5.9	0.36	1.7	0.76	0.39	0.017	0.057	0.27	0.14	3.2	1.9	0.44	1.9
54	[116, 500]	[0.0, 1.0]	[0.8, 1.2]	0.01042	6.5	0.39	1.9	0.84	0.41	0.015	0.049	0.38	0.15	2.4	1.2	0.37	1.8
55	[116, 500]	[0.0, 1.0]	[1.2, 1.6]	0.01043	6.5	0.41	1.8	0.95	0.43	0.016	0.035	0.45	0.14	1.1	0.51	0.23	1.8
56	[116, 500]	[0.0, 1.0]	[1.6, 2.0]	0.00688	8.3	0.54	2.2	1.4	0.46	0.025	0.035	0.7	0.22	2.5	0.38	0.2	1.7

Table C.18: The $\sqrt{s}$ = 13 TeV, $Z \to ee$ channel Born-level triple-differential cross-section $\frac{d^3\sigma}{dm_{\ell\ell}dcos(\theta^*_{CS})d|y_{\ell\ell}|}$. Unfolded results obtained from 4th iteration Bayesian unfolding.

Bin No.	$m_{\ell\ell}$ [GeV]	$cos(\theta^*_{CS})$	$\lvert y_{\ell\ell}\rvert$	$\frac{d^3\sigma}{dm_{\ell\ell}dcos(\theta^*_{CS})d\lvert y_{\ell\ell}\rvert}$ [pb/GeV]	$\delta^{stat,data}$ [%]	$\delta^{stat,signalMC}$ [%]	$\delta^{stat,background}$ [%]	δ^{reco} [%]	δ^{trig} [%]	δ^{iso} [%]	δ^{ttva} [%]	$\delta^{muon,cal}$ [%]	δ^{bkg} [%]	$\delta^{Multi\,jet}$ [%]	δ^{bias} [%]	δ^{lumi} [%]
1	[40, 66]	[−1.0, −0.4]	[0.0, 0.4]	0.405	4.8	1.1	0.83	0.45	0.16	0.32	0.56	0.12	1.9	1.7	0.24	1.7
2	[40, 66]	[−1.0, −0.4]	[0.4, 0.8]	0.375	5.2	1.1	0.96	0.73	0.14	0.41	0.52	0.14	2.2	2.0	0.46	1.7
3	[40, 66]	[−1.0, −0.4]	[0.8, 1.2]	0.431	4.6	1.0	0.72	0.53	0.076	0.32	0.52	0.1	1.6	1.4	0.48	1.6
4	[40, 66]	[−1.0, −0.4]	[1.2, 1.6]	0.374	5.0	1.1	0.7	0.43	0.08	0.28	0.48	0.15	1.7	1.2	0.18	1.6
5	[40, 66]	[−1.0, −0.4]	[1.6, 2.0]	0.230	7.1	1.7	1.0	0.43	0.078	0.36	0.39	0.45	0.8	0.63	1.7	1.6
6	[40, 66]	[−0.4, 0.0]	[0.0, 0.4]	0.654	4.6	1.1	0.63	0.83	0.18	0.28	0.26	0.1	0.77	0.61	0.34	1.6
7	[40, 66]	[−0.4, 0.0]	[0.4, 0.8]	0.639	4.4	1.0	0.52	0.47	0.11	0.19	0.25	0.086	1.2	0.51	0.45	1.6
8	[40, 66]	[−0.4, 0.0]	[0.8, 1.2]	0.647	4.3	1.0	0.53	0.4	0.088	0.2	0.23	0.12	0.63	0.4	0.29	1.6
9	[40, 66]	[−0.4, 0.0]	[1.2, 1.6]	0.599	4.4	1.0	0.51	0.4	0.035	0.2	0.28	0.14	0.62	0.42	0.16	1.6
10	[40, 66]	[−0.4, 0.0]	[1.6, 2.0]	0.569	4.4	1.0	0.55	0.43	0.021	0.22	0.37	0.18	1.0	0.33	0.6	1.6
11	[40, 66]	[−0.4, 0.0]	[2.0, 2.4]	0.408	6.3	1.5	0.76	0.47	0.042	0.33	0.35	0.17	0.78	0.27	0.72	1.6
12	[40, 66]	[0.0, 0.4]	[0.0, 0.4]	0.600	4.9	1.1	0.72	0.84	0.18	0.28	0.26	0.13	0.89	0.58	0.46	1.6
13	[40, 66]	[0.0, 0.4]	[0.4, 0.8]	0.623	4.4	1.0	0.67	0.47	0.11	0.2	0.27	0.13	0.7	0.53	0.45	1.6
14	[40, 66]	[0.0, 0.4]	[0.8, 1.2]	0.608	4.5	1.1	0.59	0.4	0.092	0.2	0.23	0.12	1.2	0.5	0.34	1.6
15	[40, 66]	[0.0, 0.4]	[1.2, 1.6]	0.557	4.6	1.1	0.66	0.4	0.036	0.2	0.29	0.22	0.7	0.47	0.47	1.6
16	[40, 66]	[0.0, 0.4]	[1.6, 2.0]	0.547	4.6	1.1	0.53	0.43	0.021	0.22	0.38	0.25	0.6	0.35	0.48	1.6
17	[40, 66]	[0.0, 0.4]	[2.0, 2.4]	0.402	6.4	1.6	0.58	0.47	0.042	0.33	0.35	0.2	0.88	0.28	0.6	1.6
18	[40, 66]	[0.4, 1.0]	[0.0, 0.4]	0.384	4.9	1.1	0.78	0.45	0.16	0.32	0.56	0.16	2.2	1.7	0.41	1.7
19	[40, 66]	[0.4, 1.0]	[0.4, 0.8]	0.373	5.3	1.1	0.85	0.71	0.15	0.39	0.51	0.17	2.0	1.8	0.47	1.7
20	[40, 66]	[0.4, 1.0]	[0.8, 1.2]	0.385	4.8	1.1	0.81	0.53	0.078	0.32	0.52	0.17	1.7	1.5	0.48	1.7
21	[40, 66]	[0.4, 1.0]	[1.2, 1.6]	0.341	5.1	1.2	0.78	0.42	0.082	0.29	0.5	0.18	1.3	1.1	0.25	1.7
22	[40, 66]	[0.4, 1.0]	[1.6, 2.0]	0.197	7.9	1.8	1.2	0.43	0.077	0.39	0.43	0.37	1.0	0.86	0.89	1.6
23	[66, 116]	[−1.0, −0.4]	[0.0, 0.4]	5.335	0.77	0.054	0.044	0.47	0.056	0.091	0.15	0.025	0.067	0.056	0.16	1.5
24	[66, 116]	[−1.0, −0.4]	[0.4, 0.8]	5.217	0.8	0.056	0.045	0.62	0.032	0.08	0.11	0.053	0.073	0.05	0.16	1.5
25	[66, 116]	[−1.0, −0.4]	[0.8, 1.2]	4.775	0.83	0.059	0.046	0.61	0.031	0.083	0.062	0.04	0.055	0.035	0.24	1.5
26	[66, 116]	[−1.0, −0.4]	[1.2, 1.6]	3.710	0.96	0.068	0.043	0.54	0.049	0.057	0.045	0.059	0.037	0.018	0.2	1.5
27	[66, 116]	[−1.0, −0.4]	[1.6, 2.0]	1.800	1.6	0.11	0.08	0.54	0.038	0.049	0.051	0.11	0.028	0.0088	0.92	1.5
28	[66, 116]	[−1.0, −0.4]	[2.0, 2.4]	0.155	10.0	0.77	0.61	0.72	0.084	0.11	0.11	0.57	0.6	0.0048	10.0	1.5
29	[66, 116]	[−0.4, 0.0]	[0.0, 0.4]	4.792	1.0	0.073	0.056	0.87	0.074	0.033	0.055	0.024	0.084	0.011	0.057	1.5
30	[66, 116]	[−0.4, 0.0]	[0.4, 0.8]	4.827	0.98	0.067	0.046	0.55	0.06	0.022	0.054	0.018	0.03	0.0076	0.15	1.5
31	[66, 116]	[−0.4, 0.0]	[0.8, 1.2]	4.785	0.98	0.069	0.046	0.49	0.046	0.023	0.044	0.035	0.04	0.0068	0.12	1.5
32	[66, 116]	[−0.4, 0.0]	[1.2, 1.6]	4.670	0.97	0.068	0.052	0.53	0.019	0.022	0.047	0.034	0.023	0.0055	0.14	1.5
33	[66, 116]	[−0.4, 0.0]	[1.6, 2.0]	4.363	0.98	0.069	0.043	0.6	0.013	0.03	0.059	0.029	0.041	0.0041	0.27	1.5
34	[66, 116]	[−0.4, 0.0]	[2.0, 2.4]	2.970	1.4	0.1	0.058	0.63	0.028	0.047	0.06	0.068	0.037	0.0039	0.32	1.5
35	[66, 116]	[0.0, 0.4]	[0.0, 0.4]	4.861	1.0	0.074	0.049	0.86	0.074	0.033	0.055	0.022	0.1	0.0083	0.073	1.5
36	[66, 116]	[0.0, 0.4]	[0.4, 0.8]	4.889	0.96	0.069	0.053	0.55	0.06	0.022	0.054	0.019	0.033	0.0049	0.12	1.5
37	[66, 116]	[0.0, 0.4]	[0.8, 1.2]	4.674	0.98	0.069	0.051	0.49	0.046	0.023	0.044	0.027	0.034	0.0084	0.13	1.5
38	[66, 116]	[0.0, 0.4]	[1.2, 1.6]	4.684	0.97	0.071	0.046	0.53	0.02	0.022	0.047	0.024	0.054	0.0049	0.14	1.5
39	[66, 116]	[0.0, 0.4]	[1.6, 2.0]	4.475	0.99	0.07	0.039	0.6	0.013	0.03	0.059	0.028	0.017	0.0047	0.28	1.5
40	[66, 116]	[0.0, 0.4]	[2.0, 2.4]	2.997	1.4	0.098	0.064	0.63	0.028	0.047	0.06	0.065	0.038	0.0036	0.33	1.5
41	[66, 116]	[0.4, 1.0]	[0.0, 0.4]	5.349	0.78	0.053	0.041	0.47	0.056	0.091	0.15	0.031	0.1	0.052	0.18	1.5
42	[66, 116]	[0.4, 1.0]	[0.4, 0.8]	5.255	0.81	0.056	0.056	0.62	0.032	0.079	0.11	0.048	0.076	0.053	0.15	1.5
43	[66, 116]	[0.4, 1.0]	[0.8, 1.2]	4.980	0.81	0.058	0.045	0.61	0.032	0.083	0.061	0.03	0.061	0.038	0.24	1.5
44	[66, 116]	[0.4, 1.0]	[1.2, 1.6]	3.756	0.95	0.067	0.046	0.54	0.05	0.056	0.045	0.056	0.057	0.019	0.18	1.5
45	[66, 116]	[0.4, 1.0]	[1.6, 2.0]	1.906	1.5	0.11	0.09	0.54	0.038	0.048	0.05	0.11	0.06	0.014	0.97	1.5
46	[66, 116]	[0.4, 1.0]	[2.0, 2.4]	0.151	10.0	0.79	0.83	0.73	0.087	0.11	0.11	0.54	1.3	0.02	11.0	1.5
47	[116, 500]	[−1.0, 0.0]	[0.0, 0.4]	0.01017	6.2	0.35	2.0	0.69	0.074	0.034	0.056	0.35	4.9	0.58	0.16	2.1
48	[116, 500]	[−1.0, 0.0]	[0.4, 0.8]	0.01030	5.8	0.37	2.1	0.68	0.06	0.033	0.045	0.4	2.9	0.29	0.1	1.9
49	[116, 500]	[−1.0, 0.0]	[0.8, 1.2]	0.00744	6.9	0.4	2.2	0.7	0.06	0.026	0.04	0.39	3.2	0.16	0.3	2.0
50	[116, 500]	[−1.0, 0.0]	[1.2, 1.6]	0.00649	7.1	0.45	1.8	0.74	0.04	0.035	0.043	0.42	1.2	0.088	0.67	1.8
51	[116, 500]	[−1.0, 0.0]	[1.6, 2.0]	0.00484	8.1	0.55	1.4	0.86	0.038	0.054	0.055	0.7	1.9	0.022	0.27	1.6
52	[116, 500]	[0.0, 1.0]	[0.0, 0.4]	0.01237	5.4	0.35	1.7	0.69	0.073	0.033	0.055	0.28	3.1	0.48	0.23	2.0
53	[116, 500]	[0.0, 1.0]	[0.4, 0.8]	0.01062	5.9	0.33	1.9	0.7	0.057	0.032	0.044	0.31	2.5	0.29	0.37	1.9
54	[116, 500]	[0.0, 1.0]	[0.8, 1.2]	0.01120	5.4	0.36	1.7	0.71	0.054	0.026	0.04	0.36	1.5	0.16	0.41	1.8
55	[116, 500]	[0.0, 1.0]	[1.2, 1.6]	0.00943	5.8	0.39	1.2	0.74	0.042	0.035	0.042	0.39	1.3	0.03	0.26	1.7
56	[116, 500]	[0.0, 1.0]	[1.6, 2.0]	0.00669	7.0	0.46	1.8	0.85	0.043	0.053	0.054	0.74	0.99	0.023	0.39	1.7

Table C.19: The $\sqrt{s} = 13\,\text{TeV}$, $Z \to \mu\mu$ channel Born-level triple-differential cross-section $\frac{\mathrm{d}^3\sigma}{\mathrm{d}m_{\ell\ell}\mathrm{d}cos(\theta^*_{CS})\mathrm{d}|y_{\ell\ell}|}$. Unfolded results obtained from 4th iteration Bayesian unfolding.

Bibliography

[1] Y. Fukuda et al., *Evidence for Oscillation of Atmospheric Neutrinos*, Phys. Rev. Lett. **81** (8 1998) 1562.

[2] M. Aker et al., *Direct neutrino-mass measurement with sub-electronvolt sensitivity*, Nature Phys. **18** (2022) 160, arXiv: 2105.08533 [hep-ex].

[3] P. Zyla et al., *Review of Particle Physics*, PTEP **2020** (2020) 083C01.

[4] MissMJ, Cush / Wikimedia Commons, *Standard Model of Elementary Particles*, 2019, URL: https://en.wikipedia.org/wiki/File:Standard_Model_of_Elementary_Particles.svg (visited on 28/03/2022).

[5] H. Fritzsch, M. Gell-Mann and H. Leutwyler, *Advantages of the color octet gluon picture*, Physics Letters B **47** (1973) 365, ISSN: 0370-2693.

[6] D. J. Gross and F. Wilczek, *Ultraviolet Behavior of Non-Abelian Gauge Theories*, Phys. Rev. Lett. **30** (26 1973) 1343.

[7] S. Weinberg, *Non-Abelian Gauge Theories of the Strong Interactions*, Phys. Rev. Lett. **31** (7 1973) 494.

[8] C. N. Yang and R. L. Mills, *Conservation of Isotopic Spin and Isotopic Gauge Invariance*, Phys. Rev. **96** (1 1954) 191.

[9] S. L. Glashow, *Partial-symmetries of weak interactions*, Nuclear Physics **22** (1961) 579, ISSN: 0029-5582.

[10] S. Weinberg, *A Model of Leptons*, Phys. Rev. Lett. **19** (21 1967) 1264.

[11] A. Salam, *Weak and Electromagnetic Interactions*, Conf. Proc. C **680519** (1968) 367.

[12] J. Ellis, *Higgs Physics*, (2013) 117, arXiv: 1312.5672.

[13] F. Englert and R. Brout, *Broken Symmetry and the Mass of Gauge Vector Mesons*, Phys. Rev. Lett. **13** (9 1964) 321.

[14] P. W. Higgs, *Broken Symmetries and the Masses of Gauge Bosons*, Phys. Rev. Lett. **13** (16 1964) 508.

[15] S. Weinberg, *Physical Processes in a Convergent Theory of the Weak and Electromagnetic Interactions*, Phys. Rev. Lett. **27** (24 1971) 1688.

[16] S. Bailey, T. Cridge, L. A. Harland-Lang, A. D. Martin and R. S. Thorne, *Parton distributions from LHC, HERA, Tevatron and fixed target data: MSHT20 PDFs*, The European Physical Journal C **81** (2021), ISSN: 1434-6052.

[17] V. N. Gribov and L. N. Lipatov, *Deep inelastic electron scattering in perturbation theory*, Phys. Lett. B **37** (1971) 78.

[18] V. N. Gribov and L. N. Lipatov, *Deep inelastic e p scattering in perturbation theory*, Sov. J. Nucl. Phys. **15** (1972) 438.

[19] Y. L. Dokshitzer, *Calculation of the Structure Functions for Deep Inelastic Scattering and e+ e- Annihilation by Perturbation Theory in Quantum Chromodynamics.*, Sov. Phys. JETP **46** (1977) 641.

[20] H.-L. Lai et al., *New parton distributions for collider physics*, Physical Review D **82** (2010).

[21] R. D. Ball et al., *The Path to Proton Structure at One-Percent Accuracy*, (2021), arXiv: 2109.02653 [hep-ph].

[22] A. V. Lipatov, M. A. Malyshev and N. P. Zotov, *Drell-Yan lepton pair production at high energies in the kT -factorization approach*, Journal of High Energy Physics **2011** (2011), URL: https://doi.org/10.1007%2Fjhep12%282011%29117.

[23] S. D. Drell and T.-M. Yan, *Massive Lepton Pair Production in Hadron-Hadron Collisions at High-Energies*, Phys. Rev. Lett. **25** (1970) 316.

[24] G. Arnison et al., *Experimental Observation of Lepton Pairs of Invariant Mass Around 95-GeV/c**2 at the CERN SPS Collider*, Phys. Lett. B **126** (1983) 398.

[25] P. Bagnaia et al., *Evidence for $Z^0 \to e^+e^-$ at the CERN pp collider*, Physics Letters B **129** (1983) 130, ISSN: 0370-2693.

[26] J. C. Collins, D. E. Soper and G. Sterman, *All-order factorization for Drell-Yan cross sections*, Physics Letters B **134** (1984) 263, ISSN: 0370-2693.

[27] G. T. Bodwin, *Factorization of the Drell-Yan cross section in perturbation theory*, Phys. Rev. D **31** (10 1985) 2616.

[28] J. Kubar, M. Le Bellac, J. L. Meunier and G. Plaut, *QCD Corrections to the Drell-Yan Mechanism and the Pion Structure Function*, Nucl. Phys. B **175** (1980) 251.

[29] G. Altarelli, R. K. Ellis and G. Martinelli, *Leptoproduction and Drell-Yan Processes Beyond the Leading Approximation in Chromodynamics*, Nucl. Phys. B **143** (1978) 521.

[30] J. Kubar-Andre and F. E. Paige, *Gluon Corrections to the Drell-Yan Model*, Phys. Rev. D **19** (1979) 221.

[31] G. Altarelli, R. K. Ellis and G. Martinelli,
Large Perturbative Corrections to the Drell-Yan Process in QCD,
Nucl. Phys. B **157** (1979) 461.

[32] R. Hamberg, W. L. van Neerven and T. Matsuura,
A complete calculation of the order α_s^2 correction to the Drell-Yan K factor,
Nucl. Phys. B **359** (1991) 343.

[33] W. L. van Neerven and E. B. Zijlstra,
The $O(\alpha_s^2)$ corrected Drell-Yan K factor in the DIS and MS scheme,
Nucl. Phys. B **382** (1992) 11.

[34] P. J. Rijken and W. L. van Neerven,
Order α_s^2 contributions to the Drell-Yan cross-section at fixed target energies,
Phys. Rev. D **51** (1995) 44, arXiv: hep-ph/9408366.

[35] C. Anastasiou, L. J. Dixon, K. Melnikov and F. Petriello, *High precision QCD at hadron colliders: Electroweak gauge boson rapidity distributions at NNLO*,
Phys. Rev. D **69** (2004) 094008, arXiv: hep-ph/0312266.

[36] K. Melnikov and F. Petriello,
Electroweak gauge boson production at hadron colliders through $O(\alpha_s^2)$,
Phys. Rev. D **74** (2006) 114017, arXiv: hep-ph/0609070.

[37] S. Catani, L. Cieri, G. Ferrera, D. de Florian and M. Grazzini, *Vector boson production at hadron colliders: A Fully exclusive QCD calculation at NNLO*,
Phys. Rev. Lett. **103** (2009) 082001, arXiv: 0903.2120 [hep-ph].

[38] R. Gavin, Y. Li, F. Petriello and S. Quackenbush,
FEWZ 2.0: A code for hadronic Z production at next-to-next-to-leading order,
Comput. Phys. Commun. **182** (2011) 2388, arXiv: 1011.3540 [hep-ph].

[39] C. Duhr, F. Dulat and B. Mistlberger,
Drell-Yan Cross Section to Third Order in the Strong Coupling Constant,
Phys. Rev. Lett. **125** (2020) 172001, arXiv: 2001.07717 [hep-ph].

[40] C. Duhr, F. Dulat and B. Mistlberger, *Charged current Drell-Yan production at N^3LO*,
JHEP **11** (2020) 143, arXiv: 2007.13313 [hep-ph].

[41] C. Duhr and B. Mistlberger,
Lepton-pair production at hadron colliders at N^3LO in QCD, JHEP **03** (2022) 116,
arXiv: 2111.10379 [hep-ph].

[42] M. Baak et al., *The global electroweak fit at NNLO and prospects for the LHC and ILC*,
Eur. Phys. J. C **74** (2014) 3046, arXiv: 1407.3792 [hep-ph].

[43] J. de Blas et al., *Electroweak precision observables and Higgs-boson signal strengths in the Standard Model and beyond: present and future*, JHEP **12** (2016) 135,
arXiv: 1608.01509 [hep-ph].

[44] ATLAS Collaboration, *Precision measurement and interpretation of inclusive W^+, W^- and Z/γ^* production cross sections with the ATLAS detector*,
Eur. Phys. J. C **77** (2017) 367, arXiv: 1612.03016 [hep-ex].

[45] *Standard Model Summary Plots June 2021*, tech. rep., CERN, 2021, URL: https://cds.cern.ch/record/2777014.

[46] S. Catani, L. Cieri, G. Ferrera, D. de Florian and M. Grazzini, *Vector Boson Production at Hadron Colliders: A Fully Exclusive QCD Calculation at Next-to-Next-to-Leading Order*, Physical Review Letters **103** (2009).

[47] ATLAS Collaboration, *Measurements of W and Z boson production in pp collisions at* $\sqrt{s} = 5.02$ *TeV with the ATLAS detector*, Eur. Phys. J. C **79** (2019) 128, arXiv: 1810.08424 [hep-ex], Erratum: Eur. Phys. J. C **79** (2019) 374.

[48] ATLAS Collaboration, *Measurement of the Drell–Yan triple-differential cross section in pp collisions at* $\sqrt{s} = 8$ *TeV*, JHEP **12** (2017) 059, arXiv: 1710.05167 [hep-ex].

[49] ATLAS Collaboration, *Measurement of* $W^{\pm}$*-boson and Z-boson production cross-sections in pp collisions at* $\sqrt{s} = 2.76$ *TeV with the ATLAS detector*, Eur. Phys. J. C **79** (2019) 901, arXiv: 1907.03567 [hep-ex].

[50] ATLAS Collaboration, *Measurements of top-quark pair to Z-boson cross-section ratios at* $\sqrt{s} = 13, 8, 7$ *TeV with the ATLAS detector*, JHEP **02** (2017) 117, arXiv: 1612.03636 [hep-ex].

[51] CMS Collaboration, *Measurement of the differential and double-differential Drell-Yan cross sections in proton–proton collisions at* $\sqrt{s} = 7$ *TeV*, JHEP **12** (2013) 030, arXiv: 1310.7291 [hep-ex].

[52] CMS Collaboration, *Measurements of differential and double-differential Drell-Yan cross sections in proton–proton collisions at* 8 *TeV*, Eur. Phys. J. C **75** (2015) 147, arXiv: 1412.1115 [hep-ex].

[53] CMS Collaboration, *Measurement of the differential Drell–Yan cross section in proton–proton collisions at* $\sqrt{s} = 13$ *TeV*, JHEP **12** (2019) 059, arXiv: 1812.10529 [hep-ex].

[54] CMS Collaboration, *Measurements of differential Z boson production cross sections in proton–proton collisions at* $\sqrt{s} = 13$ *TeV*, JHEP **12** (2019) 061, arXiv: 1909.04133 [hep-ex].

[55] R. Aaij et al., *Measurement of the cross-section for* $Z \to e^+e^-$ *production in pp collisions at* $\sqrt{s} = 7$ *TeV*, JHEP **02** (2013) 106, arXiv: 1212.4620 [hep-ex].

[56] R. Aaij et al., *Measurement of the forward Z boson production cross-section in pp collisions at* $\sqrt{s} = 7$ *TeV*, JHEP **08** (2015) 039, arXiv: 1505.07024 [hep-ex].

[57] R. Aaij et al., *Measurement of forward* $Z \to e^+e^-$ *production at* $\sqrt{s} = 8$ *TeV*, JHEP **05** (2015) 109, arXiv: 1503.00963 [hep-ex].

[58] R. Aaij et al., *Measurement of forward W and Z boson production in pp collisions at* $\sqrt{s} = 8$ *TeV*, JHEP **01** (2016) 155, arXiv: 1511.08039 [hep-ex].

[59] R. Aaij et al., *Measurement of the forward Z boson production cross-section in pp collisions at* $\sqrt{s} = 13$ *TeV*, JHEP **09** (2016) 136, arXiv: 1607.06495 [hep-ex].

[60] R. Aaij et al., *Precision measurement of forward Z boson production in proton-proton collisions at* $\sqrt{s} = 13$ *TeV*, (2021), arXiv: 2112.07458 [hep-ex].

[61] R. Gauld, A. G.-D. Ridder, T. Gehrmann, E. Glover and A. Huss, *Precise predictions for the angular coefficients in Z-boson production at the LHC*, Journal of High Energy Physics **2017** (2017), URL: https://doi.org/10.1007%2Fjhep11%282017%29003.

[62] J. C. Collins and D. E. Soper, *Angular distribution of dileptons in high-energy hadron collisions*, Phys. Rev. D **16** (7 1977) 2219.

[63] L. Dixon, *VRAP: A program for computing rapidity distributions for production of lepton-pairs via virtual photons, W or Z bosons at hadron colliders at NNLO in QCD*, URL: https://www.slac.stanford.edu/~lance/Vrap/ (visited on 21/02/2022).

[64] T. Gleisberg et al., *Event generation with SHERPA 1.1*, Journal of High Energy Physics **2009** (2009) 007, ISSN: 1029-8479.

[65] A. Buckley et al., *General-purpose event generators for LHC physics*, Physics Reports **504** (2011) 145, ISSN: 0370-1573.

[66] T. Sjöstrand, *A model for initial state parton showers*, Physics Letters B **157** (1985) 321, ISSN: 0370-2693.

[67] T. D. Gottschalk, *Backwards evolved initial state parton showers*, Nuclear Physics B **277** (1986) 700, ISSN: 0550-3213.

[68] B. Andersson, G. Gustafson, G. Ingelman and T. Sjostrand, *Parton Fragmentation and String Dynamics*, Phys. Rept. **97** (1983) 31.

[69] T. D. Gottschalk, *A simple phenomenological model for hadron production from low-mass clusters*, Nuclear Physics B **239** (1984) 325, ISSN: 0550-3213.

[70] ATLAS Collaboration, *ATLAS Pythia 8 tunes to 7 TeV data*, ATL-PHYS-PUB-2014-021, 2014, URL: https://cds.cern.ch/record/1966419.

[71] P. Ilten, *Tau Decays in Pythia 8*, Nuclear Physics B - Proceedings Supplements **253–255** (2014) 77, ISSN: 0920-5632.

[72] G. Aad et al., *The ATLAS Simulation Infrastructure*, The European Physical Journal C **70** (2010) 823, ISSN: 1434-6052.

[73] S. Agostinelli et al., *GEANT4–a simulation toolkit*, Nucl. Instrum. Meth. A **506** (2003) 250.

[74] J. Allison, *Geant4 developments and applications*, IEEE Trans. Nucl. Sci. **53** (2006) 270, URL: https://cds.cern.ch/record/1035669.

[75] ATLAS Collaboration, *Summary of ATLAS Pythia 8 tunes*, ATL-PHYS-PUB-2012-003, 2012, URL: https://cds.cern.ch/record/1474107.

[76] P. Nason,
A New method for combining NLO QCD with shower Monte Carlo algorithms,
JHEP **11** (2004) 040, arXiv: hep-ph/0409146.

[77] S. Frixione, P. Nason and C. Oleari, *Matching NLO QCD computations with Parton Shower simulations: the POWHEG method*, JHEP **11** (2007) 070,
arXiv: 0709.2092 [hep-ph].

[78] S. Alioli, P. Nason, C. Oleari and E. Re, *A general framework for implementing NLO calculations in shower Monte Carlo programs: the POWHEG BOX*,
JHEP **06** (2010) 043, arXiv: 1002.2581 [hep-ph].

[79] S. Alioli, P. Nason, C. Oleari and E. Re,
NLO vector-boson production matched with shower in POWHEG,
JHEP **0807** (2008) 060, arXiv: 0805.4802 [hep-ph].

[80] T. Sjöstrand, S. Mrenna and P. Skands, *A brief introduction to PYTHIA 8.1*,
Computer Physics Communications **178** (2008) 852.

[81] J. Bellm et al., *Herwig 7.0/Herwig++ 3.0 release note*, Eur. Phys. J. C **76** (2016) 196,
arXiv: 1512.01178 [hep-ph].

[82] M. Bähr et al., *Herwig++ physics and manual*,
The European Physical Journal C **58** (2008) 639.

[83] T. Gleisberg et al., *Event generation with SHERPA 1.1*,
Journal of High Energy Physics **2009** (2009) 007.

[84] S. Höche, F. Krauss, S. Schumann and F. Siegert,
QCD matrix elements and truncated showers,
Journal of High Energy Physics **2009** (2009) 053.

[85] P. Golonka and Z. Was,
PHOTOS Monte Carlo: A Precision tool for QED corrections in Z and W decays,
Eur. Phys. J. **C45** (2006) 97, arXiv: hep-ph/0506026.

[86] N. Davidson, T. Przedzinski and Z. Was,
PHOTOS Interface in C++: Technical and Physics Documentation, (2010),
arXiv: 1011.0937 [hep-ph].

[87] D. J. Lange, *The EvtGen particle decay simulation package*,
Nucl. Instrum. Meth. A **462** (2001) 152.

[88] ATLAS Collaboration, *Measurement of the Z/γ^* boson transverse momentum distribution in pp collisions at $\sqrt{s} = 7$ TeV with the ATLAS detector*,
JHEP **09** (2014) 145, arXiv: 1406.3660 [hep-ex].

[89] H.-L. Lai, M. Guzzi, J. Huston, Z. Li, P. M. Nadolsky et al.,
New parton distributions for collider physics, Phys.Rev. **D82** (2010) 074024,
arXiv: 1007.2241 [hep-ph].

[90] J. Pumplin et al.,
New generation of parton distributions with uncertainties from global QCD analysis,
JHEP **07** (2002) 012, arXiv: hep-ph/0201195.

[91] ATLAS Collaboration, *Proposal for particle-level object and observable definitions for use in physics measurements at the LHC*, ATL-PHYS-PUB-2015-013, 2015,
URL: https://cds.cern.ch/record/2022743.

[92] C. Bierlich et al.,
Robust Independent Validation of Experiment and Theory: Rivet version 3,
SciPost Physics **8** (2020), ISSN: 2542-4653.

[93] L. Evans and P. Bryant, *LHC Machine*, JINST **3** (2008) S08001.

[94] E. Mobs, *The CERN accelerator complex - August 2018. Complexe des accélérateurs du CERN - Août 2018*, 2018, URL: https://cds.cern.ch/record/2636343.

[95] ATLAS Collaboration, *The ATLAS Experiment at the CERN Large Hadron Collider*, JINST **3** (2008) S08003.

[96] ATLAS Collaboration,
Studies of the performance of the ATLAS detector using cosmic-ray muons,
Eur. Phys. J. C **71** (2011) 1593, arXiv: 1011.6665 [hep-ex].

[97] ATLAS Collaboration, *Charged-particle distributions at low transverse momentum in $\sqrt{s} = 13$ TeV pp interactions measured with the ATLAS detector at the LHC*,
Eur. Phys. J. C **76** (2016) 502, arXiv: 1606.01133 [hep-ex].

[98] K. Potamianos, *The upgraded Pixel detector and the commissioning of the Inner Detector tracking of the ATLAS experiment for Run-2 at the Large Hadron Collider*,
tech. rep., CERN, 2016, arXiv: 1608.07850.

[99] M. Capeans et al., *ATLAS Insertable B-Layer Technical Design Report*, tech. rep., 2010,
URL: https://cds.cern.ch/record/1291633.

[100] ATLAS Collaboration,
Commissioning of the ATLAS Muon Spectrometer with cosmic rays,
Eur. Phys. J. C **70** (2010) 875, arXiv: 1006.4384 [hep-ex].

[101] ATLAS Collaboration, *ATLAS Forward Detectors*, 2018,
URL: https://cds.cern.ch/record/2627582 (visited on 28/03/2022).

[102] G. Avoni et al.,
The new LUCID-2 detector for luminosity measurement and monitoring in ATLAS,
JINST **13** (2018) P07017. 33 p.

[103] M. Aaboud et al., *Performance of the ATLAS Trigger System in 2015*,
Eur. Phys. J. C **77** (2017) 317, arXiv: 1611.09661 [hep-ex].

[104] ATLAS Collaboration, *ApprovedPlotsDAQ*, 2020, URL:
https://twiki.cern.ch/twiki/bin/view/AtlasPublic/ApprovedPlotsDAQ
(visited on 28/03/2022).

[105] W. Panduro Vazquez, *The ATLAS Data Acquisition system in LHC Run 2*, J. Phys. Conf. Ser. **898** (2017) 032017, ed. by R. Mount and C. Tull.

[106] G. Aad et al., *Performance of electron and photon triggers in ATLAS during LHC Run 2*, Eur. Phys. J. C **80** (2020) 47, arXiv: 1909.00761 [hep-ex].

[107] G. Aad et al., *Performance of the ATLAS muon triggers in Run 2*, JINST **15** (2020) P09015, arXiv: 2004.13447 [physics.ins-det].

[108] ATLAS Collaboration, *Measurement of the Inelastic Proton–Proton Cross Section at $\sqrt{s} = 13$ TeV with the ATLAS Detector at the LHC*, Phys. Rev. Lett. **117** (2016) 182002, arXiv: 1606.02625 [hep-ex].

[109] ATLAS Collaboration, *Luminosity determination in pp collisions at $\sqrt{s} = 13$ TeV using the ATLAS detector at the LHC*, ATLAS-CONF-2019-021, 2019, URL: https://cds.cern.ch/record/2677054.

[110] ATLAS Collaboration, *ATLAS data quality operations and performance for 2015–2018 data-taking*, JINST **15** (2020) P04003, arXiv: 1911.04632 [physics.ins-det].

[111] S. van der Meer, *Calibration of the effective beam height in the ISR*, tech. rep., CERN, 1968, URL: https://cds.cern.ch/record/296752.

[112] ATLAS Collaboration, *Luminosity determination for low-pileup datasets at $\sqrt{s} = 5$ and 13 TeV using the ATLAS detector at the LHC*, ATLAS-CONF-2020-023, 2020, URL: https://cds.cern.ch/record/2725195.

[113] I. Zurbano Fernandez et al., *High-Luminosity Large Hadron Collider (HL-LHC): Technical design report*, **10/2020** (2020), ed. by I. Béjar Alonso et al.

[114] ATLAS Collaboration, *Measurement of the W-boson mass in pp collisions at $\sqrt{s} = 7$ TeV with the ATLAS detector*, Eur. Phys. J. C **78** (2018) 110, arXiv: 1701.07240 [hep-ex], Erratum: Eur. Phys. J. C **78** (2018) 898.

[115] ATLAS Collaboration, *Prospects for the measurement of the W-boson transverse momentum with a low pileup data sample at $\sqrt{s} = 13$ TeV with the ATLAS detector*, ATL-PHYS-PUB-2017-021, 2017, URL: https://cds.cern.ch/record/2298152.

[116] ATLAS Collaboration, *Event Displays from Run 2 physics*, 2021, URL: https://twiki.cern.ch/twiki/bin/view/AtlasPublic/EventDisplayRun2Physics (visited on 28/03/2022).

[117] ATLAS Collaboration, *Luminosity Public Results Run-2*, 2020, URL: https://twiki.cern.ch/twiki/bin/view/AtlasPublic/LuminosityPublicResultsRun2 (visited on 28/03/2022).

[118] A. Salzburger, *The ATLAS Track Extrapolation Package*, tech. rep., CERN, 2007.

[119] ATLAS Collaboration, *Charged-particle distributions in $\sqrt{s} = 13$ TeV pp interactions measured with the ATLAS detector at the LHC*, Phys. Lett. B **758** (2016) 67, arXiv: 1602.01633 [hep-ex].

[120] G. Aad et al., *Alignment of the ATLAS Inner Detector in Run-2*, Eur. Phys. J. C **80** (2020) 1194, arXiv: 2007.07624 [hep-ex].

[121] R. Frühwirth, *Application of Kalman filtering to track and vertex fitting*, Nuclear Instruments and Methods in Physics Research Section A: Accelerators, Spectrometers, Detectors and Associated Equipment **262** (1987) 444, ISSN: 0168-9002.

[122] ATLAS Collaboration, *A neural network clustering algorithm for the ATLAS silicon pixel detector*, JINST **9** (2014) P09009, arXiv: 1406.7690 [hep-ex].

[123] ATLAS Collaboration, *Study of the material of the ATLAS inner detector for Run 2 of the LHC*, JINST **12** (2017) P12009, arXiv: 1707.02826 [hep-ex].

[124] S. Boutle et al., *Primary vertex reconstruction at the ATLAS experiment*, J. Phys. Conf. Ser. **898** (2017) 042056, ed. by R. Mount and C. Tull.

[125] ATLAS Collaboration, *Electron reconstruction and identification in the ATLAS experiment using the 2015 and 2016 LHC proton-proton collision data at $\sqrt{s} = 13$ TeV*, Eur. Phys. J. C **79** (2019) 639. 40 p, arXiv: 1902.04655.

[126] G. Aad et al., *Electron and photon performance measurements with the ATLAS detector using the 2015–2017 LHC proton-proton collision data*, JINST **14** (2019) P12006, arXiv: 1908.00005 [hep-ex].

[127] W. Lampl et al., *Calorimeter Clustering Algorithms: Description and Performance*, ATL-LARG-PUB-2008-002, 2008, URL: https://cds.cern.ch/record/1099735.

[128] ATLAS Collaboration, *Improved electron reconstruction in ATLAS using the Gaussian Sum Filter-based model for bremsstrahlung*, ATLAS-CONF-2012-047, 2012, URL: https://cds.cern.ch/record/1449796.

[129] G. Aad et al., *Muon reconstruction and identification efficiency in ATLAS using the full Run 2 pp collision data set at $\sqrt{s} = 13$ TeV*, Eur. Phys. J. C **81** (2021) 578, arXiv: 2012.00578 [hep-ex].

[130] J. Schmaler, *Test and Alignment of the ATLAS Precision Muon Chambers*, (2007).

[131] ATLAS Collaboration, *Electron and photon energy calibration with the ATLAS detector using data collected in 2015 at $\sqrt{s} = 13$ TeV*, ATL-PHYS-PUB-2016-015, 2016, URL: https://cds.cern.ch/record/2203514.

[132] ATLAS Collaboration, *Electron and photon energy calibration with the ATLAS detector using 2015–2016 LHC proton–proton collision data*, JINST **14** (2019) P03017, arXiv: 1812.03848 [hep-ex].

[133] ATLAS Collaboration, *Electron and photon performance measurements with the ATLAS detector using the 2015–2017 LHC proton–proton collision data*, JINST **14** (2019) P12006, arXiv: 1908.00005 [hep-ex].

[134] T. Xu, H. Atmani and L. Aperio Bella, *Electron corrections for low pile-up runs taken in 2017 and 2018*, tech. rep., CERN, 2019, URL: https://cds.cern.ch/record/2657152.

[135] A. Sydorenko, J. A. Kremer and T. Xu, *Muon corrections for low pile-up runs taken in 2017 and 2018*, tech. rep., CERN, 2019, URL: https://cds.cern.ch/record/2657116.

[136] ATLAS Collaboration, *Muon reconstruction performance of the ATLAS detector in proton–proton collision data at* $\sqrt{s} = 13$ *TeV*, Eur. Phys. J. C **76** (2016) 292, arXiv: 1603.05598 [hep-ex].

[137] G. Aad et al., *Alignment of the ATLAS Inner Detector in Run-2*, Eur. Phys. J. C **80** (2020) 1194, arXiv: 2007.07624 [hep-ex].

[138] ATLAS Collaboration, *Studies of radial distortions of the ATLAS Inner Detector*, ATL-PHYS-PUB-2018-003, 2018, URL: https://cds.cern.ch/record/2309785.

[139] ATLAS Collaboration, *Study of alignment-related systematic effects on the ATLAS Inner Detector track reconstruction*, ATLAS-CONF-2012-141, 2012, URL: https://cds.cern.ch/record/1483518.

[140] T. Xu, 'Measurements of W boson properties at $\sqrt{s}$=5 and 13 TeV with the ATLAS detector at the LHC', PhD thesis: USTC, Hefei, 2019.

[141] ATLAS Collaboration, *MCPAnalysisGuidelinesMC15*, 2018, URL: https://twiki.cern.ch/twiki/bin/view/AtlasProtected/MCPAnalysisGuidelinesMC15 (visited on 28/03/2022).

[142] M. Krasny, J. Chwastowski and K. Słowikowski, *Luminosity measurement method for LHC: The theoretical precision and the experimental challenges*, Nuclear Instruments and Methods in Physics Research Section A: Accelerators, Spectrometers, Detectors and Associated Equipment **584** (2008) 42, ISSN: 0168-9002.

[143] V. Khoze, *Indirect luminosity measurements: theoretical assessment. Selected topics on the precision of luminometry at the LHC (as seen through the theorist's eyes)*, tech. rep., 2011, URL: https://cds.cern.ch/record/1357845 (visited on 28/03/2022).

[144] *Luminosity Determination using* $Z \to \ell\ell$ *events at* $\sqrt{s} = 13$ *TeV with the ATLAS detector*, tech. rep., CERN, 2021, URL: https://cds.cern.ch/record/2752951.

[145] Y. Li and F. Petriello, *Combining QCD and electroweak corrections to dilepton production in the framework of the FEWZ simulation code*, Physical Review D **86** (2012), ISSN: 1550-2368, URL: http://dx.doi.org/10.1103/PhysRevD.86.094034.

[146] T.-J. Hou et al., *New CTEQ global analysis of quantum chromodynamics with high-precision data from the LHC*, 2019, arXiv: 1912.10053 [hep-ph].

[147] ATLAS Collaboration,
Measurement of the transverse momentum distribution of Drell–Yan lepton pairs in proton–proton collisions at $\sqrt{s} = 13$ TeV with the ATLAS detector, (2019),
arXiv: 1912.02844 [hep-ex].

[148] D. M. Walker,
'Higher Order QCD Corrections to Electroweak Boson Production at Colliders',
PhD thesis: Durham U., 2019.

[149] T. Adye, *Unfolding algorithms and tests using RooUnfold*, 2011,
arXiv: 1105.1160 [physics.data-an].

[150] G. D'Agostini, *Improved iterative Bayesian unfolding*, 2010,
arXiv: 1010.0632 [physics.data-an].

[151] B. Efron, *Bootstrap Methods: Another Look at the Jackknife*,
The Annals of Statistics **7** (1979) 1.

[152] ATLAS Collaboration, *Measurement of the angular coefficients in Z-boson events using electron and muon pairs from data taken at $\sqrt{s} = 8$ TeV with the ATLAS detector*,
JHEP **08** (2016) 159, arXiv: 1606.00689 [hep-ex].

[153] S. Camarda et al., *DYTurbo: fast predictions for Drell-Yan processes*,
The European Physical Journal C **80** (2020).

[154] A. Glazov, *HERAverager package*, 2015,
URL: https://wiki-zeuthen.desy.de/HERAverager/HERAverager (visited on 28/03/2022).

List of Figures

List of Tables